MICRO-MECHANICAL APPROACHES FOR THE HIERARCHICAL MODELING OF SOFT BIOLOGICAL TISSUES

by

Theresa Koys Tonge

A dissertation submitted to The Johns Hopkins University in conformity with the requirements for the degree of Doctor of Philosophy.

Baltimore, Maryland

October 6, 2014

Abstract

Load-bearing soft tissues are abundant throughout the human body, including diverse examples such as skin, cornea, tendons, and blood vessels. The mechanical characterization of these tissues is important for applications such as tissue engineering, tissue pathology, and medical device/patient interface modeling. The mechanical properties of soft tissues arise from the underlying collagen microstructure, which varies across the body depending on tissue function. Such specialized microstructures are thought to arise in part from the ability of soft tissues to self-adapt to the mechanical environment by a process known as growth and remodeling. Growth and remodeling is a normal part of development and tissue maintenance, however, it is suspected that an imbalance in the process may contribute to disease states such as osteoarthritis and glaucoma. Though growth and remodeling is well documented, the mechanisms driving the process are not well understood.

This work develops a hierarchical, structure-based modeling approach for planar collagenous tissues based on the underlying collagen microstructure. The approach was applied both to characterize human skin mechanics for prosthetic/residual limb

ABSTRACT

interface modeling, and to simulate potential fiber-level mechanisms of the growth and remodeling process. The nonlinear, anisotropic properties of human skin tissues were measured with full-field inflation testing, and two different structure-based constitutive models were fit to the data using a novel analytical method to account for bending stresses. Finite element analysis was used to show that only the fully integrated distributed fiber model was could reproduce the experimentally measured anisotropy of skin tissue. To investigate potential mechanisms of growth and remodeling, the fully integrated model was extended to incorporate a micro-mechanical description of the collagen fibers. This enabled the prescription of fiber-level evolution equations for strain-protected enzymatic degradation and constant collagen deposition as potential mechanisms of the growth and remodeling process. The degradation model was calibrated to fibril-level experiments and used to predict tissue-level experiments for model validation. Strain homeostasis was achieved when the degradation model was paired with constant collagen deposition, supporting these two mechanisms as potential mechanisms of the growth and remodeling process.

ABSTRACT

Primary Reader:

Thao D. Nguyen, Associate Professor, The Johns Hopkins University

Secondary Readers:

Jeffrey W. Ruberti, Professor, Northeastern University

Kevin J. Hemker, Professor, The Johns Hopkins University

Acknowledgments

This dissertation would not be possible without the contributions of many others. First of all I would like to thank my thesis advisor, Prof. Vicky Nguyen at The Johns Hopkins University. Prof. Nguyen took me on as a graduate student in biomechanics despite my lack of a mechanical engineering background and provided excellent technical guidance, support and motivation throughout the course of this work, in addition to funding my graduate studies. I also received guidance from Dr. Liming Voo of the Johns Hopkins Applied Physics Lab on the development of the inflation testing apparatus, and from Prof. Jeffrey Ruberti of Northeastern University for many helpful conversations and insights in the development of the enzymatic degradation model. I would also like to acknowledge the readers of this dissertation for their time and attention: Prof. Vicky Nguyen, Prof. Jeffrey Ruberi, and Prof. Kevin Hemker.

I thank my labmates, past and present, for their advice and support in this work. In particular, I'd like to thank my contemporaries: Baptiste Coudrillier, Rui Xiao, Kimberly Ziegler, and Barbara Murienne. I have greatly enjoyed working with this group over the years, both professionally and as friends. Our many conversations,

both scientific and otherwise, greatly helped the completion of this work. It has also been wonderful to get to know our newer lab members over the past two years: Aurélie Azoug (who proofread this thesis), Caroline Forsell, Sarah Bentil, Dan Midgett, and Jinkai Gou. Finally, I must acknowledge Prof. Kristen Myers, a former post-doc in our lab and now an assistant professor at Columbia University, for her patience and helpful advice in my first year of graduate school.

Several Johns Hopkins undergraduate students also contributed to this work. Lorre Atlan carried out many of the final skin inflation tests and the humidity study. William Rothkopf carried out several skin tests for the preconditioning study. Stephen Alexander prepared a very helpful literature review on skin biomechanics the summer prior to my arrival in the lab, and also contributed experimental data to the preconditioning paper.

I am also grateful for my funding sources. My studies were partially funded by a Medtronic Student Scholar Fellowship, Whiting School Doctoral Fellowship, and a Mechanical Engineering Departmental Fellowship, which enabled flexibility in determining my thesis topic. My work was also funded by grants awarded to awarded to Prof. Nguyen, including a Johns Hopkins Whiting School - Applied Physics Laboratory Partnership grant, an NIH Public Health Service Research grant, and an NSF CAREER grant.

Finally, I thank my family. My parents, Dan and Mary Koys, and sister, Jennifer Koys, fielded many phone calls and text messages throughout this process, and I

am grateful for their advice and support. Most importantly, I must thank my husband, Andy, for his constant support, patience, good humor, and many home cooked dinners. It is not an exaggeration to say I could not have done this without him.

Dedication

This thesis is dedicated to my husband, Andy, who made it all possible.

Contents

List of Tables

List of Figures

Chapter 1

Introduction

The human body is a versatile mechanical system, optimized over thousands of years of evolution for the often competing goals of strength and dexterity. For example, the design of the limbs allows for fine motor control and a wide range of motion, but leaves the joints at a mechanical disadvantage: a load carried in the hand will lead to nearly ten-fold higher reaction forces in the elbow muscles and joints.[1] To compensate, the tissues of the arm, such as bone, muscle, and tendons, have been optimized for both strength and structural efficiency. Though bone is often considered the key load bearing tissue of the body, soft tissues also have an important mechanical role. Soft connective tissues include such diverse examples as tendons and ligaments, which transmit high tensile loads between bone and muscle, as well as skin, which allows a wide range of motion while simultaneously providing a protective barrier for internal organs. Ocular tissues such as the sclera and the cornea protect the delicate

internal components of the eye from external loading, and arteries resist shear forces and pressure arising from blood flow. The mechanical properties of these materials are derived from complex collagen microstructures, which can exhibit large variation between tissues. Because the mechanical properties of human tissues are critical for proper function, quantifying these properties with respect to the microstructure can lead to a better understanding of both healthy and diseased tissue function.

Living tissues are also capable of changing both mass and microstructure in response to the mechanical environment. This process, referred to as growth and remodeling, occurs on the order of weeks or months and serves to re-enforce loaded tissues and prune under-utilized tissues. Growth and remodeling is part of the normal maintenance of healthy tissue and likely plays a major role in the development of the unique tissue microstructures found throughout the body.[2] It has also been hypothesized that an imbalance in the growth and remodeling process may give rise to disease states such as osteoarthritis, cardiac hypertrophy, and glaucoma.[2–4] The societal cost of these diseases is difficult to overstate: 20 million Americans suffer form osteoarthritis at an estimated productivity loss of $60 billion per year,[5] and glaucoma is the second leading cause of blindness globally.[6] Although growth and remodeling is well documented, the underlying mechanisms driving the process are not well understood.[7]

This work focuses on soft tissues, specifically hydrated, collagen-based tissues that undergo large deformations (>1% strain) with load. Soft tissues exhibit a nonlinear

and anisotropic elastic response that is not well described by models for traditional engineering materials, necessitating the development of new constitutive theories. Soft tissues can also exhibit large variation in the elastic response between specimens. Constitutive models for soft tissues are important for a wide range of applications, including medical device-patient interface modeling, surgical planning, and tissue engineering. Further, models that link the mechanical response to the tissue microstructure allow for more generalized frameworks which can then be specified to the tissue of interest. A structure-based modeling framework to describe the mechanical properties of soft tissue could be utilized to describe both passive tissue mechanics as well as the active change in properties brought about by growth and remodeling. Structure-based models are also better suited for understanding human development, predicting disease state progression, and other applications associated with a change in the tissue microstructure.

This thesis develops a hierarchal model for planar collagenous tissues based on the underlying collagen microstructure. Planar tissues are characterized by a collagen fiber network oriented parallel to the tissue surface, and are modeled in a continuum, hyperelastic framework as composites of collagen fibers in a soft isotropic ground matrix. First, a fiber-composite style model which describes the arrangement of individual fibers is applied to characterize human skin tissues for prosthetic/patient interface model applications (Chapters 2-3). The model is then extended to include collagen fiber micro-mechanics in order to simulate potential micro-mechanisms for

the growth and remodeling process (Chapters 4 -5). In both cases, the model assumptions and resulting parameters are validated by predicting experimental data gathered in this work or available in the literature. Such an approach can give insight into the physical processes underlying tissue development and disease state progression, with the potential to identify new therapeutic targets and interventions for pathologies such as glaucoma.

1.1 Soft Tissue Material Properties

This section reviews the microstructure, mechanical properties, and common mechanical testing methods for soft planar tissues. Skin, the cornea (the translucent protective layer covering the lens of the eye), and the sclera (the white outer shell of the eye) are used as illustrative examples. All three can be considered planar tissues, with collagen fibers primarily oriented parallel to the tissue surface.

1.1.1 Microstructure of Soft Tissues

Soft tissues are composed of a network of crimped collagen fibers embedded in a compliant ground matrix of elastin and proteoglycans. Collagen is the primary load-bearing component of soft tissue, and has a complex hierarchal structure, illustrated in Fig. 1.1. Amino acids form the tropocollagen triple helix. The tropocollagen molecules then assemble into fibrils, which in turn pack into fibers. Collagen fibers,

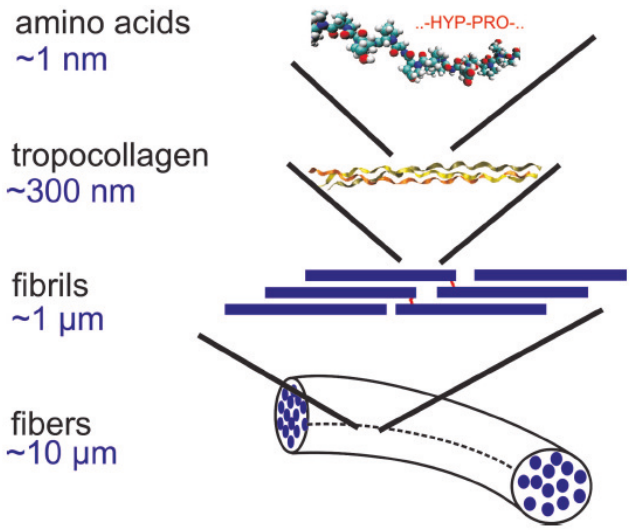

Figure 1.1: Hierarchal structure of collagen fibers. Reprinted from Buehler 2006 with permission (Copyright (2006) National Academy of Sciences, U.S.A.).[8]

the functional unit of interest in this work, are stiff in axial tension ($E = 1$ GPa), complaint under bending, and buckle under compressive forces.[9] Collagen fibers dominate the nonlinear, anisotropic large-strain response of soft tissues. The small-strain response is determined by the ground matrix, which is primarily composed of elastin and proteoglycans. Elastin is a linear elastic, fibrous protein that is stiffer than collagen at low strains, but significantly more compliant at high strains ($E = 3$ KPa). Elastin provides the recoil observed after tissue extension, and elastin fibers are often preferentially arranged in tissues. For example, elastin fibers in both the sclera and the arteries are arranged circumferentially in the plane of the tissue. Proteoglycans are large, highly charged proteins which retain water in the tissue, providing compressive strength and nearly incompressible elastic deformations.[9] Together, elastin

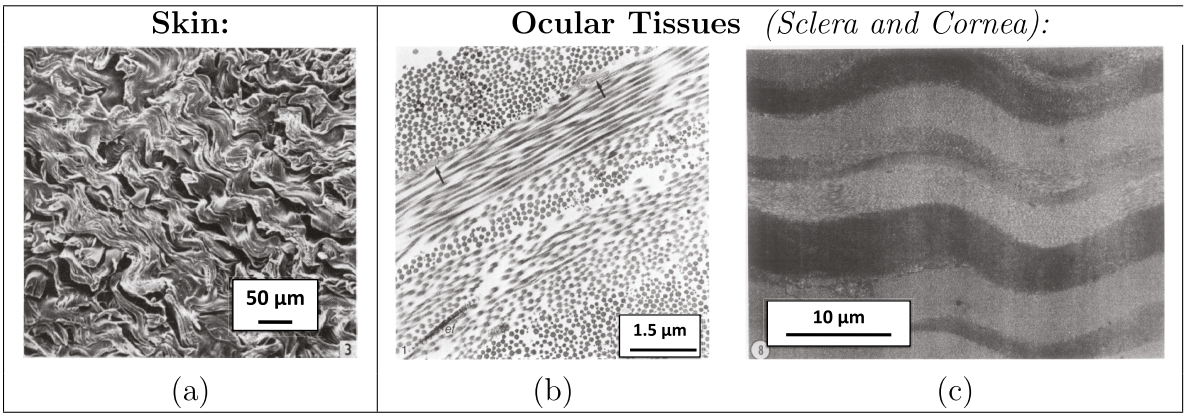

Figure 1.2: SEM images of: (a) crimped, aligned collagen fibers in human skin dermis, reprinted from Brown 1972 with permission from Wiley,[10] (b) stacked, alternating layers of fibers (lamellae) of rabbit sclera, reproduced from Young 1985 with permission from the Journal of Cell Science,[11] and (c) wavy lamellae in rabbit cornea, reprinted from Gallagher 1977 with permission from Elsevier.[12]

and proteoglycans constitute the ground matrix of the tissue.

The morphology of collagen fibers is specific to function and varies between tissues. Scanning electron microscopy images for skin, sclera, and cornea are shown in Fig. 1.2.[10] The collagen fibers of skin exhibit a high degree of initial undulation, or crimp, and the fibers are strongly aligned with the dominant fiber direction, which is diagonal in Fig. 1.2(a). In contrast, the collagen fibers in ocular tissues are arranged in alternating layers, or lamellae, shown in Fig. 1.2(b).[11] Like the collagen fibers of skin, lamellae can also exhibit an intrinsic crimp, though to a smaller degree , shown in Fig. 1.2(c).[12] The variety in collagen morphology between these three tissues arises from differences in tissue function. Skin tissue exhibits greater collagen fiber undulation to accommodate the large deformations necessary for normal movement, while ocular tissues undergo much smaller deformations in response to external loading and

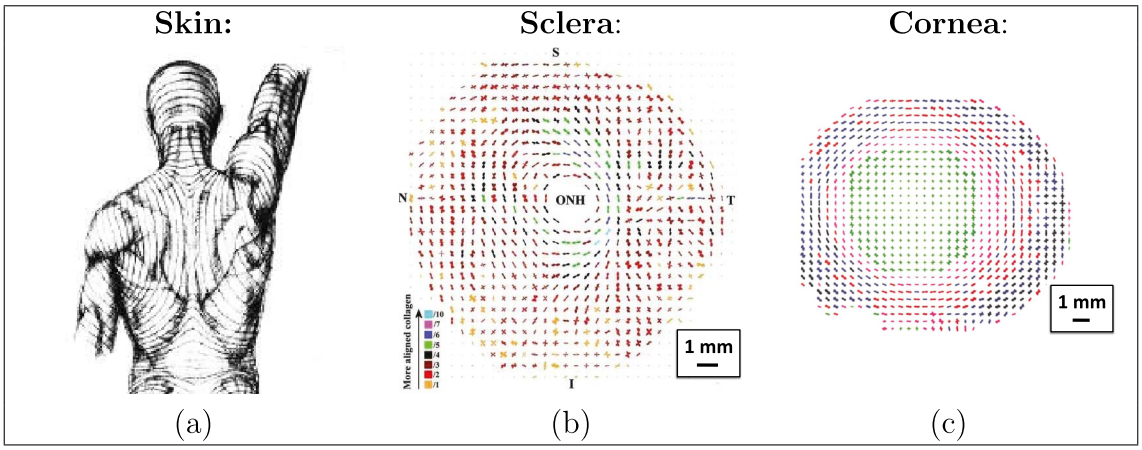

Figure 1.3: Schematic of local fiber orientations: (a) Langer's lines in for the skin of the back, reprinted from Courtiss et al. with permission from copyright holder,[13] (b) Polar plot of locally varying posterior sclera structure from Xray scatter data, reprinted from Pijanka et al. with permission from ARVO,[14] (c) plot of locally varying cornea structure from Xray data, reprinted from Aghamohammadzadeh et al. with permission from Elsevier.[15]

fluctuations in intraocular pressure.

The arrangement and strength of alignment of collagen fibers in the ground matrix also varies by tissue. Skin, cornea, and sclera all exhibit structural anisotropy arising from the collagen network. In skin, collagen fibers are strongly aligned, with the dominant direction determined by the location of the body. For example, Fig. 1.3(a) illustrates the dominant fiber direction for the skin of the back. On the lower back, collagen fibers are oriented from the left to right, while on the upper back, fibers are oriented diagonally.[16] Although the fiber direction varies with region, the fiber structure is approximately uniform within a representative area and through the thickness of the tissue. For comparison, Figs. 1.3(b) and (c) plot of the fiber orientation and the strength of alignment obtained from X-ray diffraction data for the

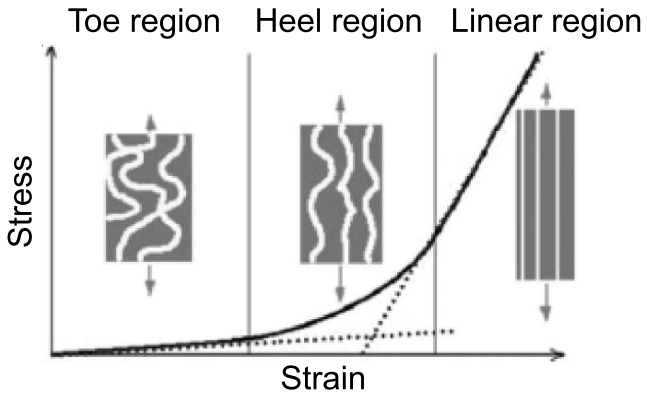

Figure 1.4: Schematic of typical nonlinear stress-strain curve for collagenous tissue as function of microstructure, reprinted from Delalleau et al. with permission from Wiley.[17]

posterior sclera and the cornea. These tissues show greater structural variation over a small area. The fibers of the sclera are aligned in ring around the optic nerve head,[14] and become more randomly oriented toward the equator. In contrast, the central region of the cornea is nearly isotropic, with fibers becoming more strongly aligned at the outer circumference, or limbus, where the cornea attaches to the sclera.[15] Differences between tissue structure can be explained by function. For example, the left-to-right fiber orientation for the skin of the lower back allows for greater flexibility along the spine. The circumferential orientation of fibers in the posterior sclera reinforces the tissue at the stress concentration caused by the mismatch between the optic nerve head and scleral material properties. Similarly the fiber structure of the cornea becomes more aligned at the limbus due to the change in curvature.

1.1.2 Mechanical Properties and Test Methods

The nonlinear stress-strain behavior of soft tissues is closely associated with the orientation and morphology of the collagen fibers. Figure 1.4 is a schematic of a typical uniaxial stress-strain curve compared to the collagen deformation for a generic planar collagenous tissue. The initial compliant region, referred to as the toe region, is dominated by the deformation of the ground matrix as the crimped collagen fibers do not contribute significantly to the stress response. As the strain increases, the tissue stiffens as the collagen fibers begin to straighten and carry load, referred to as the heel region. Finally, the stress-strain curve becomes linear as the entire load is carried by the fully straightened collagen fibers.[17] Tissues with preferentially aligned fibers will exhibit a nonlinear anisotropic stress-strain response that is stiffer in the dominant fiber direction than an in-plane perpendicular direction. Because fibers are not perfectly aligned, the perpendicular direction will also exhibit nonlinearity caused by the straightening of the collagen fibers, though with lower stiffness.

The most common mechanical test for soft tissues is the uniaxial tension test. Uniaxial tension tests are attractive because the experimental set-up and stress analysis are simple. However, uniaxial loading is not representative of the *in vivo* loading state for many tissues, and anisotropy cannot be measured from a single test. Instead, biaxial testing has become a widely used method to measure the anisotropic response of soft tissues. Like uniaxial loading, biaxial tension allows for simple stress analysis, but two orthogonal loading directions can be applied simultaneously. Loading, illus-

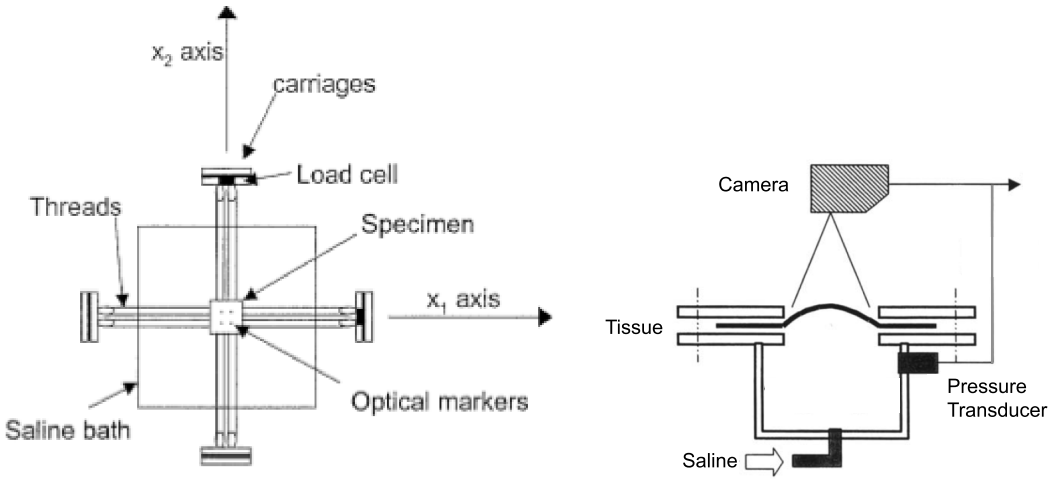

(a) (b)

Figure 1.5: (a) Schematic of typical biaxial testing set-up, reprinted from Sacks 2000 with permission from Springer,[18] (b) Schematic of typical inflation test, adapted from Li et al. with permission from Wiley.[19]

trated in Fig. 1.5 (a), is typically applied by a system of sutures or clamps applied to the edges of a square specimen and controlled by motorized pulleys or motors. Biaxial testing has been applied to a variety of planar tissues including skin,[20] pericardium,[21] and aortic valves,[22] though the boundary conditions for all schemes are complicated.

A biaxial stress state can also be achieved with inflation, or bulge, testing. The inflation test has a relatively simple set-up compared to biaxial testing and has been used for a variety of thin tissues such as pericardium,[23] arteries,[24] and cornea.[25] The tissue is clamped or glued to a fixture and pressurized with saline, illustrated in Fig. 1.5 (b), achieving a state of biaxial stress at the apex of the tissue. Unlike biaxial testing, the results of the inflation test directly identify the stiffest direction of the tissue, as the material directions to be compared are not predetermined. Further,

previous studies in our group have suggested that tissues tested by inflation do not exhibit a phenomenon known as preconditioning.[26]

Preconditioning for soft tissues is defined as a shift in the stress-strain curve with repeated loading which eventually converges to a steady state. Preconditioning is commonly observed for uniaxial and biaxial tension tests and has been incorporated into many experimental protocols to ensure a repeatable reference state. Although the origin of this phenomenon is unknown, preconditioning is suspected to arise from an alteration in the fiber structure due to repeated loading,[27] and it is desired to avoid such changes from the *in vivo* fiber structure. It is hypothesized that the inflation test better constrains the boundary of the tissue, which may prevent micro structural rearrangements, providing a more accurate measure of tissue properties. For these reasons, the inflation test method is selected to measure the anisotropic properties of human skin tissues. A more detailed review of inflation testing and preconditioning can be found in Chapters 2 and 6.

1.2 Constitutive Modeling

A variety of constitutive relations have been developed to capture the nonlinear, anisotropic mechanical behavior of planar collagenous tissues. In this work, only the elastic properties of soft tissues will be considered while neglecting viscoelastic effects. Two types of constitutive models are considered: tissue models, which describe

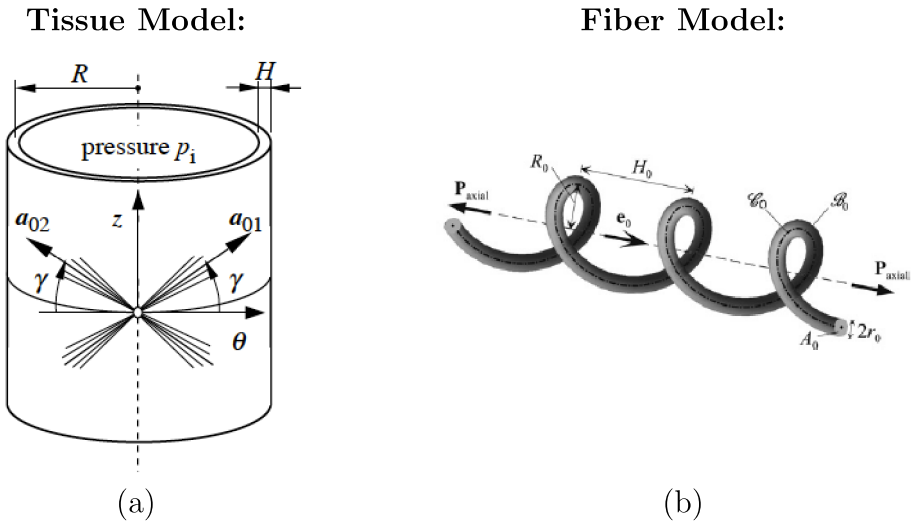

Figure 1.6: (a) Example of a structurally-inspired tissue modeling approach for an artery with two fiber distributions ($\mathbf{a}_{01}$ and $\mathbf{a}_{02}$). Reprinted from Gasser et al. with permission from the Royal Society.[28] (b) Example of a collagen fiber-level model, with parameters for fiber radius and crimp. Reprinted from Grytz et al. with permission from Elsevier.[29]

the bulk mechanical properties of soft tissues, and fiber models, which describe the mechanical behavior of individual collagen fibers. Tissue models, illustrated in Fig. 1.6 (a), are often structurally inspired, with parameters describing the fiber organization and mechanical contribution without explicitly modeling fiber deformation mechanisms. These models have great utility in describing macroscopic behavior and can be incorporated into organ-level or full body models. In contrast, fiber models, illustrated in Fig. 1.6 (b), describe the deformation mechanisms of collagen fibers directly, with model parameters relating to the fiber geometry and stiffness. These models are particularly useful to gain insights into fiber-level processes, and can be incorporated into tissue models to predict tissue-level deformations based on fiber-level mechanics. The greater computational cost of fiber models is typically prohibitive for

use in organ or full body modeling.

1.2.1 Tissue Models

Soft tissues are most commonly modeled using the theory of hyperelasticity. Given an expression for the strain energy density, Ψ, the stress for any deformation state can be computed from the deformation gradient, $\mathbf{F}$, the jacobian of the deformation gradient, $J = \det \mathbf{F}$, and the derivative of the strain energy density function with respect to the right Cauchy-Green strain tensor, $\mathbf{C} = \mathbf{F^T F}$. For a transversely isotropic material with one fiber family, the strain energy density can be written in terms of both the right Cauchy-Green strain tensor, $\mathbf{C}$, and a structure tensor, $\mathbf{A} = \mathbf{a}_0 \otimes \mathbf{a}_0$, where $\mathbf{a}_0$ is a vector defining the fiber family orientation.[30] To ensure objectivity, the strain energy density is expressed in terms of the invariants of $\mathbf{C}$ and $\mathbf{A}$ (i.e., $I_1 = \mathbf{C} : \mathbf{I}$, $I_2 = \frac{1}{2}\left[(\mathbf{C} : \mathbf{I})^2 - \mathbf{C}^2 : \mathbf{I}\right]$, $I_3 = \det \mathbf{C}$, $I_4 = \mathbf{C} : \mathbf{A}$, and $I_5 = \mathbf{C}^2 : \mathbf{A}$ for transversely isotropic materials), with the resulting Cauchy stress is computed by:

$$\sigma = \frac{2}{J}\mathbf{F}\frac{\partial \Psi(\mathbf{C}, \mathbf{A})}{\partial \mathbf{C}}\mathbf{F}^T. \tag{1.1}$$

The key differentiation between tissue constitutive models is the choice of strain energy density function. Soft tissues were first described using strain energy density functions developed for rubbers, such as the Neo-Hookean or Mooney-Rivlin potentials. In the 1970's, Y. C. Fung pioneered a new strain energy function that could

capture both the high degree of nonlinearity and anisotropy characteristic of soft tissuse.[31–33] Specifically, it was shown that the derivative of the tissue stress with respect to strain increased linearly with applied strain, supporting an exponential form of the strain energy density. The exponential dependence of the strain energy on strain proposed by Fung required 5 parameters for a transversely isotropic material, and 9 parameters for an orthotropic material. The model is purely phenomenological, and the parameters do not have a physical interpretation. However, the Fung model has had broad utility describing the mechanical behavior of a variety of soft tissues ranging from the arterial wall[34,35] to skin tissue.[32] The applicability to a wide range of tissues has made the Fung model a popular choice for describing soft tissues, and various formulations of the exponential dependence have since been proposed.[33] However, the large number of parameters without physical interpretation has led other researchers to propose structural models of the tissue strain energy density.

Lanir[36,37] was the first to model the mechanical response as a function of the tissue microstructure. In this approach, the collagen fiber contribution is modeled as a statistical distribution of fibers, $\rho(\phi)$, about a preferred fiber orientation in an isotropic ground matrix. By assuming an affine deformation, i.e. all components of the tissue are subject to the same deformation gradient, the tissue strain energy density can be written as a sum of an isotropic ground matrix contribution and the integral of individual fiber contributions oriented at an angle ϕ from the preferred

fiber orientation:

$$\Psi = \Psi_{matrix} + \int_{-\pi}^{\pi} \Psi_{fib}(\phi)\, \rho(\phi) d\phi. \tag{1.2}$$

The strain energy of the ground matrix, Ψ_{matrix} is commonly described by a Neo-Hookean potential, while the strain energy of individual collagen fibers, Ψ_{fib}, is described by a phenomenological exponential function of the stretch along the fiber direction, ϕ. This continuum approach builds upon the work of Fung by linking mechanical properties to the collagen fiber structure through the use of a structure tensor, reducing the number of parameters. However, the presence of the integral in eq. (1.2) increases the computational time for the model.

In 2006, Gasser and coworkers proposed a model based on a generalized structure tensor to greatly reducing computational time while still modeling the collagen fiber distribution.[28] In this model, the fiber distribution of eq. (1.2) is integrated one time in the reference configuration. The result is decomposed into a linear combination of the isotropic and anisotropic contribution and stored in a generalized structure tensor used for all stress calculations, eliminating the need to evaluate the integral at every time-step. The generalized structure tensor model was developed for arteries, which are typically described by two minimally dispersed fiber families. However, the model has since been widely applied to many other tissues with very different fiber structures such as skin[38] and cornea.[39] Several authors have compared the generalized structure tensor model to the fully integrated formulation of eq. 1.2 and found that the two are only equivalent in certain cases[40,41] and therefore the model may not be

appropriate for all planar tissues. In this work, both the distributed fiber model and the generalized structure tensor model will be applied to model skin tissue and finite element analysis will be used to investigate which model is better able to capture the anisotropic properties of the tissue. A more detailed review of soft tissue modeling approaches and application to skin tissue is provided in Chapter 3.

1.2.2 Fiber Models

All of the tissue-level models described in the previous section rely on phenomenological exponential functions for the fiber strain energy contribution. Alternatively, the structure and deformation mechanics of collagen fibers can be modeled, with physically meaningful parameters. Such micromechanical models capture collagen crimp by describing fibers as helical springs[29,42,43] or planar sinusoidal elastica beams.[43–45] The fiber material is assumed to be linear elastic, with the characteristic nonlinearity arising instead from the fiber crimp. Model parameters include the fiber radius, crimp, and elastic stiffness. However, the equilibrium equations for these geometries requires the solution of a 4th order partial differential equation.[46] A variety of techniques have been applied to simplify the problem, such as using free parameters to define the transition between simple bending and axial stretching,[29,42,43] or assuming that the deformed configuration occurs at the minimal strain energy configuration.[44] Alternatively, Comninou and Yannas[45] showed that the equilibrium equations for a planar sinusoidal elastica can be simplified for the case of a thin beam with small

initial curvature to model individual collagen fibers.

Though micro-mechanical fiber models provide a more detailed description of collagen fiber mechanics, these models also require more parameters and often require computationally expensive numerical solutions for fiber deformation. Incorporating fiber models into the tissue models described in the previous section can be prohibitive for many applications. As such, there has been limited work implementing fiber-level models into tissue-level simulations. Exceptions include the incorporation of a micro-mechanical model into simulations of the lamina cribrosa[47] and scleral shell[48] using the generalized structure tensor model of Gasser et al,[28] but the majority of the fiber models described above have not been incorporated into tissue level simulations. To address this gap, this work will incorporate the planar elastica model of Comninou and Yannas[45] into a tissue-level framework to study potential micro-mechanisms of the growth and remodeling process.

1.3 Growth and Remodeling

This review thus far has focused on the passive or static properties of soft tissues. Section 1.1.1 illustrated that a specific tissue's microstructure can often be directly related to the tissue's mechanical function in the body. Such specialized fiber structures are developed and maintained by the growth and remodeling process by which the tissue self-adapts to the mechanical environment. Growth and remodeling, illustrated in

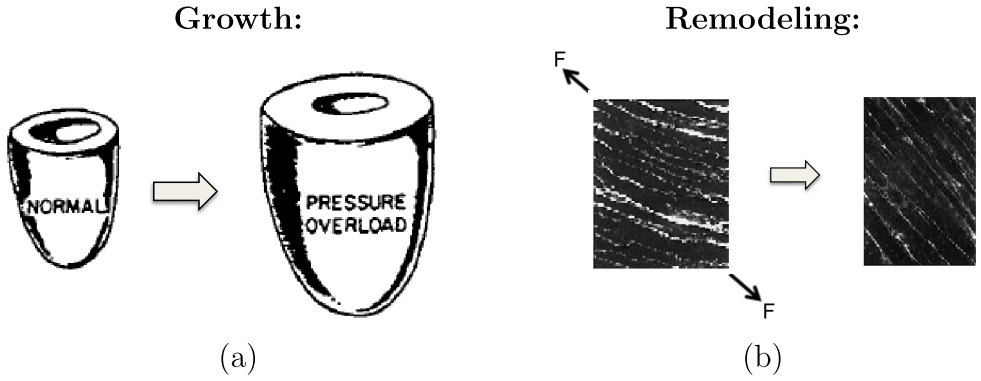

Figure 1.7: (a) Example of increase in bulk tissue volume in the heart in response to pressure overload (Growth), modified from Grossman et al. with permission from Elsevier,[49] and (b) Example of a change in the microstructural alignment of collagen in response to a change in local loading state (Remodeling), modified from Ju et al. with permission from Oxford University Press[50] .

Fig. 1.7, are defined as distinct but related processes that often occur simultaneously in response to the same mechanical stimuli. In this work, growth refers to a change in total tissue mass, while remodeling refers to a change in material properties arising from alterations in the collagen microstructure.[2,51] It has been observed that growth and remodeling has the effect of maintaining or restoring a preferred tissue stress or strain, referred to as achieving homeostasis: for example, the ventricles of the heart will thicken in response elevated blood pressure, reducing the pressure-induced stress in the tissue walls to a target level.[49] Though these effects are well documented, the driving mechanisms of growth and remodeling are not well understood. Further, it is not clear if the growth and remodeling process is stress or strain driven.[7]

It is suspected that disease states associated with a change in mechanical function may arise from a disruption or imbalance in the growth and remodeling process.[2–4] For

example, osteoarthritis is thought to begin with a disruption in the collagen structure of cartilage. The disruption leads to a loss of hydrated proteoglycans, which reduces the stress on the collagen fibers, leading to further degradation of the unstressed fibers. As a result the weakened tissue can no longer provide lubrication during normal activities.[52] A similar cyclic loss of collagen and proteoglycans is thought to occur in intervertebral disk disease, resulting in degeneration of the disc and severe back pain often requiring surgical intervention.[53] Finally, it is thought that glaucoma occurs due to axon loss and simultaneous remodeling of the connective tissue of the sclera after an increase in intraocular pressure. These changes in turn lead to increased deformation of the optic nerve head, causing a progressive loss of vision.[47,54] A better understanding of the growth and remodeling process may be key to understanding and treating these disease states. In particular, computational modeling can be used to predict disease state progression and potentially identify new therapeutic targets.

1.3.1 Tissue Homeostasis Models

The majority of computational models for growth and remodeling are based on the concept of homeostatic control of the tissue stress or strain. Stress homeostasis models are based on the assumption that the tissue seeks to maintain a physiological stress level. When a mechanical perturbation alters the tissue stress, the tissue will grow and remodel until the homeostatic stress level is recovered. An analogous approach is based on the tissue strain rather than stress. These phenomenological descriptions

of growth and remodeling are often incorporated into whole-organ or organ-system simulations to predict tissue development and disease state progression.

The majority of growth models for soft tissues are based on the concept of kinematic growth, first introduced by Skalak et al.,[55,56] and later refined in an influential work by Rodriguez and coauthors.[57] The total deformation gradient, $\mathbf{F}$, is split into an elastic part, $\mathbf{F}^e$, and a growth part, $\mathbf{F}^g$,

$$\mathbf{F} = \mathbf{F}^e\mathbf{F}^g. \tag{1.3}$$

The elastic deformation is due to external loads, while growth proceeds in a stress-free intermediate configuration. The form of the growth deformation gradient is prescribed by a constitutive law, commonly based on the homeostatic control of stress or strain as defined above. Stress-driven homeostasis models have been used to successfully to predict the the growth of the ventricles due to pressure and volume overload[58] or athletic exertion,[59] the increase in arterial wall thickness due to high blood pressure,[51] intracranial aneurysm growth,[60,61] and human development and morphogenesis.[62–64] Similarly, strain-driven homeostasis models have been used to predict cardiac growth due to pressure and volume overload[65] and the development of the heart.[66] In general, stress-driven growth laws are more commonly applied than strain-driven growth laws.

Tissues also adapt to loading by remodeling, i.e. changing the tissue microstructure and associated mechanical properties. This re-organization of the collagen net-

work has been modeled by homeostatic control of the collagen fiber orientation. In this approach, fibers are driven to a pre-set orientation defined relative to the principal stress or strain in the tissue. For example, fibers have been assumed to align along[67] or between[48,68] the principal stress directions, with evolution equations driven by the difference between the current fiber distribution and the pre-set or preferred distribution. These homeostatic fiber orientation laws can also be written with respect to the principal strain directions.[67,69] Homeostatic control of fiber orientation has been used to predict the in vivo fiber structure of arteries,[70,71] as well as the remodeling of arteries,[71] aortic valves,[72] and mitrial valves[73] in response to changes in blood pressure and flow.

In the methods reviewed above, growth and remodeling are modeled in open mass systems. Mixture theory accounts for mass conservation by tracking the change in mass of individual constituents, as well as the flux and reaction of reactants and products necessary to evolve protein and cellular mass.[7] Constrained mixture theory approximates mass change by assuming that individual mass densities and natural configurations of tissue constituent such as collagen, elastin, and smooth muscle cells can evolve independently.[51] The total mass and stress-free configuration of these constituents are allowed change independently and at different rates in response to a mechanical stimulus. The combined effect leads to both a change in the bulk tissue volume, as well as tissue mechanical properties brought about by altered relative amounts of constituents.[74–76] Again, the evolution of the individual constituents is

based on an assumption of stress or strain homeostasis of the tissue, similar to the growth and remodeling models described previously.

1.3.2 Micromechanistic Models

The tissue homeostasis models described in the previous section rely on phenomenological descriptions of growth and remodeling. Instead, micromechanical models can be used to describe growth and remodeling at the cellular and fiber level in an attempt to predict, rather than prescribe, tissue-level stress or strain homeostasis. Because these models are computationally expensive, such approaches are more commonly employed in smaller scale simulations of simple loading states to test the feasibility of potential micro-mechanisms of growth and remodeling of soft tissues. Recent experiments have begun to identify such mechanisms. It has been shown in embryonic chick eyes that fibroblast cells can apply contractive forces to collagen fibers, modulating the crimp angle,[77] and the rate of collagen deposition in engineered tissue constructs has been found to depend on applied strain.[78] In addition, it has been shown at the molecular,[79] fibril,[4,80] and tissue level[81–83] thats strain inhibits the enzymatic degradation of collagen. These mechanisms and others may work in concert to give rise to the experimentally observed growth and remodeling response of soft tissues.

Recent models have incorporated cell-mediated collagen crimp remodeling[70] and strain-sensitive collagen degradation and deposition.[47,84,85] This growing field of re-

search has made use of experimentally-informed mechanisms to predict normal tissue development and disease state progression. However, current models have not yet predicted stress or strain homeostasis without direct prescription. This work seeks to address this gap by developing a micro-mechanical model for fiber degradation based on the recent experiments of Flynn et al.[80] The model combines enzymatic degradation and collagen deposition to test the hypothesis that these mechanisms alone can lead to a tissue level homeostasis. A more detailed review of micro-mechanical models of growth and remodeling is provided in Chapter 4.

1.4 Objectives of this Work

The aim of this work is to develop a structure-based hierarchical modeling approach for planar collagenous tissues that spans the scale from the fiber the tissue level, and is sufficiently general to be applied to both the passive and adaptive properties of soft tissues. Human skin is used as a model system to establish the appropriate modeling approach to link tissue anisotropy to the fiber distribution. The characterization of the mechanical properties of skin is important for many applications, including scar formation and wound healing, tissue engineering, and prosthetic/residual limb interface modeling. However, the nonlinear, anisotropic properties of human skin tissue have not been well characterized. The fiber structure for human skin is well documented, and is expected to be uniform for an appropriate sample size (10x10

cm^2). This provides a homogenous sample for the inflation test and analysis, as well as a known fiber structure for validation of the results.

The anisotropic tissue model determined for the skin is then extended to to incorporate a micro-mechanical model to describe the individual collagen fibers. The inclusion of fiber-level mechanics enables the development of a theoretical model for strain-protected enzymatic degradation of collagen, a potential mechanism for the growth and remodeling process. The model is applied to the cornea and sclera, which are of particular interest to the growth and remodeling problem, as glaucoma, myopia, and keratoconus are suspected to be linked with pathological changes in tissue micro-structure.[54,86] The degradation model is combined with collagen deposition to test the hypothesis that stress or strain homeostasis can be achieved from these two mechanisms alone in the absence of cells.

There are four specific aims of this work: (1) To develop inflation test method to measure the anisotropic properties of human skin tissues, (2) to determine the more appropriate structure model to describe the skin inflation test data with respect to the fiber structure, (3) to incorporate a micro-mechanical description of the collagen fiber into the selected anisotropic tissue model, and (4) to develop a fiber-level mode for the strain-protected degradation of collagen within this framework as a potential mechanism for growth and remodeling. The following outlines the chapter organization of the thesis. Individual chapters contain relevant literature review and discussion.

Chapter 2 details the inflation (bulge) test method developed to measure the anisotropic properties of cadaveric skin tissues. The inflation test was applied to 6 human skin specimens. Tissues were inflated with phosphate-buffered saline (PBS) up to 30% strain and three-dimensional (stereo) full-field Digital Image Correlation was used to calculate strains and stress resultants along the stiffest and most compliant direction of the tissue, and to measure the influence of preconditioning and ambient humidity on the mechanical response. Significant age- and location-associated variation was observed between specimens. Several of the skin specimens were tested by Lorre Atlan, an undergraduate in our lab, under my direction. An early version of the experimental method was originally published in my master's thesis, "An inflation test method for the evaluation of the anisotropic properties of human skin tissues".[87] This chapter has been published in *Acta Biomaterialia*[88] with Lorre S. Atlan, Liming M. Voo, and Thao D. Nguyen as co-authors.

Chapter 3 analyzes the results of the skin inflation test experiments. The aim of this chapter is to determine the most appropriate constitutive model capable of describing the large anisotropy observed for skin tissue. A new analytical method was developed to fit the material parameters of the constitutive models to the inflation test while accounting for bending. Both the fully integrated distributed fiber model and a generalized structure tensor model developed by Gasser and coworkers[28] were considered. Finite Element Analysis was used to validate the analysis method. It was shown that only the fully integrated distributed fiber model could describe the

experimentally observed anisotropy observed for skin tissue. This chapter has been published in *Acta Biomaterialia*[89] with Liming M. Voo and Thao D. Nguyen as co-authors.

In Chapter 4, the distributed fiber model is expanded to include a micro-mechanical model of collagen and strain-protected enzymatic degradation as a potential mechanism of growth and remodeling. Collagen fibers are modeled as thin sinusoidal elastica beams, using the simplified solution of Comninou and Yannas.[45] A rate law for the degradation of the fiber radius was developed to capture the experimentally measured strain dependence of the enzymatic degradation of collagen. The kinetic parameters of the rate law were calibrated to bovine sclera fibril experiments,[80] and used to predict the degradation of bovine cornea strips.[83] It was shown that together with constant collagen deposition, strain-protected degradation can give rise to a strain homeostasis of the tissue. Chapter 4 will be submitted for publication with Jeffrey W. Ruberti and Thao D. Nguyen as co-authors.

The single-fibril degradation experiments published by Flynn et al.[80] did not exhibit strain protection after degradation was initiated. The fibrils were held under constant force as the radius was reduced by enzymatic degradation. As the fibrils degraded, cross sectional area decreased, increasing the strain as fibrils were held under constant force. However, even when strains exceeded the level required for strain protection, degradation did not halt. Chapter 5 incorporates a stress-driven damage model into the degradation model presented in Chapter 4 to illustrate that

mechanical damage could be responsible for the measured radius decrease.

It was shown in Chapter 2 and in previous published work from our group[26] that human skin and bovine cornea tested by inflation do not exhibit preconditioning effects, i.e. a shift in the loading curve with repeated loading. Chapter 6 details a more rigorous study including human skin, bovine cornea, bovine sclera, and porcine sclera to further illustrate that these tissues do not exhibit preconditioning effects, even when adequate viscoelastic recovery time is allowed. This chapter contains significant contributions from Barbara Murienne (porcine sclera), Baptiste Coudrillier (bovine sclera), and Stephen Alexander (bovine cornea), and William Rothkopf (human skin, under my direction) and has been published in *The Journal of Biomechanical Engineering*[90] with these researchers and Thao D. Nguyen as co-authors.

To conclude, Chapter 7 summarizes the key results, implications and limitations of this work, and suggests potential future applications of the model. The key contributions of this work are: (1) the development of an inflation test and analysis method to measure anisotropic material properties of planar collagenous tissues, (2) the identification of a fully-integrated fiber composite model as the most appropriate model for capturing the anisotropic properties of human skin tissue, and (3) the development of a validated theoretical model for the strain-protected degradation of collagen capable of predicting tissue strain homeostasis. Future work includes both improvements to the hierarchal model and application of the model to new problems, including other tissue systems.

The Appendix contain further details on both the experimental and data analysis methods, and individual chapters may also have an appendix section. Appendix A contains detailed protocols, test set-up drawings and part numbers as well as details on the PID control of pressure for the inflation test. Portions of this chapter previously appeared in my master's thesis.[87] Appendix B details the nonlinear solution procedures and Jacobians required to solve for the fiber and tissue level degradation problem of Chapter 4. Appendix C contains the matlab codes used for data analysis and parameter fitting for the inflation test of skin tissues in Chapters 2-3. Appendix D contains the Matlab files necessary for the fiber and tissue level enzymatic degradation simulations described in Chapter 4.

Chapter 2

A full-field bulge test method for the experimental characterization of human skin tissues

This chapter outlines the inflation (bulge) test developed for human skin tissues. Cadaveric skin specimens obtained from the lower back were inflated with saline while displacements were measured with 3D Digital Image Correlation. The dominant fiber direction of the tissue was determined from the deformed geometry of the specimen and local strains and stress resultants were calculated along both the dominant fiber direction and the perpendicular direction. Curvatures were used to calculate stress resultants rather than membrane stresses to take into account bending effects of the thick tissue. The method was applied to six cadaveric specimens, and considerable

variation in anisotropy and stiffness was observed between specimens. This chapter is reprinted from *Acta Biomaterialia*, Vol. 9, Theresa K. Tonge, Lorre S. Atlan, Liming M. Voo, Thao D. Nguyen, "Full-field bulge test for planar anisotropic tissues: Part I Experimental methods applied to human skin tissue", Pages 5913-5925, Copyright (2013), with permission from Elsevier.[88] An early version of this chapter also appeared in my master's thesis, "An inflation test method for the evaluation of the anisotropic properties of human skin tissues".[87] A method to fit material parameters to the stress resultant - stretch data will be detailed in Chapter 3.

2.1 Introduction

The characterization of human skin biomechanics is essential for a wide variety of applications, from modeling the tissue-device interface of medical devices to tissue engineering. The anisotropic properties of skin arise from the collagen-elastin fiber microstructure and can have important implications for applications such as creating accurate models of an amputee's residual limb, quantifying changes in microstructure during scarring, designing artificial skin, and imaging for cancer detection. The outermost layer of the skin, the epidermis, is 70-120 µm thick and composed primarily of cells. The 1-4 mm thick dermis is the thickest component of skin and is comprised of a collagen-elastin fiber network embedded in a ground matrix of hydrated proteoglycans.[91] The network consists predominantly of collagen, which contributes

70-80% of the dry weight of skin while elastin contributes to 2-4%. Scanning electron microscopy has shown that collagen fibers are arranged in the plane of the dermis.[92] The dermis, and specifically the collagen-elastin network, is thought to dominate the finite deformation mechanical properties of skin.[93]

Mechanical experiments have repeatedly demonstrated that skin exhibits a nonlinear and anisotropic stress response.[38,94] Much of the current literature concerning the large deformation response of skin tissue has been determined from *in vitro* uniaxial tension tests[92,95–98]. These tests have the advantage of standard implementation and straight-forward analysis. Consequently, they are often used to compare the effect of therapeutic treatments on the tissues, such as the subcutaneous expansion of skin for grafting[95–97] and wound healing.[98] Uniaxial tests have also been applied to investigate the structural origins of the large deformation mechanical behavior of skin tissues. Experiments paired with SEM imaging of the initial and deformed states have shown that the nonlinear J-shaped stress response is caused by the recruitment of crimped collagen fibers of the dermis. Stress is carried by the elastin and ground matrix in the toe region,[99] the initial compliant portion of the stress response, and by the straightened collagen fibers in the stiffened region.[92] Enzymatic subtraction studies further support that the deformation of collagen is responsible for the large stress response. Rat skin treated with elastase, which removes the elastin component of the tissue, exhibits an extended toe region and incomplete elastic recovery but the same large strain linear region.[100]

CHAPTER 2. A FULL-FIELD BULGE TEST METHOD FOR THE EXPERIMENTAL CHARACTERIZATION OF HUMAN SKIN TISSUES

Most *in vitro* studies of skin tissue have used animal models, which can have significant differences in stiffness relative to human skin.[101] For example, Dunn et al.[102] carried out uniaxial tests of human skin tissue from the chest. Evans[101] compared this data to that obtained on pig skin by Shergold et al.[103] and found large differences in the stress response, with the pig skin being approximately 30 times stiffer than human. Similar uniaxial tests have been carried out using human thigh skin,[104] rat skin,[105] and bovine dermis[93] also showed wide variation in stress response, with the pig skin exhibiting the stiffest and rat skin the most compliant response. Uniaxial tests have also been used to investigate anisotropy in the stress-strain response of skin tissue from both animal models and human specimens. The anisotropic behavior of skin has been attributed to the preferential alignment of collagen fibers in the dermis.[92] The preferred orientations vary throughout the body and have been historically described by Langer's lines.[16] For example, Dombi et al.[106] tested rat skin samples from the back oriented either parallel or transverse to the spine. Samples were tested to failure and the collagen content of the tissues was measured. It was seen that specimens loaded in the direction transverse to the spine exhibited higher tensile strength than specimens loaded parallel to the spine, and specimens with higher collagen content correlated with higher tensile strength. Similarly, Annaidh et al.[38,94] measured the stress response of human specimens from various orientations on the back and showed a large difference between different orientations.

Biaxial testing applies a stress state that is closer to *in vivo* loading and allows

for the simultaneous comparison of two material directions of the same sample. Lanir and Fung[20,36] first proposed a biaxial test system consisting of sutures on each edge of a square specimen of rabbit skin. The skin was stretched via sutures applied to all edges of a square patch of tissue. Force was applied in the longitudinal and orthogonal direction of the sample. Force-stretch curves were reported for samples where one direction was held at the reference width and the other direction was stretched. A similar biaxial experiment was carried out by Schneider et al.[107] on human abdominal skin. Compared to Lanir's data from rat skin, human skin stiffened earlier and the effect of anisotropy was not as pronounced.

To restore excised skin to its *in vivo* configuration, Reihsner et al.[108,109] developed an experimental setup to apply simultaneous radial loading at 12 points around a circular sample of human tissue. Like biaxial tension tests, this test produces a biaxial stress state at the center of the sample, but the multiple grips allow the stiffest material direction to be identified. Samples removed from the body were extended from the relaxed state back to the in-vivo configuration while force was monitored. The stiffest direction measured was interpreted as the average fiber direction over the sample and incremental elastic constants were reported. Comparing data from these tests to the uniaxial tests described previously is difficult because of the different stress state, and even within human uniaxial tests, a wide range of stress-strain behavior is observed, likely due to the different body locations tested. A similar radial test has been applied *in vivo*,[110] as well as indentation[111] and suction[112] tests. These tests

recruit subcutaneous tissues in addition to skin and require finite element analysis to extract material properties.

Bulge testing also applies a biaxial stress state when the radial stress components are small compared to those in-plane. Radial stresses are negligible for thin membranes and zero at the outer surface of the tissue. The fiber direction can be experimentally determined from the bulge test, but unlike the twelve-point test developed by Reihsner and coworkers, bulge testing allows for complete fixation of the edges of the tissue. This may prevent microstructural rearrangements with loading, and mitigate the effects of preconditioning. Preconditioning, or repeated loading prior to testing, is typically used to obtain repeatable test results from uniaxial and biaxial tests. Previous inflation tests on ocular tissue have shown repeatable measurements of the stress response with negligible effects from preconditioning.[25,26] Bulge tests are not commonly used to characterize the mechanical behavior of skin tissues. At least two studies have applied bulge testing to skin but have not determined the stress-strain response nor investigated the mechanical anisotropy.[113,114]

Bulge testing is typically used to to characterize the isotropic, elastic properties of metallic[115–117] and polymer thin films[118–120] that can be modeled as thin membranes. To calculate the membrane stresses, it is assumed that the membrane deforms into a spherical cap. This allows the principal stretches to be calculated from the difference in the arc length of the deformed cap and the initial specimen diameter[117] or the gradient of displacements measured from grid markers on the material surface.[19]

Stresses can be calculated from the applied pressure by assuming a deformed spherical shape and neglecting the effects of bending.[121] However, bending effects may dominate for an inflated film, depending on the thickness and bending stiffness of the material.[122] In cases where the material is too thick to assume membrane behavior and large deformations are present, inverse finite element methods have been applied to incorporate the effects of bending in calculating the material properties from the pressure-displacement response.[123] Bulge testing has been applied to many biological tissues such as canine pericardium,[124] canine jugular vein,[125] and murine pulmonary arteries.[24] These studies assumed the tissue could be treated as isotropic and utilized the spherical cap membrane stress approximation to determine stress-strain behavior.

Recent bulge testing methods have advanced to characterize the anisotropic properties of fibrous tissues. The orientation of the stiffest material direction in the plane of the tissue is determined from the deformed shape using 2D images of the deformed profile in 2-6 planes[24,126] or Moire interferometry.[23] For example, Zioupos et al.[23] used Moire interferometry to determine the stiffest material orientation of bovine pericardium. The authors demonstrated that the minor axis of the ellipsoid formed by inflation of a circular sample corresponded to the preferred fiber orientation using polarized light microscopy. Similarly, Drexler et al.[24] determined the stiffest direction of rat extrapulmonary arteries by imaging the profile of the inflated tissue at 30°increments. The minor axis of the ellipsoid was determined from the angle for which the profile of the tissue was minimized. Rather than determine the stiffest di-

rection of the tissue, Marra et. al.[126] imaged the profile of porcine aortic tissue in the axial and circumferential directions to compare these anatomical orientations directly. For all three studies, the normal strain components along the stiffest and least stiff directions[23,24] or axial and circumferential directions[126] were calculated globally from the arc length of the deformed tissue compared to the diameter of the undeformed tissue. The normal components of the membrane stress along these same directions were calculated from the pressure and deformed radii of curvature. However, using the membrane approximation ignores the effect of bending on the stress response of thick samples. Later work by Bischoff et al.[127] accounted for bending in the same experiment developed by Drexler et al. by utilizing inverse FEA analysis to determine material parameters from bulge test data. The inverse FEA method is more accurate than the membrane stress approximation but less efficient.

This work presents a bulge test method capable of repeatable measurements of the anisotropic nonlinear properties of human skin. The method utilizes stereoscopic Digital Image Correlation (DIC) to obtain full-field displacement measurements for the surface of the inflating tissue. The full-field measurements allow for the determination of the in-plane material directions of the tissue as well as the calculation of local strains and curvatures in the material directions. This generalizes an approach previously applied to isotropic hyperelastic elastomers[128] to the anisotropic case commonly seen in biological tissues. The method also improves upon works where strains were measured globally.[23,24,126] The curvatures can then be used to calculate stress

resultants in both directions. Unlike the membrane stress, stress resultants account for the stress gradient caused by bending moments and can be determined entirely from the curvature and inflation pressure if the effect of transverse shear stresses are small. In this Chaper, we present experimental stress resultant-stretch data for human skin specimens. In Chapter 3, we will detail a method to determine anisotropic material properties by fitting the resultant stress-stretch response to a stress-strain constitutive law.

2.2 Methods

2.2.1 Donor Tissues and Sample Preparation

Six full thickness specimens of human skin tissue were sourced through the National Disease Research Interchange (NDRI) from Caucasian donors between 43 and 83 years of age. Square specimens, 10x10 cm, were procured within 24 hours postmortem from the back torso, and the direction of the vertical body axis (Fig. 2.1) was marked on the specimen. For 3 specimens, the location of the specimen on the back was also indicated. Tissues were immediately flash frozen and shipped on dry ice. Upon delivery, tissues were stored at -20°C until use. Previous studies on storage conditions and mechanical properties of skin tissues have found that mechanical properties were minimally affected if the tissue was frozen quickly after procurement.[129] Table 2.1 lists the age, race, and sex of the donor for the six specimens.

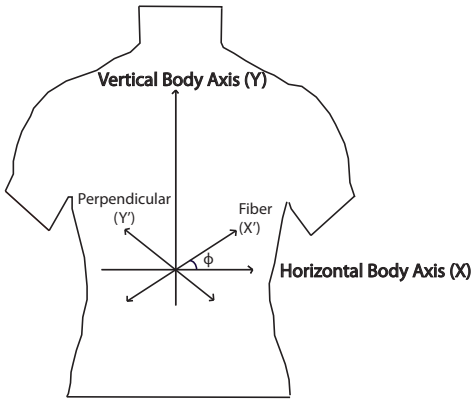

Figure 2.1: Definition of the material coordinate system with respect to the body axes on the back torso: the fiber direction (X') and perpendicular direction (Y') are defined with respect to the horizontal body axis by the dominant fiber direction angle ϕ.

Table 2.1: Donor and specimen information.

Age	Gender	Race	Thickness [mm]	Location
43	M	C	4.86 ± 0.32	Lower Back
44	M	C	4.38 ±0.27	Lower Back
59	F	C	5.18 ± 0.56	unknown
61	M	C	2.01 ± 0.15	Left Upper Back
62	F	C	2.95 ±0.42	unknown
83	M	C	2.43 ± 0.50	unknown

Tissue specimens were thawed in phosphate buffered saline (PBS) overnight at 4°C prior to testing. The adipose tissue was removed using fine dissectors. Tissue thickness was evaluated by averaging four measurements taken at the center of each edge of the tissue with a dial caliper (Mitutoyo 505-671, 0.03 mm accuracy). Caliper measurements were recorded when the caliper was visibly determined to make contact with the specimen. The calipers measurements were made three times at each location and the average of all the measurements was reported as the thickness. It has been

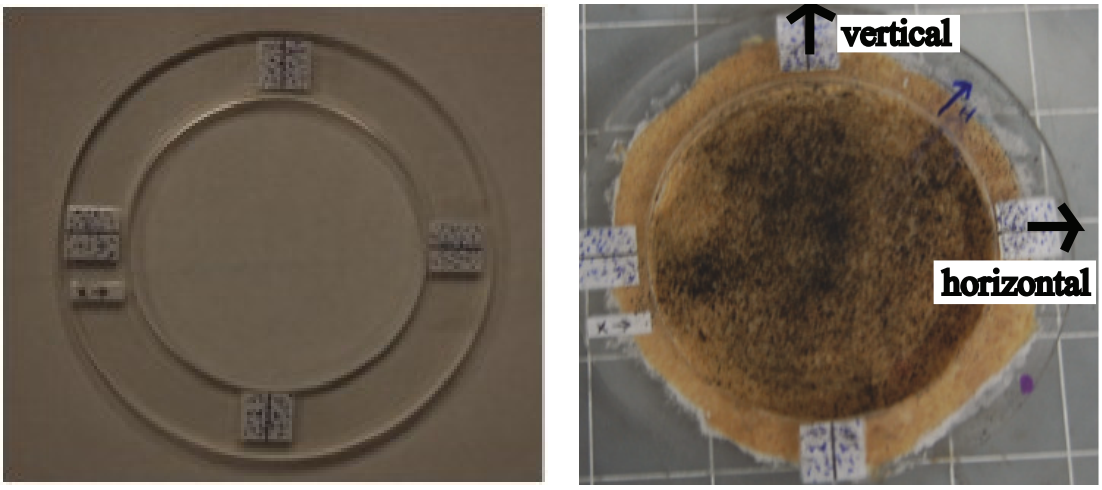

(a) (b)

Figure 2.2: (a) Acrylic fixture with 7.5 cm aperture, and (b) trimmed skin specimen speckled with graphite powder and glued to fixture, with horizontal and vertical body axes marked.

shown that with correct technique, a non-rotating Mitutoyo gauge performed as well as more complicated measurement techniques such as a custom gauge with high-resolution contact-force measurement.[130] Table 2.1 lists the averaged thickness for the 6 specimens. The standard deviations between all four locations were comparable with the measurement error (the standard deviation of the three repeated measurements); thus the specimens were assumed to be uniform in thickness. Specimens were glued to a Plexiglass ring of 7.5 cm inner diameter, 9.5 cm outer diameter and 5 mm thickness (Fig. 2.2). The DIC coordinate system was set such that the Y axis corresponded with the vertical body axis (Fig. 2.1). This enabled the determination of displacements and strains with respect to the body axes. In addition to a layer of glue between the tissue surface and the fixture, the tissue was scored with a scalpel at approximately 5 mm intervals along the circumferential edge of the fixture. These

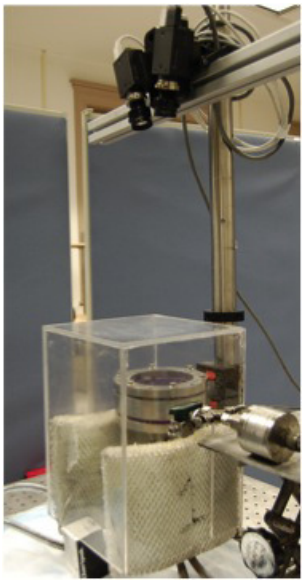

Figure 2.3: Custom pressure-controlled inflation system, including pressure chamber, pressure transducer, humidity chamber, and two stereo cameras for Digital Image Correlation.

scores were impregnated with glue to produce a rigid boundary condition through the thickness of the tissue. Visual inspection of the tissue showed that the glue did not diffuse into the specimen. The excess tissue was trimmed and a final layer of glue applied at the edges of tissue (Fig. 2.2). The specimen and holder were mounted onto a customized pressurization chamber (Fig. 2.3).

The specimens were inflated by an MTS Insight 5 driven syringe (MTS, Eden Prairie, MN, USA) injection of PBS into the pressurization chamber. Pressure was monitored at the chamber by a TJE pressure transducer (Honeywell, Morristown, NJ, USA) with 2 psig range and $\pm$ 0.002 psig accuracy. The loading regimen was prescribed by TestWorks4 using manually tuned Proportional-Integral-Derivative (PID) control parameters optimized to the protocol. Pressure and pressure-rate were con-

Table 2.2: Temperature and humidity conditions during testing.

Sample	Temp (°F)	Humidity
43/M	76	42%
44/M	78	50%
59/F	74	34-26%
61/M	75	36%
62/F	79	45-52%
83/M	76	15%
Average	76.3	37%
Std. Dev.	1.9	13 %

trolled by the displacement of the MTS crosshead based on feedback from the pressure transducer.

Samples were tested inside a Plexiglass chamber for humidity monitoring and control (Fig. 2.3). Water-logged insulation material was placed in the chamber to provide elevated humidity conditions. The humidity level was controlled by varying the volume and temperature of water held within the insulation material. A temperature and humidity gauge (McMaster-Carr, Elmhurst, IL, USA) with 2°F temperature accuracy and 8% humidity accuracy was mounted at the top of the chamber. The interior surface of the humidity chamber was treated with anti-fog spray (Speedo, New York, NY, USA) prior to testing to prevent condensation. No fogging was observed on the plexiglass chamber during testing. Preliminary tests comparing the effects of the plexiglass chamber on the DIC measurements showed that imaging through the plexiglass imparted a small consistent shift to the displacements measurements but did not alter the strain measurements. Samples were tested at a targeted relative

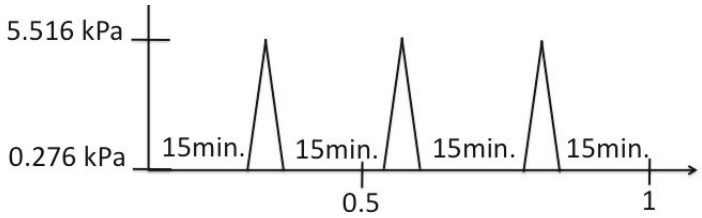

Figure 2.4: Schematic of pressure loading regimen. Samples were loaded from a baseline pressure of 0.276 kPa to a maximum pressure of 5.516 kPa at a rate of 0.069 kPa/s. Samples were held for 15 minutes at the baseline pressure before, between, and after each load-unload cycle.

humidity of 40% to ensure tissue hydration. However, due to difficulty in controlling the humidity level, the humidity in the chamber ranged from 15% to 52%. Exact temperature and humidity conditions for each test can be found in Table 2.2. To assess the effect of humidity, three specimens were retested at multiple humidity levels ranging from 15%-100%. It was observed that the variation with humidity level did not impact the mechanical behavior of the tissue (see Section 2.3.2) .

The tissue specimen was brought to a baseline pressure of 0.276 kPa and held for 15 minutes prior to testing to ensure the specimen was at equilibrium.[131] It was desired to begin the test from a planar reference state. The baseline pressure was applied to prevent the specimen from buckling under its own weight. The specimens were subjected to three load-unload cycles at a rate of 0.069 kPa/s from the baseline pressure to a maximum pressure of 5.516 kPa. Each specimen was held at the baseline pressure of 0.276 kPa for 15 minutes between each cycle to allow for specimen recovery (see schematic in Fig. 2.4). The three loading cycles were used to assess the effects of preconditioning on the measured response.

The deforming specimen surface was imaged by two stereoscopically arranged cameras with 1/1.8" image sensors (Point Grey, Richmond, BC, Canada) and 16 mm focal length lenses (Edmund Optics, Barrington, NJ, USA) at an aperture of f/8. The optical axes of the cameras were positioned 38 cm above the chamber and 7.5 cm apart, such that the total angle between the two cameras was 12°. This configuration had a depth of field of 5.8 cm, sufficient to capture the deformations of the compliant tissue. Images were collected during testing at a rate of 0.5 Hz by VicSnap 2009 and correlated by Vic3D 2009 (Correlated Solutions Inc., Columbia, SC, USA).

The error in the DIC displacement measurements was evaluated by comparing the displacements between two pictures taken within 2 seconds with no pressure change (no deformation). The measurement error was defined at the apex as,[26]

$$\text{Measurement Error} = \pm\sqrt{(U_2 - U_1)^2 + (V_2 - V_1)^2 + (W_2 - W_1)^2} \qquad (2.1)$$

where U_1, V_1 and W_1 are the displacement components in laboratory coordinates for the first image taken, and U_2, V_2 and W_2 are the displacement components for the second image taken. The average error at the apex for all tests was found to be ± 3.75 µm.

2.2.2 Data Analysis

The bulge test measured the components of the displacements in body axes coordinates (Fig. 2.1), providing the U, V, and W components of the displacement field in X, Y, and Z directions. The inflation of the circular planar specimens to an elliptical dome indicated the presence of material anisotropy. The material axes were defined by the major and minor axes of the ellipsoidal shape, which correspond to the most compliant and stiffest directions of the tissue, respectively. The material axes were determined by fitting an analytical general ellipsoid to the deformed positions of the specimen surface at the maximum pressure (5.516 kPa) using the function *ellipsoid_fit.m* [1], which returned the magnitude and direction of the principal radii. The dominant fiber direction was identified for the specimen from the direction of the minor axis in the specimen plane, and the dominant fiber orientation angle ϕ was defined with respect the horizontal axis, X (Fig. 2.1).

The in-plane components of the Green-Lagrange strain tensor were calculated for the specimen surface from the DIC displacement field. For each test, the U, V, and W DIC measured displacement components were obtained for a grid of material points evenly spaced at 0.570 mm intervals at each pressure step. The displacements were smoothed over a grid with 0.25 mm spacing. To obtain the displacement components in the material coordinate system (Fig. 2.1), the displacement field was rotated by the angle ϕ to obtain displacement component U' in the fiber direction X' and displace-

[1] Yury Petrov, http://www.mathworks.com/matlabcentral/fileexchange/24693-ellipsoid-fit

ment component V' in the perpendicular direction Y'. The out-of-plane displacement component W in the Z direction was not affected by the coordinate transformation. The normal and shear strain components of the specimen surface were calculated from the rotated displacement field as:

$$\begin{aligned} E_f &= E_{X'X'} = \frac{\partial U'}{\partial X'} + \frac{1}{2}\left[\left(\frac{\partial U'}{\partial X'}\right)^2 + \left(\frac{\partial V'}{\partial X'}\right)^2 + \left(\frac{\partial W}{\partial X'}\right)^2\right], \\ E_p &= E_{Y'Y'} = \frac{\partial V'}{\partial Y'} + \frac{1}{2}\left[\left(\frac{\partial U'}{\partial Y'}\right)^2 + \left(\frac{\partial V'}{\partial Y'}\right)^2 + \left(\frac{\partial W}{\partial Y'}\right)^2\right], \\ E_{fp} &= E_{X'Y'} = \frac{1}{2}\left[\frac{\partial U'}{\partial Y'} + \frac{\partial V'}{\partial X'} + \frac{\partial U'}{\partial X'}\frac{\partial U'}{\partial Y'} + \frac{\partial V'}{\partial X'}\frac{\partial V'}{\partial Y'} + \frac{\partial W}{\partial X'}\frac{\partial W}{\partial Y'}\right]. \end{aligned} \tag{2.2}$$

The stretch along the fiber and perpendicular directions were calculated from the strain components in eq. (2.2) as,

$$\begin{aligned} \lambda_f &= \sqrt{2E_f + 1}, \\ \lambda_p &= \sqrt{2E_p + 1}. \end{aligned} \tag{2.3}$$

The displacement gradients in eq. (2.2) were evaluated by fitting the displacements across the X' or Y' axis to a 9^{th} order polynomial, and differentiating analytically. To validate this method, the displacement gradients were also calculated using the central difference approximation,

$$\frac{\partial U_i'}{\partial X_j'} = \frac{U_i'(k+1) - U_i'(k-1)}{X_j'(k+1) - X_j'(k-1)}. \tag{2.4}$$

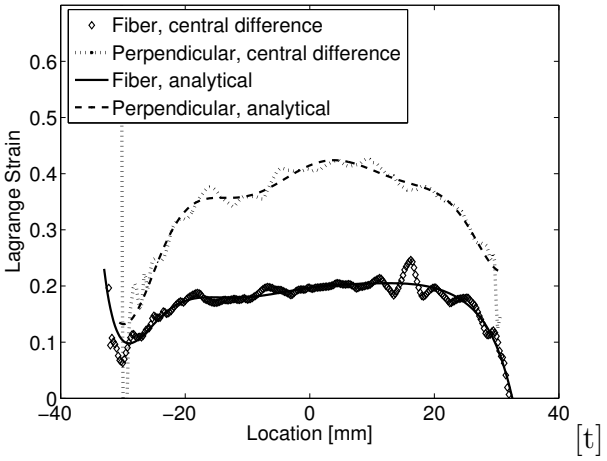

[t]

Figure 2.5: Strain calculated across the fiber direction and perpendicular direction of a representative specimen (44/M). The displacement derivatives were computed by fitting the displacements to polynomials and taking the derivatives analytically. The calculation was compared to derivatives computed by the central difference method for method validation.

The two strain measures are shown for a typical specimen in Fig. 2.5. Results

Table 2.3: Range of strain measurement within ± 1 mm of the apex.

Sample	E_f range	E_p range
56/F	0.46%	0.06%
44/M	0.30%	0.88%
61/M	0.02%	0.10%
83/M	0.29%	0.34%
62/F	0.29 %	1.60%
43/M	0.40%	0.17%
Average	0.29%	0.53%
Std. Dev.	0.15%	0.61 %

from the two methods of strain calculation differed by less than 10%. The central difference method was more susceptible to experimental noise. Therefore, the strain components were calculated from the gradients of the smoothed displacement field at the apex. These values were calculated at all pressure steps. The variation of

the strain measurements calculated over a range of ± 1 mm of the apex (Table 2.3) ranged from 0.06% variation to 1.6% variation among all of the specimens.

The stress state developed during bulge testing is typically determined by modeling the deformed specimen as a thin membrane. This is advantageous because the membrane stresses can be determined from the applied pressure, curvature, and thickness of the deformed geometry. However, this approach neglects the presence of stress gradients caused by bending. Bending moments generate a stress gradient that would cause the membrane stresses to underestimate the stresses at the outer surface of the tissue where strains are measured. The stress gradients can be large even for a thin material due to the nonlinear stress response. To account for the presence of non-negligible stress gradients, we chose to determine the stress resultants in the fiber and perpendicular directions rather than the membrane stress. These stress resultants are related to the stress components in the fiber and perpendicular directions, σ_f and σ_p, by,

$$\begin{aligned} N_f &= \int_{-h/2}^{h/2} \sigma_f(z)\,\mathrm{d}z, \\ N_p &= \int_{-h/2}^{h/2} \sigma_p(z)\,\mathrm{d}z. \end{aligned} \tag{2.5}$$

where h is the thickness of the tissue.

To determine the stress resultants, the inflated tissue specimen was modeled as a thin shell. At the apex, far away from the clamped boundaries, the transverse shear

stresses for the pressurized shell are negligible. The stress resultants are statically determined from the inflation pressure P and the curvature, K_f and K_p, at the apex in the fiber and perpendicular direction by the equations,

$$\begin{aligned} N_f^{exp} &= \frac{P}{2K_p}, \\ N_p^{exp} &= \frac{P}{K_p}\left(\frac{2K_p - K_f}{2K_p}\right). \end{aligned} \tag{2.6}$$

These solutions were initially derived for axisymmetric thin shell problems,[132–134] where the curvatures K_f and K_p are the principal radii of curvature for a surface of revolution. However, the equations have been generalized to convex shells of arbitrary smooth shape if K_f and K_p are local principal radii of curvatures at the point of interest.[135] These relations have been used by a number of researchers to calculate the stress resultants for non-axisymmetric geometries, including the deformed shapes of aneurisms[136] and aortic tissues subjected to inflation testing.[126] Lu and co-authors[135–138] applied finite element analysis to show that the stress resultants calculated by eq. (2.6) for generalized surfaces with positive curvatures were statically determined and did not depend on the specified material model or material parameters. In Chapter 3, we will present a finite element study to further validate the use of eqs. (2.6) to determine the local stress resultants evaluated for the bulged skin specimen.

The local curvatures were calculated at the apex for the deformed specimen by fitting different 2D ellipses to the meridians in the fiber and perpendicular directions

using the MatLab function fit_ellipse.m [2]. For each meridian, the ellipse fit returned the radii, a and b, and the angle of tilt θ of the ellipse. The principal curvatures were calculated from the geometrical parameters as,[134]

$$K_f = \frac{\left(a_f^2 \sin^2(\theta_f) + b_f^2 \cos^2(\theta_f)\right)^{3/2}}{a_f^2 b_f^2}, \qquad K_p = \frac{\left(a_p^2 \sin^2(\theta_p) + b_p^2 \cos^2(\theta_p)\right)^{1/2}}{a_p^2}. \tag{2.7}$$

These equations are equivalent when the angles of tilt θ_f and θ_p are zero. To calculate stress resultants, the measured pressure was tared by the baseline pressure, resulting in zero stress and zero strain at the reference state. From the full-field displacements, the middle 75% of the specimen surface was used to fit the ellipses to avoid edge effects. We also found that using less than 50% of the specimen surface gave poor fits. Alternatively, the stress resultants can be determined from the solution for a general ellipsoidal shell.[134] The generalized ellipsoidal model was used by Drexler el. al.[24] to determine the stress response of inflated arteries. This requires the deformed geometry to be fit to a general 3D ellipsoid. For most specimens in this study, the general ellipsoid provided a poor fit to the deformed geometry (Fig. 2.6), which can generate large errors in the stress resultant calculations. The accuracy of applying eq. (2.6) to approximate the stress resultants and comparison to a generalized ellipsoid stress resultant calculation will be addressed in Chapter 3.

[2] Ohad Gal, http://www.mathworks.com/matlabcentral/fileexchange/3215-fitellipse

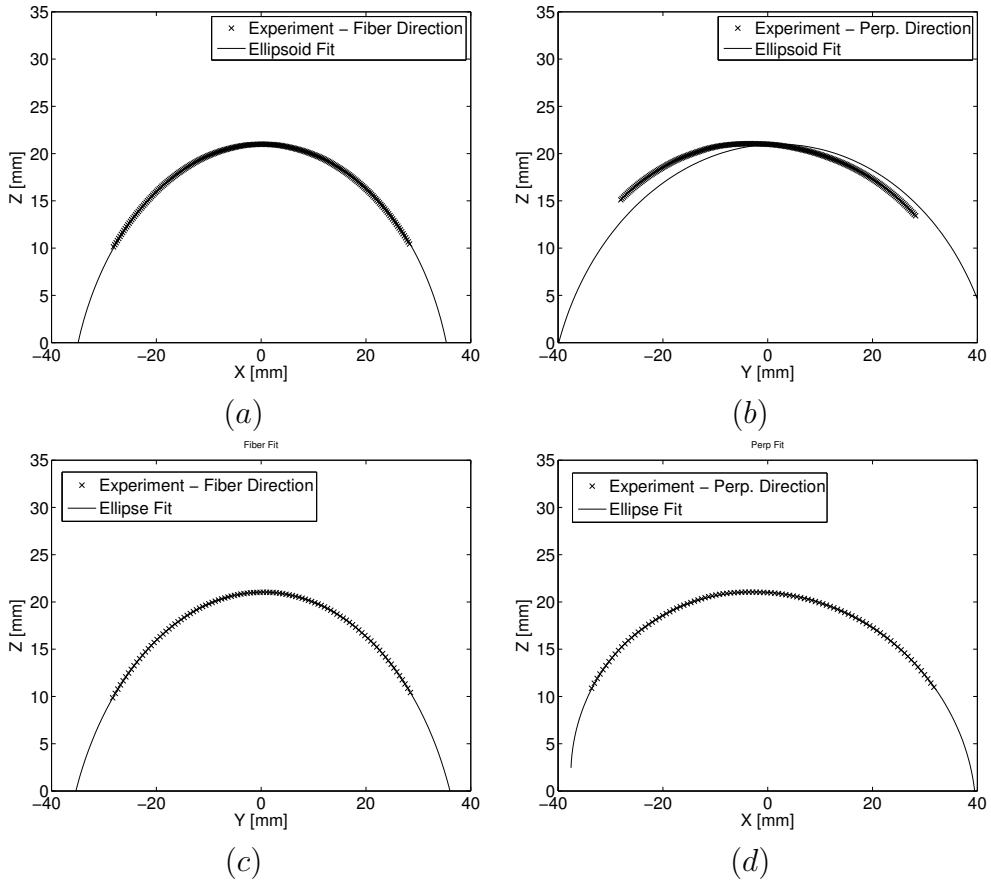

Figure 2.6: Comparing the 3D ellipsoidal fit to the deformed surface and 2D ellipse fits to the deformed meridians of a representative skin specimen. The ellipsoidal fit provided an accurate representation of the deformed meridian in the (a) fiber direction but not the (b) perpendicular direction, whereas the 2D ellipse fits accurately reproduced the deformed meridian in both the (c) fiber direction and (d) perpendicular direction.

2.3 Results

A total of six specimens from six Caucasian donors were tested, identified by (Age/Sex). Preconditioning and humidity were found to have a negligible effect on the mechanical response. The fiber orientation and anisotropic stress resultant-stretch relationship was characterized and the degree of anisotropy appeared to vary substan-

tially between specimens.

2.3.1 Preconditioning

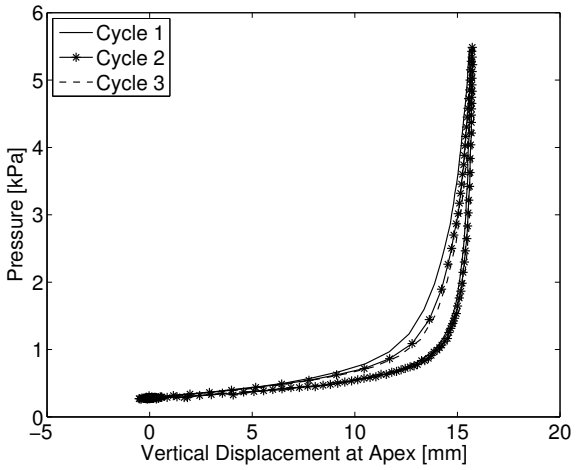

Figure 2.7: Results of repeated loading for representative specimen (59/F) at a loading rate of 0.069 kPa/s. The inflation response is negligibly altered by preconditioning.

Figure 2.7 plots the apex displacement, defined as the out-of-plane displacement component (W) of the apex, for the first three preconditioning loading cycles for the (59/F) specimen. The maximum apex displacement measured over the three load cycles was 15.73 $\pm$ 0.0968 mm, or a 0.615 % variation compared to the mean. These results indicate that preconditioning minimally affected the mechanical response of the tissue at the maximum displacement. Consequently, the first loading curve was used to calculate the stress resultant and strain response.

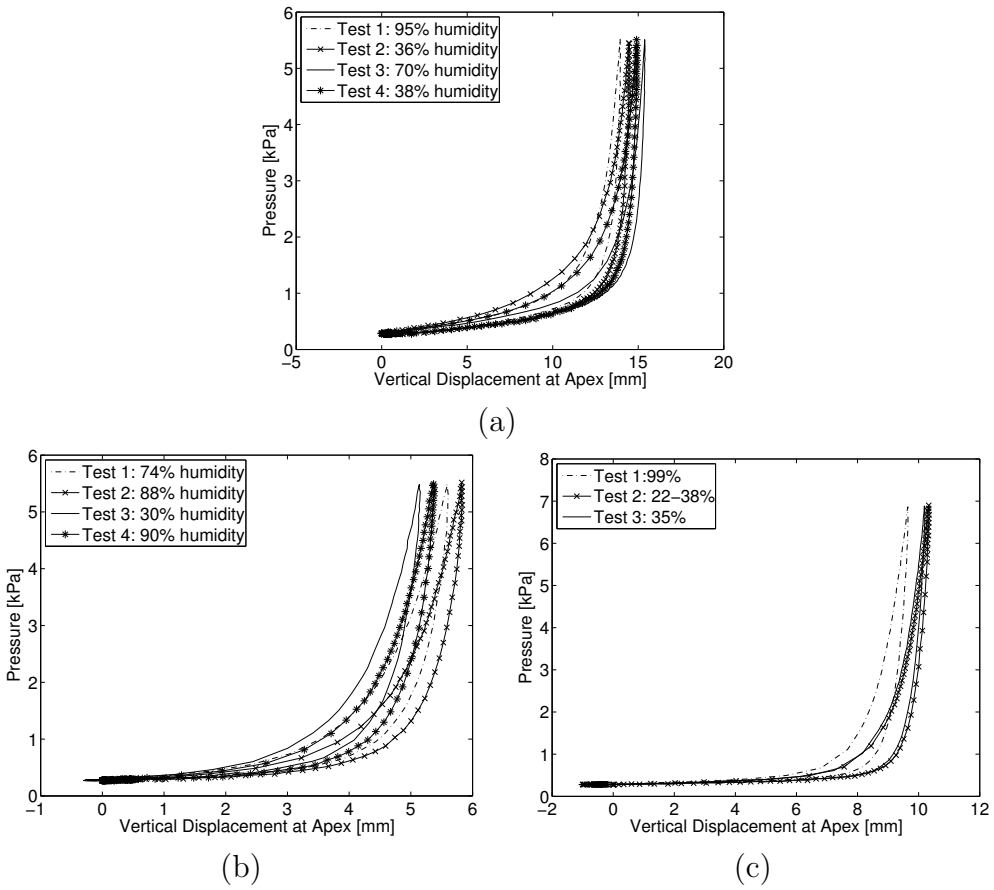

Figure 2.8: Result of varying humidity after re-testing thawed frozen specimens for (a) 43/M (b) 61/M (c) 83/M. The humidity levels were applied in a random order indicated by the order listed in the legend and the mechanical response is not seen to vary with humidity level.

2.3.2 Humidity Effects

Figure 2.8 shows the apex displacement with pressure for three specimens tested at varying humidity levels. The variation between tests was small compared to the maximum apex displacement. The variation also appeared random and did not correlate with humidity level, indicating that humidity effects were smaller than experimental error. We suspect that the displacement response was insensitive to the humidity level

because the mechanical behavior of skin tissue under large deformation is dominated by the dermis, which remained hydrated by PBS in the inflation chamber throughout the test (Fig. 2.3). A two-tailed paired student t-test comparing the maximum apex displacement of specimens tested at the lowest humidity (30-40%) and the highest humidity (90-100%) levels did not reject the null hypothesis that the two groups are equivilent ($p = 0.38$). However due to the limited sample size of three, the statistical power of the result was low, 0.03. A total of 200 samples would have to be tested to achieve a power of 0.80.

2.3.3 Full-field Displacement Contours and Fiber Angle

Figures 2.9-2.10 plot the 3 displacement components in body axes coordinates. Most of the specimens deformed from a circular sheet to an ellipsoidal dome indicating the presence of material anisotropy. This is seen in the contours of the out-of-plane displacement component (W), which form concentric ellipses rather than concentric circles that would be observed if the deformed shape was a spherical cap. The material axes of the elliptical contours were rotated from the body axes. The contours for the in-plane vertical displacement component (V) and horizontal displacement component (U) were symmetric with respect to the major and minor axis. This indicates that the major and minor axes were the most compliant and stiffest material directions,

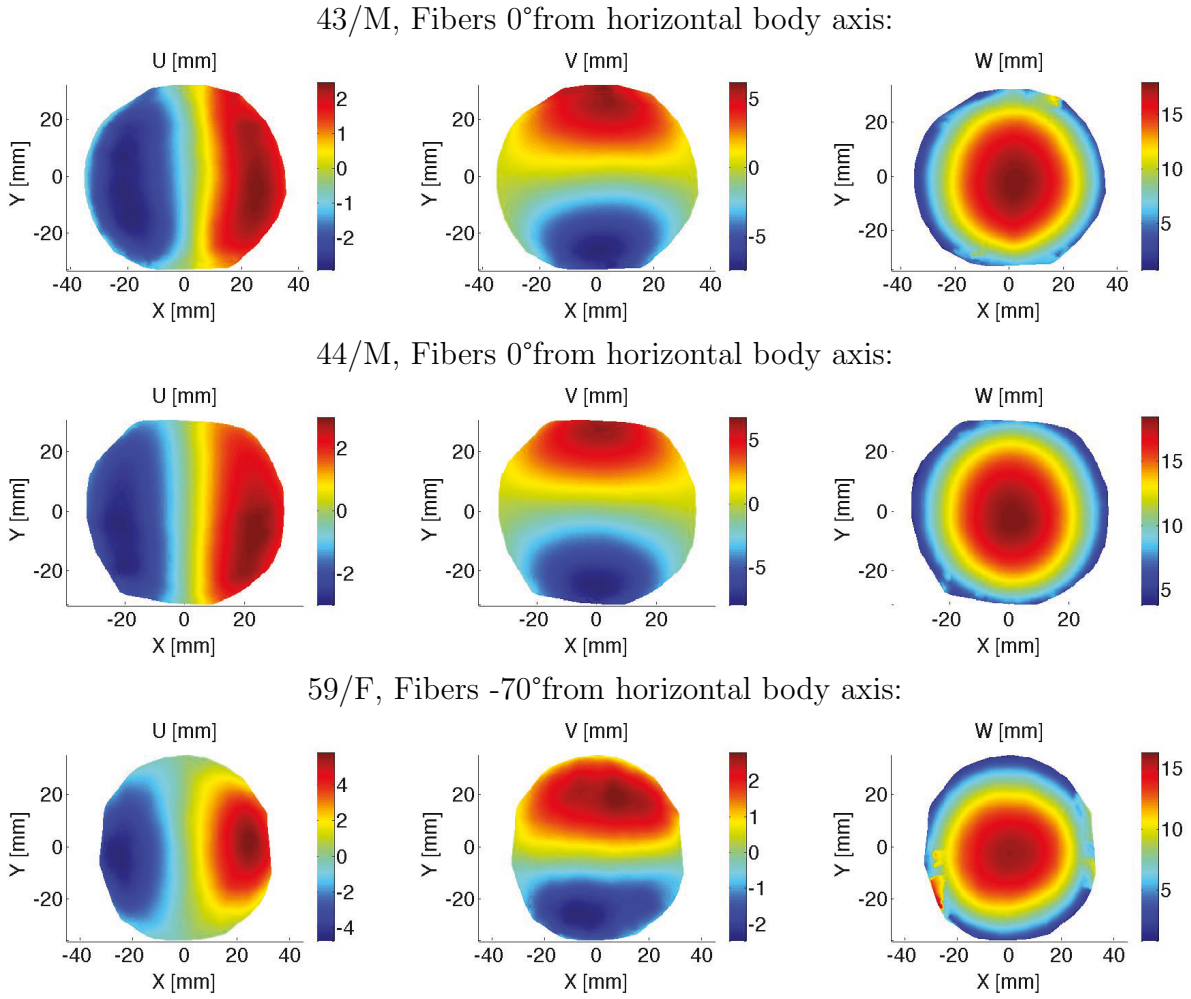

Figure 2.9: Contours of displacement components in the body axis coordinates (U, V, W) at the maximum pressure. The anisotropy of the tissue is evident from the rotated U and V contours and the elliptical W contours [*continued in Fig. 2.10*].

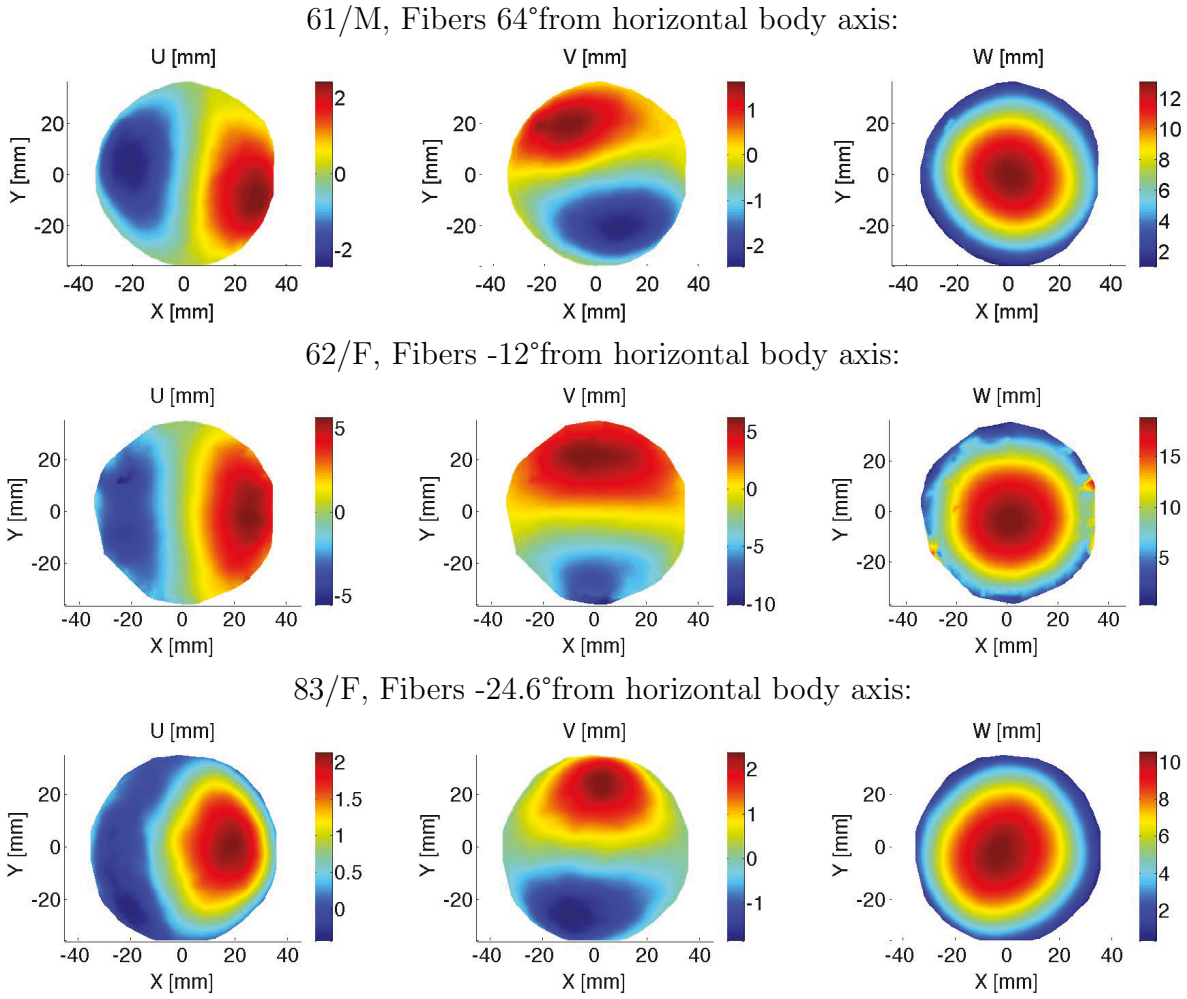

Figure 2.10: Contours of displacement components in the body axis coordinates (U, V, W) at the maximum pressure. The anisotropy of the tissue is evident from the rotated U and V contours and the elliptical W contours [*continued from Fig. 2.9*].

Table 2.4: The dominant fiber angle determined from the deformed tissue geometry for each specimen, compared to body location if known.

Sample	Fiber Angle (from horizontal body axis)	Location from Back
43/M	0°%	Lower Back
44/M	0°%	Lower Back
59/F	70°%	unknown
61/M	64°%	Left Upper Back
62/F	-12°%	unknown
83/M	-25°%	unknown

respectively. The orientation of the minor axis was interpreted to be the dominant fiber direction of the specimen. The orientation of the dominant fiber direction was measured with respect to the horizontal body axis and results are reported in Table 2.4. Location information was only available for three specimens. It was observed that for these three donors, lower back specimens exhibited a horizontal fiber direction while the upper back specimen exhibited diagonal fiber direction. This correlates with what is known from Langer's Lines.[16] For specimens without back location information, the orientations can be inferred from the fiber angle by comparison with Langer's lines orientations. Specifically, we inferred that 59/F is from the left upper back, while 62/F and 83/M may be from the right upper back.

2.3.4 Stress Resultant - Stretch Relationship

The experimentally calculated in-plane stress resultants are plotted against the experimentally measured in-plane stretches at the apex for the first loading curve of each specimen in Fig. 2.11 for all six specimens tested. The stress resultants

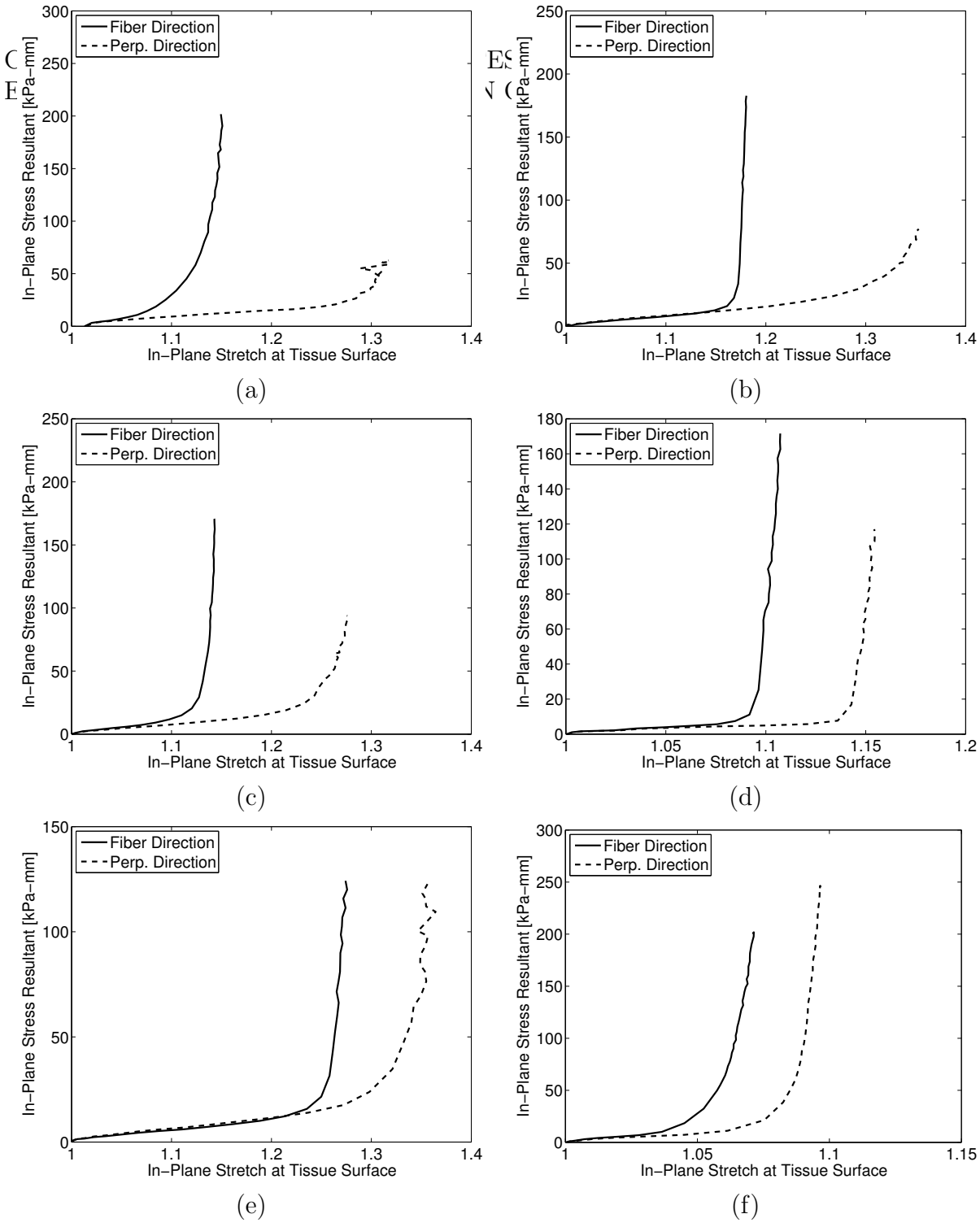

Figure 2.11: Experimentally calculated in-plane stress resultants vs experimentally measured stretches in both the fiber and perpendicular directions for (a)43/M (b) 44/M (c) 59/F (d) 61/M (e) 62/F (e) 83/M. Variation in stiffness and anisotropy is evident between specimens.

Table 2.5: Comparing the stiffness and nonlinearity of the stretch-stress resultant plots: slope of stiffening curve in fiber direction, slope of stiffening portion of curve in perpendicular direction, and transition stretch marking the end of the toe region and onset of stiffening.

Sample	Fiber Direction Stiffness [kPa-mm]			Perpendicular Direction Stiffness [kPa-mm]		
	Toe Region	Linear Region	Transition Stretch	Toe Region	Linear Region	Transition Stretch
43/M	178.6	8504.3	1.07	104.2	1399.5	1.11
44/M	77.6	19223.0	1.16	86.5	1480.7	1.31
59/F	103.2	11471.0	1.10	73.4	4145.0	1.21
61/M	73.7	12686.0	1.09	42.6	8663.6	1.14
62/F	48.4	6045.2	1.21	53.7	2233.0	1.27
83/M	272.2	13132.0	1.03	187.7	24481.0	1.05
Average	125.6	11843.6	1.11	91.4	7067.1	1.18
Std. Dev.	84.6	4510.8	0.07	52.1	8955.8	0.10

and stretches are shown along the fiber direction and in the perpendicular direction. The stress response varied greatly between specimens in the degree of anisotropy, nonlinearity, and stiffness. To evaluate the differences between specimens, the stiffness of the stress resultant response was defined as the secant slope of the stress resultant curves. The stiffness of both the initial toe and linear region were calculated for the fiber and perpendicular directions. The transition stretch between the toe and linear regions was defined as the stretch at which the stress resultant exceeded the linear fit for the toe region by 3 kPa-mm. The stiffness for the toe region was calculated by fitting a straight line to the stretch-stress resultant curve prior to the transition stretch. For the linear region, the stiffness was calculated from the final 0.01 stretch range of the stress resultant curve, e.g. from λ_f = 1.34-1.35 for 44/M in the fiber direction. The results for these 6 measures are listed for all specimens in Table 2.5.

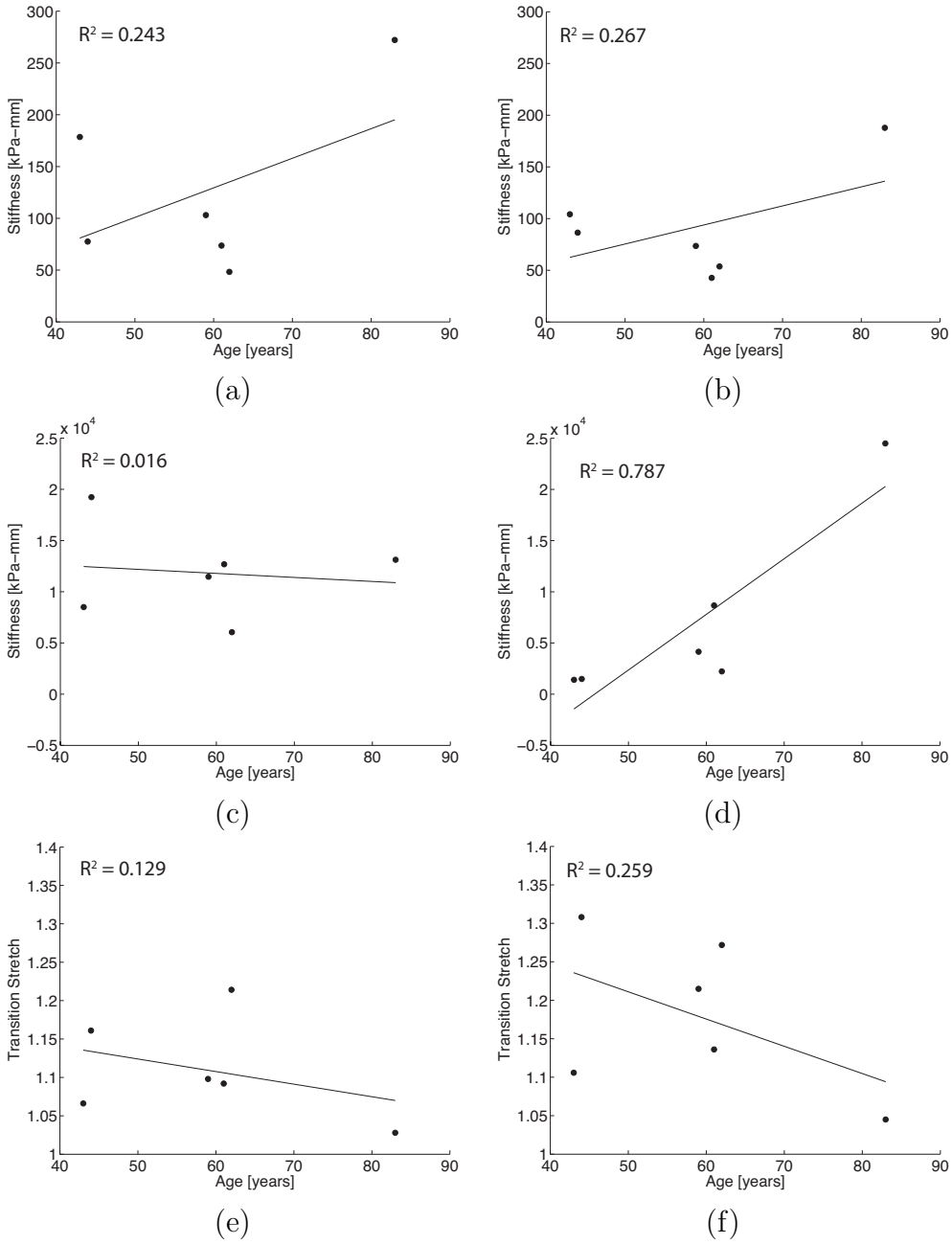

Figure 2.12: Parameters from Table 2.5 plotted against age with linear regression for (a) stiffness of the toe region, fiber direction, (b) stiffness of the toe region, perpendicular direction, (c) stiffness of the linear region, fiber direction, (d) stiffness of the linear region, perpendicular direction, (e) transition stretch from toe to stiffened region, fiber direction, and (f) transition stretch from toe to stiffened region, perpendicular direction. In general the stiffness increase with age, while the transition stretch decreases with age.

Table 2.6: Comparing the anisotropy of the stretch-stress resultant plots: ratio of the stiffness in the toe and linear regions.

Sample	Stiffness Ratio (Fiber/Perpendicular)	
	Toe Region	Linear Region
43/M	1.72	6.08
44/M	0.90	12.98
59/F	1.41	2.77
61/M	1.73	1.46
62/F	0.90	2.71
83/M	1.45	0.54
Average	1.35	4.42
Std. Dev.	0.37	4.59

The limited number of specimens precludes conclusions regarding the effect of age, gender, and location on the mechanical behavior of skin tissues; however several observations can be made. Fig. 2.12 plots all 6 measures against specimen age. These plots indicate that older specimens appear to stiffen sooner, as evidenced by a decrease in the transition stretch with age for both directions. The specimens also appeared to have higher stiffness with age, as three of the four stiffness measures increased with age. Additionally, older specimens appear to be less anisotropic than other specimens tested. Table 2.6 lists the ratio of the fiber to perpendicular stiffnesses of the stretch-stress resultant curves for the toe and linear regions to provide a comparison measure for the anisotropic stress response and its variation with age. Figure 2.13 plots these stiffness ratios with age. The toe region is on average more isotropic than the linear region, and the anisotropy ratio for the toe region does not change significantly with age. In contrast, the anisotropy ratio in the linear region exhibits a noticeable decrease with age. Specimens from younger donors exhibited a considerably more compliant

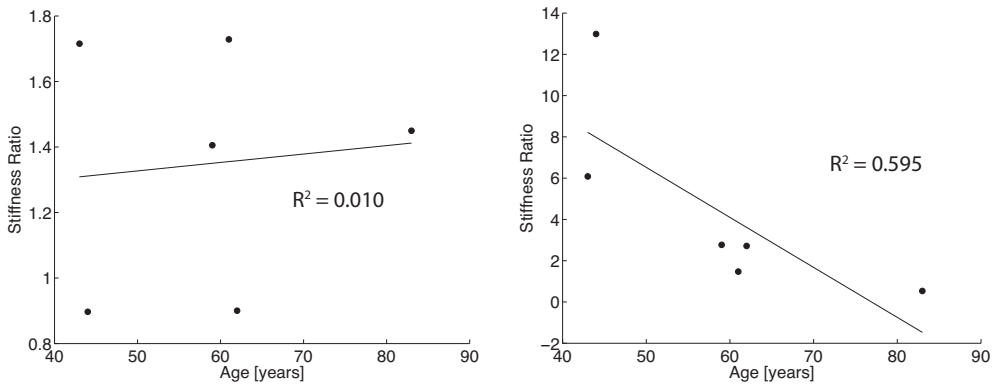

(a) (b)

Figure 2.13: Ratio of fiber stiffness over perpendicular stiffness from Table 2.6, plotted against age with linear regression for (a) toe region and (b) linear region. There is little change in the stiffness ratio with age in the toe region, and a decrease in stiffness ratio with age in the linear region.

stress response in the perpendicular than fiber direction.

It also appears that anisotropy may be correlated with body location. Referring to Tables 2.4 and 2.6, specimens from the lower back were the most anisotropic. For a specimen from the lower back (44/M), the stiffness ratio for the linear region was 12.98. The stiffness ratio for a specimen from the left upper back (61/M) was a considerably smaller 1.46. These trends will be analyzed further in Chapter 3 by fitting the stress resultant - stretch relationships to a hyperelastic anisotropic constitutive model.

2.4 Discussion

The experimental method presented here improves upon previous bulge tests of planar tissues. DIC was used to obtain full-field displacement data, from which

local curvatures and surface strains were calculated. The dominant fiber direction was determined from the test and data was analyzed in the material coordinates. This improved upon works where strains were measured globally[23] or where cameras at fixed locations were used to measure strains and curvatures.[126] Here we limited our analysis to the apex, but this analysis could be used to evaluate strain and stress resultants at other points on the surface of the tissue sufficiently far from the fixed edges. The mechanical response of the tissue was minimally affected by preconditioning. We suspect that the fixed boundary condition provided by bulge testing limits rearrangements of the collagen fibers, that might contribute to the typical preconditioning response. This is supported by Tower et al.[27] who showed a rearrangement of fibers under cyclic uniaxial loading. It follows that by limiting such microstructure rearrangement, the fiber structure tested by bulge testing may be more representative of the *in vivo* fiber structure.

The small number of specimens tested precluded statistical comparison for age, race, and sex; however older specimens generally exhibited a stiffer response in both the fiber and perpendicular directions. This observation is consistent with recent mechanical characterizations of the sclera[54] arteries[139] and aorta[140] and has been previously observed for skin *in vivo*.[141] Age-related stiffening is likely due to the increase in collagen cross-linking with age.[142] It was also observed that skin becomes more isotropic with age. This could also be explained by increased cross-linking between adjacent fibers. However, the degree of anisotropy is known to depend strongly on

tissue location, which may have been a confounding factor in this study. It does not appear that the mechanical response differed among male and female donors. Although other soft tissues such as brain tissue,[143] arteries,[144] and ligaments[145] have been observed to have gender-specific properties, *in vivo* studies on skin tissue[146] have also shown no gender dependence. In Chapter 3, we will introduce an analytical method to quantify these properties by determining material parameters from the bulge test.

There are limitations of bulge testing compared to uniaxial or biaxial testing. The bulge test cannot prescribe a specific biaxial stress state nor multiple biaxial stress states. The need for some pre-inflation to prevent a buckled reference state is another disadvantage of the bulge test. It has been previously reported for thin films that the error introduced by pre-inflation can be significant.[147] Stress can not be obtained directly in a bulge test because of bending and finite thickness effects. Bending stiffness can be significant for thick tissue specimens inflated from a planar state and exhibiting a nonlinear stress response. Here, we applied an ellipsoidal shell model to calculate the stress resultants from the applied pressures and measured curvatures. The stress resultant calculation depends directly on the accuracy of the curvature measurements. In Chapter 3 we will present an analytical method to obtain material parameters for a hyperelastic model from the stress resultants while accounting for bending, and investigate two different distributed fiber model approaches to describe the nonlinear anisotropic properties of human skin tissues.

2.5 Conclusions

We have developed a bulge test method with 3D DIC measurements to obtain the stress resultant and strain response of human skin tissues. The methods presented in this Chapter are sufficiently general to be applied to other planar tissues such as pericardium or gastrointestinal tissues. We have shown that the mechanical properties of human skin tissues obtained by bulge testing are not significantly impacted by ambient humidity or mechanical preconditioning. We applied the method to measure the stress resultant and stretch response of the tissue along the fiber and perpendicular directions and observe trends in stiffness with age. A key limitation of the bulge test method is the difficulty of calculating stress and material parameters due to the presence of bending effects. In Chapter 3, we will present an analytical method based on a thin shell model for determining the nonlinear anisotropic material parameters from the stress resultant and strain.

Chapter 3

Comparison of two structural constitutive modeling approaches for human skin tissues

This chapter develops an analytical method to fit the parameters of a constitutive model to the bulge test data presented in Chapter 2 while accounting for bending. Both a Fully Integrated distributed fiber model (FI model) and a generalized structure tensor model developed by Gasser, Odgen and Holzafel (GOH model) were fit to bulge test measurements of human skin tissue. Finite element analysis was used to validate the analysis method and to show that only the fully integrated distributed fiber model was capable of describing the experimentally measured anisotropy of human skin tissue. The chapter is reprinted from *Acta Biomaterialia*, Vol. 9, Theresa K. Tonge,

CHAPTER 3. COMPARISON OF TWO STRUCTURAL CONSTITUTIVE MODELING APPROACHES FOR HUMAN SKIN TISSUES

Liming M. Voo, Thao D. Nguyen, "Full-field bulge test for planar anisotropic tissues: Part II A thin shell method for determining material parameters and comparison of two distributed fiber modeling approaches", Pages 5913-5925, Copyright (2013), with permission from Elsevier.[89]

3.1 Introduction

Chapter 2, presented a bulge test method for planar tissues and applied the method to characterize the stress resultant- stretch response of human skin tissues. In this Chapter, we present an analytical method to determine the parameters of a hyperelastic constitutive model for the anisotropic, nonlinear stress response of the tissue from the bulge test measurements. The method was applied to two distributed fiber models commonly used for collagenous tissues, the fully integrated distributed fiber model[22,148–150] and the pre-integrated Gasser-Ogden-Holzapfel model,[28] which is based on a generalized structure tensor approach.

The majority of bulge test methods have been developed to measure the isotropic elastic properties of thin metallic films[115–117] which undergo small deformations. The method typically measures the displacement response at the apex to an applied pressure. For sufficiently thin specimens, the effects of bending can be neglected and a spherical cap geometry can be assumed for the deformed shape. This allows the hoop strains to be calculated from the difference in the arc length of the spherical cap and

the diameter of the undeformed specimen. Likewise, the membrane hoop stresses are statically determined from the pressure, radius of curvature, and thickness.[151] For thicker specimens, where bending stresses are not negligible, the specimen can be modeled as a plate subjected to a uniformly distributed lateral force. Analytical solutions have been developed by assuming small lateral displacements that relate the applied pressure to apex displacement in terms of the Young's modulus and Poisson's ratio.[152]

Bulge testing of polymers and tissues induces large deformations and a nonlinear stress response. For thin specimens, the effects of bending can be neglected, and the membrane strains and stresses can be determined analytically by assuming a spherical cap geometry for isotropic materials[23,121] or an ellipsoidal cap geometry for anisotropic materials.[24] The specimen can be modeled as a two-dimensional (2D) continuum, and the parameters of a 2D hyperelastic model can be determined by modeling the deformed geometry as a shell and calculating the membrane stress resultants from the applied pressure and principal radii of curvature.[153] Alternatively, the material parameters of a three-dimensional (3D) hyperelastic constitutive model can be determined by calculating the membrane stresses from the stress resultants divided by the deformed thickness. The latter can be evaluated from the undeformed thickness assuming incompressibility.[126] This approach assumes negligible through-thickness variation in the in-plane stress response.

For soft tissues, the effects of bending on the stress and strain response are exag-

gerated by nonlinear material behavior. A nonlinear material response can transform a small linear strain gradient through the thickness into a large nonlinear stress gradient. This has been observed in finite element studies of the inflation response of isotropic[154] and orthotropic hyperelastic[128] materials, particularly at low pressures where bending is the dominant deformation mode for initially planar structures. The stress state of a shell is not statically determined in the presence of significant bending moments and transverse shear resultants. Under these more general loading conditions, inverse finite element analysis has proven to be a powerful approach for determining material properties from bulge and inflation tests. The method optimizes the parameters of a generalized constitutive model to minimize the difference between the computed and measured surface displacement response.[123,127,155] For a 2D modeling framework, the effects of bending have also been incorporated by assuming that the 2D strain energy density can be decomposed additively into membrane, bending, and transverse shear contributions.[156] Zhou et. al.[137] developed a finite element method for inverse shell analysis to determine the material parameters of a hyperelastic model that included a Fung potential for the membrane contribution and quadratic potentials for the bending and transverse shear contributions. Inverse finite element analysis additionally can consider specimen-specific models with spatial variation in the specimen geometry, material properties, and microstructural features such as fiber orientation.[157] The major disadvantage of inverse finite element methods is that they are computationally expensive and time consuming, because both

the forward elastostatic problem and optimization problem can be highly nonlinear.

The nonlinear behavior of skin tissue is caused in part by its microstructure.[92] The extracellular matrix (ECM) of skin tissues is described by a network of long collagen and elastic fibers in a hydrated proteoglycan matrix. The collagen fibers are initially crimped at low strains, but as strain levels increase the collagen fibers become engaged, causing dramatic stiffening of the stress-strain response.[92] The fiber network exhibits a dominant fiber orientation that leads to anisotropic material behavior. Previous modeling efforts have described the anisotropic mechanical behavior of skin using the distributed fiber model for rabbit[37] and porcine[158] skin, a generalized structure tensor model for human skin,[38] the Fung orthotropic model for rabbit skin,[32] the Arruda-Boyce 8-chain model for rabbit skin [69,159–161], a structure tensor model with non-dispersed fibers for rat skin,[162] and a model that includes the fiber-fiber interactions for rabbit skin[163]. Scanning electron microscope (SEM) studies of human skin tissue suggest that the distributed fiber model is more representative of the collagen structure of the dermis, which dominates finite-strain behavior.[92,99] In this work, we examined the ability of three distributed fiber models to describe the anisotropic nonlinear elastic behavior of human skin tissues.

Distributed fiber models describe the microstructural origin of mechanical anisotropy by assuming a strain energy density at the fiber-level rather than at the tissue level. The strain energy density of the fibers is averaged over a continuous probability density distribution (PDD) of the fiber orientations to obtain the anisotropic component

of the strain energy density of the tissue. The PDD describes the dominant fiber orientation and the degree of anisotropy caused by dispersion in the fiber orientation. When there is no dispersion in the fiber orientation, the distributed fiber model reduces to a structure tensor model,[30] which expresses the strain energy density as an isotropic function of the deformation tensor and structure tensors denoting the orientation of discrete fiber families. Lanir[37,164] first modeled connective tissue as a statistical distribution of collagen fibers undergoing affine deformation with the ground matrix. Since then, distributed fiber models based on a planar orientation PDD have been applied to the cornea,[148] pericardium,[149] aortic valves,[22] and scleral tissue.[150]

The constitutive relations for distributed fiber models involve evaluating an integral expression over the a unit circle for a planar fiber structure or a unit sphere for generalized fiber structure. The integral formulation in general does not admit an analytical solution, except for specific forms of the PDD and fiber strain energy density,[165] and numerical evaluation of the distributed fiber model is computationally expensive compared to those based on structure tensors. To address this, Gasser et. al.[28] introduced a generalized structure tensor model for a distributed fiber structure, referred to in this paper as the Gasser-Odgen-Holzapfel (GOH) model. In this model, a 3D PDD for the fiber orientation is pre-integrated in the reference configuration over a unit sphere to determine an equivalent generalized structure tensor. For a fiber structure described by one dominant fiber orientation, the resulting generalized

structure tensor is a linear mixture of an isotropic tensor representing the fraction of fibers equally distributed in all orientations and a transversely isotropic structure tensor for the dominant fiber orientation. The strain energy density of the GOH model is expressed as an isotropic function of the deformation tensor and generalized structure tensor. The GOH model has been predominantly applied to arteries,[68] but has also been applied to other tissues such as the cornea,[39] and recently to human skin tested in uniaxial tension[38]. The GOH model and the analogous fully integrated (FI) distributed fiber model are equivalent only for planar distributions under equibiaxial stretch. Moreover, the two demonstrate good agreement only for cases where all fibers are loaded in tension and the fiber dispersion is small.[40,166]

In this paper, we will present an analytical method to determine material parameters of an anisotropic hyperelastic model from bulge test measurements. The bulge test measures the surface displacement field under controlled pressurization. The method fits the parameters of a constitutive relation for the biaxial stress-strain response to the surface stretch calculated from the displacement gradients and the in-plane stress resultants calculated from the applied pressure and principal radii of curvature of the deformed surface. The method accounts for a linear strain gradient through the thickness caused by the presence bending moments. We will apply the method to determine parameters of an FI and analogous GOH distributed fiber models with a planar distribution and a 3D transversely isotropic distribution. The results will be employed in finite element models of the bulge test to validate the assumptions

of the analysis method and to compare the ability of the GOH and FI distributed fiber models to reproduce the experimentally measured bulge test response.

3.2 Methods

3.2.1 Constitutive Models

We compared the ability of three distributed fiber models to describe the nonlinear anisotropic behavior of skin tissues: an FI model with a planar distribution, a 3D GOH model with a transversely isotropic distribution, and a 2D GOH model with a planar distribution. A central assumption of the distributed fiber models is that the tissue microstructure can be described as a distribution of collagen fibers in an isotropic incompressible matrix of proteoglycans, elastin, and other ECM proteins. The collagen fibers are arranged in all orientations in the tissue but exhibit a dominant fiber direction in the plane of the tissue. The fibers and matrix are assumed to share the same macroscopic deformation gradient $\mathbf{F}$ of the tissue. Furthermore, the strain energy density of the tissue can be expressed as the sum of a contribution from an incompressible isotropic matrix phase, represented by a Neo-Hookean potential, and a model-specific anisotropic potential for the fiber phase,

$$\Psi = \frac{\mu}{2}(I_1 - 3) - \frac{p}{2}(I_3 - 1) + \Psi_{aniso}, \tag{3.1}$$

where $\mathbf{C} = \mathbf{F}^{\mathrm{T}}\mathbf{F}$ is the right Cauchy-Green deformation tensor. The variables $I_1 = \mathbf{C} : \mathbf{I}$ and $I_3 = \det[\mathbf{C}]$ are the first and third invariants of the deformation tensor. The shear modulus μ describes the contribution of the isotropic matrix and the parameter p is the Lagrange multiplier for the incompressibility constraint.

We assume that the dominant fiber direction and perpendicular direction align with the principal strain directions. This was verified experimentally for select specimens in Chapter 2 by calculating the shear strain component E_{fp} from the displacement field measured by digital image correlation (DIC). The shear strains were smaller by an order of magnitude compared to the normal strain components in the fiber and perpendicular directions. Consequently, a triaxial deformation gradient is assumed for the following stress analysis in the fiber coordinate system,

$$\mathbf{F} = \lambda_f \mathbf{e}_f \otimes \mathbf{e}_f + \lambda_p \mathbf{e}_p \otimes \mathbf{e}_p + \lambda_z \mathbf{e}_z \otimes \mathbf{e}_z, \tag{3.2}$$

where λ_f, λ_p, and λ_z are the stretch along the dominant fiber direction $\mathbf{e}_f$, perpendicular direction $\mathbf{e}_p$, and normal direction $\mathbf{e}_z$. The invariants can be expressed in terms of the stretch components as $I_1 = \lambda_f^2 + \lambda_p^2 + \lambda_z^2$ and $I_3 = \lambda_f^2 \lambda_p^2 \lambda_z^2$.

Away from the clamped boundaries, the deformed specimen is assumed to be in a state of biaxial plane stress. In the following, the stress-stretch response in the fiber and perpendicular directions are determined for the FI and GOH models. Following the theory of hyperelasticity, the Cauchy stress tensor can be determined from the

strain energy density by,

$$\sigma = \frac{2}{J}\mathbf{F}\frac{\partial \Psi}{\partial \mathbf{C}}\mathbf{F}^{\mathbf{T}}, \tag{3.3}$$

where $J = \sqrt{I_3}$. The stress response in the fiber and perpendicular directions are obtained by applying the triaxial deformation in eq. (3.2) and the plane stress condition, $\sigma_z = 0$, to determine the incompressibility constraint, p. We also apply the incompressibility condition, $J = 1$, to obtain $\lambda_z = (\lambda_f \lambda_p)^{-1}$. Therefore the normal stress components in the fiber and perpendicular directions can be expressed in terms of the principal stretches λ_f and λ_p for each model.

3.2.1.1 Fully-integrated distributed fiber model

The FI distributed fiber model describes a 2D arrangement of collagen fibers in the plane of the tissue. It is assumed that the distributed fiber structure can be represented by the semi-circular von Mises distribution function,

$$\rho(\theta) = \frac{\exp(b\cos(2\theta))}{2\pi I_0(b)}, \tag{3.4}$$

where θ indicates the fiber angle in the plane of the tissue defined relative to the dominant fiber direction $\mathbf{e}_f$ and b is the concentration parameter for the degree of fiber alignment along the dominant orientation. The term $I_0(b)$ is the modified Bessel function of the first kind of order zero, $I_o(b) = \frac{1}{\pi}\int_0^{\pi} \exp\left(b\cos(\theta)\right) d\theta$. The von Mises distribution function descibes one fiber family and is capable of capturing a range

of anisotropic behavior, though the true fiber structure is only approximated. The orientation of each fiber is represented by a unit vector $\mathbf{a}_0(\theta) = \cos(\theta)\mathbf{e}_f + \sin(\theta)\mathbf{e}_p$. The stretch for a fiber oriented θ from the dominant fiber orientation is defined as, $\lambda^2(\theta) = \mathbf{C} : (\mathbf{a}_0(\theta) \otimes \mathbf{a}_0(\theta))$. The fiber stretch can be expressed in terms of the stretch in the dominant fiber and perpendicular directions as,

$$\lambda^2(\theta) = \lambda_f^2 \cos^2(\theta) + \lambda_p^2 \sin^2(\theta). \tag{3.5}$$

A strain energy density is assumed at the level of the fibers. Specifically, we apply an empirical exponential potential[167] to describe the stiffening response of the fibers,

$$\Psi_{fiber}(\lambda) = \frac{k_1}{2k_2}\left(\exp\left[k_2\left(\lambda^2(\theta) - 1\right)^2\right] - 1\right). \tag{3.6}$$

The fiber parameter k_1 has units of stiffness and describes the tensile properties of the fiber family. The fiber parameter k_2 is dimensionless and describes the nonlinearity of the fiber family, with higher values of k_2 indicating that the fibers stiffen at lower strain values.

The anisotropic contribution of the fiber phase to the strain energy density is defined for the FI model as the integration of the strain energy density of the individual fibers weighted by the continuous PDD of fiber orientations,

$$\Psi_{aniso} = \int_{-\pi}^{\pi} \Psi_{fiber}(\lambda(\theta))\rho(\theta)d\theta. \tag{3.7}$$

Applying eq. (3.3), the Cauchy stress tensor can be evaluated from the strain energy density as,

$$\sigma = \frac{1}{J}\left[\mu\mathbf{b} - p\mathbf{I} + \int_{-\pi}^{\pi} \frac{1}{\lambda}\frac{\partial \Psi_{fiber}}{\partial \lambda}\mathbf{F}\left(\mathbf{a_0}(\theta) \otimes \mathbf{a_0}(\theta)\right)\mathbf{F}^{\mathrm{T}}\rho(\theta)d\theta\right], \tag{3.8}$$

where $\mathbf{b} = \mathbf{F}\mathbf{F}^{\mathrm{T}}$ is the left Cauchy-Green deformation tensor and $J = \det[\mathbf{F}] = 1$ for the incompressible case. Substituting eqs. (3.7) and (3.2) into eq. (3.8) and applying the plane stress condition gives the following expression for the stress components in the fiber and perpendicular directions:

$$\begin{aligned}
\sigma_f(\lambda_f, \lambda_p) &= \mu\left(\lambda_f^2 - \frac{1}{(\lambda_f\lambda_p)^2}\right) + 2k_1\lambda_f^2\int_{-\pi}^{\pi}\left(\lambda^2(\theta)-1\right)\exp\left(k_2(\lambda^2(\theta)-1)^2\right)\cos^2(\theta)\rho(\theta)\mathrm{d}\theta, \\
\sigma_p(\lambda_f, \lambda_p) &= \mu\left(\lambda_p^2 - \frac{1}{(\lambda_f\lambda_p)^2}\right) + 2k_1\lambda_p^2\int_{-\pi}^{\pi}\left(\lambda^2(\theta)-1\right)\exp\left(k_2(\lambda^2(\theta)-1)^2\right)\sin^2(\theta)\rho(\theta)\mathrm{d}\theta.
\end{aligned} \tag{3.9}$$

The stress response is composed of an incompressible Neo-Hookean contribution from the matrix and anisotropic contribution from the distributed fiber structure. Numerical integration is needed to evaluate the anisotropic contribution.

3.2.1.2 3D Gasser-Ogden-Holzapfel Model

The 3D GOH model applies a transversely isotropic PDD, $D(\theta)$, to describe the distribution of collagen fibers, where θ is measured from the fiber direction. The transversely isotropic PDD is developed by normalizing the semi-circular von Mises

PDD in eq. (3.4) over the surface of a unit sphere:[28]

$$D(\theta) = \frac{2\rho(\theta)}{\int_0^\pi \rho(\theta)\sin(\theta)\mathrm{d}\theta} = 4\sqrt{\frac{b}{2\pi}}\frac{\exp[b(\cos(2\theta+1))]}{\mathrm{erfi}(\sqrt{2b})}. \tag{3.10}$$

While the FI model attributes the anisotropic stress response directly to the distribution in fiber orientation, the GOH model describes the anisotropic stress response using a generalized structure tensor derived from the fiber distribution. This allows the GOH model to define a closed-form expression for strain energy density at the tissue level.

To describe the anisotropic structure of the undeformed tissue, the GOH model applies $D(\theta)$ to define a generalized structure tensor $\mathbf{A}$ as follows,

$$\mathbf{A} = \frac{1}{4\pi}\int_{-\pi}^{\pi}\int_0^\pi D(\theta)\mathbf{M}(\theta,\phi)\otimes\mathbf{M}(\theta,\phi)\sin(\theta)\mathrm{d}\theta\mathrm{d}\phi, \tag{3.11}$$

where $\mathbf{M} = \sin(\theta)\cos(\phi)\mathbf{e_f} + \sin(\theta)\sin(\phi)\mathbf{e_p} + \cos(\theta)\mathbf{e_z}$ represents the orientation vector of the fibers distributed over a sphere. The integral over the transverse orientation ϕ can be evaluated analytically to simplify the expression in eq. (3.11) to,

$$\mathbf{A} = \kappa\mathbf{I} + (1-3\kappa)\mathbf{e}_f\otimes\mathbf{e}_f, \tag{3.12}$$

where $\mathbf{e}_f$ is the dominant fiber direction. The dispersion parameter κ is defined by

the fiber distribution,

$$\kappa = \frac{1}{4}\int_0^{\pi} D(\theta)\sin^3(\theta)\mathrm{d}\theta. \tag{3.13}$$

The generalized structure tensor $\mathbf{A}$ conveys the preferred fiber orientation and the degree of anisotropy of the undeformed tissue. The latter is evident in the formulation of $\mathbf{A}$ as a mixture of an isotropic tensor, representing the fraction of randomly oriented fibers, and a structure tensor, $\mathbf{e}_f \otimes \mathbf{e}_f$, for the preferred fiber orientation. The dispersion parameter κ measures the relative contributions of the isotropic and anisotropic fractions of the fiber distribution and has a one-to-one correspondence with the concentration parameter b of the von Mises distribution (Fig. 3.1).

Defining the generalized structure tensor allows the anisotropic contribution of the strain energy density, Ψ_{aniso}, to be defined at the tissue level, rather than fiber level for the FI model. Specifically, Ψ_{aniso} is expressed as a function of the psuedo-invariant, $I_\alpha = \mathbf{C} : \mathbf{A}$, of the right Cauchy-Green deformation tensor and generalized structure tensor, which evaluates to,

$$I_\alpha = \kappa I_1 + (1 - 3\kappa)\lambda_f^2. \tag{3.14}$$

The same exponential potential used for the strain energy density of the collagen fibers in the FI model[167] is used here for the tissue to capture the strain stiffening

behavior associated with fiber recruitment,

$$\Psi_{aniso}(I_\alpha) = \frac{k_1}{2k_2}\left(exp\left[k_2\left(I_\alpha - 1\right)^2\right] - 1\right). \tag{3.15}$$

The biaxial stress-strain relation for the 3D GOH model is obtained from the strain energy density via eq. (3.3),

$$\begin{aligned}\sigma_f(\lambda_f, \lambda_p) &= \left(\mu + 2k_1\kappa(I_\alpha - 1)\exp\left[k_2(I_\alpha - 1)^2\right]\right)\left(\lambda_f^2 - \frac{1}{(\lambda_f\lambda_p)^2}\right) \\ &\quad + 2k_1(1 - 3\kappa)(I_\alpha - 1)\exp\left[k_2(I_\alpha - 1)^2\right]\lambda_f^2, \\ \sigma_p(\lambda_f, \lambda_p) &= \left(\mu + 2k_1\kappa(I_\alpha - 1)\exp\left[k_2(I_\alpha - 1)^2\right]\right)\left(\lambda_p^2 - \frac{1}{(\lambda_f\lambda_p)^2}\right).\end{aligned} \tag{3.16}$$

The stress response of the fiber phase contains an isotropic component that describes the contribution of the fibers randomly distributed in all orientations. It also contains an anisotropic contribution from the preferentially aligned fibers. The anisotropic contribution appears in the fiber stress component σ_f but not the perpendicular stress component σ_p. The use of the generalized structure tensor eliminates the need for numerical integration to calculate the fiber contribution to the stress.

3.2.1.3 2D Gasser-Ogden-Holzapfel Model

For the 2D GOH model, the fibers are assumed to distribute only in the plane of the tissue. The von Mises PDD is used to describe the planar arrangement. The generalized structure tensor is obtained for the 2D GOH model by integrating the

fiber distribution over all possible orientations in the plane:

$$\mathbf{A} = \frac{1}{2\pi}\int_{-\pi}^{\pi} \rho(\theta)\mathbf{M}(\theta)\otimes\mathbf{M}(\theta)\mathbf{d}\theta. \tag{3.17}$$

where $\mathbf{M} = \cos(\theta)\mathbf{e_f} + \sin(\theta)\mathbf{e_p}$ is an arbitrary two-dimensional unit orientation vector. The generalized structure tensor can be expressed in the following compact form,

$$\mathbf{A} = \kappa_{2D}\left(\mathbf{e}_f\otimes\mathbf{e}_f + \mathbf{e}_p\otimes\mathbf{e}_p\right) + (1-2\kappa_{2D})\mathbf{e}_f\otimes\mathbf{e}_f, \tag{3.18}$$

where κ_{2D} is the 2D dispersion parameter defined as follows,

$$\kappa_{2D} = \frac{1}{2\pi}\int_{-\pi}^{\pi}\rho(\theta)\sin^2(\theta)d\theta. \tag{3.19}$$

Here the generalized structure tensor $\mathbf{A}$ is a linear mixture of a 2D isotropic tensor and a structure tensor for the preferred orientation in the plane. The dispersion parameter, κ_{2D}, denotes the relative contribution of the isotropic and anisotropic fractions of the planar fiber distribution and again has a one-to-one correspondence with the concentration parameter b of the von Mises distribution (Fig. 3.1). For the 2D GOH model, the pseudo-invariant, $I_\alpha = \mathbf{C}:\mathbf{A}$, evaluates to,

$$I_\alpha = \kappa_{2D}\lambda_p^2 + (1-\kappa_{2D})\lambda_f^2. \tag{3.20}$$

An exponential potential is assumed for the anisotropic component of the strain energy density of the tissue,

$$\Psi_{aniso}(I_\alpha) = \frac{k_1}{2k_2}\left(exp\left[k_2\left(I_\alpha - 1\right)^2\right] - 1\right). \tag{3.21}$$

After applying eq. (3.3), the resulting biaxial stress-strain relation for 2D GOH model is:

$$\begin{aligned}\sigma_f(\lambda_f, \lambda_p) &= \mu\left(\lambda_f^2 - \frac{1}{(\lambda_f\lambda_p)^2}\right) + 2k_1(1-\kappa_{2D})\left(I_\alpha - 1\right)\exp\left[k_2(I_\alpha - 1)^2\right]\lambda_f^2, \\ \sigma_p(\lambda_f, \lambda_p) &= \mu\left(\lambda_p^2 - \frac{1}{(\lambda_f\lambda_p)^2}\right) + 2k_1\kappa_{2D}\left(I_\alpha - 1\right)\exp\left[k_2(I_\alpha - 1)^2\right]\lambda_p^2.\end{aligned} \tag{3.22}$$

Unlike the 3D GOH model, there is no isotropic contribution to Ψ_{aniso} from the fiber structure.

3.2.1.4 Material Parameters

The distributed fiber models share three common parameters: the shear modulus μ, the fiber family stiffness parameter k_1, and the fiber family nonlinearity parameter k_2. The significance of the parameters are directly comparable between the models. However, the anisotropy parameter differs between models (b, κ, κ_{2D}). For the FI distributed fiber model, the concentration parameter b ranges from 0 to infinity, with 0 describing a randomly oriented fibers and infinity describing perfectly aligned fibers. The fiber distribution parameter κ ranges from $0 - 1/3$ for the 3D GOH model, while

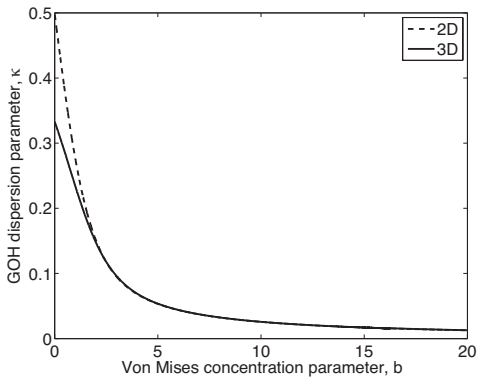

Figure 3.1: Relation between 2D and 3D version of structure tensor dispersion parameter κ and von Mises concentration parameter b. A value of $b = 0$ indicates isotropy and $b = \infty$ indicates perfect alignment of fibers.

κ_{2D} ranges from $0 - 1/2$ for the 2D GOH model. For both GOH models $\kappa = 1/3$ and $\kappa_{2D} = 1/2$ denotes a random fiber orientation and $\kappa = \kappa_{2D} = 0$ describes a perfect alignment of fibers. The three anisotropy parameters are related and can be translated between the models for direct comparison by eqs. (3.13) and (3.19). The relation between the three anisotropy parameters is plotted in Figure 3.1.

It is apparent from Figure 3.1 that although κ_{2D} ranges from 0.5 and 0 and κ ranges from .333 and 0, the two are nearly identical for strongly anisotropic cases where the concentration parameter b is large.

3.2.2 Calculating the Stress Resultants

For a curved shell, the in-plane stress resultants can be defined for the dominant fiber and perpendicular directions as,

$$\begin{aligned} N_f &= \int_{-t/2}^{t/2} \sigma_f\big(\lambda_f(z), \lambda_p(z)\big)\,(1 + K_p z)\,\mathrm{d}z, \\ N_p &= \int_{-t/2}^{t/2} \sigma_p\big(\lambda_f(z), \lambda_p(z)\big)\,(1 + K_f z)\,\mathrm{d}z, \end{aligned} \tag{3.23}$$

where t is the deformed thickness of the tissue, z is the direction normal to the surface, and K_f and K_p are the curvatures of the fiber and perpendicular meridians, respectively.

We assume that $Kt << 1$, i.e. the curvatures and thickness are small. The expressions for the stress resultants can be simplified to the familiar expressions for a plate,[132]

$$\begin{aligned} N_f^m &= \int_{-t/2}^{t/2} \sigma_f\big(\lambda_f(z), \lambda_p(z)\big)\,\mathrm{d}z, \\ N_p^m &= \int_{-t/2}^{t/2} \sigma_p\big(\lambda_f(z), \lambda_p(z)\big)\,\mathrm{d}z. \end{aligned} \tag{3.24}$$

The thickness t of the deformed specimen can be determined from the initial thickness by using the incompressibility condition as follows,

$$t = \frac{t_0}{\lambda_f \lambda_p}. \tag{3.25}$$

To evaluate eq. (3.24) for the constitutive relations in Section 3.2.1, we assume that the in-plane stretches exhibit linear variation through the thickness caused by the presence of bending moments about the fiber and perpendicular directions. We also assume that the variation in the curvature through the thickness is negligible. Consequently, the in-plane stretches at any point through the thickness of the tissue can be calculated from the stretches, λ_f^s, λ_p^s, and curvatures, K_f, K_p, measured at the surface of the tissue,

$$\begin{aligned} \lambda_f(z) =& \lambda_f^s + K_f \left(z - \frac{t}{2} \right), \\ \lambda_p(z) =& \lambda_p^s + K_p \left(z - \frac{t}{2} \right). \end{aligned} \tag{3.26}$$

The DIC measurements for the displacement field showed that the initially flat, circular tissue specimen bulged into a ellipsoidal cap. The surface of the ellipsoidal cap at any given point can be characterized by two principal curvatures. At the apex, the principal curvatures correspond to the curvature of the deformed meridians along the dominant fiber and perpendicular directions. Thus, to determine the curvature of the fiber meridian, we fit a 2D general ellipse to the deformed meridian to obtain the major and minor radii, a_f and b_f, and angle of tilt, θ_f, as described in detail in Chapter 2. The procedure was repeated for the perpendicular meridian to obtain the major and minor radii, a_p and b_p, and angle of tilt, θ_p. The curvature of the

perpendicular and fiber meridians were determined locally at the apex[168] as follows,

$$\begin{aligned} K_f &= \frac{\left(a_f^2 \sin^2(\theta_f) + b_f^2 \cos^2(\theta_f)\right)^{3/2}}{a_f^2 b_f^2}, \\ K_p &= \frac{\left(a_p^2 \sin^2(\theta_p) + b_p^2 \cos^2(\theta_p)\right)^{1/2}}{a_p^2}. \end{aligned} \tag{3.27}$$

To evaluate the stress resultants N_f and N_p from the experimental measurements of pressure and deformed curvatures, we modeled the bulged specimen as an axisymmetrically loaded thin shell. At the apex and far from the clamped boundaries, we assumed that the transverse shear resultants are negligible compared to N_f and N_p. Under these conditions, the in-plane stress resultants at the apex are statically determined from the applied pressure and curvature of the deformed surface[136]. Specifically, for a thin shell subjected to internal pressure loading P, the in-plane principal stress resultants are given by[126,135],

$$\begin{aligned} N_f^{exp} &= \frac{P}{2K_p}, \\ N_p^{exp} &= \frac{P}{K_p}\left(\frac{2K_p - K_f}{2K_p}\right), \end{aligned} \tag{3.28}$$

where P is the inflation pressure and K_f and K_p are the local principal curvatures. For the bulged skin specimens, the principal directions correspond to the fiber and perpendicular directions at the apex, where there are negligible shear strains.[88] The relations in eq. (3.28) are solutions to the equilibrium equations for the stress resultants in the meridional and circumferential directions of an axisymmetric shell.[134]

However, the relations have been applied in the literature more generally to calculate the principal stress resultants for thin shells with smooth convex curvatures.[126,135,136]

The bulged surface can alternatively be modeled as a general ellipsoid, with a major radius, a and two different minor radii b and c. A solution for the normal stress resultants was developed by Flugge.[134] At the apex, the resultants in the fiber and perpendicular directions can be expressed in term of the major and minor radii of the ellipsoidal dome as,

$$\begin{aligned} N_f^{exp} &= \frac{Pc}{2}\left(\frac{ab}{c^2} - \frac{a}{b} + \frac{b}{a}\right)\frac{a}{b}, \\ N_p^{exp} &= \frac{Pc}{2}\left(\frac{ab}{c^2} - \frac{b}{a} + \frac{a}{b}\right)\frac{b}{a}. \end{aligned} \tag{3.29}$$

In Chapter 2 we showed that fitting a general 3D ellipsoid to the bulged surface to determine the major and minor radii produced a less accurate representation of the perpendicular meridian compared to the method of fitting 2D ellipses directly to the fiber and perpendicular meridians. In Section 3.3, we will show that the use of the general ellipsoid fit for curvature calculations causes significant errors in the stress resultant calculations. These errors most likely arise from the difficulty in obtaining accurate curvatures for the general ellipsoid model.

3.2.2.1 Parameter Determination

Six cadaveric human skin specimens from the back torso were subjected to bulge testing. The experimental stress resultants in both the fiber and perpendicular direc-

tions were computed from DIC data using eq. (3.28). We developed a procedure to determine the parameters of the constitutive relations for the three distributed fiber models in Section 3.2.1 to minimize the difference between the experimental stress resultants calculated using eq. (3.28) and the stress resultants computed from the constitutive relations using eq. (3.24). Parameters were determined iteratively by numerical integration of eq. (3.24).

The shear modulus μ of the ground matrix was determined first by assuming that the stress response of the initial compliant toe region is dominated by the matrix. This was defined as the region prior to the onset of stiffening, where stretches in the fiber and perpendicular directions were typically less than 1.10 and 1.15, respectively. The stress resultant was computed using eq. (3.24) and fit to this region only for the contribution of the matrix to the stress response,

$$\begin{aligned} \sigma_f &= \mu \left(\lambda_f^2 - \frac{1}{(\lambda_f \lambda_p)^2} \right), \\ \sigma_p &= \mu \left(\lambda_p^2 - \frac{1}{(\lambda_f \lambda_p)^2} \right). \end{aligned} \tag{3.30}$$

To fit the remaining parameters associated with the fiber phase, an unconstrained global search optimization algorithm (fminsearch.m in Matlab) was used to search for the minimum of the cost function,

$$C = \frac{1}{n} \sum_{i=1}^{n} \sqrt{\left(N_{f_i}^m \left(\sigma_f(\beta, \lambda_f, \lambda_p)\right) - N_{f_i}^{exp}(P)\right)^2 + \left(N_{p_i}^m \left(\sigma_p(\beta, \lambda_f, \lambda_p)\right) - N_{p_i}^{exp}(P)\right)^2}, \tag{3.31}$$

Model	Fitting Method	b_0 or κ_0	$k_{1,0}$	$k_{2,0}$
2D FI	resultant fit	0.01	10	1
2D GOH	resultant fit	0.18	1	100
3D GOH	resultant fit	0.18	1	100
2D FI	membrane fit	1	1	10

Table 3.1: Initial guesses for parameter determination.

where n is the number of pressure steps and β is a vector of the parameters for the selected constitutive model. The parameters are $\beta = [k_1, k_2, b]$ for the FI model and $\beta = [k_1, k_2, \kappa]$ for the GOH models.

To evaluate of the effect of bending stress gradients, the parameters of the FI distributed fiber model were also determined by modeling the bulged specimens as a membrane. The membrane stresses are constant through the thickness and can be calculated from the experimentally determined stress resultants as,

$$\begin{aligned} \sigma_f^{mem} &= \frac{N_f^{exp}}{t}, \\ \sigma_p^{mem} &= \frac{N_p^{exp}}{t}, \end{aligned} \tag{3.32}$$

where t is the deformed thickness calculated using eq. (3.25). The same unconstrained global search optimization algorithm (fminsearch.m in Matlab) was used to minimize the cost function,

$$C = \frac{1}{n}\sum_{i=1}^{n} \sqrt{\left(\sigma_{f_i}(\beta, \lambda_f, \lambda_p) - \sigma_{f_i}^{mem}(P)\right)^2 + \left(\sigma_{p_i}(\beta, \lambda_f, \lambda_p) - \sigma_{p_i}^{mem}(P)\right)^2}, \tag{3.33}$$

where σ_{f_i} and σ_{p_i} are computed by eq. (3.9). The same optimization algorithm was

used as for the resultant fitting method.

The initial guesses for all models for both the stress resultant and membrane stress fits are listed in Table 3.1. The converged parameters were then used as the initial guess for a second minimization to ensure convergence. The converged parameters were not found to be sensitive to small changes in the initial guess.

3.2.3 Finite Element Model

Finite element studies of the bulge tests were performed to validate the assumptions of the analysis method and the material parameters determined for the three distributed fiber models. The simulations were performed using Tahoe©, an open source finite element code originally developed by Sandia National Labs, Livermore, CA [1]. Specimen-specific geometries were created using the diameter of the aperture of the inflated specimens (7.5 cm) and the thickness measured for each specimen. The geometry was discretized using 8-node brick elements. A mixed element formulation that provided for a trilinear displacement interpolation and a piecewise constant dilatational strain projection was used to account for the effects of incompressibility. The mesh had 10 elements through the thickness and a total of 5400 elements. This mesh design provided high resolution through the thickness to capture bending gradients. A coarser mesh discretization was used in the plane because experimental measurements showed that the in-plane strain components exhibited little variation

[1] http://sourceforge.net/projects/tahoe/

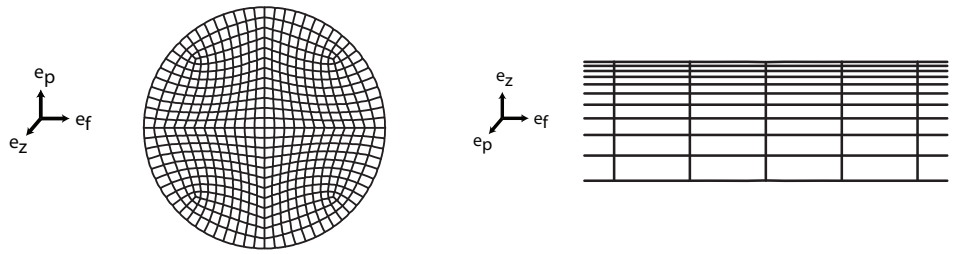

(a) (b)

Figure 3.2: Finite element mesh (a) top view and (b) cross section through thickness. The element size through the thickness was graded to resolve the nonlinear bending gradients and to mitigate the effects of volumetric locking.

in a large region surrounding the apex. The element size through the thickness was graded, with the thinnest elements near the surface where the stress gradients were highest, to further resolve the nonlinear stress gradient through the thickness (Fig. 3.2) and mitigate the effects of volumetric locking. The displacement components were fixed at the edge and a Cauchy traction, corresponding to the pressure applied in experiments, was applied normal to the bottom surface. Pressure was modeled using the pressure history recorded for each experiment. The experimental pressure increase with time was not strictly linear, particularly in the toe region where the applied pressure lagged the target pressure. This resulted in slower loading rates for the toe region.

The material behavior was described using a quasi-incompressible implementation of the distributed fiber models described in Sec. 3.2.1.1-Sec 3.2.1.2. A quasi-incompressible rather than an incompressible model was used because the latter was not implemented in the FEA program Tahoe. The strain energy for the compressible

model was additively decomposed into a compressible isotropic contribution for the matrix and and an anisotropic contribution for the fiber,

$$\Psi = \Psi_{matrix} + \Psi_{fiber}. \tag{3.34}$$

A compressible Neo-Hookean potential was used to describe the matrix contributions:

$$\Psi_{matrix}(\bar{I}_1, I_3) = \frac{K}{4}(I_3 - 1 - \ln I_3) + \frac{\mu}{2}(\bar{I}_1 - 3), \tag{3.35}$$

where K is the bulk modulus, and $\bar{I}_1 = I_3^{-1/3} I_1$ is the first invariant of the deviatoric component of the right Cauchy-Green deformation tensor $\bar{\mathbf{C}} = I_3^{-1/3}\mathbf{C}$. The matrix contribution to the Cauchy stress response was evaluated according to hyperelasticity as,

$$\sigma_{matrix}(J, \bar{I}_1, \bar{\mathbf{b}}) = \frac{K}{2}(J - \frac{1}{J})\mathbf{I} + \frac{\mu}{J}(\bar{\mathbf{b}} - \frac{1}{3}\bar{I}_1\mathbf{I}). \tag{3.36}$$

where $\bar{\mathbf{b}} = I_3^{-1/3}\mathbf{b}$ is the deviatoric component of the left Cauchy-Green deformation tensor. The same strain energy Ψ_{aniso} in eq. (3.9),(3.16), and(3.22) was used for each distributed fiber model. For all simulations, the bulk modulus K was set as 80 kPa. This value was selected such that the Jacobian J obtained at the maximum pressure for all simulations was less than 1.003, indicating that less than 0.3% volume change was observed.

The thin shell analysis was applied to determine the parameters for the three

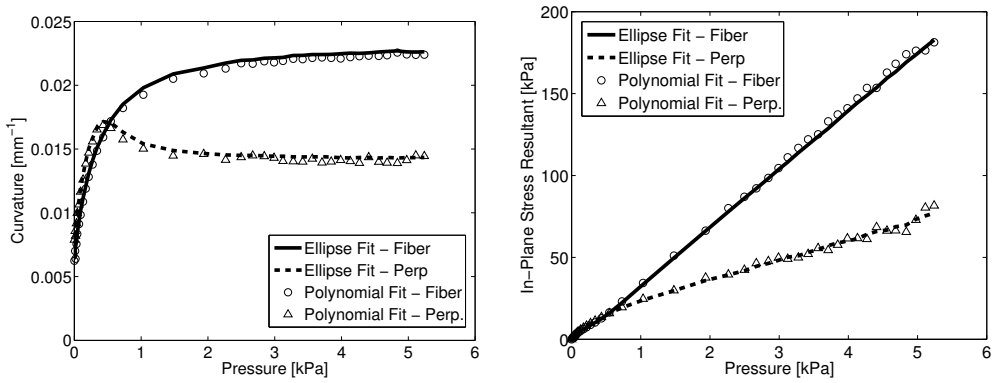

(a) (b)

Figure 3.3: Comparisons of the ellipse fit [eq. (3.27)] and polynomial fit [eq. (3.37)] method to calculate (a) curvatures from the experimentally measured displacement field for a representative 44/M specimen. The stress resultants calculated from the curvatures are compared in (b).

distributed fiber models: the 2D FI , 3D GOH, and 2D GOH models, presented in Sec. 3.2.1.1-3.2.1.3. The 2D FI model was applied for finite element simulation of the bulge test to validate key assumptions of the analysis method. Specifically, we examined the variation of the strain through the thickness of the specimen, the presence of transverse and in-plane shear strains near the apex, and the ability of eq. (3.28) used with eq. (3.27) for local curvature calculations and eq. (3.29) for the general ellipsoid model to accurately calculate the in-plane stress resultants.

Unlike for the experimental data, there were not enough points (nodes) to accurately fit an ellipse to the meridian. The use of quadratic elements instead of linear elements would provide more nodes for curvature fitting, but at the expense of computational time. Instead, the curvatures for the simulation were calculated by fitting a 6^{th} order polynomial $f(x)$ to each meridian and calculating the curvature at the

apex by,

$$K = \frac{|\frac{\partial f(x)}{\partial x}|}{\left[1 + \left(\frac{\partial f(x)}{\partial x}\right)^2\right]^{-3/2}}. \tag{3.37}$$

Figure 3.3 shows for a representative specimen (44/M) that this polynomial curvature calculation provided equivalent results as the ellipsoidal calculation in eq. (3.27) used for the experiments.

Finally, the parameters for all three models were implemented to evaluate numerically the anisotropic pressure-stretch and pressure-stress resultant response for all tested specimens. These were compared to the experimentally measured relations to validate the thin shell analysis and parameter determination method.

3.3 Results

3.3.1 Model Parameter Determination

Table 3.2 lists parameters governing the stress response of the 2D FI distributed fiber model in eq. (3.9), while Tables 3.3 and 3.4 list the parameters for the 2D GOH model presented in eq. (3.16) and 3D GOH model in eq. (3.22). Notable variation in the parameters between specimens was observed. The matrix shear modulus was identical for all models because a Neo-Hookean model was used to describe the matrix contribution for all three distributed fiber models and μ was determined from the toe-region of the stress resultant response independent of the fiber parameters. The fiber

specific parameters k_1 and k_2 were similar between the 2D FI and 2D GOH model, but were higher for the 3D GOH model. To compare the anisotropy parameters, the dispersion parameter κ for the 3D GOH model and κ_{2D} for the 2D GOH model were converted to the von Mises concentration parameter b used in by the 2D FI model. The results are presented in Table 3.5. A paired t-test was used to determine if there was a significant difference ($p > 0.05$) in the anisotropy parameters between models. It was found that the 2D FI model concentration parameter was significantly larger than both the 3D GOH model ($p = 0.0275$) and 2D GOH model ($p = 0.0265$). Among the GOH models, although the average concentration parameter was slightly higher for the 2D than 3D model, the difference was not significant ($p = 0.183$). However, the paired t-test has very low power due to the small number of samples and wide standard deviations compared.

Figure 3.4 plots the fit for the stress resultant for a representative specimen (44/M) for all three models. The fit was near exact for both GOH models but underestimated the stiffening region stress resultant for the FI distributed fiber model.

Table 3.2: Specimen Parameters: 2D Fully Integrated Distributed Fiber Model.

Sample	μ [kPa]	b	k_1 [kPa]	k_2
43/M	6.804	8.869	5.209	32.721
44/M	5.648	16.467	0.025	58.737
59/F	4.773	8.880	1.039	54.497
61/M	8.262	4.199	0.782	123.241
62/F	6.286	2.649	0.073	15.876
83/M	22.637	1.693	8.200	202.926
Average	9.068	7.126	2.555	81.333
Std. Dev.	6.749	5.505	3.374	69.885

Table 3.3: Specimen Parameters: 3D Gasser-Ogden-Holzapfel Model.

Sample	μ [kPa]	κ	k_1 [kPa]	k_2
43/M	6.804	0.120	9.850	52.529
44/M	5.648	0.183	0.380	89.842
59/F	4.773	0.236	4.770	161.862
61/M	8.262	0.293	14.137	1103.900
62/F	6.286	0.318	0.999	78.841
83/M	22.634	0.336	2427.700	5984.200
Average	9.068	0.248	409.639	1245.196
Std. Dev.	6.748	0.084	988.658	2356.668

Table 3.4: Specimen Parameters: 2D Gasser-Ogden-Holzapfel Model.

Sample	μ [kPa]	κ_{2D}	k_1 [kPa]	k_2
43/M	6.804	0.107	3.766	30.739
44/M	5.648	0.195	0.040	39.131
59/F	4.773	0.271	0.281	45.959
61/M	8.262	0.369	0.221	120.852
62/F	6.286	0.467	0.006	18.845
83/M	22.634	0.540	4.636	200.967
Average	9.068	0.325	1.446	76.082
Std. Dev.	6.748	0.165	2.040	71.001

Table 3.5: Translated Anisotropy Parameters (b - von Mises concentration parameter)

Sample	2D FI Distributed Fiber Model	3D GOH model	2D GOH Model
43/M	8.869	2.459	2.710
44/M	16.467	1.545	1.557
59/F	8.880	0.984	1.033
61/M	4.199	0.424	0.543
62/F	2.649	0.167	0.132
83/M	1.693	0.000	0.000
Average	6.070	0.996	0.930
Std. Dev.	3.850	1.020	0.940

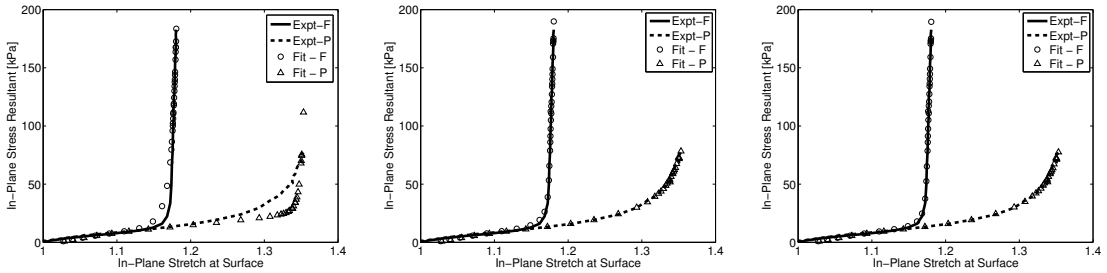

(a) (b) (c)

Figure 3.4: Stress resultant fit to experimental data for a representative specimen (44/M) for (a) the 2D FI distributed fiber model, (b) the 3D GOH model and (c) the 2D GOH model.

3.3.2 Finite Element Validation of Thin Shell Method Assumptions

The parameters of the 2D FI distributed fiber model were applied to simulate the bulge test for a representative specimen (44/M) to validate key assumptions of the thin-shell analysis method: the accuracy of using eq. (3.28) along with eq. (3.27) for the local curvature calculations to determine the stress resultants in the fiber and perpendicular directions, the assumptions of linear strain gradient through the specimen thickness, and the assumption of no transverse shear. Figure 3.5 (a) plots the through-thickness variation for the stretch in the fiber and perpendicular directions at the apex and at the maximum inflation pressure. The strain gradient is small and approximately linear through the thickness, as evidenced by the linear regression fits displayed on the plots. The linear regression R^2 values for all six 2D FI model simulations are reported in Table 3.6. Additionally, Fig. 3.5 (b) plots the in-plane (σ_{fp}) and transverse (σ_{fz}, σ_{pz}) shear stress for the same simulation at the apex for the maximum simulation pressure. The transverse shear stresses are effectively zero (σ_{fz} and $\sigma_{pz} < 10^{-11}$ kPa) and the in-plane shear is less than 0.02% of the normal in-plane stress, σ_f.

For the experiments, the stress resultants were determined using eq. (3.28) from the inflation pressure and local principal curvatures. To assess the accuracy of this assumption, the stress resultants of the finite element simulations were evaluated by

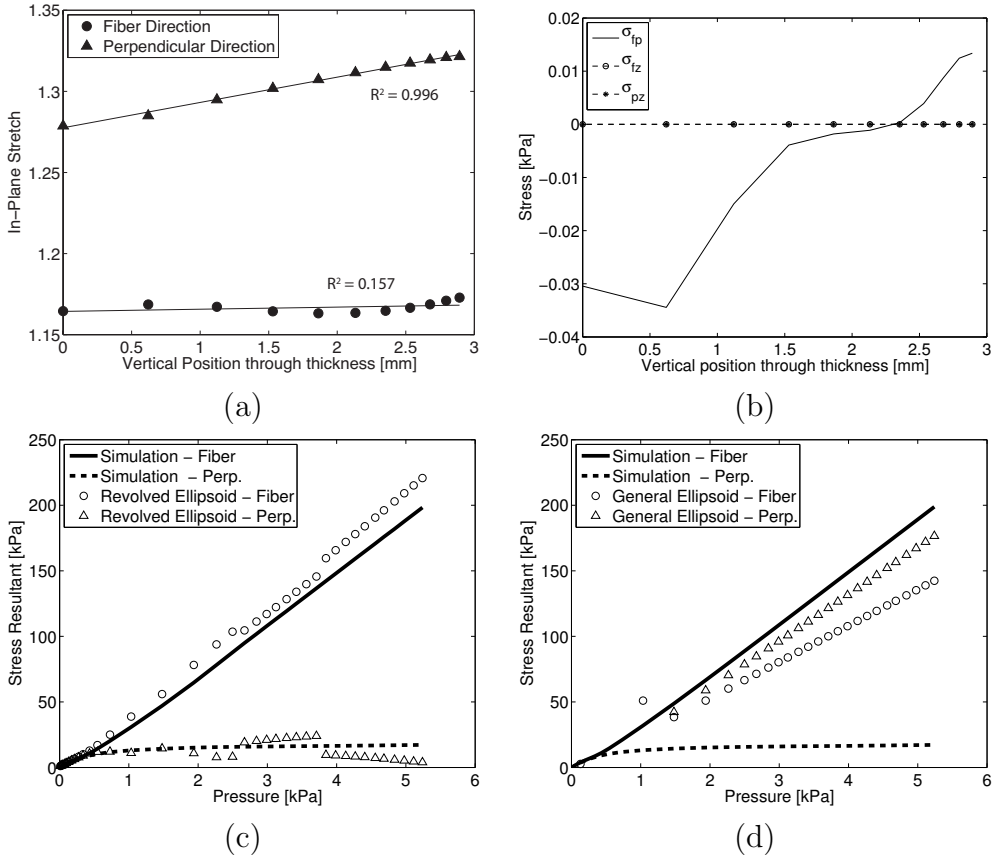

Figure 3.5: Validation of thin shell method assumptions, based on 44/M parameters with the 2D FI distributed fiber model: (a) strains through the thickness of FE simulation with linear regression fits, (b) in-plane and transverse shear stresses through the thickness at the apex of the simulation at the maximum inflation pressure, (c) FE simulation results for the stress resultant compared to theoretical model in eq. (3.28) using curvatures determined from eq. (3.27), and (d) FE simulation results for the stress resultant compared to the theoretical ellipsoidal shell model in eq. (3.29).

Table 3.6: R^2 value for linear regression of stretches through the thickness at the apex of the simulation of the 2D FI model.

Sample	Fiber	Perpendicular
43/M	0.824	0.995
44/M	0.157	0.996
59/F	0.103	0.996
61/M	0.925	0.993
62/F	0.998	0.992
83/M	0.993	0.993
Average	0.667	0.994
Std Dev	0.421	0.002

integrating the nodal stresses at the apex through the thickness using the definitions in eq. (3.24). In addition, the stress resultants were calculated by treating the finite element simulations as an experiment. The finite element displacement fields were used to calculate the curvature of the fiber and perpendicular meridians at the apex using eq. (3.37). These curvatures were then used to calculate the stress resultant using eq. (3.28). Figure 3.5 (c) compares the stress resultant calculated for the FEA simulations using the fundamental definitions in eq. (3.24) and theoretical model in eq. (3.28). Good agreement is seen for both the fiber and perpendicular directions for this representative specimen. Plots for all specimens tested can be found Fig. 3.6. Again, good agreement is seen for all specimens, with nearly exact agreement for more isotropic specimens.

Alternatively, the inflated specimen could be modeled as a general ellipsoid, where the stress resultants at the apex would be calculated from the pressure and major and minor radii of the deformed ellipsoidal cap using eq. (3.29). Figure 3.5 (d) compares

the general ellipsoidal shell model for the stress resultant to those calculated by integrating the nodal stresses through the thickness. Plots for all specimens tested can be found in Fig. 3.7. The general ellipsoid calculation severely overestimated the stress resultant in the perpendicular direction. Moreover, it could not reproduce the large difference in the stress resultant response of the perpendicular and fiber directions. The material parameters used in the simulation were determined using the local curvature fitting method, but it has been shown that the stress resultant calculation is statically determined from the inflation pressure and radii and is not influenced by choice of material model or material parameters.[135] The same inaccuracies in the general ellipsoid stress resultant calculation were observed for simulations with parameters determined using the general ellipsoid model. It was observed that the general ellipsoid provided a poor fit for the curvature in the perpendicular and fiber meridian. This is likely responsible for the inaccurate approximation of the stress resultants. The same problem was encountered when fitting a general 3D ellipsoid to the DIC data to determine the principal curvatures for the bulged surface in Chapter 2.

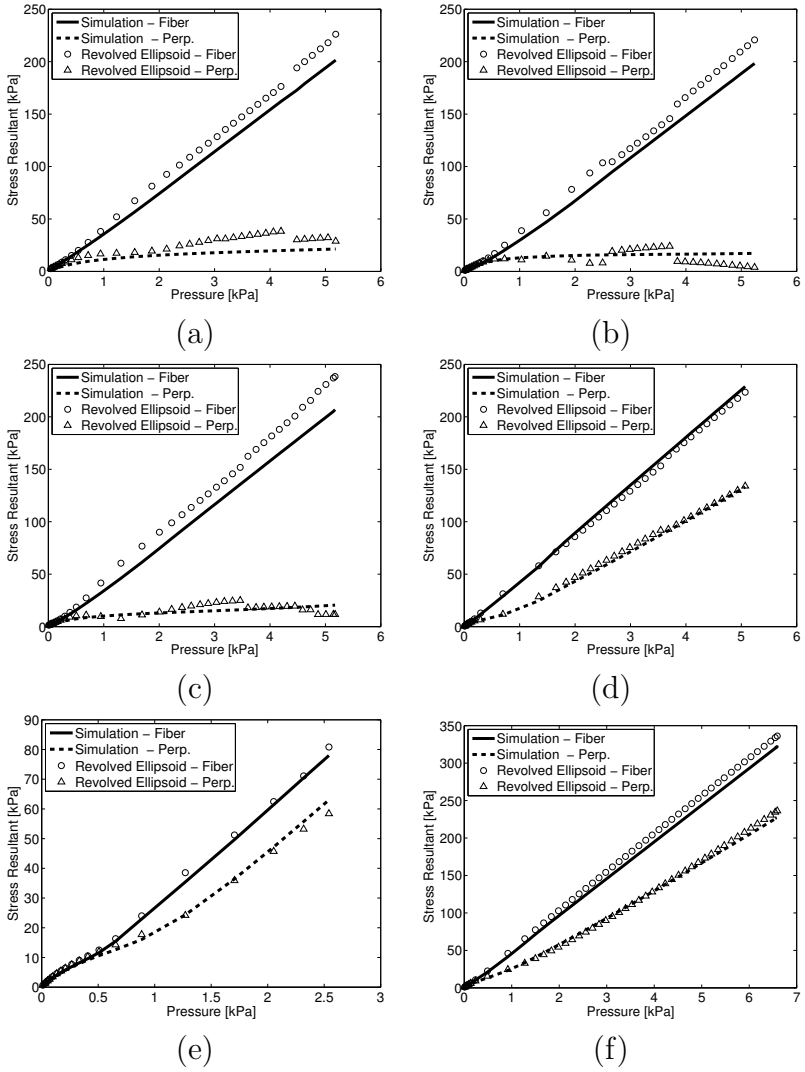

Figure 3.6: FE simulation results for the stress resultant compared to theoretical model in Eq. (28) using curvatures determined by Eq. (27) for (a) 43/M, (b) 44/M, (c) 59/F, (d) 61/M, (e) 62/F, and (f) 83/M specimens. As discussed in Section 3.2, good agreement is observed for all specimens in both the fiber and perpendicular directions.

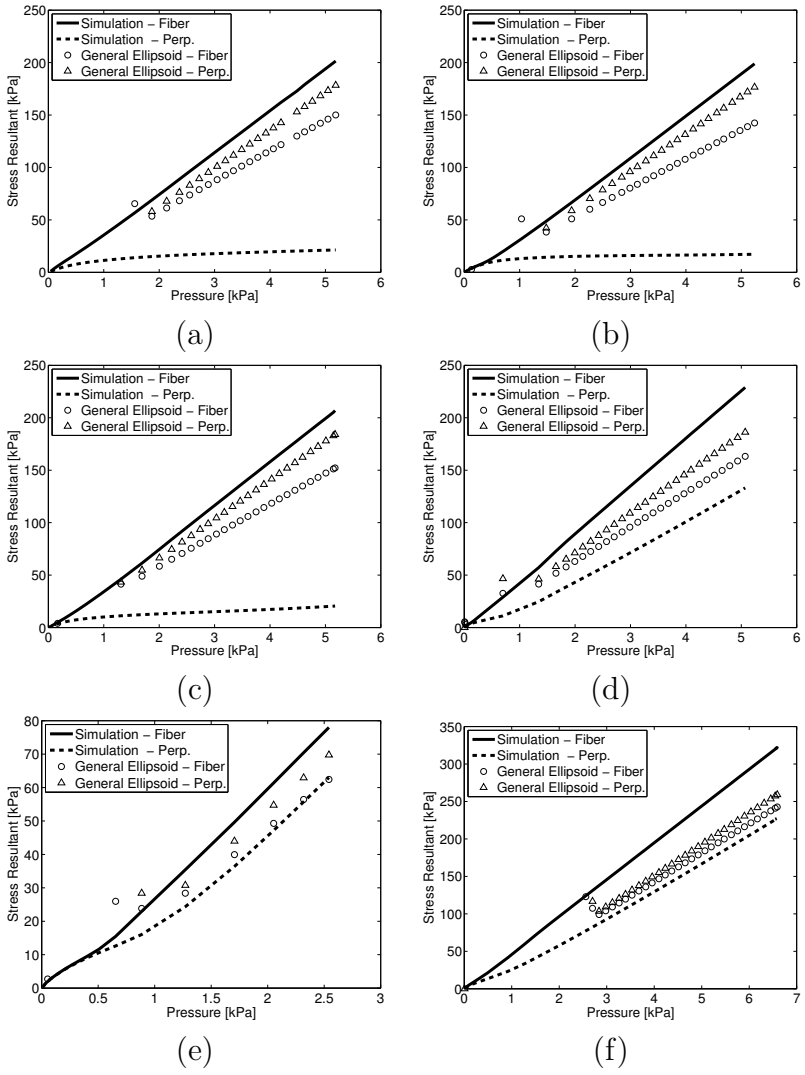

Figure 3.7: FE simulation results for the stress resultant compared to the theoretical ellipsoidal shell model in Eq. (29) for (a) 43/M, (b) 44/M, (c) 59/F, (d) 61/M, (e) 62/F, and (f) 83/M specimens. As discussed in Section 3.2, poor agreement is seen between the simulation and theoretical calculation for all specimens. This is likely due to difficulties in obtaining accurate curvatures for the ellipsoid previously discussed in Chapter 2.

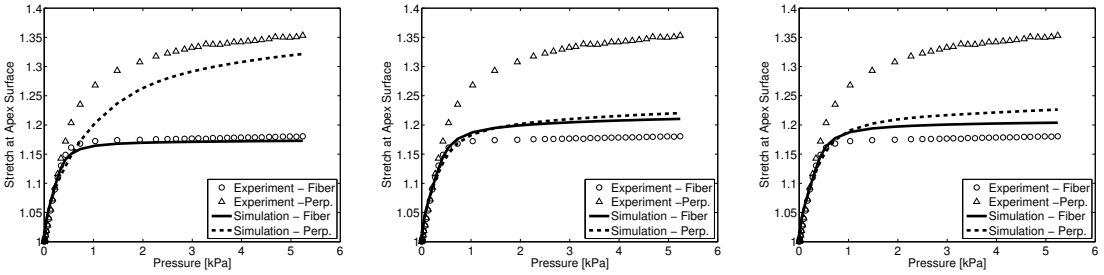

Figure 3.8: Comparison of the experimentally measured stretch-pressure response for a representative specimen (44/M) and results of specimen-specific FE simulations using the analytically determined model parameters of the (a) the 2D FI distributed fiber model, (b) the 3D GOH model and (c) the 2D GOH model. Comparisons for all other specimens are shown in Fig. 3.9 - 3.11.

3.3.3 Finite Element Validation of Model Parameters

The material parameters determined for the three distributed fiber models were applied in specimen-specific finite element simulations of the bulge test for all of the specimens. The pressure-stretch response from simulations and experiments were compared to validate the thin-shell analysis and parameter determination methods, and to compare the ability of the thin shell method to accurately determine material parameters from the bulge test. Results for a representative specimen (44/M) are shown in Fig. 3.8, while those for the remaining specimens are shown in Fig. 3.9 - 3.11. This specimen was the most anisotropic specimen tested, with the highest value of the concentration anisotropy parameter b in Table 3.2. The results for the 2D FI model show that the simulation slightly underestimated the experimental stretch in

the perpendicular direction; however the model reproduced the stretch in the fiber direction and captured the large difference in fiber and perpendicular stretches (Fig. 3.8 (a)). Fig. 3.9 shows that the experimental results were nearly exactly reproduced for more isotropic specimens. In contrast, the parameters obtained for the two GOH model greatly underestimated this difference in perpendicular and fiber stretch response, as seen in Fig. 3.8 (b) and (c) for the same specimen. The differences in the ability of the FI and GOH models to reproduce the experimental data reflect the differences in the concentration parameters obtained for each model reported in Table 3.5, where the 2D FI model had a significantly larger concentration parameter than either version of the GOH model.

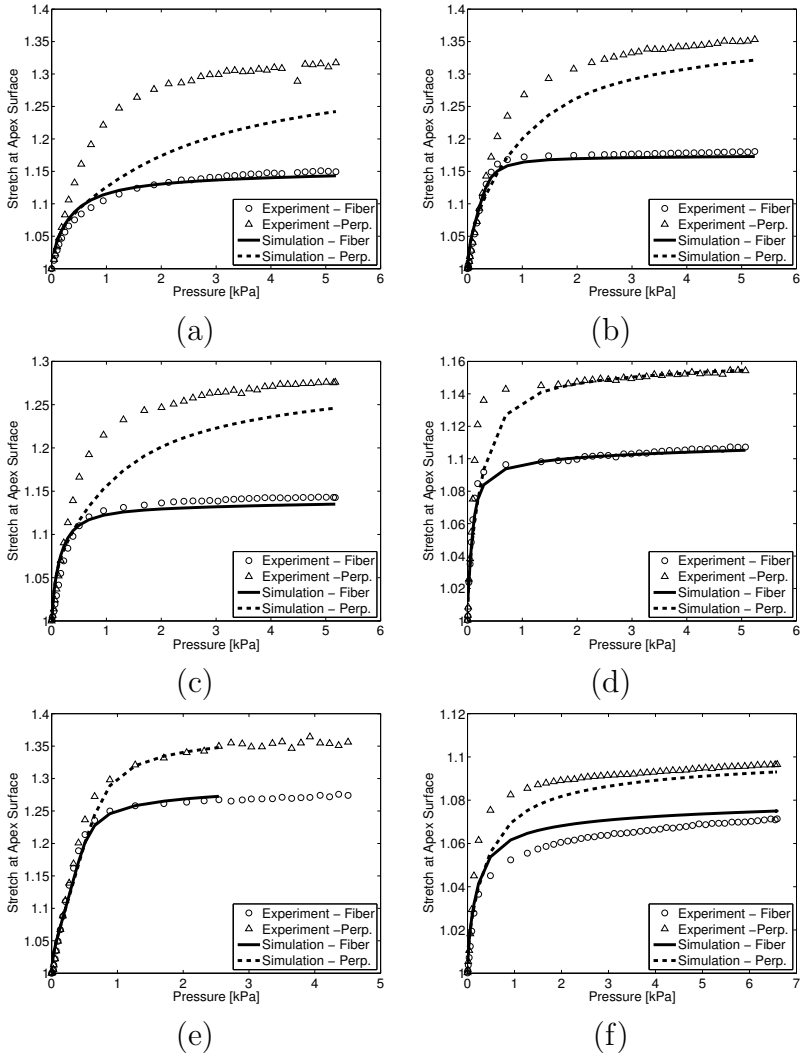

Figure 3.9: 2D FI distributed model: Comparison of experimental data for the in-plane pressure-stretch response and specimen-specific FEA simulation for different specimens: (a)43/M (b) 44/M (c) 59/F (d) 61/M (e) 62/F (f) 83/M.

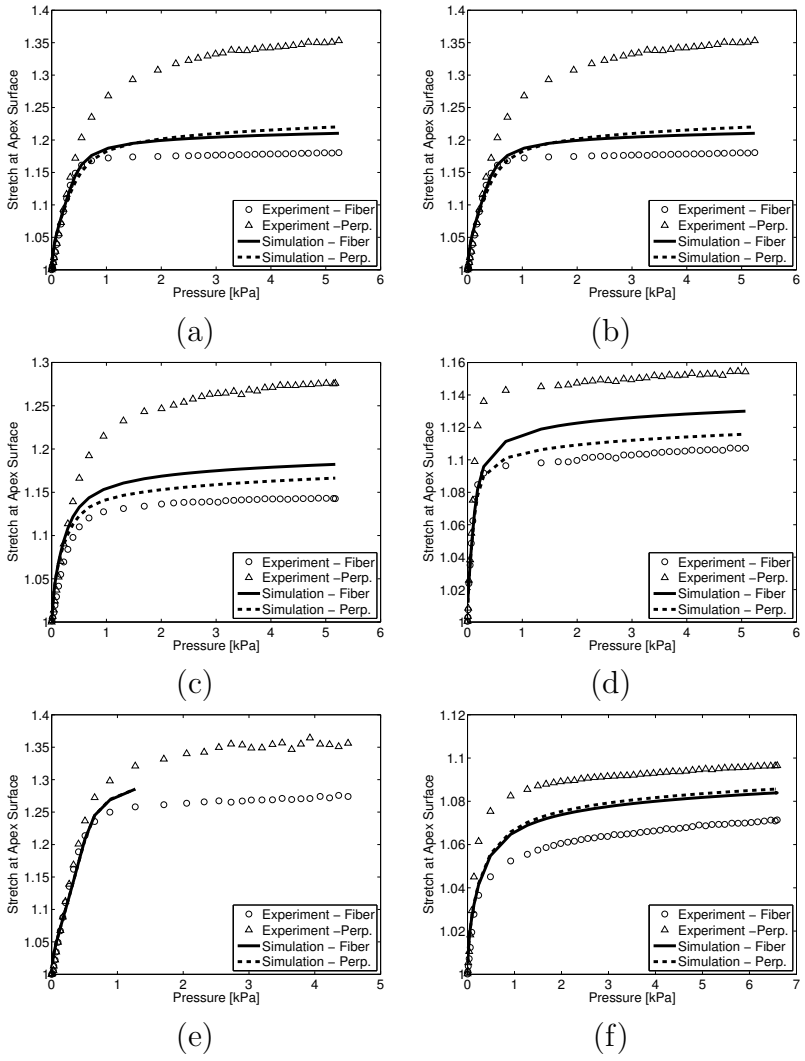

Figure 3.10: 3D GOH model: Comparison of experimental data for the in-plane pressure-stretch response and specimen-specific FEA simulation predictions for different specimens: (a)43/M (b) 44/M (c) 59/F (d) 61/M (e) 62/F (f) 83/M.

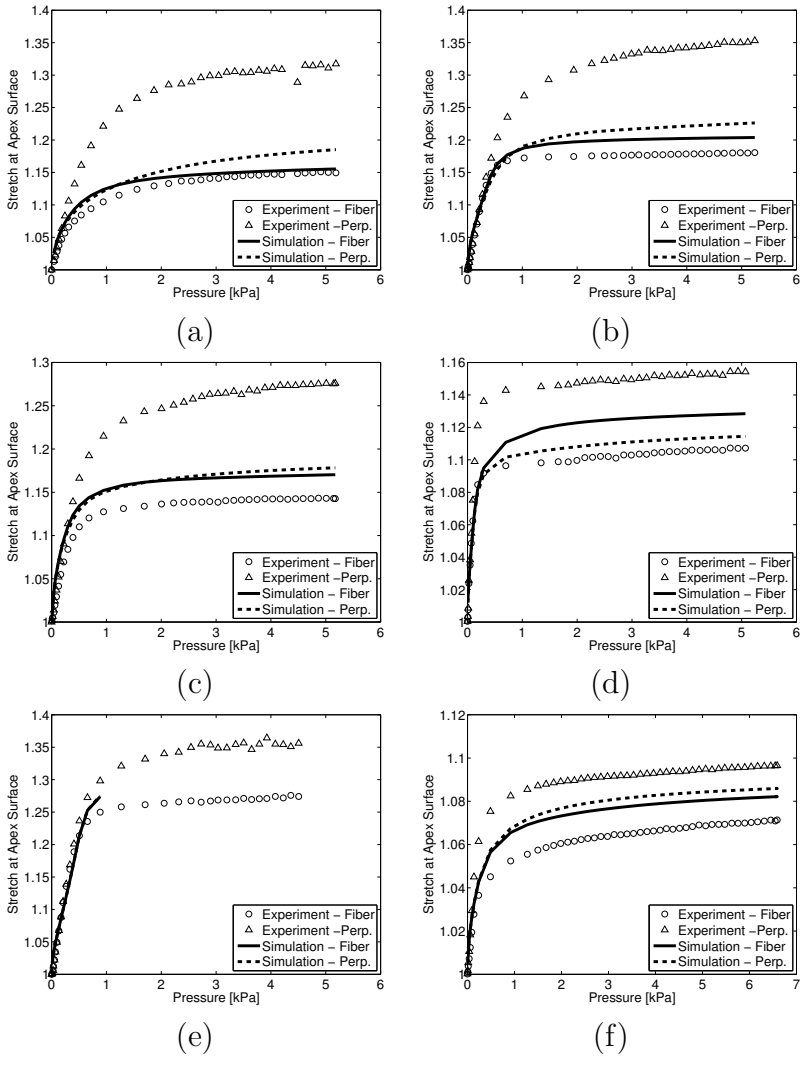

Figure 3.11: 2D GOH model: Comparison of experimental data for the in-plane pressure-stretch response and specimen-specific FEA simulation predictions for different specimens: (a)43/M (b) 44/M (c) 59/F (d) 61/M (e) 62/F (f) 83/M.

Table 3.7: RMS error between simulations and experimentally measured stretch-pressure relationship.

Sample	2D FI	3D GOH	2DGOH
43/M	0.060	0.082	0.080
44/M	0.026	0.070	0.066
59/F	0.026	0.064	0.059
61/M	0.010	0.025	0.029
62/F	0.015	0.016	0.018
83/M	0.007	0.013	0.011
Average	0.024	0.045	0.044
Std. Dev.	0.019	0.030	0.028

To quantify these observations, the root mean square (RMS) error, was calculated for the difference between the experimentally measured pressure-stretch relationship and that predicted by the finite element simulation. The RMS error was calculated as,

$$\text{RMS} = \sqrt{\frac{\sum (\lambda_{sim} - \lambda_{exp})^2}{n}}, \tag{3.38}$$

where λ_{sim} is the stretch predicted by the simulation, λ_{exp} is the experimentally measured stretch, and n is the total number of pressure points. The resulting RMS error for all specimens are reported in Table 3.7. The RMS error for the 2D FI model was significantly lower than both the 2D GOH (p=0.023) and 3D GOH model (p=0.0305). The error of the 2D GOH model was slightly lower than 3D GOH, but this difference was not significant (p=0.450).

To investigate the source of discrepancy in the calculations, we examined the ability of the simulations to reproduce the curvatures measured in the experiments. The resulting finite-element analysis curvatures for a representative specimen (44/M)

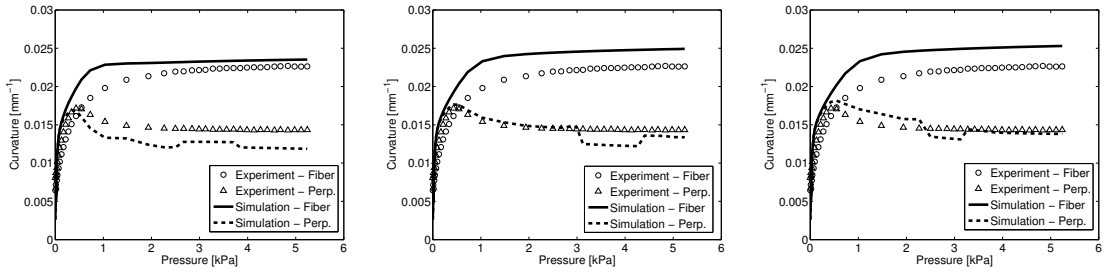

(a) (b) (c)

Figure 3.12: Comparison of the experimentally determined curvatures for a representative specimen (44/M) and results of specimen-specific FE simulations for the (a) 2D FI Distributed Fiber model (b) 3D GOH model, and (c) 2D GOH model.

were compared to the curvature calculated from the experimental DIC data for the same specimen. Figure 3.12 shows that for the FI model, the simulation curvature was higher in the fiber direction and lower in the perpendicular direction compared to experiments. For both GOH models, the simulation curvature was closer to the experimental curvature in the perpendicular direction, but the simulation curvature in the fiber direction overestimated the experimental curvature. These differences could lead to the difference in perpendicular stretch seen in Figure 3.8.

Table 3.8: 2D FI Distributed Fiber Model - Membrane Stress Fit Parameters

Sample	μ [kPa]	b	k_1 [kPa]	k_2
43/M	5.395	8.322	2.302	28.930
44/M	4.437	6.554	1.992	18.742
59/F	4.095	3.878	7.504	17.518
61/M	7.409	3.392	1.065	91.924
62/F	5.422	1.494	1.393	7.588
83/M	17.415	1.655	4.447	171.483
Average	7.362	4.216	3.117	56.031
Std. Dev.	5.058	2.724	2.455	64.144

3.3.4 Impact of Bending Effects on Model Parameters

To evaluate the importance of bending effects on the stress response, the membrane stress model in eq. (3.32) was used to fit the parameters of the 2D FI model to the bulge test measurements while ignoring bending effects. The results are listed in Table 3.8. Compared to parameters determined by the thin shell analysis in Table 3.2, the membrane model produced a similar matrix shear modulus μ, a smaller anisotropy parameter b, a higher k_1, and lower k_2 for the collagen fibers. To assess the net effect of these differences, the stress response in the fiber and perpendicular directions were calculated for each specimen using stretches λ_f and λ_p measured at the surface, and the parameters determined from both the thin shell analysis in Table 3.2 and membrane analysis in Table 3.8. Figure 3.13 compares the results for two representative specimens: one showing the closest agreement between the two sets of parameters (43/M) and one showing the largest difference (44/M). Results for all

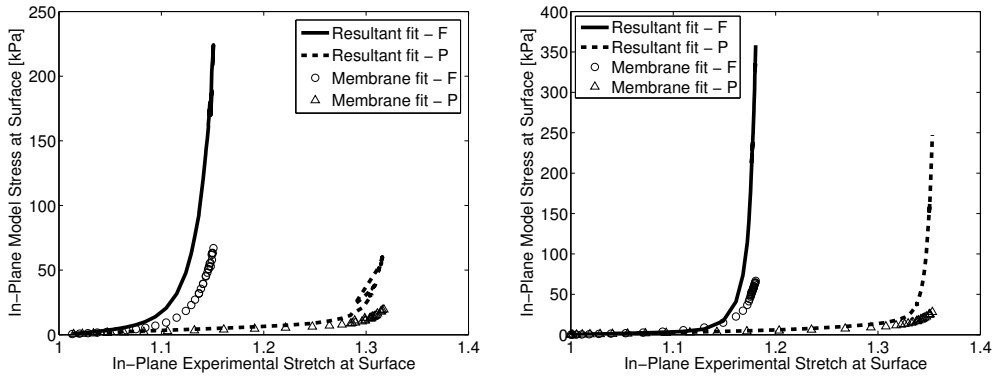

Figure 3.13: Comparison of parameters determined accounting for bending (stress resultant method) and ignoring bending (membrane stress approximation) for (a) specimen with closest observed agreement (43/M), and (b) specimen with worst observed agreement (44/M). Results for all specimens can be found in Figure 3.14.

specimens can be found in Figure 3.14. The membrane analysis significantly underestimated the material stiffness and stress state at the specimen surface, where strains were measured in the bulge tests. This is expected as the membrane stresses are lower than the bending stresses at the surface of the tissue. This difference is exacerbated by the nonlinear material behavior. A paired t-test confirmed that the difference in maximum stress was significant in both the fiber ($p = 0.003$) and perpendicular ($p = 0.017$). The results also showed that accounting for bending was more important for stiffer and thicker specimens.

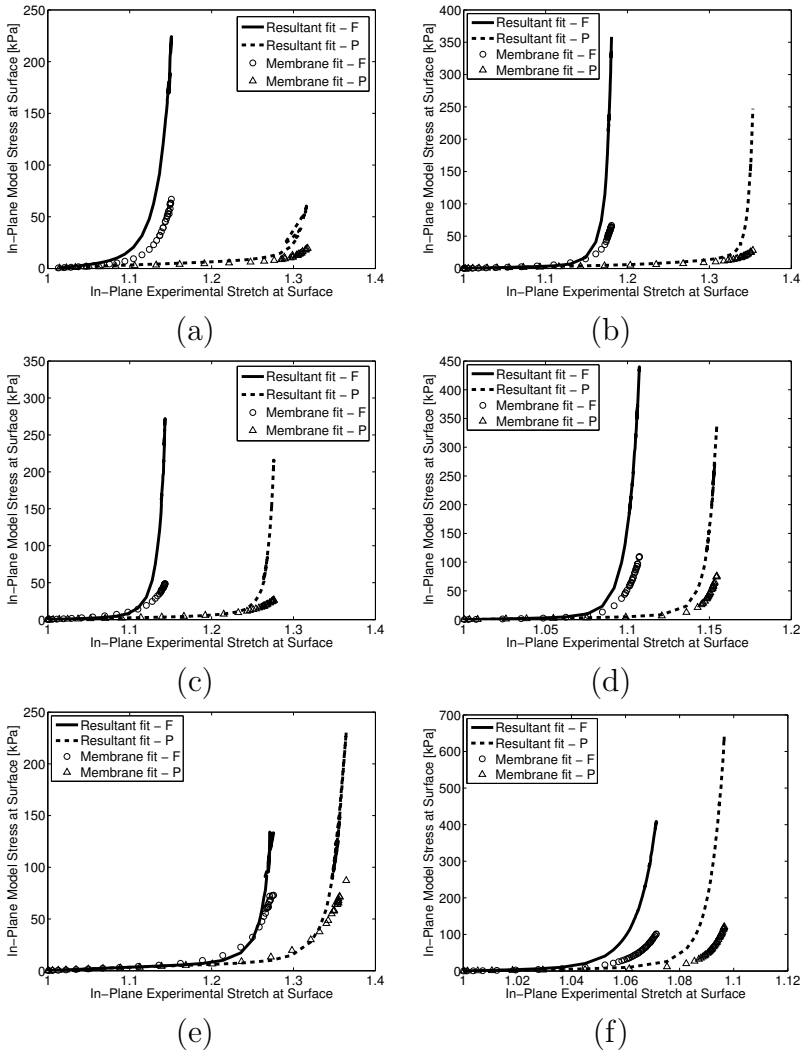

Figure 3.14: Comparison of stress response for parameters determined for the 2D FI model by both the resultant fitting method and the membrane fitting method for (a)43/M (b) 44/M (c) 59/F (d) 61/M (e) 62/F (f) 83/M.

3.4 Discussion

We have developed a new method to analytically determine the anisotropic material properties of planar tissues from bulge testing while accounting for bending. Previous bulge tests applied to polymers and tissues have been limited to conditions where the effects of bending are negligible. However, the effects of bending can become significant for thicker specimens, e.g., for human skin specimens, and for a nonlinear stress response that transforms small gradients in strains to large gradients in stress. Bending can be accounted for using inverse finite element analysis but analytical methods can provide significant time-savings and efficiency. The results of this study demonstrate that the commonly used membrane stress approximation leads to significant underestimation of tissue stress and stiffness for skin tissue. Instead, we propose a new thin-shell analysis method which takes into account bending effects and has been validated by finite element analysis. This thin shell method has not been previously applied to bulge and inflation testing.

We have observed differences between a fully integrated distributed fiber model and a pre-integrated distributed fiber model. Of the three models evaluated here, only the parameters determined for the FI model were capable of reproducing the experimentally measured anisotropy of skin tissue in finite element simulations. In contrast, parameters determined for both the 2D and 3D GOH models significantly under-represented the anisotropy of the tissue. This is in spite of the fact that the curvatures in the perpendicular direction were more accurately reproduced for the

GOH models than for the FI model. Both the 2D FI and 2D GOH models applied a planar distribution to describe the fiber structure, which is more representative of the ECM structure of human skin tissues than the 3D transversely isotropic structure of the 3D GOH model.[92,99] However, adapting the GOH model to a 2D fiber structure tensor did not significantly improve the fit. Instead, the difference in the resulting material parameters between models is attributed to the pre-integration of the fiber distribution of both GOH models. We hypothesize that the discrepancy arises from the large fiber rotations induced by the inflation test, and the high degree of fiber dispersion of skin collagen fibers. This is expected as the GOH model was developed for arteries, which have a small degree of fiber dispersion and experience relatively uniform loading in the body. Similar differences between the FI distributed fiber model and pre-integrated GOH models have been reported previously by Cortes et al.[40] and Pandolfi and Vasta.[41]

A wide range of values were obtained for the anisotropic parameters of each model. For example, for the 2D FI model the fiber stiffness parameter k_1 ranged from 0.025 - 8.200 kPa and the fiber nonlinearity parameter k_2 ranged from 15.876 - 202.926. This indicates a large specimen-to-specimen variation in anisotropic material properties that was likely caused by the large age range, which spanned 40 years. In contrast, the matrix shear modulus μ was similar among all specimens, with an average value of 9.068 $\pm$ 6.749 kPa. The shear modulus signified the isotropic response of the ground matrix of proteoglycans and elastin. These results suggests that the variation

in human skin tissue specimens may arise from collagen-fiber specific characteristics rather than from the ground matrix or elastin contribution. However, this result could also occur because the matrix shear modulus was fit to the toe region alone, while the fiber parameters were fit to the full stress-strain curve using a multi-parameter fit.

The material parameters provide a quantitative comparison of the trends observed in the experimental results of Chapter 2. Samples from the lower back region exhibited the most anisotropic stress response. The concentration parameter b for the 2D FI model ranged from a strongly anisotropic value, 16.467, for the specimens of the lower back to a nearly isotropic 1.693 for a specimen likely from the upper back. The degree of anisotropy decreased with age, though the sample size was too small to perform a statistical comparison. The oldest specimen had the highest fiber tensile parameter k_1, indicating stiffer fibers, and the highest fiber nonlinearity parameter k_2, indicating that the onset of stiffening occurred at lower strains. This is in agreement with previous work showing that increased collagen cross-linking causes skin to stiffen with age.[169,170]

Recent work by Ni Annaidh et. al.[38,94] on human skin tissue from the back torso measured the 3D GOH concentration parameter b from histology and the remaining material parameters of the 3D GOH model from uniaxial stress-strain data. The specimens were tested to failure and the stresses measured were on the order of MPa, considerably higher than in this work. This difference is likely because the donors were

considerably older (81 - 97 years old) than most donors in our study (43-83 years old) and testing to failure brought the specimens to much higher strains than in this work. Looking at the stress-strain curves for the 83/M specimen in Fig. 3.14, it is clear that if the specimen was tested to higher strains it would have quickly approached the stress levels measured by Ni Annaidh and coworkers. The concentration parameters b determined from histology ($0.793\pm$ 0.229) by Ni Annaidh et al.[38,94] were similar to those measured mechanically in our study (0.996 ± 1.020). Differences can be attributed to the assumption of Ni Annaidh et. al. that human skin is described by two equal fiber families symmetric about the loading axis while this work assumed only one family of fibers aligned with the principal stretch direction. Additional differences among the material parameters measured by Ni Annaidh et al.[38,94] and presented in this work may be caused by differences in test methods, stress levels tested, and fitting methods.

Our study has several limitations. Too few specimens were tested for statistical comparison of material parameters and specimens were limited to the back from Caucasian donors to limit heterogeneity and variability. The analysis examines only one material point (the apex) and therefore is limited to homogeneous tissues. In this study heterogeneity was limited by only choosing skin specimens from the back where the fiber direction is known to be uniform. We were unable to obtain detailed location information for the tested specimens. All models investigated in this work neglect fiber-fiber and fiber-matrix interactions. Such interactions become important

for the time-dependent response. Finally, the 2D FI model did show a slight underestimation of in-plane stretches in the initial toe region. This was also observed for simulations using parameters determined by the membrane analysis, suggesting that the discrepancy arose from the 2D FI model rather than the thin-shell analysis method.

3.5 Conclusions

We have developed a novel method for analytically obtaining material parameters from the bulge test while taking into account bending effects. We have validated the assumptions of the method and the resulting material parameters with finite element analysis. The thin shell method was used to compare three different distributed fiber models to describe the anisotropic properties of human skin tissues. We found that both the 3D Gasser-Odgen-Holzapfel model[28] as well as a version with a 2D fiber distribution were unable to capture the significant anisotropy measured by the bulge test. In contrast, parameters determined for a Fully Integrated distributed fiber model based on a 2D fiber distribution were able to reproduce the structural response of skin to the bulge test. We conclude that the Fully Integrated distributed fiber model is the most appropriate model for bulge testing of skin tissues. The thin shell analysis method presented in this work has been applied to skin tissue but can be generalized to analyze the inflation response of other planar anisotropic tissues such as pericardium,

mitral valves, gastrointestinal tissues, aortic valves, or fetal membranes.

Chapter 4

Modeling the strain-protected enzymatic degradation of collagen with applications to growth and remodeling

This chapter presents a hierarchical model for a planar collagenous tissue that is applied to study potential mechanisms of growth and remodeling. The Fully Integrated distributed fiber model described in Chapter 3 is extended to include fiber-level descriptions of collagen fibers. Fibers are described as planar sinusoidal elastica beams and strain-protected enzymatic degradation is modeled by a reducing in fiber radius based on a local fiber micro-stretch. The degradation rate law is developed

and calibrated based on the fibril-level experiments reported by Flynn et al.[80] The same kinetic parameters are then used to predict the results of tissue-level bovine cornea degradation experiments reported by Zareian et al.[83] Degradation is paired with deposition to demonstrate that tissue strain homeostasis can be predicted from these two fiber-level mechanisms alone. This chapter will be submitted for publication under the title, "Modeling the Strain-Protected Enzymatic Degradation Mechanism of Growth and Remodeling of Soft Tissues ", with Jeffrey W. Ruberti and Thao D. Nguyen as co-authors.

4.1 Introduction

Collagen is the most abundant protein in the human body and is a key structural component in connective tissues, such as skin, cornea, tendon, and blood vessels. These tissues exhibit a highly organized structure, where stiff collagen fibrils are arranged in a soft matrix of proteoglycans, water, cells, and other non-fibril forming proteins. The collagen fibrils are organized further into crimped fibers, sheets, and other organ-specific larger scale structures. The production and organization of the collagen structures can change in response to mechanical stimuli. The resulting net production of tissue mass is defined as growth, while alterations in the collagen structure and resulting properties is defined as remodeling. Though described as distinct phenomena, remodeling is usually accompanied by growth.[7] Growth and remodeling

under physiological mechanical conditions occurs as a normal part of development and aging. However, disordered or uncontrolled remodeling can also occur under pathological conditions and has been implicated in a wide range of disease states, such as cardiac fibrosis,[171] osteoarthritis,[52] and glaucoma.[172] Despite the clinical importance of collagen remodeling, the underlying mechanisms of collagen remodeling and their relations to disease processes are not well understood.

Computational modeling of the growth and remodeling process is an active area of research. Of particular interest is the development of constitutive laws for both the growth deformation gradient as well as internal variables for the change in tissue microstructure. A common modeling approach is to prescribe phenomenological growth laws driven by a tissue-level homeostatic stress[51,59,62] or strain.[65,173,174] Such methodologies have been successful in describing the development of the heart and arteries,[63,64,175] the growth of arteries caused by changes in blood flow,[74,174,176] the growth of intracranial aneurysms,[60,61] and the thickening of ventricles caused by volume or pressure overload.[58,59,177] A slightly different approach modifies collagen fiber orientations based on the orientations of the principal stretch[69,71] or stress[67,68] of the tissue. These methodologies have proven capable of predicting the collagen structure of the artery wall,[73,84] aortic heart valves,[67] tendons,[69] and the cornea and sclera under physiological loading.[48]

Computational modeling efforts have begun to incorporate potential micro-mechanisms of growth and remodeling. For example, recent experiments have shown evidence

of cell-mediated collagen crimp remodeling[77] and strain-dependent collagen production.[78] Micro-mechanical models can be used to test the feasibility of these particular processes as mechanisms of growth and remodeling. Baaijens et al.[84] developed a fiber-level growth model for the accumulation of collagen based on experimental evidence for stretch-mediated collagen production. The model was able to predict the observed collagen structure of arteries and aortic heart valves. Watton et. al.[70] modeled collagen crimp remodeling by the deposition of collagen fibers in a pre-stretched state. This mechanism was shown to lead to a homeostatic fiber stretch and predicted the course of aneurysm development. Grytz et al.[47] modeled the same mechanism using homeostatic control of the collagen fibril stretch to predict the collagen structure of the lamina cribosa under in vivo loading.

The selective enzymatic degradation of collagen has recently been identified as another potential mechanism for growth and remodeling. It has been shown at the molecular,[79] fibril[4,80,178] and tissue level[3,81–83,179] that mechanical strain protects collagen from enzymatic degradation by decreasing the degradation rate. This effect has been referred to as a mechanical switch by Flynn et al.[80] because the degradation rate can decrease dramatically for a small increase in applied stretch. This rapid decrease occurs when the initially crimped collagen fiber is nearly straightened, corresponding to the heel region of the stress-strain curve for collagenous tissues.[80,81] It has been suggested that straining the collagen fibril protects molecules from enzymatic cleavage by fully incorporating naturally unfolded chains into the triple helix structure.[180]

CHAPTER 4. MODELING STRAIN-PROTECTED DEGRADATION WITH APPLICATIONS TO GROWTH AND REMODELING

Previous efforts modeling strain-protected collagen degradation have relied on phenomenological descriptions of the effect of strain on the degradation rate. These include an exponential dependence on fiber strain,[85,181] a logistic dependence on fiber strain,[182] a bounded evolution equation based on a homeostatic fiber stretch,[47] or combined with collagen deposition for a total collagen mass dependent on the square of the fiber stretch.[84]

The aim of this work is to investigate the role of strain-protected enzymatic degradation in the growth and remodeling of collagen structures by developing a mechanistic model of the dramatic onset of strain protection[80–82] based on recently published experimental data by Flynn and coworkers.[80] We hypothesize that strain-protected enzymatic degradation may work in concert with collagen deposition to give rise to the stress or strain homeostasis that is characteristic of growth and remodeling. To test this hypothesis, collagen fibers are described as planar elastica beams based on the work of of Cominou and Yannis.[45] Enzymatic degradation is described as a zero-order reduction in the fiber radius inhibited by the axial strain energy of an extended fiber, with parameters calibrated to the single-fibril degradation data of Flynn et al.[80] This fiber-level model is scaled up to the tissue level by describing the tissue as a distribution of degrading fibers in an isotropic ground matrix and used to predict the results of tissue-level enzymatic degradation experiments reported by Zareian at al.[83] and Ellsmere et al.[183] Degradation is then paired with constant collagen deposition to investigate the response of the tissue to changes in loading conditions.

The results of this experimentally informed theoretical study support the inclusion of strain-protected enzymatic degradation as a potential mechanism for the growth and remodeling process.

4.2 Methods

This section presents a constitutive model for the effect of the enzymatic degradation of collagen fibers on the growth and remodeling of collagenous tissues. We begin by briefly describing the elastica model of Comninou and Yannas[45] used to describe the strain-stiffening stress response of the collagen fibers. Next, we present an evolution equation for the degradation of the fiber radius that depends on the axial strain energy density of the collagen fibers. The fiber-level models are incorporated into a hyperelastic, distributed fiber model for the stress response of the tissue. We assume that degradation of the collagen fibers also produces a change in the tissue volume, defined as negative growth, and present a constitutive relation for the volumetric growth deformation. Finally, we describe a method developed to calibrate the parameters of the evolution equation from single-fibril enzymatic degradation experiments carried out by Flynn et al,[80] and the parameters of the elastica from the equilibrium stress-strain data for bovine cornea strips measured by Zareian.[83]

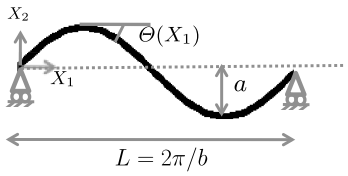

(a)

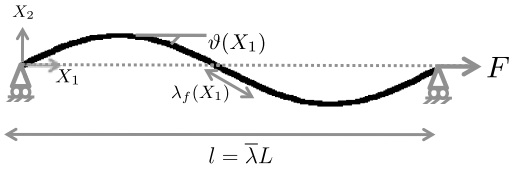

(b)

(c)

Figure 4.1: Schematic of the sinusoidal elastica model used to represent individual collagen fibers in the (a) undeformed and (b) deformed configurations. When a force F is applied to the beam, the deformed configuration is defined by the deformed rotation angle $\vartheta(X_1)$ from equilibrium.[45] Both the fiber-level micro-stretch, λ_f, and the tissue-level macro-stretch $\overline{\lambda}$, can be computed from the deformed configuration. (c) The cross section of the beam is assumed to be circular with initial radius R and degraded radius r.

4.2.1 Elastica model

The elastica model of Comninou and Yannas[45] was applied to describe the non-linear, strain-stiffening stress response of a wavy collagen fiber. The undeformed configuration of the wavy beam is described by a planar sine wave, $X_2 = a\sin(bX_1)$, where (X_1, X_2) are the coordinates along the horizontal and vertical directions, $\mathbf{e_1}$ and $\mathbf{e_2}$, as illustrated in Fig. 4.1. For small crimp angles, the rotation angle of the midline, defined as $\tan\Theta = dX_2/dX_1$, can be approximated as $\Theta(X_1) = ab\cos(bX_1)$. For simplicity, we assume a circular cross-section for the elastica with an original radius R, cross-sectional area $A_0 = \pi R^2$, and second moment of area $I_0 = \frac{\pi}{4}R^4$. We assume that enzymatic degradation causes the fiber radius to decrease, as has been observed experimentally.[184] The material is linear elastic, described by a Young's Modulus, E, and EA and EI denote the current axial and bending stiffness. Fibers are allowed to compress, although the compressive stiffness is much lower than the bending or axial stiffness.

Assuming that the beam has a thin cross-section compared to the length, a small initial crimp angle, small fiber micro-strain, and negligible transverse shear deformation (Euler bending), we can derive analytical solutions for the deformed rotation angle $\vartheta(X_1)$, fiber micro-stretch, $\lambda_f(X_1) = 1 + F\cos\vartheta/(EA)$, and fiber macro-stretch, $\overline{\lambda} = (x_1(L) - x_1(0))/L$, for an applied end-tip force, F. The length of the undeformed fiber is $L = 2\pi/b$. We refer to Comninou and Yannas[45] for the solution of the deformed rotation angle $\vartheta(X_1)$ and the deformed tip position $x_1(X_1)$. The following

non-dimensional parameters are introduced,

$$\alpha = \frac{F}{EA}, \quad \beta = b^2 R^2, \tag{4.1}$$

where α is the applied force normalized by the axial stiffness, and β is proportional to the radius of gyration. These two parameters and the initial crimp angle, $\Theta_0 = ab$, fully define the properties of the elastica. Then, the deformed rotation angle, fiber micro-stretch, and fiber macro-stretch can be written as,

$$\vartheta(X_1) = \frac{\beta}{4\alpha\,(1+\alpha)+\beta}\Theta(X_1), \tag{4.2}$$

$$\lambda_f(X_1) = 1 + \alpha\cos(\vartheta(X_1)), \tag{4.3}$$

$$\overline{\lambda} = \frac{1}{L}\int_0^L \lambda_f \frac{\cos(\vartheta)}{\cos(\Theta)} dX_1. \tag{4.4}$$

The solutions given in eqs. (4.2)-(4.4) are for the deformed configuration given an applied end-tip force. Alternatively, the force for an applied macro-stretch $\overline{\lambda}$ can be solved iteratively as described in Sec. 4.2.5.

The total strain energy of the collagen fiber can be written as the sum of a bending and axial energy as,

$$U_{fib} = \int_0^L \frac{EI}{2}\left(\frac{d\vartheta}{dX_1} - \frac{d\Theta}{dX_1}\right)^2 dX_1 + \int_0^L \frac{EA}{2}(\lambda_f - 1)^2 dX_1 \tag{4.5}$$

where I and A are the current second moment of area and cross-sectional area of the fiber. For the case of small fiber strains, the effect of Poisson's contraction on the fiber radius is neglected for simplicity. As a result, I and A are constants for fibers not subjected to enzymatic degradation. For a degrading fiber we can define a strain energy density per degraded volume as, $\Psi^0_{fib} = U_{fib}/(AL)$, where $A = \pi r^2$ is the degraded cross-sectional area and r is the degraded fiber radius. Expressions for Ψ^0_{bend} and Ψ^0_{axial} in terms of the non-dimensional fiber parameters are obtained by applying the definitions of A and I for a circular cross-section and rearranging terms, shown in eq. (4.6):

$$
\begin{aligned}
\Psi_{bend} &= \frac{U_{bend}}{AL} = \int_0^L \frac{EI}{2AL}\left(\frac{d\vartheta}{dX_1} - \frac{d\Theta}{dX_1}\right)^2 dX_1 \\
&\frac{d\vartheta}{dX_1} = \frac{\beta}{4\alpha(1+\alpha)+\beta}\frac{d\Theta}{dX_1} \\
&\frac{d\Theta}{dX_1} = -ab^2\sin(bX_1) \\
\Psi_{bend} &= \frac{1}{L}\int_0^L \frac{EIb^2}{2A}\left(\frac{\beta}{4\alpha(1+\alpha)+\beta} - 1\right)^2 \left(ab\sin(bX_1)\right)^2 dX_1 \\
&\int_0^L \left(ab\sin(bX_1)\right)^2 dX_1 = \int_0^L \left(ab\cos(bX_1)\right)^2 dX_1 = \int_0^L \Theta^2 dX_1 \\
\Psi_{bend} &= \frac{1}{L}\int_0^L \frac{EIb^2}{2A}\left(\frac{\beta\Theta}{4\alpha(1+\alpha)+\beta} - \Theta\right)^2 dX_1 \\
&\vartheta(X_1) = \frac{\beta\Theta}{4\alpha(1+\alpha)+\beta} \\
\Psi_{bend} &= \frac{1}{L}\int_0^L \frac{EIb^2}{2A}\left(\vartheta(X_1) - \Theta(X_1)\right)^2 dX_1 \\
&\frac{Ib^2}{A} = \frac{\pi R^4 b^2}{4\pi R^2} = \frac{\beta}{4} \\
\Psi_{bend} &= \frac{1}{L}\int_0^L \frac{E\beta}{8}\left(\vartheta(X_1) - \Theta(X_1)\right)^2 dX_1,
\end{aligned}
\tag{4.6}
$$

$$
\Psi_{axial} = \frac{U_{axial}}{AL} = \frac{1}{L}\int_0^L \frac{E}{2}(\lambda_f - 1)^2 dX_1.
$$

The strain energy density per undegraded fiber volume for the entire fiber follows as the sum of the axial and bending contributions:

$$
\Psi^0_{fib} = \frac{1}{L}\int_0^L \underbrace{\left[\frac{E\beta}{8}\left(\vartheta(X_1) - \Theta(X_1)\right)^2\right]}_{\Psi^0_{bending}} dX_1 + \frac{1}{L}\int_0^L \underbrace{\left[\frac{E}{2}(\lambda_f(X_1) - 1)^2\right]}_{\Psi^0_{axial}} dX_1. \tag{4.7}
$$

Additionally, we can define a strain energy density per initial undegraded volume as, $\Psi_{fib} = U_{fib}/(A_0 L)$, where $A_0 = \pi R^2$ is the initial undegraded cross-sectional area and R is the initial fiber radius. Applying the definition for the degraded A and I and the undegraded A_0 gives,

$$\Psi_{fib} = D^2 \Psi^0_{fib}, \tag{4.8}$$

where $D = r/R$ is the ratio of the degraded and original fiber radius. It follows that the factor D^2 in eq. (4.8) reflects the change in cross-sectional area of a fiber with degradation. The term is analogous to a mass concentration ratio and is used to describe the effect of degradation on altering the stiffness and mass distribution of fibers (see for example, Demirkoparan et al.[181] and Kroon et al.[185]).

4.2.2 Collagen degradation and deposition law

Experimental studies of unstrained collagen fibrils subjected to bacterial collagenase have shown that degradation proceeds by progressive reduction in the radius of the fiber[184] and previous works have described the phenomena by prescribing a constitutive relation for the fiber radius.[85,181] We take the same approach and prescribe a zero order degradation law for the fiber radius. The choice of a zero order kinetic relation is motivated by enzymatic degradation experiments of both strained and unstrained collagen fibers in collagenase showing a constant degradation rate,[80,186] and is consistent with zero-order Michaelis-Menten kinetics for an enzyme-mediated

reaction in the presence of excess enzyme.

Experiments have also shown that the degradation rate depends on applied strain. Collagen fibers exhibit an abrupt decrease in the degradation rate with applied strain, an effect commonly referred to as strain protection.[3,4,80,178] The onset of strain protection has been observed to coincide with the straightening of the collagen fiber,[80–82] suggesting that distortion of the collagen backbone may inhibit enzyme binding or cleavage.[180] This feature has previously been modeled as a homeostatic fiber micro-stretch or macro-stretch.[47,70] We model the strain dependence by adding a mechanical activation energy term associated with the axial strain energy density to the degradation rate:

$$\frac{dr}{dt} = -C_1 \exp\left[-\frac{E_a + C_2 \Psi^0_{axial}}{k_b T}\right]. \tag{4.9}$$

The constant C_1 is the intrinsic reaction rate, C_2 is a mechanical activation volume, E_a is the thermal activation energy, k_b is the Boltzman constant, and T is the temperature. The rate law depends on the axial strain energy density Ψ^0_{axial} of the fiber per degraded volume, rather than Ψ_{axial} of the undegraded volume, because it describes the intrinsic material properties of the fiber. We substitute eq. (4.7) into eq. (4.9) and define the non-dimensional constants $G_1 = -C_1/R \exp\left[-E_a/k_b T\right]$ and

$G_2 = k_b T/EC_2$ to obtain the final non-dimensional form of the degradation law:

$$\begin{aligned} \frac{dD}{dt} &= -G_1 \exp\left[-\frac{\overline{\epsilon_f^2}}{2G_2}\right], \\ \overline{\epsilon_f^2} &= \frac{1}{L}\int_0^L (\lambda_f(X_1)-1)^2 dX_1. \end{aligned} \tag{4.10}$$

The non-dimensional constants G_1 and G_2 describe the thermal and mechanical contributions to the activation energy, and the rate law depends directly on the square of the fiber averaged micro-strain $\overline{\epsilon_f^2}$, i.e. the "backbone strain" of the fiber. By penalizing the axial stretching of fibers, the model allows degradation to proceed only at low stress levels during the straightening of the crimped fibrils.

For the studies in Sec 4.3.4, we incorporate the effect of fiber-level collagen deposition to investigate the development of homeostasis. Collagen deposition has been shown to depend on fiber stretch,[78] but for simplicity we consider only a constant deposition rate. It is assumed that collagen deposition proceeds by increasing the fiber radius as new collagen monomers are incorporated into the surface. A constant collagen deposition term, k_d, is added to eq. 4.10:

$$\frac{dD}{dt} = k_d - G_1 \exp\left[-\frac{\overline{\epsilon_f^2}}{2G_2}\right]. \tag{4.11}$$

This simplified model of collagen deposition does not describe the ability of collagen deposition to change the collagen crimp. Collagen deposition instead affects only the fiber radius, resulting in a change in the bending and axial stiffness of the fiber. If

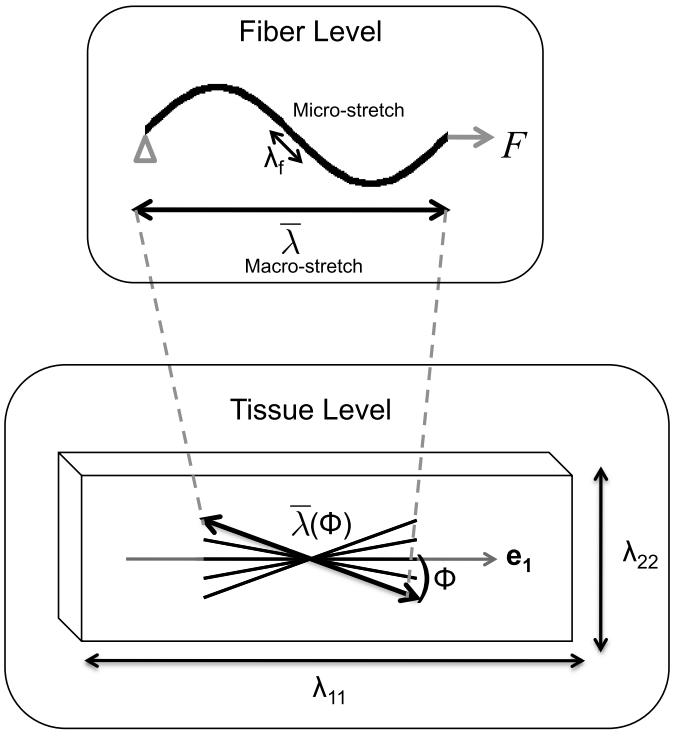

Figure 4.2: Schematic of anisotropic hyperelastic model for the tissue as a distribution of elastica fibers in the plane of the tissue. The tissue-level deformation $(\lambda_{11}, \lambda_{22})$ imparts an orientation-dependent deformation $(\overline{\lambda})$ on each elastica fiber, resulting in a fiber-level stretch (λ_f) dependant on the properties of the elastica fiber model.

deposition is not considered, $k_d = 0$ and eq. 4.11 reduces to eq. 4.10.

4.2.3 Anisotropic hyperelastic model for collagen tissues

At the tissue level, the collagen structure is modeled as a distribution of fibers in the tissue plane, $(\mathbf{e}_1, \mathbf{e}_2)$, illustrated in Fig 4.2. Individual collagen fibers are represented by a unit vector, $\mathbf{a_0}(\phi) = \cos(\phi)\mathbf{e}_1 + \sin(\phi)\mathbf{e}_2$, describing the orientation of a fiber at an angle ϕ from $\mathbf{e_1}$. The fiber orientations can also be described as a

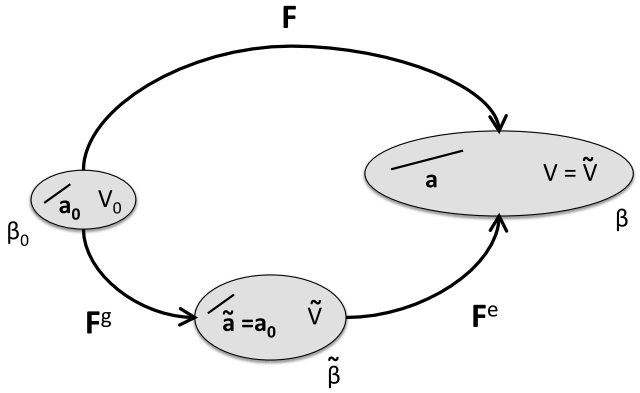

Figure 4.3: Schematic of multiplicative split of the total deformation tensor, $\mathbf{F} = \mathbf{F}^e\mathbf{F}^g$, for growth at constant density. The growth component of the deformation gradient, $\mathbf{F}^g$, maps the reference state, β_0, to the intermediate or grown state, $\tilde{\beta}$. The elastic component of the deformation gradient, $\mathbf{F}^e$, maps the intermediate state $\tilde{\beta}$ to the current state, β. It is assumed that the initial fiber orientations, $\mathbf{a_0}$, are not changed by growth, and the intermediate volume $\tilde{V}$ is not changed by elastic deformation.

structure tensor,

$$\mathbf{A}(\phi) = \mathbf{a_0}(\phi) \otimes \mathbf{a_0}(\phi). \tag{4.12}$$

The collagen fiber structure of the tissue is prescribed by a statistical distribution of fiber orientation in the plane, $\rho(\phi)$. In this work we assume that the orientation distribution of the undegraded tissue is isotropic, $\rho(\phi) = \frac{1}{2\pi}$.

As shown in eq. (4.8) for the strain energy density of the collagen fiber, enzymatic degradation decreases the stiffness of the fibers. At the tissue level, we assume that enzymatic degradation also leads to a reduction in the total mass and subsequently the volume of the tissue. This assumption is motivated by experimental observations of a decrease in tissue thickness during enzymatic degradation.[83] We treat this degradation-induced volumetric deformation as tissue-level growth, and multiplica-

tively split the continuum deformation gradient into a growth and elastic part,[57]

$$\mathbf{F} = \mathbf{F}^e\mathbf{F}^g, \tag{4.13}$$

where $\mathbf{F}^{\mathrm{e}}$ represents the deformation occurring from externally applied loads and $\mathbf{F}^g$ represents the volume change due to degradation or deposition induced growth, illustrated in Fig. 4.3. We assume that the growth associated with fiber-level degradation occurs only in the direction orthogonal to the fiber plane. Moreover, this change in the tissue thickness scales with the change in the thickness of the individual fibers, $D(\phi) = r(\phi)/R$, averaged over all possible fiber orientations:

$$\begin{aligned} \mathbf{F}^g &= \mathbf{e}_1 \otimes \mathbf{e}_1 + \mathbf{e}_2 \otimes \mathbf{e}_2 + \lambda_g \mathbf{e}_3 \otimes \mathbf{e}_3, \\ \lambda_g &= \int_{-\pi}^{\pi} D(\phi)\rho(\phi)d\phi. \end{aligned} \tag{4.14}$$

As the surface of individual fibers are gradually eroded, bonds with the surrounding elastin and proteoglycans of the ground matrix may also be disrupted, leading to bulk loss of both fiber and ground matrix material. The form of eq. (4.14) is motivated by the assumption that this loss of bulk matrix material will be most pronounced for the thickness ($\mathbf{e}_3$) direction of the tissue, as cleaved molecules can easily diffuse away from the material.

We assume that the elastic component of the deformation is incompressible ($J^e = \det F^e = 1$). A change in mass induces a volume change in the stress free intermediate

configuration ($\tilde{\beta}$), rather than densification, and the volume of the current configuration β is unchanged from the intermediate configuration. Furthermore, we assume that the fiber orientation distribution is unchanged by growth, and the fiber orientation $\mathbf{a_0}$ is the same in the reference β_0 and intermediate $\tilde{\beta}$ configurations. This is strictly true for a planar fiber structure and growth only in the out-of-plane (thickness) direction. We also assume that the fibers deform affinely with the continuum deformation gradient, such that the elastic fiber stretch is given by $\overline{\lambda}^e(\phi) = \mathbf{a}_0 : \mathbf{C}^e : \mathbf{a}_0$,

$$\overline{\lambda}^e(\phi) = \sqrt{(\lambda^e_{11})^2 \cos^2(\phi) + (\lambda^e_{22})^2 \sin^2(\phi)}. \tag{4.15}$$

For the form of the growth tensor specified in eq. (4.14), $\overline{\lambda} = \overline{\lambda}^e$.

The choice of normalizing volume for the strain energy density is important for a tissue of changing mass.[173,187] We define the strain energy density of the tissue for the intermediate configuration, $\tilde{\beta}$, which is equivalent to the tissue density times the strain energy per unit mass. Both are immutable by growth, and the strain energy density of the intermediate configuration represents the intrinsic material properties of the tissue. In contrast, the strain energy density of the reference configuration β_0 decreases with decreasing mass. We apply the standard assumption that the strain energy density of the tissue can be decomposed additively into an isotropic component

describing the ground matrix and an anisotropic component for the fiber structure,

$$\Psi(\mathbf{C}^e) = \Psi_{matrix}(\mathbf{C}^e) + \int_{-\pi}^{\pi} \Psi_{fib}(\overline{\lambda}^e(\phi))\, \rho(\phi) d\phi. \tag{4.16}$$

The anisotropic contribution is obtained by integrating the strain energy density of the fibers weighted by the probability density distribution of fiber orientation. The elastically incompressible Neo-Hookean model, $\Psi_{matrix}(\mathbf{C}^e) = \frac{\mu}{2}(I_1^e - 3) - \frac{p}{2}(I_3^e - 1)$, where μ is the shear modulus, is used to describe the matrix. The strain energy density of the elastica of eq. (4.8) is used for Ψ_{fib} to describe the effect of collagen degradation on the fiber stiffness. The Cauchy stress can be evaluated from the strain energy density of the intermediate configuration as,

$$\sigma = \frac{1}{J^e}\mathbf{F}^e \frac{\partial(\Psi(\mathbf{C}^e))}{\partial \mathbf{C}^e}\mathbf{F}^{e,T}. \tag{4.17}$$

Substituting eq. (4.16) to eq. (4.17) and applying the chain rule gives,

$$\sigma = \mu \mathbf{b}^e - p\mathbf{I} + \int_{-\pi}^{\pi} \frac{\partial \Psi_{fib}(\phi)}{\partial \overline{\lambda}^e(\phi)} \frac{1}{\overline{\lambda}^e(\phi)} \mathbf{F}^e \mathbf{A}(\phi) \mathbf{F}^{e,T} \rho(\phi) d\phi. \tag{4.18}$$

The derivative of the fiber strain energy in eq. (4.8) with respect to the fiber-level elastic stretch, $\overline{\lambda}^e(\phi)$, is given in Table 4.1 of Sec. 4.2.5.

Alternatively, the strain energy density of the tissue can be written with respect

to the reference volume:

$$\Psi^{ref} = J\Psi. \tag{4.19}$$

The Cauchy stress can be computed from eq. (4.19) as,

$$\sigma = \frac{1}{J}\mathbf{F}\frac{\partial(\Psi^{ref}(\mathbf{C}^e))}{\partial \mathbf{C}}\mathbf{F}^T \tag{4.20}$$

where $J = J^e J^g$ and $J^g = \det \mathbf{F}^{\mathrm{g}}$ is the total volume change ratio from growth. Substituting eq. (4.19) into eq. (4.20) results in the same eq. (4.18) for the Cauchy stress.

4.2.4 Application to uniaxial tension

For uniaxial tension caused by an applied force $\mathbf{f} = F_1\mathbf{e}_1$, the Cauchy traction can be evaluated to give,

$$\sigma_{11} = \frac{F_1}{a}, \quad \sigma_{22} = \sigma_{33} = 0, \tag{4.21}$$

where a is the deformed cross-sectional area of the tissue. For an incompressible isotropic material with an initially random fiber orientation distribution, the total deformation gradient is triaxial and can be written as,

$$\mathbf{F} = \lambda^e_{11}\mathbf{e}_1 \otimes \mathbf{e}_1 + \lambda^e_{22}\mathbf{e}_2 \otimes \mathbf{e}_2 + \frac{\lambda_g}{\lambda^e_{11}\lambda^e_{22}}\mathbf{e_3} \otimes \mathbf{e}_3. \tag{4.22}$$

where λ_g is the growth deformation in the thickness direction in eq. (4.14). Substituting eq. (4.22) into eq. (4.18) and applying the plane stress condition $\sigma_{33} = 0$ to solve for $p = \mu\left[(\lambda^e_{11}\lambda^e_{22})\right]^{-2}$, yields the following biaxial Cauchy stress response,

$$\begin{aligned}\sigma_{11}(\lambda^e_{11},\lambda^e_{22}) &= \mu\left[(\lambda^e_{11})^2 - \frac{1}{(\lambda^e_{11}\lambda^e_{22})^2}\right] + \int_{-\pi}^{\pi} \frac{\partial \Psi_{fib}(\phi)}{\partial \overline{\lambda}^e(\phi)} \frac{(\lambda^e_{11})^2}{\overline{\lambda}^e(\phi)} \cos^2(\phi)\rho(\phi))d\phi \\ \sigma_{22}(\lambda^e_{11},\lambda^e_{22}) &= \mu\left[(\lambda^e_{22})^2 - \frac{1}{(\lambda^e_{11}\lambda^e_{22})^2}\right] + \int_{-\pi}^{\pi} \frac{\partial \Psi_{fib}(\phi)}{\partial \overline{\lambda}^e(\phi)} \frac{(\lambda^e_{22})^2}{\overline{\lambda}^e(\phi)} \sin^2(\phi)\rho(\phi))d\phi.\end{aligned} \tag{4.23}$$

The elastic stretches, λ^e_{11} and λ^e_{22}, are evaluated by setting $\sigma_{11}(\lambda^e_{11},\lambda^e_{22}) = F_1/a$ and $\sigma_{22}(\lambda^e_{22},\lambda^e_{22}) = 0$. The resulting nonlinear system of equations can be solved using an iterative Newton solver as shown in the next section.

4.2.5 Numerical Implementation

The simulation for a degrading tissue under constant uniaxial force requires the solution of two nonlinear systems: an outer loop for the tissue-level stretches $(\lambda_{11}, \lambda_{22})$ given a prescribed biaxial stress state $(\sigma_{11} = F/a, \sigma_{22} = 0)$, and an inner loop for the fiber stress and degradation ($\alpha(\phi)$, $D(\phi)$) for a given the fiber elastic macro-stretch $(\overline{\lambda}^e(\phi))$ at time t. An algorithm for the solution of this nonlinear system for a single timestep is given in Table 4.1. Derivatives necessary to evaluate the Jacobins can be found in Appendix B.

To compute the stretch with time for constant uniaxial force, we apply the boundary conditions $(\sigma_{11} = \frac{F_1}{a}, \sigma_{22} = 0)$ to the biaxial stress-stretch constitutive relation of

Table 4.1: Algorithm for degradation and deformation for a single timestep.

GLOBAL ITERATION:	Solve for $\lambda_{11}, \lambda_{22}, \lambda_{33}$ for iteration n+1
Initial Guess:	$\lambda_{11}^{n+1} = \lambda_{11}^{n}$, $\lambda_{22}^{n+1} = \lambda_{22}^{n}$, $\lambda_{g}^{n+1} = \lambda_{g}^{n}$
	$\lambda_{11}^{e,n+1} = \lambda_{11}^{n+1}$, $\lambda_{22}^{e,n+1} = \lambda_{22}^{n+1}$, $\lambda_{33}^{e,n+1} = \lambda_{33}^{n+1}/\lambda_{g}^{n+1}$
Local Iteration:	$\frac{\partial \Psi_{fib}}{\partial \overline{\lambda}^{e}}^{n+1}(\phi)$, $D^{n+1}(\phi)$, for $\phi = [0 : d\phi : 2\pi]$
Tissue Stress:	$\sigma_{11}^{n+1} = \mu\left[(\lambda_{11}^{e,n+1})^2 - (\lambda_{11}^{e,n+1}\lambda_{22}^{e,n+1})^{-2}\right] + \int_{-\pi}^{\pi} \frac{\partial \Psi_{fib}}{\partial \overline{\lambda}^{e}}^{n+1} \left[\lambda_{11}^{e,n+1}\right]^2 \left[\overline{\lambda}^{e,n+1}\right]^{-1} \cos^2(\phi)\rho(\phi))d\phi$
	$\sigma_{22}^{n+1} = \mu\left[(\lambda_{22}^{e,n+1})^2 - (\lambda_{11}^{e,n+1}\lambda_{22}^{e,n+1})^{-2}\right] + \int_{-\pi}^{\pi} \frac{\partial \Psi_{fib}}{\partial \overline{\lambda}^{e}}^{n+1} \left[\lambda_{22}^{e,n+1}\right]^2 \left[\overline{\lambda}^{e,n+1}\right]^{-1} \sin^2(\phi)\rho(\phi))d\phi$
	$\lambda_{g}^{n+1} = \int_{-\pi}^{\pi} \left(D^{n+1}\right)^2 d\phi$
do:	$\begin{bmatrix}\Delta\lambda_{11}^{e,n+1} \\ \Delta\lambda_{22}^{e,n+1}\end{bmatrix} = -\begin{bmatrix}\frac{\partial f_1}{\partial \lambda_{11}^{e}} & \frac{\partial f_1}{\partial \lambda_{22}^{e}} \\ \frac{\partial f_2}{\partial \lambda_{11}^{e}} & \frac{\partial f_2}{\partial \lambda_{22}^{e}}\end{bmatrix}^{-1} \begin{bmatrix}f_1^n \\ f_2^n\end{bmatrix}$
	$f_1^{n+1} = \sigma_{11}^{n+1} - \frac{F_1 \lambda_{11}^{e,n+1}}{\lambda_{g}^{n+1} A_0}$
	$f_2^{n+1} = \sigma_{22}^{n+1} - 0$
while:	$\lvert\sqrt{(f_1^{n+1})^2 + (f_2^{n+1})^2}\rvert \ > \text{tol}$
	$\lambda_{11}^{n+1} = \lambda_{11}^{e,n+1}$, $\lambda_{22}^{n+1} = \lambda_{22}^{e,n+1}$, $\lambda_{33}^{n+1} = \lambda_{33}^{e,n+1}\lambda_{g}^{n+1}$
LOCAL ITERATION	Solve for α, D for iteration k+1
Initial Guess:	$\alpha^{k+1} = \alpha^{k}, D^{k+1} = D^{k}$
	$\overline{\lambda}^{e,n+1} = \sqrt{(\lambda_{11}^{e,n+1})^2 \cos^2(\phi) + (\lambda_{22}^{e,n+1})^2 \sin^2(\phi)}$
Fiber Deformation:	$\overline{\lambda}^{k+1} = \frac{1}{L}\int_0^L \lambda_f^{k+1}\cos(\vartheta^{k+1})/\cos(\Theta)\, dX_1$
	$\overline{\epsilon^2}^{k+1} = \frac{1}{L}\int_0^L \left(\lambda_f^{k+1} - 1\right)^2 dX_1$
	$\vartheta^{k+1} = \beta^{k+1}\Theta\left(4\alpha^{k+1} + 4\left(\alpha^{k+1}\right)^2 + \beta^{k+1}\right)^{-1}$
	$\lambda_f^{k+1} = 1 + \alpha^{k}\cos(\vartheta^{k+1})$
	$\beta^{k+1} = (D^{k+1})^2\beta^{t=0}$
do:	$\begin{bmatrix}\Delta\alpha^{k+1} \\ \Delta D^{k+1}\end{bmatrix} = -\begin{bmatrix}\frac{\partial f_1}{\partial \alpha} & \frac{\partial f_1}{\partial D} \\ \frac{\partial f_2}{\partial \alpha} & \frac{\partial f_2}{\partial D}\end{bmatrix}^{-1} \begin{bmatrix}f_1^n \\ f_2^n\end{bmatrix}$
	$g_1^{n+1} = \overline{\lambda}^{e,n+1} - \overline{\lambda}^{k+1}$
	$g_2^{n+1} = D^{k+1} - D^{t-1} + \Delta G_1 \exp\left[-\overline{\epsilon^2}^{k+1}/(2G_2)\right]$
while:	$\lvert\sqrt{g_1^2 + g_2^2}\rvert \ > \text{tol}$
for tissue stress:	$\frac{\partial \Psi_{fib}}{\partial \overline{\lambda}^{e}}^{k+1} = \left(\frac{(D^{k+1})^2}{L}\int_0^L \left[\frac{E\beta^{k+1}}{4}\left(\vartheta^{k+1} - \Theta\right)\frac{d\vartheta}{d\alpha} + E\left(\lambda_f^{k+1} - 1\right)\frac{d\lambda_f}{d\alpha}\right] dX_1\right)\frac{d\alpha}{d\overline{\lambda}^{e}}$
	$\frac{d\alpha}{d\overline{\lambda}^{e}} = \left[\frac{1}{L}\int_0^L \left(\frac{d\lambda_f}{d\alpha}\frac{\cos(\vartheta^{k+1})}{\cos(\Theta)} - \frac{\lambda_f^{k+1}\sin(\vartheta^{k+1})}{\cos(\Theta)}\frac{d\vartheta}{d\alpha}\right) dX_1\right]^{-1}$
	$\frac{d\lambda_f}{d\alpha} = \cos(\vartheta^{k+1}) - \alpha^{k+1}\sin(\vartheta^{k+1})\frac{d\vartheta}{d\alpha}$
	$\frac{d\vartheta}{d\alpha} = \frac{-\beta^{k+1}(4+8\alpha^{k+1})\Theta}{(4\alpha^{k+1}(1+\alpha^{k+1})+\beta^{k+1})^2}$

eq. (4.23) and solve the nonlinear system of equations iteratively using the Newton-Raphson method. The system is discretized over time and the solutions for the previous timestep are used as the initial guess for the next timestep. The tissue is assumed initially undegraded ($\mathbf{F}^g(0) = \mathbf{I}$, $D(\phi; 0) = 0$ for $\phi = [0 : 2\pi]$) with an initial cross-sectional area $a(0) = A_0$.

For each global iteration step, the deformation of a fiber is solved iteratively with a Newton-Raphson scheme for the nonlinear system of the equilibrium fiber macro-stretch [eq. (4.4)] and the degradation law [eq. (4.10)] discretized over time using a backward Euler approximation. The solutions of α^{t-1} and D^{t-1} from the previous timestep are used as the initial guess. Solving the system yields the internal variable α, a measure of the normalized fiber stress, and the fiber degradation D at the current time-step. These values are passed to the global loop after local convergence.

4.2.6 Parameter Determination

Table 4.2 lists the parameters of the growth and remodeling model. The parameters for the degradation rate law were calibrated to the single-fibril experiments of Flynn et al,[80] which degraded isolated bovine scleral fibrils in bacterial collagenase under zero, low (2 pN/monomer), and high (24 pN/monomer) loads. The axial stiffness of the fibrils were mechanically probed at loads up to 40 pN/monomer every 300 seconds during the degradation experiment and used to calculate the change in the fibril radius with time. The loss in structural stiffness was assumed to arise solely

Table 4.2: Model parameters

Fiber Degradation Parameters	G_1	Unstrained degradation rate
	G_2	Strain sensitivity parameter
Elastica Parameters	E	Fiber Young's modulus
	β	Fiber bending stiffness
	Θ_0	Initial fiber crimp angle
Tissue Parameters	μ	Ground matrix shear modulus

from loss in fibril radius, and the degraded radius was computed from the initial fibril radius and a constant Young's modulus of $E = 0.7$ GPa. Low and medium load fibrils exhibited a linear decrease in radius with time, with low load fibrils degrading faster than medium load. High load fibrils did not exhibit degradation and were not mechanically probed. Control fibers were also held under high force with no enzyme exposure.

The elastica fiber model in Sec. 4.2.1 was applied to model the enzymatic degradation of the uncrimped fibrils ($\Theta_0 = 0$) under uniaxial tension. Previous measurements of the enzymatic cutting rate normalized by force per monomer show that the degradation rate constant is similar for collagen monomers, isolated sclera fibrils, and strips of cornea tissue.[79,80,83] The micro-stretch for a straight fiber is uniform and

the force-stretch relationship can be determined analytically as,

$$F = E\pi D^2 R^2 \left(1 - \frac{1}{\lambda_f}\right). \tag{4.24}$$

The degradation law for the straight fiber simplifies to the following,

$$\frac{dD}{dt} = -G_1 \exp\left[-\frac{(\lambda_f - 1)^2}{2G_2}\right]. \tag{4.25}$$

The initial fibril diameters, R, were extrapolated from the diameter vs. time data reported by Flynn et al.[80] and found to be 415 nm for zero load fibrils, 275 nm for low load fibrils, and 225 nm for control fibrils. Because the fibrils varied in diameter, the total force applied to each fibril was computed based on the initial fibril diameter. We follow Tzafriri et al.[186] to convert from pN/monomer to total force for a given fiber diameter. The number of monomers, N, per fibril of diameter d_f and monomer diameter d_m is calculated by:

$$N = \frac{\pi}{4}\left(\frac{d_f}{d_m}\right)^2. \tag{4.26}$$

Following Flynn et al.,[80] we assume a monomer spacing of $d_m = 1.6$ nm. Applying this calculation to low-load fibrils of $d_f = 275$ nm results in $N = 2.32$e4 monomers/fibril. The 2 pN/monomer force can be converted to a total applied force by:

$$\frac{2 \text{ pN}}{\text{monomer}} * \frac{2.32e4 \text{ monomers}}{\text{fibril}} = 46 \text{ nN}. \tag{4.27}$$

This 46 nN load applied over a fibril of radius 275 nm will result in a 0.1% strain for the assumed Young's modulus of 0.7 GPa. An analogous calculation for high-load fibrils based on the control fibril initial diameter of 225 nm yields an applied load of 373 nN to reach 24 pN/monomer. Instead, we applied to 1054 nN high load force reported in the caption of Fig. 1 of Flynn et al., though both load levels give the same result of completely protected fibrils. We also simulated mechanical probing for low and medium load simulations. Because high load samples were not probed, but were found equivalent to control load fibrils (i.e. no radius change), we compared our high load simulations to the control load results.

The intrinsic degradation rate G_1 was determined from the slope of the fibril radius plotted as function of time for the zero load case in the first 1000 s of the degradation experiment. The parameter G_2 was fit to fibril radius measurements in the first 1000 s of the experiments for the low load case while ensuring that the high load case remained undegraded. The simulations were limited to the first 1000 s of the experiments to avoid consideration of the effects of mechanical damage inflicted by the applied load on the severely degraded fibrils. We found that adding a simple fiber-level damage model to the simulations was able to capture the full 4000 s experiment, but necessitated two additional material parameters. Details and results for simulations with fiber-level damage can be found in Chapter 5.

The Cauchy stress relation in eq. (4.23) was applied to simulate the uniaxial tension experiments of bovine cornea strips reported by Zareian et al.[83] to determine the

mechanical parameters of the elastica model for a collagen fiber. These experiments were also used to validate model predictions of tissue-level enzymatic degradation, described in the following section. In the experiments, a force $\mathbf{f} = F_1\mathbf{e}_1$ was applied to strips of dimensions, 0.75mm thick, 6 mm wide, and 17.5 mm long, and held for 15 minutes to allow for creep without the presence of enzymes. Three different force levels were examined, $F_1 = 0.1$ N, 0.25 N, and 0.5 N, and the strain measurements at the end of the 15 minute hold period were used to the determine the elastica parameters. For the simulations, we set $\lambda_g = 1$ and $\lambda_i^e = \lambda_i$ for no degradation, applied $\sigma_{11} = F_1/a$ and $\sigma_{22} = 0$, and solved iteratively for the stretches λ_1 and λ_2 given an undeformed cross-sectional area of $A_0 = 4.5$ mm^2. A more detailed explanation of the solution method is shown in the Appendix of this chapter.

A value of μ=26 MPa was used for the matrix shear modulus of the tissue. The value was obtained from inverse finite element analysis of inflation tests of bovine cornea.[157] The remaining three elastica parameters for the fiber modulus E, bending stiffness parameter β, and crimp angle Θ_0 were chosen to fit the stress-strain data points at the end of the 15 minute creep period for the three load-levels. A unique optimized fit was not possible for the available number of data points. To further constrain the problem, we followed the analysis of Zareian et al.,[83] which showed that the strain-stiffening behavior of the collagen fibers occurred between the 0.1 N and 0.25 N, to select Θ_0. The axial stiffness parameter E was tuned to match the slope between the 0.25 N and 0.5 N data point, and the bending stiffness parameter β was

tuned to match the slope between the 0.1 N and 0.25 N data points.

For a secondary validation, we used the same methods to calibrate the mechanical parameters to similar constant force experiments reported by Ellsmere et al.[183] In these experiments, strips of bovine pericardium 16 mm long and 4.5 mm wide were held at $F_1 = 1$ g, 10g, and 60 g constant force while exposed to collagenase. Thickness was not reported but was inferred from the reported associated stress to be 0.61-0.65 mm, similar to the Zareian et al. experiments. The parameters of the elastica model were fit to the initial stress and strain reported for each load level. The tissue was again assumed isotropic, and the shear modulus was selected to be the same as for cornea ($\mu = 46$ MPa). Similar to Zareian et al., the authors reported that the three force levels were selected so that the stiffening transition occurred between the medium and high force levels. We used this to select Θ_0. We then varied the axial stiffness parameter E and the bending stiffness parameter β in the same manner described above to match the stress-strain curve.

4.2.7 Modeling tissue degradation

Enzymatic degradation of the bovine corneal strips in the Zareian et al.[83] experiments was initiated after the 15 minute creep period by introducing 0.05 mM of bacterial collagenase while maintaining the constant uniaxial force. The creep strain caused by degradation of the cross-section was measured for 2 hours. The parameters calibrated in Sec. 4.2.6 and listed in Table 4.2 were applied to predict the results of

the degradation-induced uniaxial creep response under constant load, for the three different load levels, 0.1 N, 0.25 N, and 0.5 N. We simulated only the first 6 minutes of the experiment, where the reaction speed is expected to dominate over diffusion. Results for the absolute creep rate at each applied load, as well as the normalized creep rates between loads were compared between experiments and simulations.

We also applied the same methods to predict the enzymatic degradation of the bovine pericardium strips reported by Ellsmere et al.[183] In these experiments, bovine pericardium strips were ramped up and held at constant 1 g, 10 g, or 60 g force while exposed to 20 U/mL collagenase. The creep strain was recorded over a much longer timeframe, up to 50 hours. Again, the parameters calibrated in Sec. 4.2.6 were used to predict the uniaxial creep under constant load. Because the tissue thickness was similar to the Zairean experiments, we only simulated the first 6 minutes of the experiment, and again the absolute and normalized creep rates were compared between experiments and simulations.

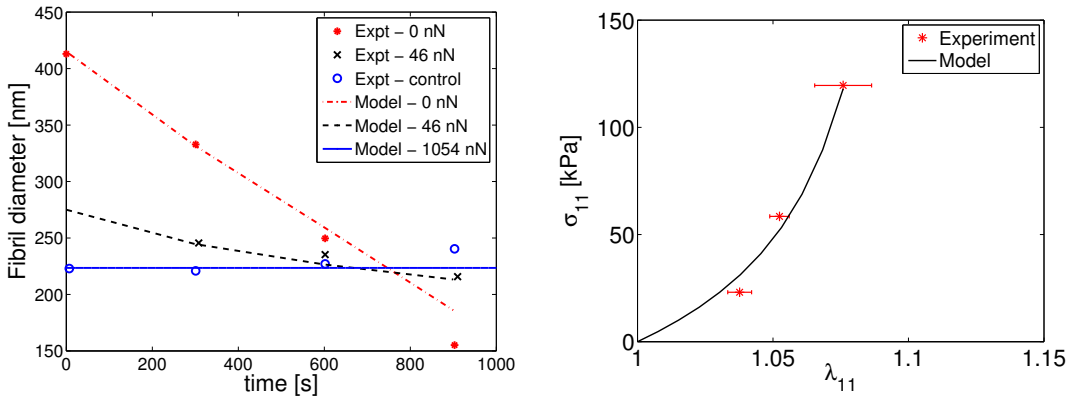

(a) (b)

Figure 4.4: Model calibration: (a) fit of fiber degradation kinetic parameters to single-fibril degradation data collected by Flynn et al[80] for isolated bovine sclera fibrils, (b) fit of tissue-level mechanical model to equilibrium data of Zareian et al[83] for undegraded bovine cornea tissue.

4.3 Results

4.3.1 Enzymatic degradation of single collagen fibrils and tissue strips

Figure 4.4(a) plots the change in fibril diameter with time for data measured experimentally by Flynn et al.[80] for three different load levels, compared to simulations of a straight collagen fiber under uniaxial tension at the same applied loads using eqs. (4.24) and (4.25). The parameters G_1 and G_2 were fit to the 0 nN and 46 nN cases. Good good agreement between model and experiments were obtained for the fitted parameters. The model showed complete strain protection at the high 1054 nN load.

Figure 4.4(b) compares the modeling results and experimental measurements of

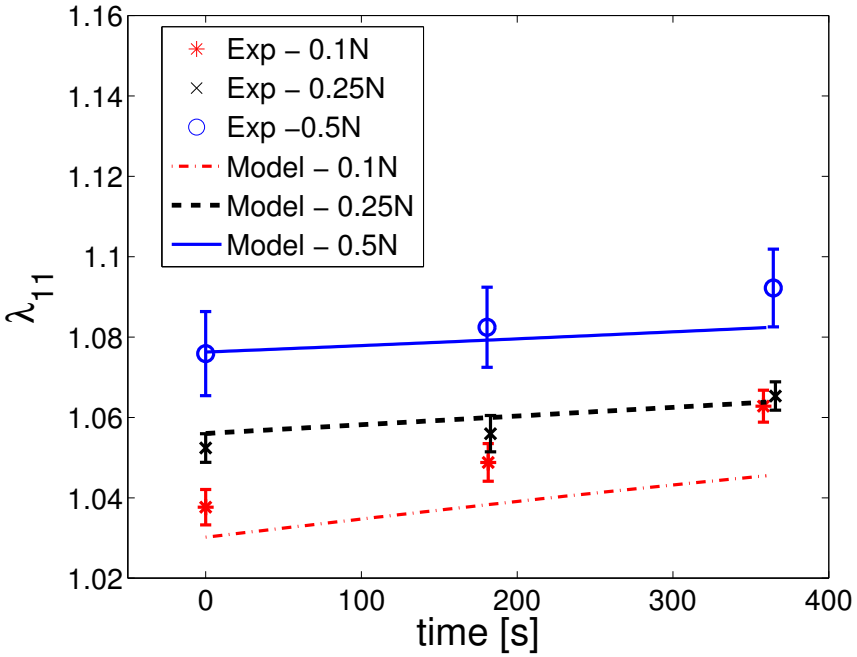

Figure 4.5: Prediction of tissue-level creep data for degrading bovine cornea tissue measured by Zareian et al.[83] using the kinetic degradation parameters calibrated to bovine scleral fibrils in Fig. 4.4(a).

Zareian et al.[83] for the true stress response of bovine cornea under uniaxial tension. The elastica parameters, $\beta = 0.02$, $\Theta_0 = 30^\circ$, and $E = 50$ MPa provided a good fit to the data. The modeling results fell within the experimental variation for the middle and high load data, but was above the measurements for low load data. The initial crimp angle $\Theta_0 = 30^\circ$, was chosen to ensure that the transition stretch occurred between the low and medium load levels, discussed in Zareian et al.[83]

Figure 4.5 compares the model predictions and experimental measurements of Zareian et al.[83] for the degradation-creep response of bovine corneal strips under constant load. The simulations used the fibril-level degradation rate parameters determined from Fig. 4.4(a) and the elastica parameters determined from Fig. 4.4(b)

Table 4.3: Absolute and normalized creep rates for the bovine cornea experimental data reported by Zareian et al.[83] and model prediction using fibril-calibrated kinetic degradation parameters.

Loading	Experimental Creep		Model Prediction	
	Absolute Rate	Normalized Rate	Absolute Rate	Normalized Rate
0.1 N	7.02e-5 s^{-1}	**1.57**	4.27e-5 s^{-1}	**2.52**
0.25 N	3.54e-5 s^{-1}	**0.79**	2.17e-5 s^{-1}	**1.28**
0.5 N	4.48e-5 s^{-1}	–	1.70e-5 s^{-1}	–

to model the tissue-level degradation experiments. The simulation results fell within experimental error for the medium and high load levels, but below the experiments for the low load. This was likely caused by the poorer representation of the uniaxial stress response at low loads in Fig. 4.4(b).

The absolute and normalized creep rates for all three loads are listed in Table 4.3 for both the experimental and modeling results. The absolute creep rates were calculated by linear regression to the stretch-time data of Fig. 4.5. The normalized creep rates were computed by normalizing the absolute creep rate by the slowest creep rate for the 0.5 N loading case. While the model under-predicted the absolute creep rate, the normalized creep rates between loads were similar to the experiments. In particular, both the simulation and experiments report that the the low-load creep rate was nearly twice the high-load creep rate, while the medium and high creep rates were similar.

The elastica model was also able to obtain good agreement with the initial bovine pericardium stress-strain data. The fitted parameters were similar to the bovine cornea, but with lower bending stiffness ($\beta = 0.003$) and larger crimp angle ($\Theta_0 =$

Table 4.4: Absolute and normalized creep rates for bovine pericardium experimental data reported by Ellsmere et al.[183] and model prediction using fibril-calibrated kinetic degradation parameters.

Loading	Experimental Creep		Model Prediction	
	Absolute Rate	Normalized Rate	Absolute Rate	Normalized Rate
1 g	3.25e-6 s^{-1}	**2.48**	5.67e-5 s^{-1}	**3.63**
10 g	6.23e-7 s^{-1}	**0.48**	1.22e-5 s^{-1}	**0.78**
60 g	1.31e-6 s^{-1}	–	1.56e-5 s^{-1}	–

36°). The tensile stiffness ($E = 50$ GPa) was found to be the same. Table 4.4 lists the absolute and normalized creep rates for both the experimental results of Ellsmere et al.[183] and the model prediction based on these parameters and the same kinetic parameters calibrated in 4.4(a). In this case, the model over-predicted the absolute creep rate of the tissue, but again the normalized creep rates were similar between the model and experiments. In fact, the model was able to predict that the low force (1 g) would exhibit the highest creep rate, while the slowest creep rate was for the middle force (10 g).

4.3.2 Single Fiber Simulations

This section investigates the fiber-level implications of the degrading elastica model. First, the fiber-level constitutive relations of eq. (4.2)-(4.4) were applied to simulate the undegraded fiber deformation for the mechanical parameters determined for bovine cornea in Sec. 4.2.6. Figure 4.6(a) plots the relationship between the micro-stretch, λ_f, computed by eq. (4.3), and the macro-stretch, $\overline{\lambda}$, computed by eq. (4.4) over the same range for a single non-degraded elastica fiber. The micro-

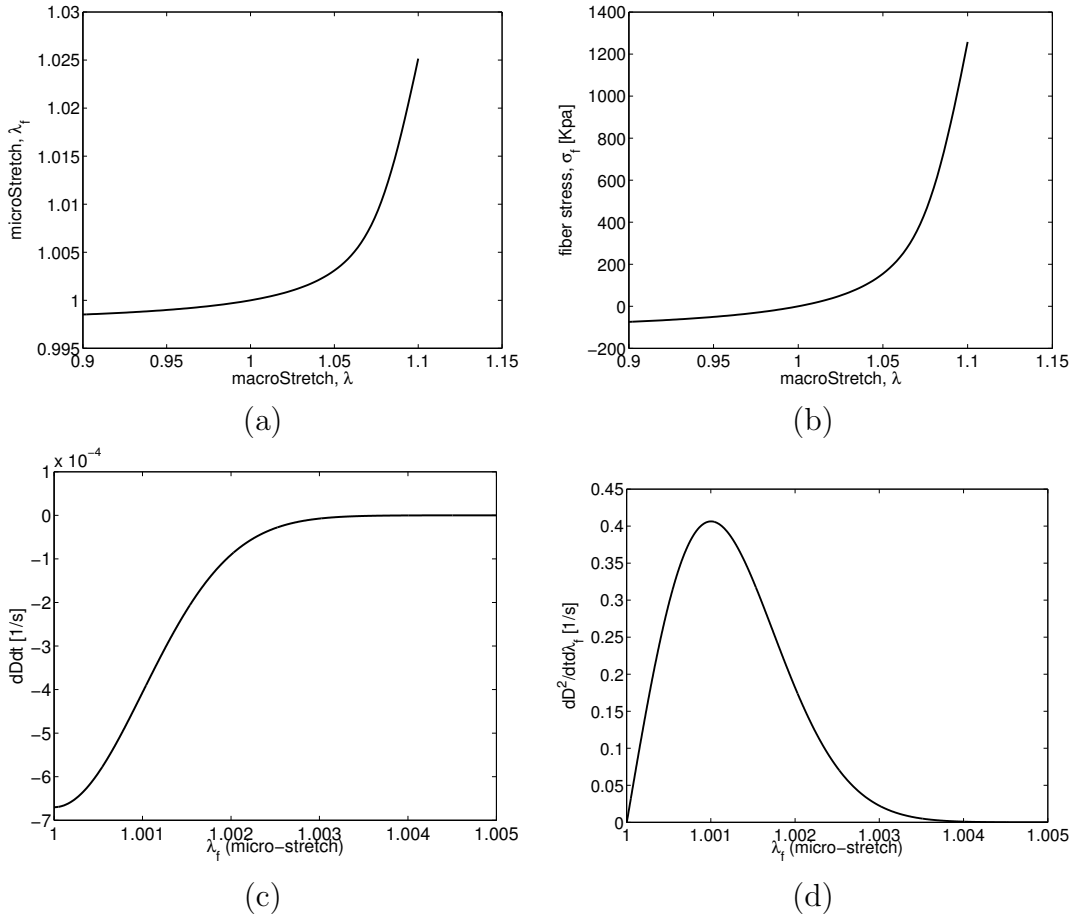

Figure 4.6: Fiber-level results a single elastica: (a) Relation between the micro-stretch and macro-stretch for a single elastica; (b) Dependence of the degradation rate for a single fiber on the micro-stretch [eq. (4.10)], (c) stress-macrostretch relation for single elastica, (d) Derivative of degradation rate for a single fiber with respect to the micro-stretch [eq. (4.10)] for the experimentally calibrated parameters.

stretch remains small (less than 2.5%) over the range of macro-stretches plotted. The micro-stretch begins to increase after $\overline{\lambda} = 1.06$, as the dominant fiber deformation mode transitions from bending to axial stretching. Figure 4.6(b) plots the stress for a single non-degraded elastica over a range of macro-stretches of 0.90 - 1.10. The stress-stretch curve exhibits the characteristic stiffening expected for a collagen fiber as the elastica unbends. The compressive response of the fiber is small, as expected for collagen fibers: a 10% extension corresponds to a 1258 kPa tensile stress, while a 10% compression corresponds to a -74 KPa compressive stress, or less than 6% of the tensile stress.

Next, we plot the degradation rate dependence on the fiber micro-stretch, λ_f, prescribed by eq. (4.10) for the kinetic parameters fit in Sec. 4.2.6. As shown in Fig. 4.6(c), the degradation rate is seen to decrease linearly with the micro-stretch, then slowing significantly at $\lambda_f = 1.002$ before becoming nearly zero at $\lambda_f = 1.003$. Figure 4.6(d) plots the derivative of the degradation rate with respect to the micro-stretch. There is an inflection point at $\lambda_f = 1.001$, indicating that degrading fibers are the most sensitive to changes in stretch in this stretch. Referring to Figs. 4.6(a)-(b), $\lambda_f = 1.001$ corresponds to a macro-stretch of approximately $\overline{\lambda} = 1.03$, and occurs at the "knee" or transition region between bending and axial stretching.

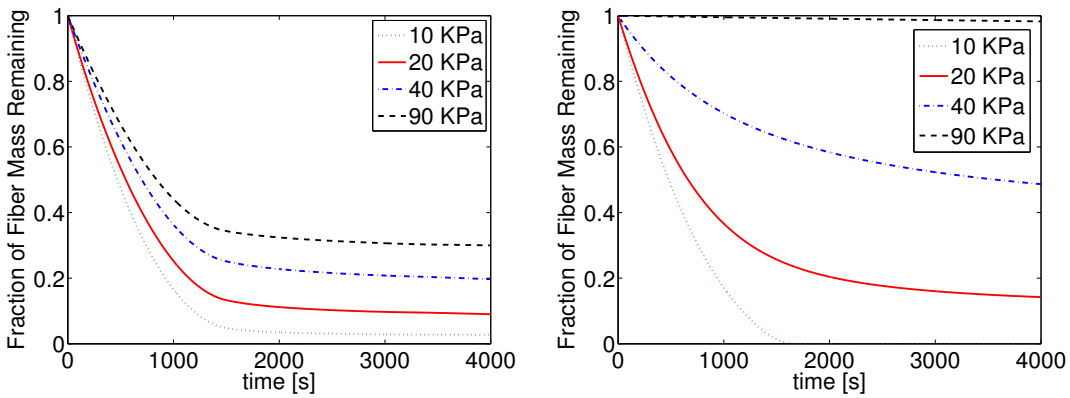

Figure 4.7: The fraction of fiber mass remaining with time as degradation proceeds for differing levels of (a) uniaxial stress and (b) equibiaxial stress.

4.3.3 Degradation of a tissue material under different stress states

The constitutive relations in eq. (4.23) and the mechanical parameters for bovine cornea were applied to simulate the degradation of an initially isotropic tissue material under a constant uniaxial or biaxial applied stress state. We first assessed the effect of different stress levels on the total fiber mass. Figure 4.7 plots the fraction of the fiber mass remaining, defined as $\frac{1}{2\pi}\int_{-\pi}^{\pi} D(\phi)^2 d\phi$, over 4000 s for a tissue degrading under constant uniaixial or equibiaxial stress ranging from 10 kPa to 90 kPa. Uniaxial simulations exhibited a rapid degradation rate which abruptly decreased after 1500 s, though the rate of fiber mass loss remained finite for all applied stresses. Higher stress resulted in a higher fraction of fiber mass remaining, and complete degradation of the fibers was not achieved for any stress level. In contrast, simulations of equibiaxial

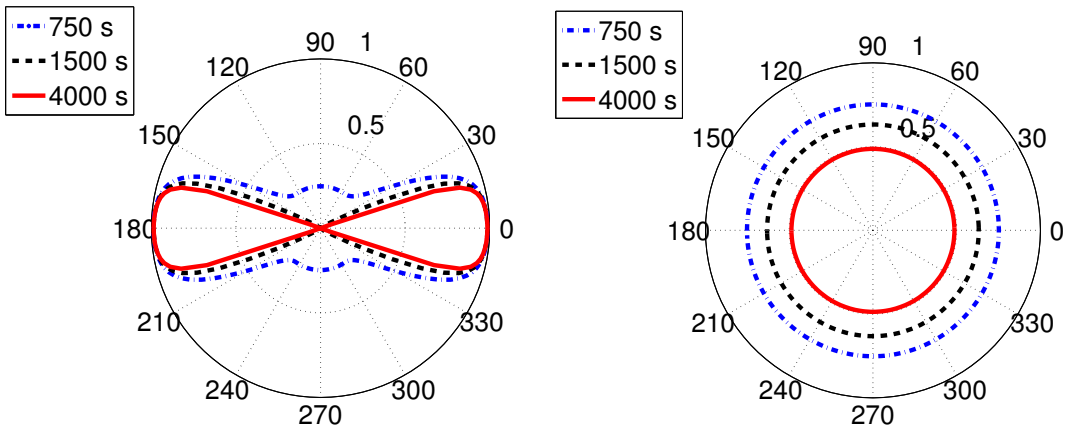

Figure 4.8: Polar plot of the fiber mass distribution after 750 s, 1500 s, and 4000 s of degradation for 40 kPa constant stress applied (a) uniaxialy, at $\phi = 0°$, and (b) equibiaxially, at $\phi = 0$ and 90°.

loading exhibited complete degradation for lower applied stresses. Moreover, the applied stress had a larger effect on the degradation rate. The rate of fiber mass loss in the first 500 s decreased by 16% between 20 kPa and 40 kPa for uniaxial tension compared to 38% for biaxial tension.

To understand these results, Fig. 4.8 plots the fiber mass distribution, normalized by the initial fiber mass, $D(\phi)^2$, at 750 s, 1500 s, and 4000 s for the 40 kPa uniaixal and equibiaxial simulations. For uniaxial loading at $\phi = 0°$, an initially isotropic distribution became strongly anisotropic, as fibers orthogonal to the loading axis are fully degraded, while a tissue loaded equibiaxially at $\phi = 0°$ and 90° remained isotropic because all fibers degraded at the same rate. The sudden decrease in degradation rate at 1500 s for uniaxial loading occurred after all unloaded fibers were completely degraded and only loaded fibers remained. Because unstrained fibers degraded at

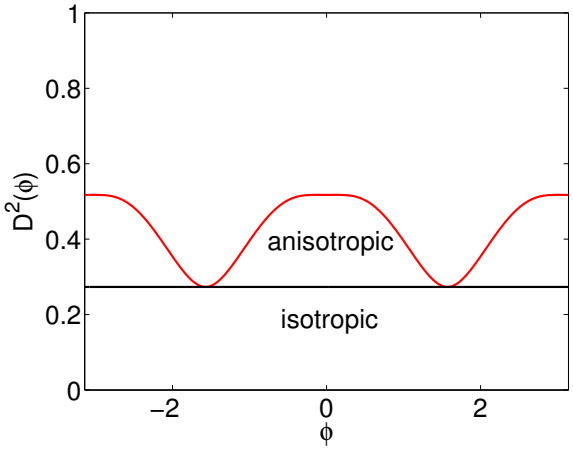

Figure 4.9: Illustration of the calculation of the anisotropy ratio. The anisotropy ratio is computed as the mass of the anisotropic component over the total fiber mass (anisotropic + isotropic mass).

the same rate, this transition occurred at approximately the same time for all stress levels. In contrast, for the biaxial case, all fibers were loaded equally and degraded uniformly, at a rate determined by the fiber stretch. As fibers degraded, the stretch on individual fibers increased under constant stress, slowing degradation. For a very low equibiaxial stress, fibers degraded completely because the matrix carries the majority of the load, preventing the the large fiber stretches that would halt degradation.

While uniaxial loading can lead to strongly anisotropic fiber structures, many tissues in the body exhibit fiber structures of varying degrees of anisotropy. We next explore the effect of a non-equibiaxial stress state on the degraded fiber mass distribution. Following Pijanka et al.,[14] we quantified the anisotropy ratio by computing the ratio of the anisotropic component of the fiber mass to the total fiber mass, as illustrated in Fig. 4.9. The uniaxial stress state described previously resulted

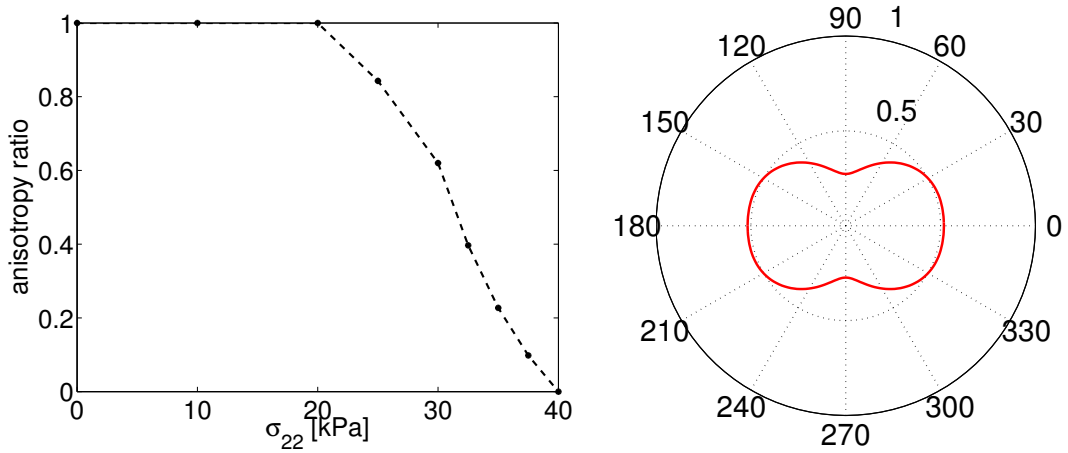

(a) (b)

Figure 4.10: (a) Anisotropy ratio when σ_{22} is varied while σ_{11} is held constant at 40 kPa, (b) polar plot of mass fraction remaining of an initially isotropic distribution for $\sigma_{22} = 33$ kPa and $\sigma_{11} = 40$ kPa , resulting in an anisotropy ratio of 0.36, in the range reported by Pijanka et al.[14] for human posterior sclera.

an a completely anisotropic fiber structure with no isotropic component (anisotropy ratio = 1), while the equibiaxial stress state maintained a fully isotropic structure (anisotropy ratio = 0). Figure 4.10(a) plots the anisotropy ratio resulting from varying the ratio of σ_{22}/σ_{11} from 0 to 1 for $\sigma_{11} = 40$ kPa. Below $\sigma_{22}/\sigma_{11} = 0.5$, the tissue became fully anisotropic as off-axis fibers were not strained sufficiently to halt degradation. However, at $\sigma_{22}/\sigma_{11} > 0.5$, the anisotropy ratio ranged from fully anisotropic to fully isotropic, illustrating that small changes in the biaxial stress state can lead to large changes in the anisotropy of the fiber structure. Fig. 4.10(b) plots the fiber mass distribution for a tissue held at $\sigma_{11} = 40$ kPa and $\sigma_{22} = 33$ kPa. The anisotropy ratio for this stress state was 0.36, within the range of anisotropy ratios reported by Pijanka et al.[14] for human posterior sclera. In contrast, a tissue held at $\sigma_{11} = 40$

kPa and $\sigma_{22} = 20$ kPa will have an anisotropy ratio of 1, similar to fiber anisotropy measured for human skin tissues.[89]

4.3.4 Effect of fiber collagen degradation and deposition on the tissue growth and remodeling

The following numerical study examined the effect of collagen degradation and deposition on the growth and remodeling of a thin spherical tissue structure. Though idealized, this geometry is a first order approximation of tissue systems such as the eye-wall or heart ventricles. The spherical structure is assumed to have an initial radius of $R_0 = 12.5$ mm, thickness of $t_0 = 1$ mm and uniform pressure loading of $P = 2$ kPa. These values approximate the dimensions of the human sclera and the intraocular pressure. The model parameters listed in Table 4.2 were used to describe the material properties of the tissue, which included the parameters calibrated from experiments as described in Sec. 4.2.6 for bovine cornea. In addition, the simulation included a finite collagen deposition rate of $k_d = 1e-4$. This collagen deposition rate was chosen to offset the slow degradation of strained collagen fibers seen in Fig. 4.7.

The hoop stresses for the thin pressurized spherical shell are,

$$\sigma_{11} = \sigma_{22} = \frac{PR}{2t} \tag{4.28}$$

where R and t are the radius and thickness of the sphere in the current configuration

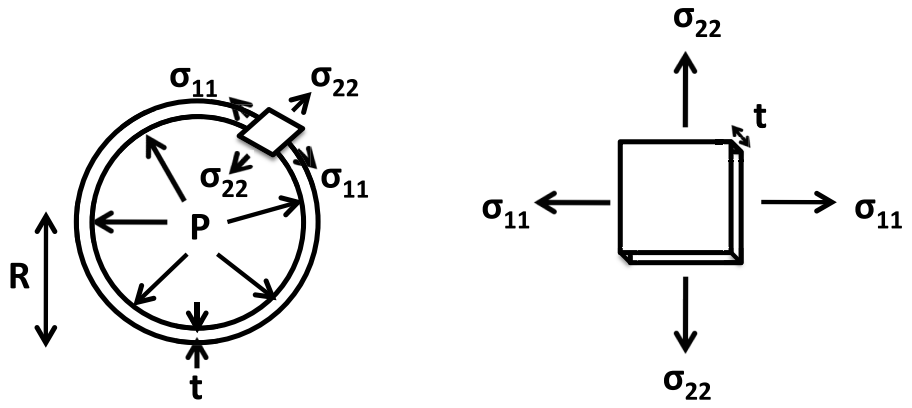

Figure 4.11: Schematic of constant pressure simulations for a spherical tissue with radius R, thickness t, and internal pressure, P. A small patch can be modeled as subject to a equibiaxial load, where $\sigma_{11} = \sigma_{22} = PR/2t$. The pressure P is assigned and R and t are updated throughout the simulation as collagen degradation and deposition proceed.

(β). The internal pressure was held constant at 2 kPa for 4000 seconds, until the tissue reached a steady stress and strain state and a steady thickness and radius. The biaxial stress response in eq. (4.23), growth relation in eq. (4.14), and degradation law in eq. (4.10) were used to calculate the stretch λ_{11} and λ_{22} as well as the growing thickness $\tilde{t} = \lambda_g t_0$, where t_0 is the initial thickness, in response to an applied pressure. After 4000 seconds, a step increase or decrease in the pressure of $\Delta P = 0.25kPa$ was applied. The deformed radius and thickness were computed from the stretch by $R = \lambda_{11}^e R_0 = \lambda_{22}^e R_0$, and $t = (\lambda_{11}^e \lambda_{22}^e)^{-1} \tilde{t}$.

Figure 4.12 plots the tissue thickness, stress, and stretch with time for simulations with a step increase or decrease in pressure. Increasing the pressure at 4000 s caused

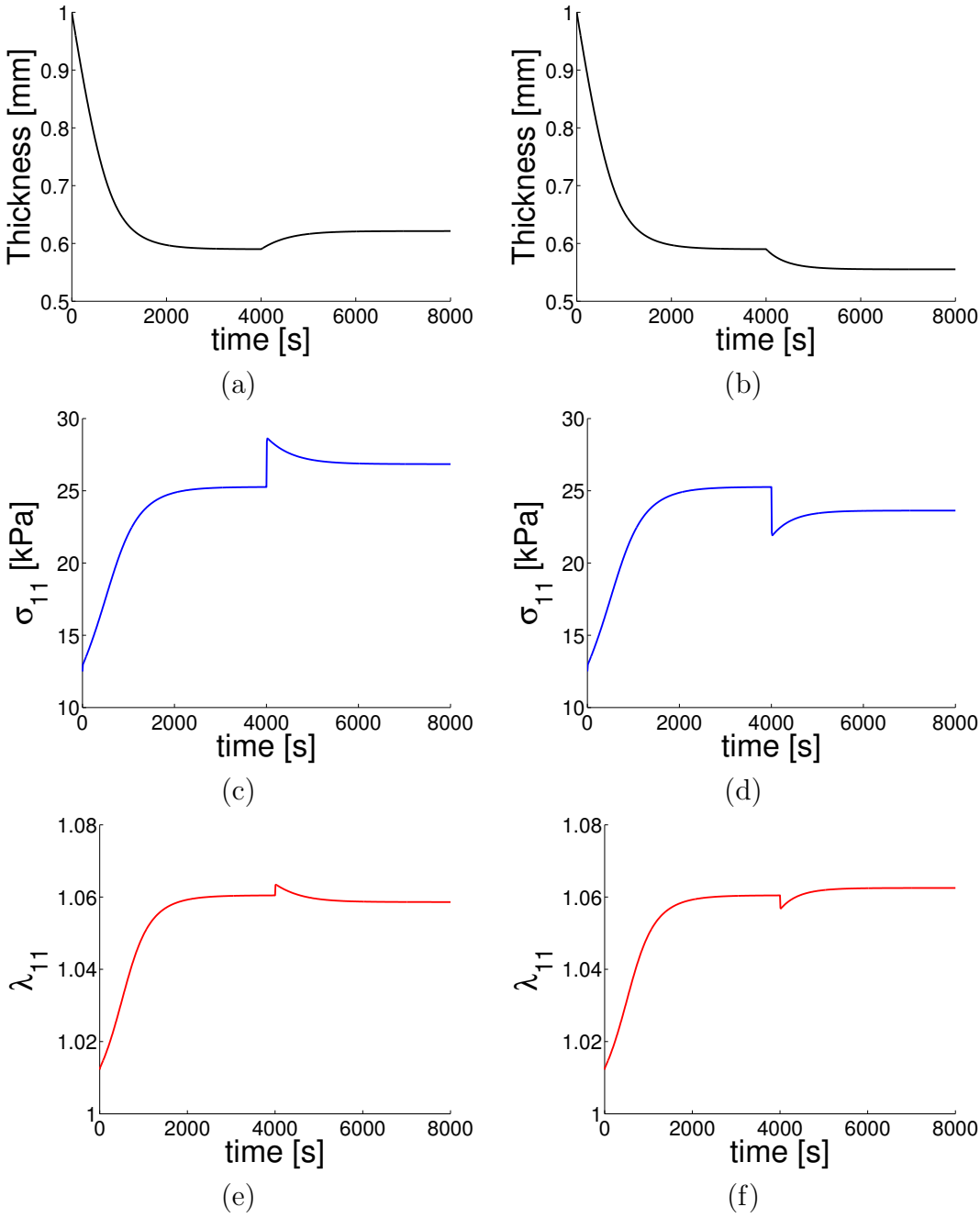

Figure 4.12: Results of constant pressure application and subsequent step increase (a, c, e) or decrease (b, d, f) in pressure at $t = 4000s$ for simulations with enzymatic degradation and constant collagen deposition. Tissue responds to the pressure perturbation by increasing or degreasing thickness (a-b). After perturbation, stress levels approach the steady-state value but remain offset (c-d), while strain levels are restored to the steady-state value (e-f).

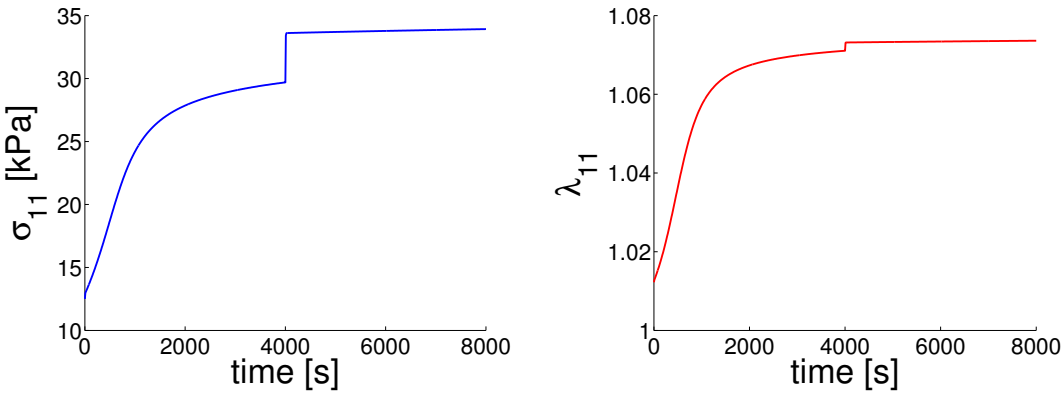

(a) (b)

Figure 4.13: Results of constant pressure application and subsequent step increase in pressure at $t = 4000s$ for simulations without collagen deposition. Neither stress nor strain recovered the steady-state value.

the thickness to increase in the presence of collagen deposition, which caused the hoop stress and strain to decrease asymptotically from the initial response to the applied 0.25 kPa perturbation. The strain recovers the steady-state value of the initial pressure loading, while the equilibrium stress settled at a higher steady-state level. For a step decrease in the pressure, collagen degradation occurred at a faster rate, and the tissue thickness decreased. Both cases produced a steady state response, where deposition and degradation were balanced, i.e. when the fibers were mostly straightened.

To assess the importance of including collagen deposition as an opposing mechanism to degradation, Fig. 4.13 plots the stress and strain with time in response to the step increase in pressure for a simulation with no collagen deposition ($k_d = 0$). When degradation was not included, neither the stress nor strain recovered the original steady-state. When there is no opposing mechanism to balance degradation, the

tissue has no way to increase the thickness in response to the increase in pressure, preventing a recovery of the stress and strain levels.

4.4 Discussion

In this work, we presented a micro-mechanical model for the strain-protected enzymatic degradation of collagen. The collagen fibers were modeled as a planar crimped elastica and the degradation rate of a fiber was inhibited by the axial strain energy density, which increased the activation energy for the degradation reaction. The use of a micro-mechanical model for crimped collagen fibers allowed for the calculation of the axial strain energy directly from the micro-stretch of the collagen fiber. Although the model did not take into account the stochastic nature of the chemical reactions between the enzyme and collagen molecules, it reproduced the rapid onset of strain protection observed experimentally. Moreover, the model associated the onset of the inhibition in enzymatic degradation with the straightening of the fiber as observed in experiments.[80–82] The micro-mechanical model for a degrading fiber was incorporated into a distributed fiber hyperelastic model for the stress response and an anisotropic growth model for a collagen tissue.

The kinetic parameters of the degradation rate law were calibrated to the degradation experiments of Flynn et al.[80] for collagen fibrils isolated from bovine sclera and subjected to uniaxial loading. The parameters were used to predict the tissue-level

degradation experiments of Zareian et al.[83] for bovine corneal strips and Ellsmere et al.[183] for bovine pericardium strips under uniaxial tension. The tissue experiments reported both the absolute creep behavior with time, as well as normalized creep rates between experiments. The absolute creep rates incorporated the effects of deformation processes, such as viscoelasticity and damage, which were not considered in the model. As a results, the model under-predicted the absolute creep rates for the cornea. The normalized creep rates can be interpreted as a measure of the maximum cutting rate of the enzyme at a given strain level. The model predictions for the normalized creep rates agreed well with experiments, even though the parameters of the degradation rate law were calibrated using data for scleral fibrils, which were 10 times larger than corneal fibrils. Moreover, the tissue model assumed an isotropic distribution of collagen fibers, which produced a nonuniform orientation distribution of fiber stretch. The strain-protected degradation model was also capable of predicting the normalized creep rates of the bovine pericardium data reported by Ellsmere et al.,[183] although these results were initially interpreted as evidence for strain-accelerated degradation. Similarly, molecular-level degradation experiments have also suggested that mechanical strain increases the degradation of heterotrimeric collagen by matrix metalloproteinases,[188,189] in contrast to the results of similar experiments by Camp et al.[79]

We applied the model to explore the implications of stretch-mediated enzymatic degradation for tissues under different loading states. Under uniaxial loading, off-

axis fibers were quickly degraded, while load-bearing fibers were preserved, which were consistent with experimental observations.[3] This results in a strongly anisotropic fiber structure. In contrast, tissues under constant equibiaxial stress degraded uniformly, maintaining an isotropic fiber distribution, and more slowly than tissues loaded by the same stress level under uniaxial tension. Applying a non-equibiaxial stress state with a sufficiently large stress ratios resulted in an anisotropic fiber structure, where the degree of fiber alignment depended on stress ratio of the biaxial stress state. For example, applying a stress ratio of 0.825 resulted in an degree of fiber alignment within the range reported for the human mid-posterior sclera by Pijanka et al.,[14] while a stress ratio of 0.5 resulted in a highly aligned fiber structure consistent with those measured for skin tissue.[89] These results suggest that strain-dependent enzymatic degradation is an important mechanism for the development of a variety of anisotropic fiber structures found in tissues throughout the body.

We investigated the interaction of collagen degradation and deposition mechanisms in tissue-level growth and remodeling. *In vivo*, collagen is constantly deposited and degraded as part of the normal collagen turnover process. A constant deposition rate was incorporated into the micro-mechanical model and applied to an idealized model of a spherical tissue undergoing a pressure perturbation. When both deposition and degradation were present, the wall stress and strain will return to a steady state after a positive or negative pressure perturbation. However, only the strain will recover the initial value before perturbation. Therefore our model predicts that

degradation and deposition may work together to maintain a strain homeostasis for this idealized case.

Whether tissues seek a strain or stress homeostasis remains an open question in soft tissue biomechanics. Models based on a stress homeostasis assumption have been able to successfully reproduce changes in cardiac tissue with increased pressure and shear flow,[51,58] while models based on strain homeostasis have been used to describe the growth of the ventricles in response to pressure or volume overload.[65] The prediction of strain homeostasis in this work for a pressurized spherical membrane arises from the fact that the micromechanical degradation model was associated with the onset of strain inhibition when the collagen fibers were nearly straightened. The balance of the collagen deposition and strain-protected degradation mechanism caused the collagen fibers to attain a unique equilibrium stretch given an initial crimp morphology. Adding a strain-dependence to the deposition model would also result in a tissue strain homeostasis, but at a different equilibrium stretch. Our results support the hypothesis that there may exist an energetically favorable collagen fiber configuration, supported by experimental evidence that both active cellular contraction[77] and thermal denaturation[190] favor nearly straightened collagen fibrils. We speculate that active cellular contraction in addition to collagen degradation and deposition is needed to obtain stress homeostasis.

A limitation of our approach concerns the difference between a collagen fibril and fiber structures. We fit our degradation parameters to single-fibril experiments, and

ascribed the same parameters for the degradation of a single fiber. In the cornea, collagen fibrils are arranged in parallel into lamellae, referred to as fibers, and the fibers are stacked in different orientations to form the corneal stroma. Incorporating the structural organization of fibrils into fibers may change the predicted degradation rate for a tissue. Specifically, while it has been shown that strain can halt the degradation of collagen fibrils,[80] tissues continue to degrade, though at a significantly reduced rate.[83] It has been speculated that fibrils arranged in fibers experience strain shielding, which causes them to be degraded even at large tissue stretch. Though we did not consider this effect, the model was able to capture the effect of applied tensile loads on the creep rate of the tissue degradation experiments.

The elastica parameters were fit to uniaxial tensile experiments of tissue strips after a 15 minute creep, and were more compliant than measured in previous *in vitro* inflation tests of bovine cornea.[25,157] The parameters produced an initial crimp angle of 30°, which is significantly larger than measured by histology for rabbit cornea.[12] The radiation of gyration parameter $\beta = 0.02$ was also smaller than computed based on the histological measurements for the rabbit cornea. Additionally, only three stress levels were available to fit three mechanical parameters. To limit the potential parameter space, we followed the force-per-monomer calculations of Zareian et al.,[83] indicating that the straightening transition occurred between the medium (0.25 N) and high (0.5 N) force levels. This fixed the crimp angle and the remaining two parameters were tuned to the toe and linear region. More data is needed to ensure

an optimized parameter set. Finally, the fiber structure of the tissue was assumed to consist of continuous long fibers arranged in the plane of the tissues. Each fiber was assumed to deform affinely with the continuum deformation gradient. Therefor the model neglected the presence of fibers that run through the thickness of the tissue.

Experiments have elucidated many potential remodeling mechanisms that were not included in this work. We assume a constant rate of collagen deposition which has the effect of only increasing the existing fiber radii. In fact, collagen deposition has been shown to depend on strain[78] and is also associated with the formation of new collagen fibers, which may be deposited in a state of pre-stretch. This more precise description of collagen deposition has been modeled by others and shown to cause to macroscopic growth.[70] We also do not take into account the effects of active cellular contraction, which may be necessary to obtain stress homeostasis. Finally, we apply simple biaxial loading conditions to our material-point model as an approximation of the complex stress states found throughout the body.

4.5 Conclusions

This work has presented a micro-mechanical model for the strain-protected enzymatic degradation of collagen tissues that is capable of predicting tissue-level results from fibril-calibrated parameters. The model is built upon upon the assumption that axial strain energy of collagen fibrils, and by extension local fiber micro-strain, in-

hibits collagen degradation. It has been suggested that distortion of the collagen backbone physically alters the configuration of binding sites available to collagenase.[4] We hypothesize that the stretching of the collagen backbone leads to such conformational changes, resulting in the dramatic slowing of collagen degradation with strain. This assumption requires a micro-mechanical model so that the axial component of the strain energy can be separated from the bending contribution, linking the deformed fiber shape and micro-strain to a specific loading state. Representation of the initial crimp is crucial to this approach. The model has been used to successfully describe fibril-level degradation experiment and to predict tissue-level degradation experiments of bovine cornea. Pairing the degradation model with collagen deposition predicts strain homeostasis for a pressure perturbation. Thus our model implies that degradation is an important tool in maintaining tissue homeostasis, likely working in concert with deposition and cellular traction. Future work will incorporate these mechanisms for a more complete description of the growth and remodeling process.

Chapter 5

Incorporating fiber-level damage into the enzymatic degradation model

This chapter extends the fiber-level degradation model of Chapter 4 by incorporating a model for stress-driven damage. In this chapter, a simple mechanical damage model is incorporated to describe the full 4000 s of degradation data. Portions of this chapter were submitted to *Biomaterials* with the previous chapter as Online Supplementary Material.

5.1 Introduction

In the previous chapter, the first 1000 s of the single fibril degradation experiments by Flynn et al[80] were used to calibrate the degradation law. This is because later in the experiments, fibril damage, evidenced by an increased reference length and eventual fibril failure, becomes important. The fiber radii reported in the experiments were not measured directly, but instead computed from the measured structural stiffness during mechanical probing by assuming a constant fibril stiffness of $E = 0.7$ GPa. If fibers are damaged and the stiffness is reduced, this damage will be interpreted as a reduction in radius due to degradation.

The single-fibril degradation experiments demonstrated that strain can slow the degradation of collagen fibrils. However, a seemingly contradictory result from the experiments was that although applying a low force lowered the degradation rate and a higher force halted degradation entirely, low force fibrils did not self-protect as degradation proceeded under constant force. As the strain increased, it was expected that the degradation would eventually halt, but this was not observed in the experiments. We hypothesize that the fibers sustained damage as the radii decreased, particularly during mechanical probing. This loss in fiber stiffness would result in computed fiber diameters that appear to continue to degrade even above the strain protection threshold. In the previous chapter, we avoided accounting for damage by only modeling the first 1000 seconds of the experiments, before damage to fibers was observed. In this chapter, we include damage in our model and attempt to pre-

dict the entire time-course of the experiments (4000 seconds) and explain the lack of self-protection for low load fibrils.

5.2 Methods

Damage is modeled as a simple reduction in the stiffness by a damage factor, $0 \leq \xi \leq 1$. Following the work of Simo and Ju,[191] the stress of a damaged fiber is computed by $\overline{\sigma} = (1-\xi)E_0\epsilon_f$, where E_0 is the initial, undamaged fiber stiffness and $\epsilon_f = \lambda_f - 1$ is the fiber strain. We assume that the damage rate depends linearly on the current stress, and occurs after a minimum stress (σ_{min}) is surpassed:

$$\frac{d\xi}{dt} = \begin{cases} C\left(\sigma/\sigma_{min} - 1\right), & \text{if } \sigma/\sigma_{min} > 1 \\ 0, & \text{otherwise.} \end{cases} \tag{5.1}$$

Substituting $\sigma = (1-\xi)E_0(\lambda_f - 1)$ and non-dimensionalizing the result, the damage law for an axial fiber is written as:

$$\frac{d\xi}{dt} = \begin{cases} C\left[\frac{(1-\xi)(\lambda_f-1)}{H} - 1\right], & \text{if } \frac{(1-\xi)(\lambda_f-1)}{H} > 1 \\ 0, & \text{otherwise,} \end{cases} \tag{5.2}$$

where $H = \sigma_{min}/E_0$ a the non-dimensionalized measure of the initiation stress and C is the rate dependence of damage after initiation.

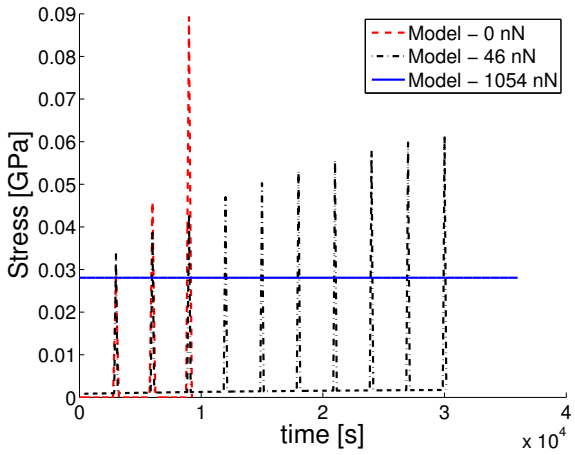

Figure 5.1: Stresses at mechanical probing for simulations of single fibrils with degradation only (no damage). The stress threshold for damage($\sigma_{min} = 37MPa$) was selected to occur between the stress for the second mechanical probe of low load fibrils and the stress of the high load fibrils to be consistent with experimental observations.

To simulate the single-fibril degradation experiments, fibrils are modeled as elastic rods with initial stiffness of $E_0 = 0.7$ GPa. The fiber is allowed to sustain both degradation and damage while loaded. The fiber radius is computed from the simulation based on the same assumption of constant stiffness made by Flynn et al.:

$$\begin{aligned} \sigma &= \frac{F}{\pi r^2} \\ &= E_0(\lambda_f - 1), \end{aligned} \tag{5.3}$$

$$r = \sqrt{\frac{F}{E_0 \pi (\lambda_f - 1).}} \tag{5.4}$$

This value of the radius computed by eq. (5.4) will be lower than the true radius as the stiffness is lowered by damage.

The damage parameters H and C were fit to the experimental data sequentially.

First, the damage threshold parameter was determined. The stress in the fibrils both during degradation and mechanical probing for simulations with degradation only are plotted in Fig. 5.1. The non-dimensionalized initiation value was selected to be $H = 0.053$, which corresponds to $\sigma_{min} = 37$ MPa for $E = 0.7$ GPa. The minimum stress value is higher than the stresses in the high load fibers but is reached by the second probe of the zero load fibers illustrated in Fig. 5.1, consistent with experimental observations that zero load fibers begin to fail but high load fibers do not. The damage rate parameter $C = 0.05$ was then tuned to match the experimentally calculated radius vs. time data.

5.3 Results and Conclusions

Figure 5.2 plots the experimentally calculated fiber radius against the model prediction. Very good agreement is seen over the course of the experiment, suggesting that damage can account for the lack of strain protection for low-load fibrils after 1000 s. Figure 5.3(a) plots the degradation ratio, $D = r/R$, for the simulations. It is seen that degradation does slow for low-loaded fibrils. However, as shown in Fig. 5.3(b), damage is significant for the fibrils, particularly after each mechanical probe. Therefore the simulations suggests that the degradation of low-load fibril would indeed slow with time, but this effect is masked by the accumulation of damage.

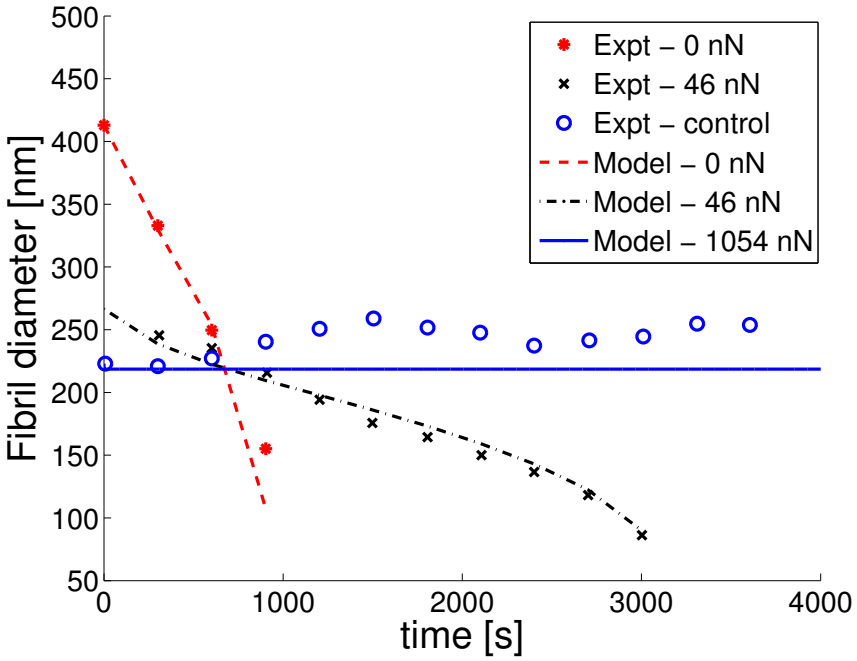

Figure 5.2: Prediction of single-fibril degradation experiments of Flynn et al.[80] while accounting for damage.

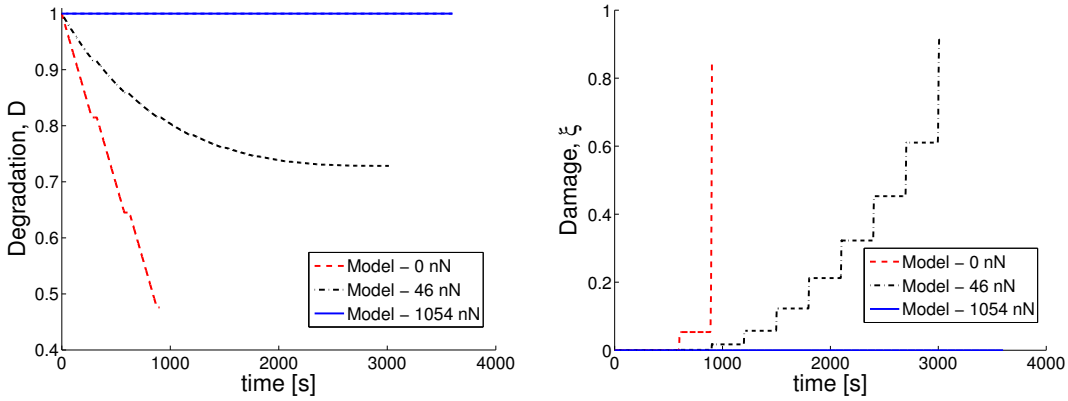

(a) (b)

Figure 5.3: Model prediction for (a) degradation, $D = r/R$, and (b) damage, $0 \leq \xi \leq 1$, for simulations plotted in Fig. 5.2. The probe force caused discrete increases in ξ.

Chapter 6

Investigating the effects of preconditioning on inflation tests of planar tissues

In Chapter 2, it was observed that skin tissue tested by inflation (bulge) testing did not exhibit the evolving mechanical response to cyclic loading commonly attributed to preconditioning. This chapter extends these results by conducting a more extensive study on a variety of tissues including human skin, bovine cornea, bovine sclera, and porcine sclera. All four of tissues exhibited a negligible preconditioning response for the inflation test regardless of strain history. Tissues obtained complete recovery to the reference state, and strain contours across the entire specimen were nearly identical at the maximum pressure of each load cycle. These results suggest

that the commonly observed effects of preconditioning may be experimental artifacts rather than an intrinsic property of the tissue and may avoided by experimental design. This chapter is reprinted from *The Journal of Biomechanical Engineering*, Vol. 135, Theresa K. Tonge, Barbara J. Murienne, Baptiste Coudrillier, Stephen Alexander, William Rothkopf, Thao D. Nguyen, "Minimal Preconditioning Effects Observed for Inflation Tests of Planar Tissues", Pages 114502-1 - 114502-14, Copyright (2013), with permission from ASME.[90] The chapter was written primarily by me but includes significant contributions from the co-authors of the paper, particularly Barbara J. Murienne (porcine sclera), Baptiste Coudrillier (bovine sclera), and Stephen Alexander (bovine cornea).

6.1 Introduction

Preconditioning, or the use of repeated load cycles to obtain a repeatable mechanical response, is a common procedure in the testing of soft biological tissues. Preconditioning effects refer to an evolving mechanical response to repeated loading and were first described for uniaxial tensile testing of skin.[31] Characteristic changes with repeated loading include rightward shifting of the load-elongation curve accompanied by permanent elongation, reduced hysteresis, and a decrease in the peak stress for the same applied stretch.[33] These effects occur even when the tissue is allowed to viscoelastically recover between load cycles. The changes lessen with successive load

cycles, eventually achieving a repeatable state, commonly after 3-10 cycles.[97,192,193]

It is commonly accepted that tissues must be preconditioned to obtain repeatable measurements. However, preconditioning may induce non-physiological changes to the tissue. This can be avoided by only using data from the first loading curve[131] but often studies require comparison of subsequent tests (e.g., comparing the effects of loading rates). Preconditioning is most commonly applied for uniaxial[194] and biaxial[36] tension, but has also been applied for indentation,[195,196] aspiration,[197] confined compression, and shear tests.[198] The effects of preconditioning for uniaxial tensile tests[199] are more severe than for biaxial tension tests,[18] with more dramatic shifting of the load-elongation curve and often more loading cycles required to reach a repeatable reference state. Although the need for preconditioning is well accepted, the preconditioning protocols for particular tests are not standardized. Moreover, important details of the protocol are often not reported. For example, the rest periods between each preconditioning cycle needed for viscoelastic recovery are usually either not included nor specified.[18,20,193,194] The number of loading cycles is also often not reported, and can vary significantly from study to study, e.g., 3-9 preconditioning cycles for uniaxial tension testing of skin,[97,192] 5 cycles for bovine cornea,[200] 10 cycles for rabbit[201] and porcine[202] sclera, and 160 cycles for tendons and ligaments.[203]

A number of studies have proposed guidelines for preconditioning. In general, the preconditioning loading protocol should be as similar as possible to the loading protocol applied in the test. This was first proposed for biaxial testing of skin by

Lanir and Fung,[20] where it was observed that specimens to be tested biaxially must also be preconditioned biaxially to obtain repeatable results. Similarly, Carew et al.[204] reported that tissues to be tested by stress relaxation must be preconditioned with repeated stress relaxation tests. It has also been reported that a specimen must be preconditioned to the same strain level as in the test, and if a specimen is preconditioned to a certain strain level and a new strain level is to be tested, a new round of preconditioning is required.[33,105,194] Strain history can also impact preconditioning protocols. Carew et al.[205] applied quasilinear viscoelastic theory to model the preconditioning response and concluded that the preconditioned state was a function of the strain history seen by the tissue. Significant rest periods, on the order of 24 hours, were necessary prior to testing in order to erase the strain history.

Precise knowledge of the preconditioning protocol is important because repeated loading can have a significant effect on the stress response, often leading to a rightward shift of the stress-strain curve and stiffer response in the linear region.[33,200] Preconditioning causes a lengthening of the reference length of the material.[206] However, the stress-strain responses are often plotted with respect to the initial length at the beginning of the first cycle. This is why preconditioning is often described as a softening effect.[33] If the displacements for each load cycle were tared such that the reference length were the length at the beginning of each cycle, the load-unload curves would show a stiffening effect for many cases. This has been observed for bovine cornea.[200]

Despite widespread use, the mechanisms responsible for preconditioning effects are still poorly understood. Some of the reported preconditioning effects may be due to viscoelastic effects, as many preconditioning protocols do not provide a recovery time between loading cycles.[18,20,193,194] This can lead to a conflation of recoverable viscoelastic behavior with nonrecoverable microstructural changes induced by loading. However, even among studies where recovery time was allowed,[33,200,205] mechanical changes and lengthening of the tissue have still been observed. Indeed, viscoelastic theory alone cannot explain the preconditioning response. Graf et al.[207] modeled the viscoelastic relaxation effects of preconditioned tissue and found that preconditioning effects were lessened when recovery time was allowed between cycles but the effect still remained even after 30 minutes. The fact that a portion of the mechanical shift is not recoverable after many hours suggests that some kind of permanent structural change is induced in the tissue by repeated loading.[33] Such structural changes could arise from a permanent rearrangement of fibers with loading. Imaging studies with polarized light microscopy have shown that the collagen fibers align with the loading direction during preconditioning, and that this change in alignment is maintained after the load is removed.[27,208,209] Such non-affine reorganization of the fibers could account for the non-viscoelastic changes seen with preconditioning as well as the stiffening reported in bovine cornea[200] for the linear part of the curve. Finally, damage may occur at the fibrillar level for high applied loads. Preconditioning effects caused by damage have been described as a Mullins effect, where the breaking of collagen

cross-links may account for the observed softening with repeated loading.[210,211] This could also account for nonrecoverable lengthening of the tissue.

The objective of this work is to investigate the preconditioning effects for inflation testing of planar tissues. The term planar tissues here refers to soft tissues in which the extracellular matrix is characterized by a network of long collagen fibers oriented primarily parallel to the tissue surface. We have designed our test to eliminate the three possible mechanisms of preconditioning: we allow a rest period at nominally zero load between cycles to fully recover viscoelastic deformation, we completely fix the specimen boundaries to avoid rearrangement of the long collagen fibers during loading, and we limit the applied loading to physiological limits to avoid tissue damage. It has been previously reported by our lab that pressure-displacement results for bovine sclera,[26] human sclera[54] and human skin[88] do not suffer significant preconditioning effects due to repeated loading. Here we present pressure-strain data from human skin tissue, porcine sclera, bovine cornea, and bovine sclera showing minimal preconditioning effects when subjected to inflation testing. This is in contrast to studies on the same tissues using uniaxial and biaxial loading configurations.[20,192,200,201] We achieved complete recovery of the local pressure-strain response between cycles when comparing both the pressure-strain response for a specific point and the strain contours over larger regions at the maximum pressure of each cycle. This indicated that there was no permanent deformation of the material induced by repeated pressurization. We also illustrate how neglecting to include recovery periods between

each loading cycles can lead to the rightward shift in the strain response commonly attributed to preconditioning. Finally, we show that the deformation response was repeatable even when the specimen was subjected to extended creep and to pressure load-unload cycles at different rates.

6.2 Methods

This section describes the inflation test methods applied to human skin, bovine cornea, porcine sclera, and bovine sclera. These inflation methods have been described in detail in previous publications for bovine sclera,[26] human sclera[54,86], bovine cornea,[25] and human skin,[88] as well as in Chapter 2 of this work for skin tissue. In general, all specimens were cleaned of extraneous tissues and attached to custom plastic holders using cyanoacrylate glue. The specimen and fixture were mounted onto an inflation chamber enclosed by a humidity chamber and subjected to repeated pressurization cycles with rest periods between each load cycle. Samples were imaged with two stereoscopically arranged cameras and displacements were measured using Digital Image Correlation (DIC). Strains were calculated directly from the DIC displacements along two in-plane material directions. These strains were plotted against pressure for the entire test to evaluate the effects of preconditioning. Strain contours are also presented over a larger area of the tissue to evaluate local effects of

preconditioning.

6.2.1 Specimen Preparation

Skin specimens 10 x 10 cm in dimension were obtained from the back torso of male human donors ages 43 - 83 through the National Disease Research Interchange (Philadelphia, PA). Specimens were flash-frozen after procurement and shipped on dry ice. Prior to testing the specimens were thawed in phosphate-buffered saline (PBS) and adipose tissue was removed using fine dissectors.

Bovine eyes from animals 30 months or younger and porcine eyes from 6-9 month old animals were procured from Animal Technologies, Inc. (Tyler, TX). Specimens were received the day after slaughter and stored at 4°C until tested. Internal structures and external fat and muscle were removed from the globe to obtain a clean scleral surface. The more delicate bovine corneas were tested after within 24 hours of delivery, while both bovine and porcine sclera were tested within 72 hours of animal death.

Tissue samples were glued to custom acrylic fixtures (Fig. 6.1). Skin tissue was glued to a fixture with a 7.5 cm circular aperture. Ocular tissue specimens were glued to a smaller fixture at the limbus (Bovine cornea and sclera) or 3 mm posterior to the equator (porcine sclera). To secure the attachment of the specimens to the fixture, the entire perimeter was scored through the thickness with a scalpel, and the scores were impregnated with cyanoacrylate glue. This provided a fully fixed boundary condition

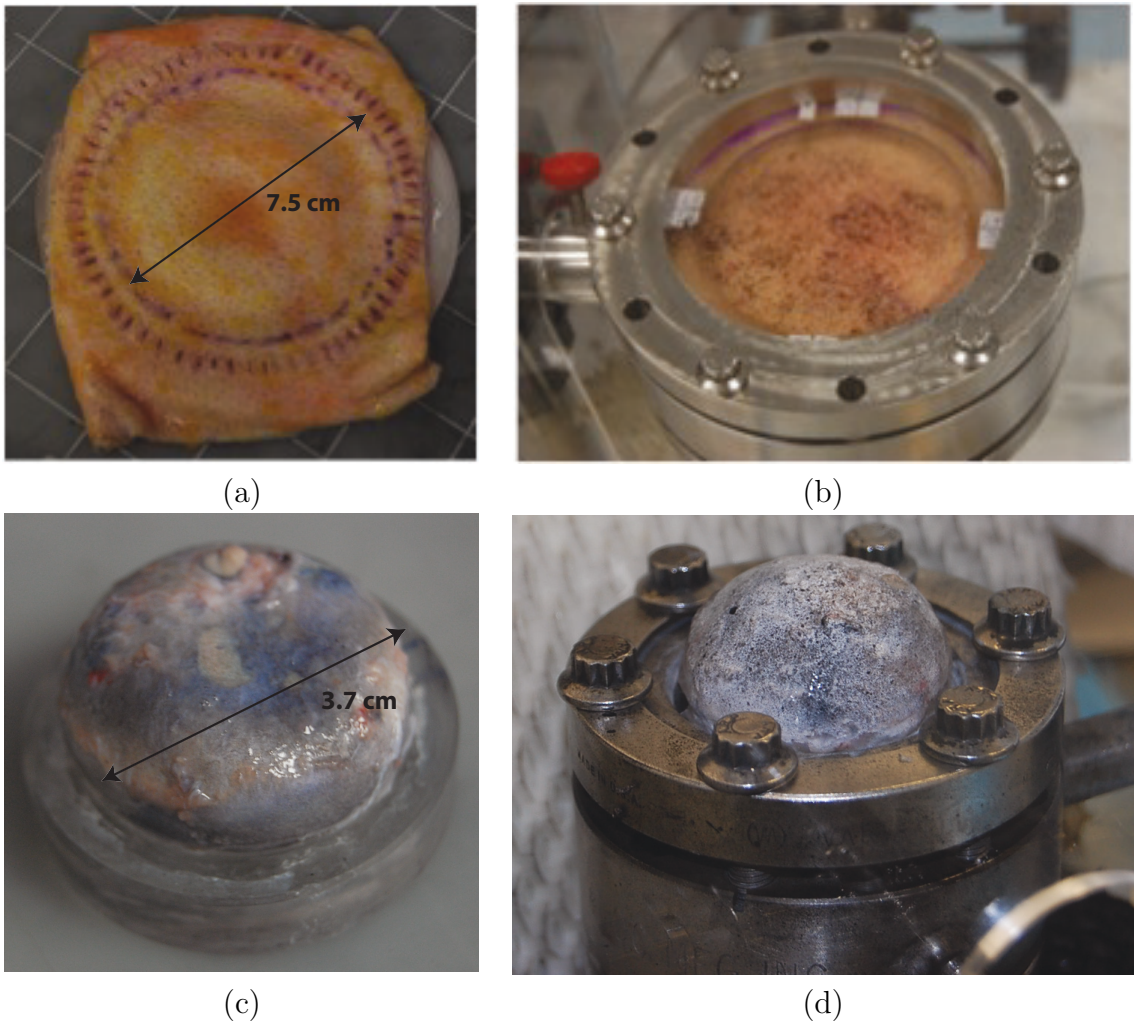

(a) (b)

(c) (d)

Figure 6.1: Tissue, fixture and inflation chamber. (a) Skin specimen glued to the back of the fixture, scored through the thickness at the gluing site, and the scored cuts further filled with glue to create a rigid boundary; (b) skin specimen on inflation chamber; (c) bovine sclera similarly glued to fixture; and (d) bovine sclera on inflation chamber.

through the thickness of the tissue and prevented leakage during inflation testing and excessive shearing at the edge of the deforming specimen.

6.2.2 Loading Protocols

All samples were speckled for digital image correlation with either graphite (skin tissues) or black India Ink (ocular tissues). Specimens were inflated by pressure-controlled injection of PBS controlled by an MTS-driven syringe pump (MTS, Eden Prairie, MN). All tests were performed at room temperature, and all specimens except for the bovine cornea were tested inside a humidity chamber to prevent dehydration. The short duration of the test and the fact that the cornea was hydrated from the bottom by the inflation fluid prevented significant dehydration, confirmed by the repeatability observed between cycles in Section 6.3.2.

Pressure in the inflation chamber was monitored using a TJE pressure transducer (Honeywell, Morristown, NJ) with 2 psig range and $\pm$ 0.002 psig accuracy. The deforming tissue was imaged at a rate of 0.5 Hz by two cameras arranged in stereo with 1/1.8" image sensors (Point Grey, Richmond, BC, Canada) controlled by VicSnap 2010 (Correlated Solutions Inc., Columbia, SC). Displacements were determined by DIC using Vic3D 2010 (Correlated Solutions Inc., Columbia, SC).

Prior to starting the pressure loading protocol, specimens were allowed to relax at a baseline pressure for 15 minutes to ensure an equilibrium reference state. The specimens were then subjected to three load-unload cycles from the baseline pressure

	Human Skin (slow)	Human Skin (fast)	Bovine Cornea	Porcine Sclera	Bovine Sclera
Baseline Pressure [kPa]	0.28	0.28	0.21	0.28	0.21
Maximum Pressure [kPa]	5.52	5.52	6.21	6.00	4.0
Loading Rate [kPa/s]	0.07	0.70	0.06	0.13	0.13
Rest Period [min]	15.0	5.0	15.0	15.0	15.0

Table 6.1: Minimum and maximum pressures, loading rates, and rest times for each type of tissue tested.

to the maximum pressure with 15 minute rest periods at the baseline pressure between each cycle. Slightly different pressures and loading rates were chosen for each tissue type and species, enumerated in Table 6.1. The baseline pressure (0.21 - 0.28 kPa) was chosen to prevent tissue buckling in the reference state. The maximum inflation pressure for skin (5.52 kPa) was large enough to probe the full toe-linear stress response of the tissue, while the maximum inflation pressure for the ocular tissues (4.0 - 6.0 kPa) corresponded to pathologically relevant elevated intraocular pressures. The slow loading rates (0.06 - 0.13 kPa/s) were chosen to measure the quasi-static response of the tissue. Skin specimens were also tested at a tenfold higher loading rate (0.70 kPa/s) to examine if changing the loading rate for the same specimens would affect the preconditioning response. Finally, the recovery time was selected based on preliminary experiments indicating that complete strain recovery of the tissue was obtained within 15 minutes for the slow loading rates (0.6 - 0.13 kPa/s) and within 5 minutes for the faster loading rate applied to skin (0.70 kPa/s).

In a separate set of experiments, the skin specimens were also subjected to five preconditioning cycles without recovery periods to demonstrate the effects of vis-

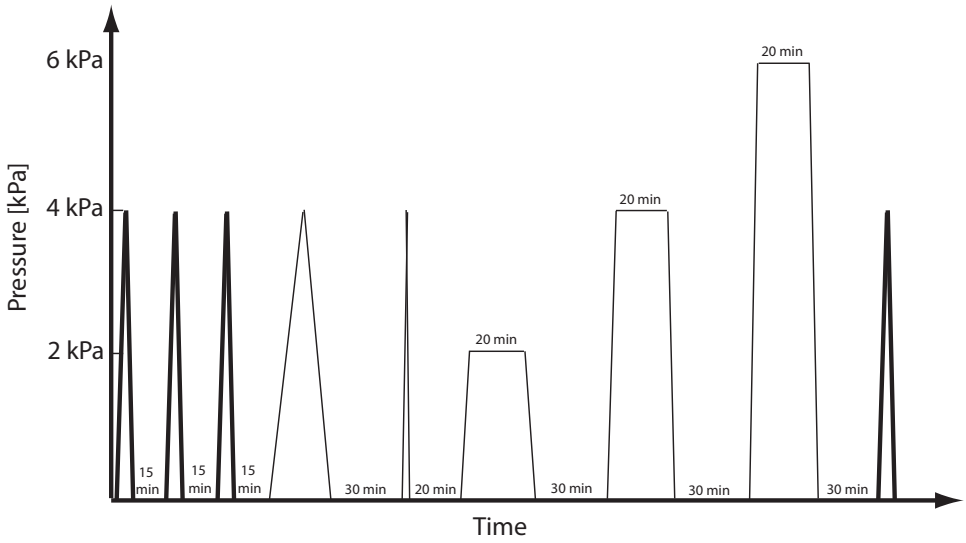

Figure 6.2: Schematic of additional loading regime for bovine sclera. After the three preconditioning cycles prescribed in Table 6.1, two additional load cycles and three creep tests were preformed prior to a final load-unload cycle identical to the first. [*Figure created by Baptiste Coudrillier*].

coelasticity on the deformation response. We also present test results for the bovine sclera[26] where the tissue was subjected to 4 hours of additional testing after the initial preconditioning cycles (Fig. 6.2). Specifically, after preconditioning the tissue was subjected to two additional load-unload cycles at 0.7 kPa/s and 0.007 kPa/s with 20 and 30 minute recovery periods, respectively, and three 20 minute creep tests at 2.0 kPa, 4.0 kPa, and 6.0 kPa, each followed by 30 minute recovery periods. Finally, the tissue was subjected to a single load-unload test identical to the first preconditioning cycle to compare to the three initial cycles.

6.2.3 Strain Calculations

The effects of preconditioning are typically reported for the stress-strain response,

but the stress calculation for the inflation specimens is non-trivial, particularly for the thick skin specimens where bending cannot be neglected.[89] Similarly, the presence of the compliant optic nerve head creates a stress concentration in the sclera. Instead, the pressure-strain response was plotted for all specimens tested. Strains were calculated directly from the displacement components of a smoothed DIC displacement field along two material directions. Additionally, strain contours over a larger portion of the surface of the tissue were computed to compare preconditioning effects at different locations.

6.2.3.1 Skin Tissue Strain Calculations

The method of strain calculation for skin specimens has been previously reported.[88] Briefly, specimens were positioned so that the X-coordinate was aligned with the horizontal axis of the body, the Y-coordinate was aligned with the vertical axis, and the Z-coordinate was the out-of-plane direction. The components of the displacement field U, V, and W along the X-, Y-, and Z- directions were extracted at 0.570 mm intervals and then interpolated over a grid of 0.25 mm spacing.

The inflation of a planar anisotropic tissue such as skin results in an ellipsoidal bulge. The stiffest in-plane direction of the tissue (the fiber direction) and the least stiff in-plane direction (the perpendicular direction) were identified from the ellipsoidal shape of the inflated tissue. The displacement field was rotated to obtain the displacement components U' along the fiber direction X' and V' along the perpendicular direction Y'. The out-of-plane displacement component W was unchanged.

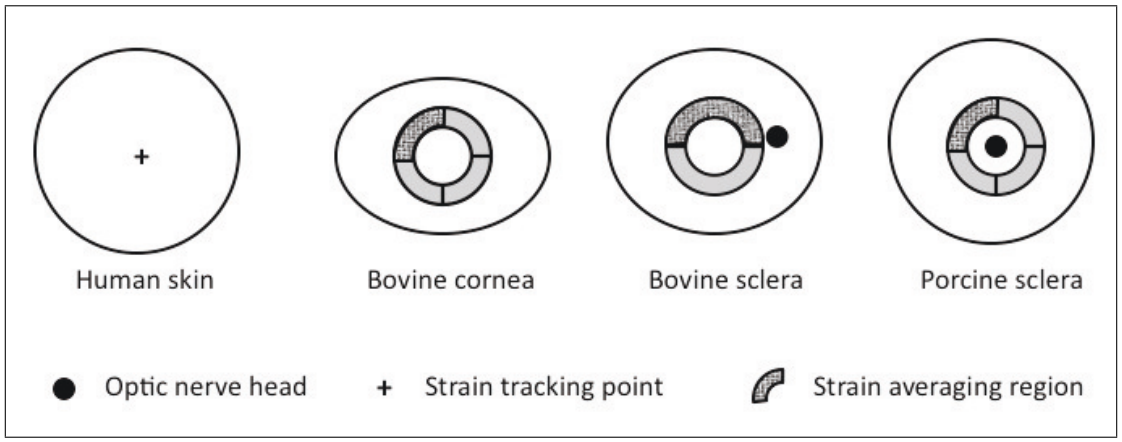

Figure 6.3: Schematic of top view of specimens, showing points or regions where strains were reported. Strains were reported for a single point at the apex for human skin tissue. Average strains over a region were reported for ocular tissue to minimize the effects of noise. Strain contours are also reported over the entire surface for skin tissues and all quadrants for ocular tissues. [*Figure created by Barbara J. Murienne*].

Lagrange strains along both the fiber direction and the in-plane perpendicular direction were computed by eq. (6.1):

$$E_f = E_{X'X'} = \frac{\partial U'}{\partial X'} + \frac{1}{2}\left[\left(\frac{\partial U'}{\partial X'}\right)^2 + \left(\frac{\partial V'}{\partial X'}\right)^2 + \left(\frac{\partial W}{\partial X'}\right)^2\right], \tag{6.1}$$

$$E_p = E_{Y'Y'} = \frac{\partial V'}{\partial Y'} + \frac{1}{2}\left[\left(\frac{\partial U'}{\partial Y'}\right)^2 + \left(\frac{\partial V'}{\partial Y'}\right)^2 + \left(\frac{\partial W}{\partial Y'}\right)^2\right].$$

The displacement gradients were calculated by fitting the displacements along the X' or Y' axis to a 9^{th} order polynomial and differentiating analytically.

Strains in both directions were plotted against pressure at a single point at the apex of the inflated tissue (Fig. 6.3). Strain contours in both the fiber and perpen-

dicular directions were also computed over the entire specimen.

6.2.3.2 Ocular Tissue Strain Calculations

The strain calculation methods for the bovine corneal and scleral tissues have been previously described.[54,86] Similar methods were used for the porcine sclera. Briefly, the DIC measured displacements were interpolated onto a reference grid based on the initial geometry of the tissue. For the bovine cornea and sclera, we constructed a 2D polar reference grid centered on the specimen apex, and interpolated the vertical positions and the three components of the displacement to points on the grid. The vertical positions were used to transform the polar grid into a 3D grid. For the porcine sclera, which is quite smooth and almost spherical in young pig eyes, we defined a 3D spherical grid based on a spherical fit of the reference configuration. The DIC measured displacements were interpolated to the points of the spherical grid.

For all ocular tissues, stretches in the circumferential, λ_θ, and meridional directions, λ_φ, were calculated as:

$$\begin{aligned} \lambda_\theta &= \frac{l_\theta}{L_\theta}, \\ \lambda_\varphi &= \frac{l_\varphi}{L_\varphi}, \end{aligned} \tag{6.2}$$

where l_θ and L_θ are the deformed and undeformed lengths calculated between two adjacent grid points in the circumferential direction and l_φ and L_φ are the deformed and undeformed lengths calculated between two adjacent grid points in the meridional

direction. The Lagrangian strains in each direction, $E_{\theta\theta}$ and $E_{\varphi\varphi}$, were calculated from the stretches as follows:

$$\begin{aligned} E_{\theta\theta} &= \frac{1}{2}(\lambda_\theta^2 - 1), \\ E_{\varphi\varphi} &= \frac{1}{2}(\lambda_\varphi^2 - 1). \end{aligned} \tag{6.3}$$

For the sclera, surface features such as blood vessels can lead to significant variability in local strain measurements. To mitigate the effect of local strain variability, ocular strains were averaged over small regions (Fig. 6.3). The exact area of the averaging region varied slightly due to the different shapes and sizes of the tissue types and species and to avoid anatomical structures such as the optic nerve head (ONH). For the bovine cornea and sclera, averaging was performed over quadrants and half-circles, respectively. A larger averaging region was used for the bovine sclera as features inherent to the tissue, in particular its blue coloration and apparent vessels, contributed to a locally elevated level of noise. The bovine cornea quadrant was 4 mm wide and located 4 mm from the apex, while the bovine sclera half-circle was 5 mm wide and located 1 mm from the apex (Fig. 6.3). For the porcine sclera, strains were averaged over a quadrant 2.34 mm wide and located 2 mm away from the ONH. These average strains were plotted against pressure to assess the effects of the preconditioning cycles on the mechanical response. Strain contours were also plotted for the entire circular region at the maximum pressure of the first and final

load cycle to assess local changes between cycles over a larger area. Strain contours were plotted for an annulus of data to avoid the optic nerve head (for scleral tissue) and because the radial grid used to calculate strains leads to an infinitely dense grid at the center of the specimen (for cornea).

6.3 Results

The result for three representative skin specimens and three representative ocular tissues (one bovine cornea, one porcine sclera, one bovine sclera) are presented in this work. We present pressure-strain data at a single point (skin) or averaged over a small region (ocular tissues) for two in-plane material directions (fiber and perpendicular for skin, meridional and circumferential for ocular tissues). We also present strain contours over a larger region of the tissue for comparison between the first and last preconditioning cycle.

6.3.1 Human Skin

The three human skin specimens tested are identified by (Sex/Age). Figure 6.4 plots the pressure-strain response in both the fiber and perpendicular directions for two specimens at the slow 0.070 kPa/s loading rate with 15 minute recovery time. Figure 6.5 plots pressure-strain response for the same two specimens for the fast 0.70 kPa/s loading rate with 5 minute recovery time. The differences in the maximum

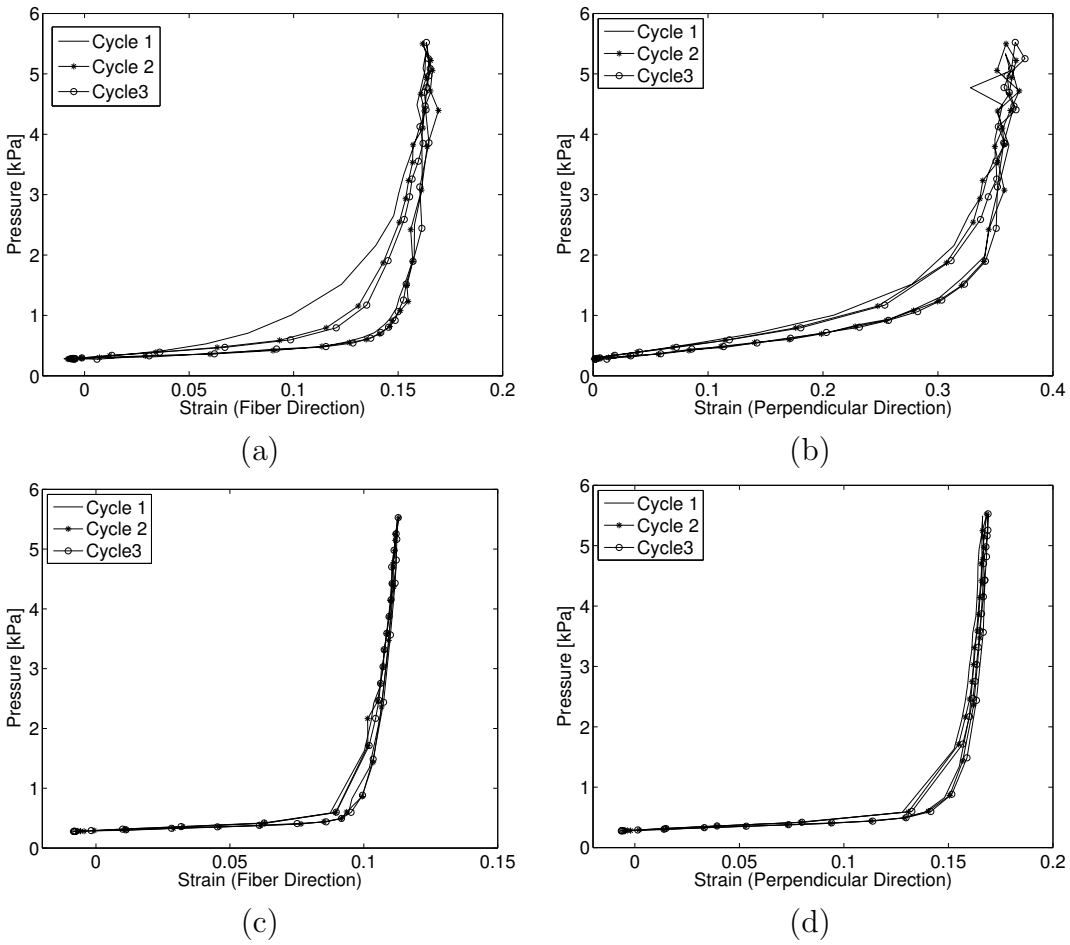

Figure 6.4: Pressure-strain response for two human skin specimens tested at a slower rate of 0.07 kPa/s with 15 minute recovery periods: (a) M/43 - fiber direction, (b) M/43 - perpendicular direction, (c) M/61 - fiber direction, (d) M/61 - perpendicular direction.

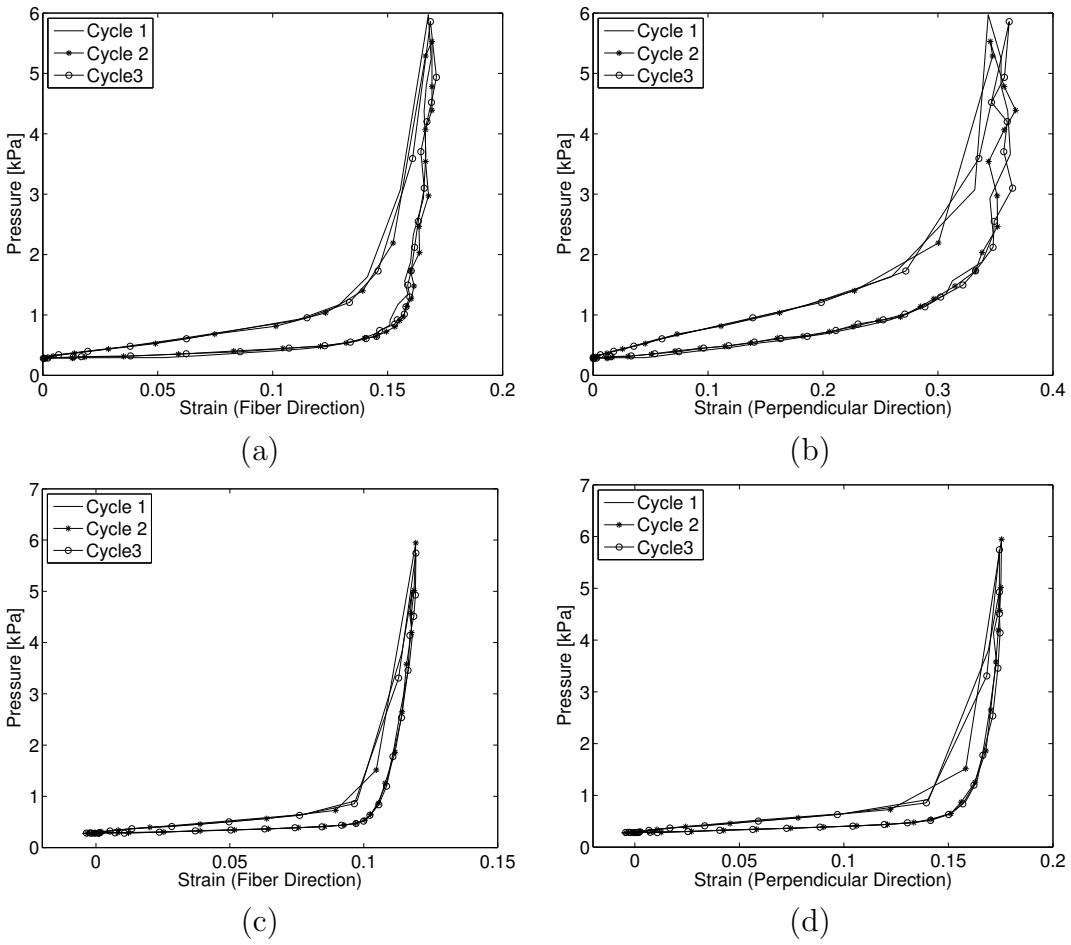

Figure 6.5: Pressure-strain response for two human skin specimens tested at ten-fold faster loading rate of 0.70 kPa/s with 5 minute recovery periods: (a) M/43 - fiber direction, (b) M/43 - perpendicular direction, (c) M/61 - fiber direction, (d) M/61 - perpendicular direction.

strain between each subsequent cycle were small, less than 2% of the total applied strain for 14 of the 16 comparisons, and random. Both positive and negative differences were calculated between successive cycles. The differences between cycles as a percent of the total strain for all samples and strain rates are listed in Table 6.2. Some of this small variability in strains could be attributed to the accuracy of the DIC displacement measurement and of the pressure transducer. We have also previously

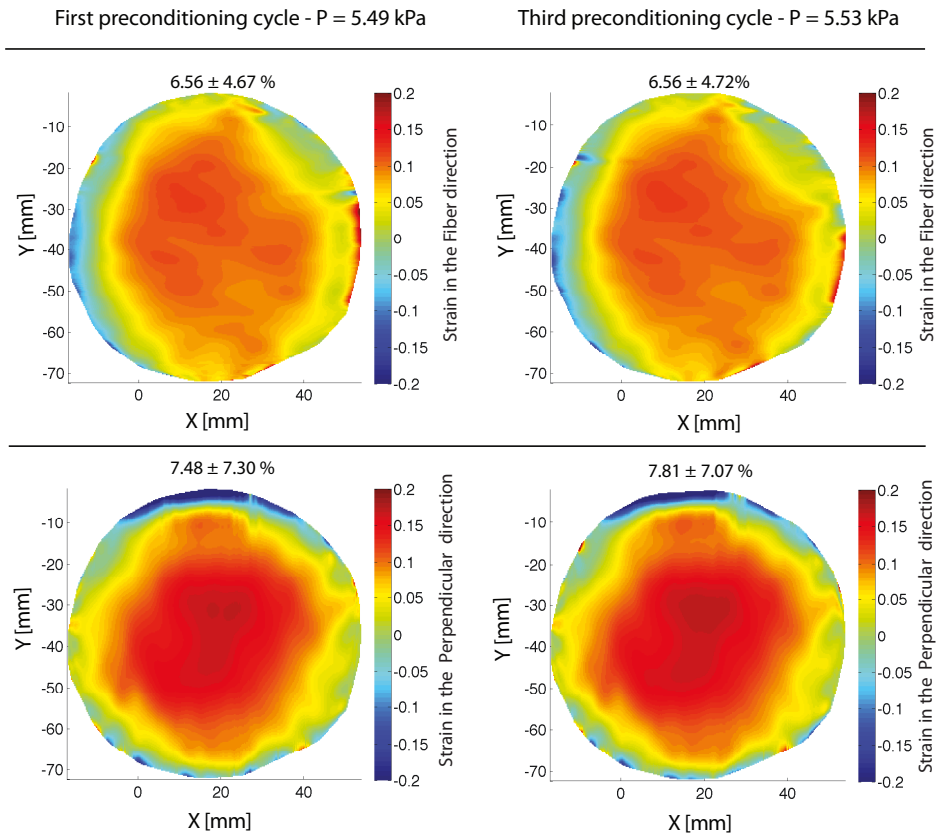

Figure 6.6: Contours of the strain in the fiber and perpendicular directions at the maximum pressure of the first and final cycle for the (M/61) specimen tested at the slower 0.07 kPa/s loading rate with 15 minute recovery periods. The mean and standard deviation of the strains across the entire contour are reported above each figure.

reported that strains calculated at a single point for human skin tissue can vary by up to 1.6% strain over a range of ± 1 mm of the apex.[88]

Complete strain recovery was achieved during each cycle for both the (M/43) and (M/61) specimens. A slight decrease in hysteresis was noted between the first and second load cycle for the perpendicular direction for the (M/43) sample only. Figure 6.6 shows a contour plot of the strains in both the fiber and perpendiculars directions for the (M/61) specimen comparing the maximum pressure of the first

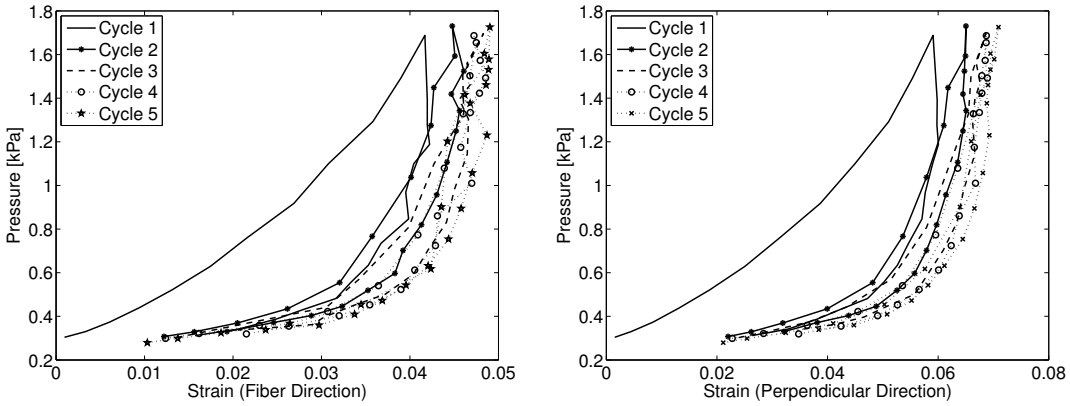

Figure 6.7: Pressure-strain response for a skin specimen (M/83) subjected to pressure cycles at 0.07 kPa/s without intervening recovery periods, measured for the fiber and perpendicular directions.

		0.07 kPa/s		0.70 kPa/s	
Specimen	Compared Cycles	Fiber	Perpendicular	Fiber	Perpendicular
M/43	Cycle 1 and Cycle 2	-0.92%	0.17%	0.95%	0.49%
	Cycle 2 and Cycle 3	1.11%	2.23%	-0.41%	4.80%
M/61	Cycle 1 and Cycle 2	0.53%	1.20%	0.00%	0.46%
	Cycle 2 and Cycle 3	-0.27%	0.36%	0.08%	-0.57%

Table 6.2: Difference in maximum strain between adjacent cycles as a percentage of the total strain for all human skin data plotted in Figures 6.4 and 6.5.

and third cycle at 0.07 kPa/s. The strain contours are nearly identical between the two cycles. Finally, Fig. 6.7 plots the pressure-strain response for a third specimen (M/83) subjected to five successive load-unload cycles not separated by a recovery period. The resulting dramatic rightward shift of the strain response compared to the results in Fig. 6.4 was caused by viscoelastic effects.

6.3.2 Bovine Cornea

Figure 6.8 (a) plots the pressure-strain response for both the meridional and circumferential directions for the bovine cornea. Reflections from the shiny wet surface of the bovine cornea affected the quality of the images and the DIC correlation, contributing to the noise in the pressure-strain curves. However, negligible differences in the loading and unloading curves were observed between the three cycles. In addition, full recovery was achieved upon unloading. The differences in the peak strains between each cycles were small: the percent differences in the meridional and circumferential strains between the first and second cycle were 0.7 % and 1.0 % of the strains at the maximum pressure, and the percent differences in the meridional and circumferential strains between the second and third cycle were 0.3 % and 1.0 % of the strains at the maximum pressure. These differences are negligible compared to those obtained by Boyce et al.[200] for uniaxial tension tests of the bovine cornea., where the difference in the peak strains before and after preconditioning was 47% of the total applied strain (Fig. 6.11). This large preconditioning effect was obtained

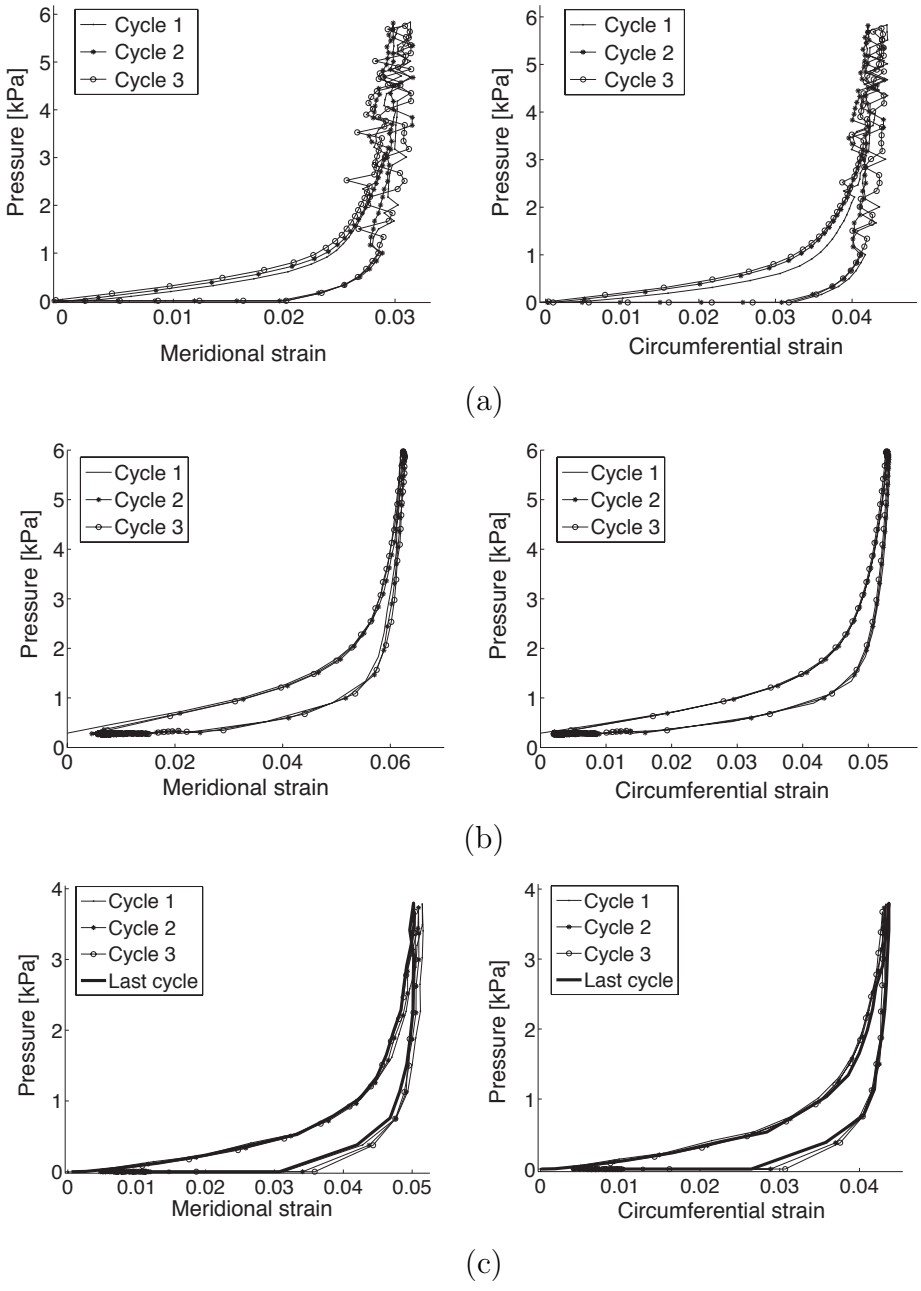

Figure 6.8: Pressure-strain response computed over an averaged region in the meridional and circumferential directions for three successive cycles for (a) bovine cornea, (b) porcine sclera, and (c) bovine sclera. The bovine sclera plot in (c) included a final cycle after four hours of additional testing including two creep tests and a slow load-unload test. [*Data collected by Baptiste Coudrillier, Barbara J. Murienne, and Stephen Alexander*].

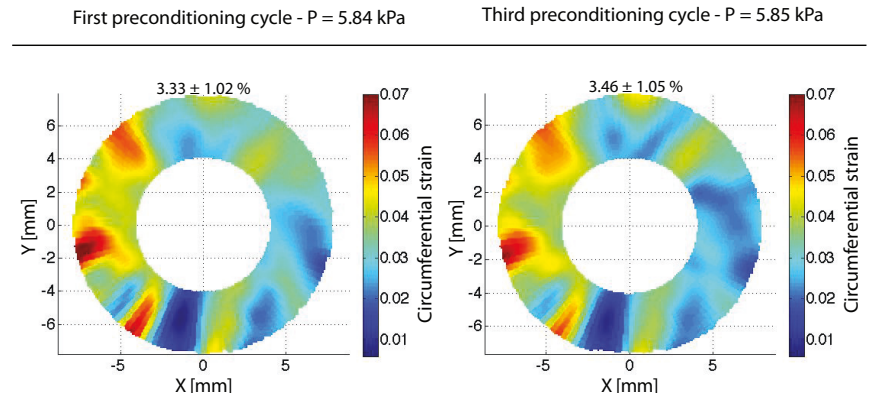

(a)

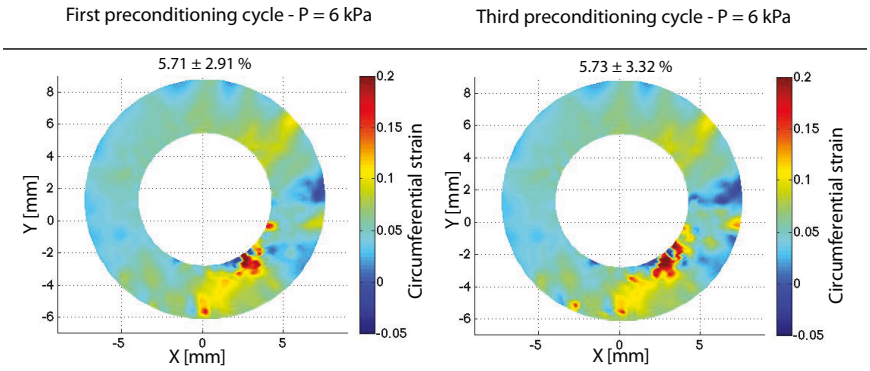

(b)

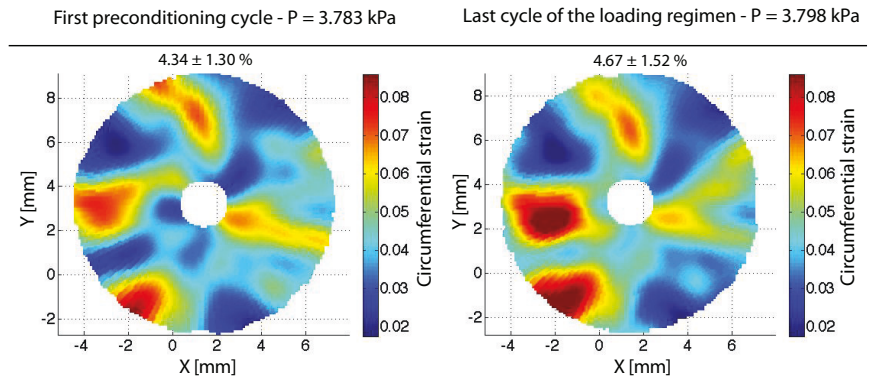

(c)

Figure 6.9: Contour plots of the circumferential strains at the maximum pressure of the first and final pressure cycles for (a) bovine cornea, (b) porcine sclera, and (c) bovine sclera. The bovine sclera plot in (c) included a final cycle after four hours of additional testing including two creep tests and a slow load-unload test. The mean and standard deviation of the strains across the entire contour are reported above each figure. [*Data collected by Baptiste Coudrillier, Barbara J. Murienne, and Stephen Alexander*].

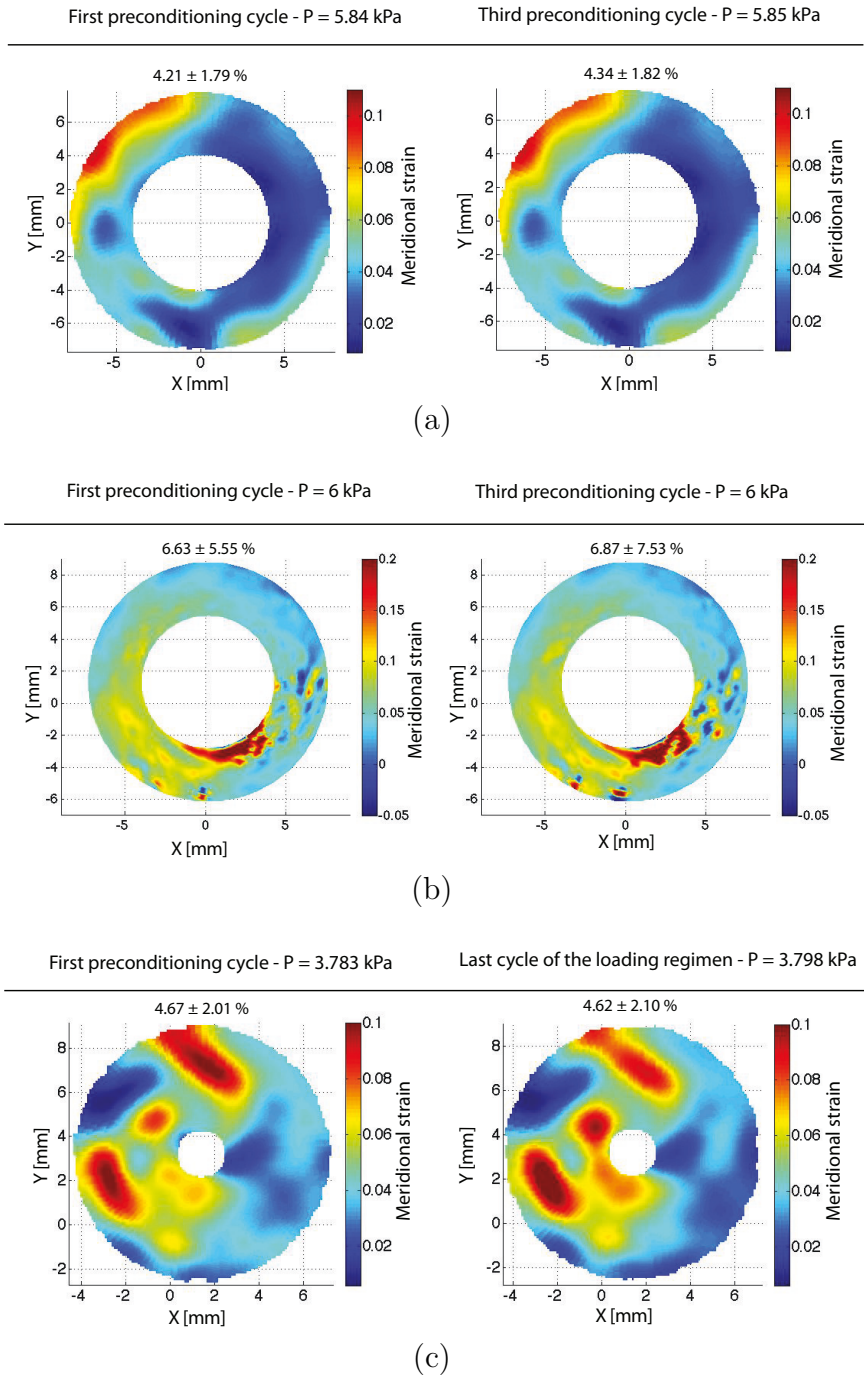

Figure 6.10: Contour plots of the meridional strains at the maximum pressure of the first and final pressure cycles for (a) bovine cornea, (b) porcine sclera, and (c) bovine sclera. The bovine sclera plot in (c) included a final cycle after four hours of additional testing including two creep tests and a slow load-unload test. The mean and standard deviation of the strains across the entire contour are reported above each figure. [*Data collected by Baptiste Coudrillier, Barbara J. Murienne, and Stephen Alexander*].

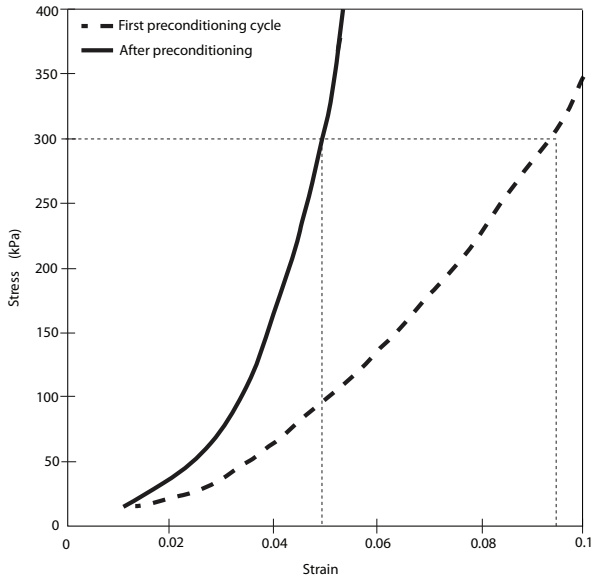

Figure 6.11: Uniaxial stress-strain curves measured for bovine cornea comparing the response from the loading portion of the first pressure cycle (–) of the preconditioning protocol and from the loading portion of a pressure cycle after preconditioning (-). Results show a large stiffening effect associated with preconditioning. The specimen was allowed to rest at the baseline pressure for an extended period of time after the preconditioning. [*Adapted from Fig. 7 of Boyce et al.*[200] *by Baptiste Coudrillier.*]

even though the specimen was allowed to recover for an extended period of time at baseline at the end of the preconditioning protocol.

Figure 6.9 (a) shows the contours of the circumferential strain at the maximum pressure of the first load and the final load for a 4 mm wide annulus located 4 mm from the apex. While the majority of the plotted area shows good agreement, we observed a slight stiffening between the first and the third cycles that was likely caused by a loss of hydration during the time of testing. Previous studies by Boyce et al. [25, Fig. 10] showed that when a proper humidity level was maintained during inflation testing, the pressure-displacement response was nearly identical between each loading cycle. The meridional strain contours, plotted in Figure 6.10(a), showed the same trend.

6.3.3 Porcine Sclera

Figure 6.8 (b) plots the pressure-strain relationship in both the meridional and circumferential directions for three preconditioning cycles for the porcine sclera. As reported for the bovine cornea, little difference was observed in the loading or unloading curves between the cycles. Moreover, both strain directions exhibited complete recovery within experimental error. The differences in peak strains between loading cycles were random and small: the percent differences in the meridional and circumferential strain between the first and second cycles were 0.80% and -0.38% of the strains at the maximum pressure, and the percent differences between the second and third cycle were -0.16% and -0.19% of the strains at the maximum pressure.

Figure 6.9 (b) shows the contours of the circumferential strain at both the maximum pressure of the first load and the final load for a 2.34 mm wide annulus located 2 mm away from the apex. Strain contours at the maximum pressure were similar between the first and final cycle of the loading regimen, demonstrating repeatability of the surface strain field. The meridional strain contours, plotted in Figure 6.10(b) , supported the same conclusions.

6.3.4 Bovine Sclera

Figure 6.8 (c) plots the pressure-strain relationship in both the meridional and circumferential directions for the first three preconditioning cycles and the final load-

unload cycle of the bovine sclera loading protocol after 4 hours of testing (Fig. 6.2). No significant softening/stiffening effect or change in the hysteresis was observed and the final load cycle was nearly identical to the first load-unload cycle. The differences in peak strains between cycles were small: the percent differences in the meridional and circumferential strains between the first and second cycle were -0.23% and -1.15% of the strains at the maximum pressure, and the percent differences in the meridional and circumferential strains between the second and third cycle were -0.69% and -0.98% of the strains at the maximum pressure. The percent difference in the meridional and circumferential strains between the first and final cycle after 4 hours of additional testing were 1.83% and -2.35% of the strains at the maximum pressure. This demonstrates that the pressure-strain response was repeatable after 4 hours of testing, during which load-unload cycles at 2 different pressure rates and ramp-hold tests at 3 different pressures were performed. The specimens exhibit complete recovery after each load cycle.

Figure 6.9 (c) shows the circumferential strain contours at the maximum pressure of the first and final loading cycle over a 5 mm wide annulus located 1 mm from the apex. Strain contours at the maximum pressure were similar between the first cycle and final cycle of the loading regimen, demonstrating repeatability of the surface strain field. The meridional strain contours, plotted in Figure 6.10(c), supported the same conclusions. The difference in the local value of the strain could be large in some areas, particularly in the lower left quadrant of Fig. 6.9 (b). This is probably due to

a degradation of the speckling pattern caused by the high humidity level maintained during the time of testing, or the presence of anatomic features such as veins.

6.4 Discussion

We have shown that the mechanical response of bovine cornea, porcine sclera, bovine sclera, and human skin tissue measured by inflation tests exhibited minimal preconditioning effects compared to the mechanical response of the same tissues measured by uniaxial and biaxial tests.[20,192,200,201] Nearly the same peak strain was achieved for each load cycle, no shifting was seen between load cycles, and the specimens achieved complete strain recovery. The differences observed in the peak strain between loading cycles for all tissue specimens were small, less than 2% of the total strain for all but 3 of the 26 loading cycles, and were random. Both positive and negative differences in the peak strain were calculated between successive cycles and the differences did not in general evolve systematically with the number of cycles. The small differences measured in the inflation response were substantially lower than the 47% difference generated by the preconditioning protocol for uniaxial tension testing of bovine cornea as reported by Boyce et al.[200] The small variations observed can be attributed to experimental and numerical noise, particularly for the skin strain data which was calculated at a single point and has been reported to vary by up to 1.6 % over a range of $\pm$ 1 mm.[88] Variability could also have arisen from experimental

conditions such as loss of hydration, particularly for the bovine cornea which was not tested inside a humidity chamber and was only hydrated by the inflation fluid. These results were not found to depend on loading rate or loading history. Moreover, strain contours calculated at the maximum pressure for the first and last load cycles showed that repeatability was achieved not just at one point or on average over a region, but over larger areas of the specimen surface. The repeatable results were obtained for loading regimens that included a rest period between each loading cycle to achieve complete viscoelastic strain recovery. We further illustrated that if the recovery periods were not allowed, the viscoelastic response of the tissue produced the characteristic rightward shift of the pressure-strain response commonly attributed to preconditioning. Previous inflation testing of bovine cornea[25] and mouse carotid artery by Ning et al.[155] also showed only small differences in the pressure-displacement response after repeated loading. The latter subjected the mouse carotid artery to four pressure cycles.

Preconditioning protocols are commonly used to obtain a repeatable mechanical response in uniaxial and biaxial strip tests but can be time-consuming and restrictive. The preconditioning effects are often sensitive to many factors, including strain rate, strain levels, strain history, and the applied strain state;[20,194,205] thus achieving repeatable results for a particular loading regimen requires custom preconditioning protocols and multiple rounds of preconditioning to measure the mechanical response to different strain rates and strain states. The observation that preconditioning effects

arise from load-induced changes in the tissue fiber structure[27,33] indicates that the mechanical properties measured may not be representative of the native tissue. Some authors avoid the preconditioning effects by only using data from the first loading curve,[131] but this is not feasible if multiple tests need to be carried out on the same tissue. Other authors model the structural change of preconditioning as an unrecoverable deformation[206] in order to back out *in vivo* properties; however this can be computationally intensive and inefficient. If the effects of preconditioning could be avoided all together, testing procedures and analysis could be greatly simplified.

We propose that our inflation test protocol produces negligible load-induced changes to the deformation response because it avoids three possible mechanisms associated with preconditioning: viscoelastic effects, fiber re-arrangement with loading, and microstructural damage to the tissue. The inclusion of recovery periods after each load-unload cycle to allow complete recovery of the specimens eliminates viscoelastic memory effects. If these recovery periods are not included, the tissue will viscoelastically lengthen to produce the commonly observed rightward shift of the load-elongation curves. We demonstrated the effect of viscoelasticity here for cyclic loading of skin tissue. This is in contrast to previous works on uniaxial tests[33,205,207] where even though recovery periods are allowed, shifting is still observed as the gage length of the tissue progressively increases with loading cycles.[206] These results suggest that there is a permanent change induced in the tissue by cyclic uniaxial loading that is not encountered in our inflation testing protocol.

We speculate that the permanent deformation incurred during preconditioning is caused either by a reorientation of fibers along the loading direction or damage to the fibers and matrix constituents of the extracellular matrix of the tissue (e.g., the breaking of collagen crosslinks). Optical studies by Tower et al.[27] and Quinn and Winkelstein[209] of a tissue stimulant under uniaxial loading showed that the fibers reoriented along the loading direction with repeated cycles, eventually reaching an equilibrium "preconditioned" state. Moreover, the changes to the fiber structure persisted after the load was removed. For the inflation tests, the specimen boundary is fully glued to the holder, and this likely limits the reorientation of the long collagen fibers during testing. Furthermore, the applied pressure is limited to a physiological range to prevent damage to the tissue structure. Our results suggest that mechanical tests of soft tissues can be designed to limit the effects of preconditioning, and it is likely that other tests could be devised based on the same principles to avoid evolving mechanical behavior with loading. Further testing is required to confirm if these results can be general for inflation testing of other planar tissues characterized by long fibers oriented parallel to the surface of the tissue.

The results presented in this paper were obtained using our previously published implementations of 3D-DIC.[54,86,88] Digital image correlation has become widely used to measure displacements and strains of soft tissues and a number of authors have calculated the accuracy and resolution of 3D-DIC displacements[212–216] and strains[215,217,218] using methods similar to those described here. For example, Sutton et al.[217] reported

a standard deviation of 0.03-0.08% strain for a 3D translation of a cylinder. However, more work is needed to measure and validate the resolution of 3D-DIC strain measurements in tissues. This is not critical for the conclusions drawn in our present study because they are dependent on strain comparisons rather than absolute values of strains. We observed repeatable strain measurements between cycles for both skin and ocular tissues, despite the fact that strains levels for skin were up to 10 times higher than for ocular tissues. Moreover, we obtained cycle-to-cycle repeatability for a wide range of pressure levels and strain rates. Any preconditioning-associated shift that was too small to be resolved by our system would still be negligible compared to the shifts observed for uniaxial and biaxial tests. The consistency of the conclusions between tissue type, species, and strain rate indicates that our results are insensitive to resolution limitations.

Our conclusions are tempered by several limitations. We have thus far demonstrated these effects for a limited number of tissues. All tissues tested in this work have in common a 2D in-plane network of long fibers; fully fixing the boundaries may not have the same effect for tissues comprised of shorter or out-of-plane fibers such as cardiac tissue. Poroelastic issues such as cartilage may also have a different response than tissues dominated by a viscoelastic ECM network. DIC displacement uncertainty and numerical differentiation of the displacements contribute to uncertainty in the strain calculation. To avoid noisy pressure-strain curves for ocular tissues, we averaged the strain over a small region instead of plotting point-wise strain as we

did for skin tissues. However, strains computed at a single point still do not show preconditioning, only a higher level of noise. We also did not carry out any imaging studies to confirm the lack of fiber rearrangement or damage to the tissue after repeated loading, leaving this for future studies.

6.5 Conclusions

We have shown that the inflation responses of bovine cornea, porcine sclera, bovine sclera, and human skin exhibit negligible preconditioning effects compared to those observed for the same tissues in uniaxial and biaxial tension tests.[20,192,200,201] These results suggest that preconditioning effects can be avoided for certain tissues by experimental design. The inflation test methods presented minimized the effects of preconditioning by (I) allowing adequate recovery time between cycles, (II) fully fixing the boundary of the tissue to prevent fiber rearrangements, and (III) limiting the applied loading to physiological levels to prevent microstructural damage to the tissue. These results are likely limited to planar tissues with long fibers parallel to the tissue surface, but may be extended to planar tissues other than those tested here to allow for more accurate, repeatable measurements of mechanical properties. The findings of this work may help to guide the design of other experimental systems to minimize the effect of preconditioning on the mechanical response of soft tissues.

Chapter 7

Conclusions and Future Work

This work developed a hierarchical modeling approach capable of describing both the bulk material properties of skin tissue as well as the fiber-level mechanisms of growth and remodeling. Human skin tissue experiments and finite element analysis were used to identify the most appropriate constitutive model to link tissue anisotropy to the fiber structure, while also illustrating that the generalized structure tensor model could not capture the experimentally measured anisotropy of skin tissues. The resulting tissue model was extended to incorporate fiber-level deformations, enabling evolution equations for the strain-protected enzymatic degradation of collagen. The model was used to illustrate that strain-protected enzymatic degradation and collagen deposition can lead to strain homeostasis, suggesting that selective degradation and deposition are potential mechanisms of the growth and remodeling process.

7.1 Summary of Findings

Chapter 2 developed a inflation (bulge) test for human skin tissues. There is limited experimental data available for the anisotropic, large-strain response of human skin tissue, with most skin tissue models calibrated to rat or porcine tissue. Most human skin testing has been carried out using uniaxial testing, which exhibits an evolving material response with preconditioning. As illustrated in Chapter 6, skin and ocular tissues tested by the inflation test did not exhibit a significant preconditioning response, defined as an evolving mechanical response to repeated loading. Though the inflation test has been applied to thin membranes such as the pericardium, it is not commonly applied to skin tissue, partially because the thick tissue precludes traditional stress analysis. Three-dimensional digital image correlation was used to identify the dominant fiber direction of the tissue, which agreed with what is known in the literature.[16] Instead of computing membrane stresses, stress resultants were computed for both the fiber and perpendicular direction of the tissue specimens, taking into account bending effects. From the stretch-stress resultant relationships, it was shown that skin tissues tested by the inflation test were insensitive to preconditioning and ambient humidity. A limited number of samples were tested, and large specimen-to-specimen variation was observed between donors. However, general trends observed for the specimens, such as increased stiffness and isotropy with age, were similar to what has been measured for skin tissue by other authors[141,219] and are consistent with the known effect of increased tissue cross-linking with age.[142]

Traditional stress analysis for the inflation test neglects bending, as the test is more commonly applied to thin materials.[116,117] Chapter 3 developed a new analytical method to fit a stress-stretch constitutive law to the stress resultant-stretch relationships measured for human skin tissue while accounting for bending stresses. This is a key contribution of this work and could be applied to extend the utility of the inflation test to other thick tissues. The analysis method was used to fit the parameters of two different structurally-based constitutive models to the nonlinear anisotropic response of skin tissue measured by the inflation test. Finite element analysis was used both to support the analysis method and to illustrate that only the more rigorous, fully-integrated distributed fiber model was capable of describing the experimentally measured anisotropy of the skin tissue. The model parameters quantified the observations of the previous chapter, namely that stiffness and isotropy increased with age, while also suggesting that the variation between specimens arises from the collagen fibers rather than the ground matrix. In contrast, the more computationally efficient generalized structure tensor model greatly underestimated the tissue anisotropy. It is hypothesized that the generalized structure tensor model under-predicted tissue anisotropy because the pre-integration of the fiber distribution does not capture the large fiber rotations caused by the inflation test.

Chapter 4 extends these results to incorporate potential fiber-level mechanisms of the growth and remodeling process. Though growth and remodeling is well documented experimentally, the underlying mechanisms are not well understood. The

fully-integrated distributed fiber model was used to describe the organization of collagen fibers, but instead of describing the fibers phenomenologically, fibers were described as planar sinusoidal elastica beams following Comninou and Yannas.[45] This enabled the prescription of evolution equations for the fiber radius that were dependent on the micro-stretch of the fiber. The degradation model captured the rapid decrease in degradation rate with applied strain and was calibrated to degradation experiments on isolated bovine scleral fibrils reported by Flynn et al.[80] The model demonstrated predictive power by simulating the normalized creep rates between force levels for tissue-level bovine cornea and pericardium experiments[83,183] based on the fibril-calibrated parameters, in spite of significant morphological differences between these tissues. The degradation model was paired with constant collagen deposition to illustrate that these two mechanisms alone can give rise to strain homeostasis in response to a pressure perturbation, supporting degradation and damage as potential mechanisms of the growth and remodeling process.

7.2 Key Contributions

This work included three key contributions to the field of soft tissue biomechanics:

(1) The development of an inflation test and analysis method to measure anisotropic material properties for human skin tissues while accounting for bending. The inflation test has the advantages of a relatively simple set-up

and minimal preconditioning effects, but bending effects have often precluded the use of the inflation test for thick tissues. Inverse finite element analysis can be used to fit constitutive model parameters while accounting for bending, but this approach is time-consuming and computationally expensive. The analytical analysis method developed in this work may enable the application of the inflation test to other thick tissue systems, such as arteries or gastrointestinal tissues. Further, the human skin study should be expanded to include a much larger number of specimens to better characterize the nonlinear anisotropic material properties of skin tissue.

(2) The demonstration of significant differences between the fully-integrated distributed fiber model and the pre-integrated generalized structure tensor models when applied to skin tissue. When both models were fit to the inflation tests of skin tissue, the anisotropy parameters were significantly different. Finite element analysis was used to compare model predictions to the structural response of the inflated tissue. The results demonstrated that while the fully-integrated model was in good agreement with experimental measurements, the generalized structure tensor model greatly underestimated tissue anisotropy. The results support the findings of other authors[40,41] who have also found discrepancies between the two models. Such discrepancies are not unexpected, because generalized structure tensor models are approximations of the fully-integrated models. Generalized structure tensor models were originally developed for application to arteries by Gasser et al.[28] The

collagen structure of arteries is characterized by two fiber families with small dispersion, and arteries do not undergo large rotations when loaded. For such a tissue, pre-integrating the fiber distribution is a reasonable approximation. The success of the model for arteries has lead to implementation into commercial software packages such as Abaqus. The accessibility of the model has lead researchers to apply it to a range of soft tissues with very different structures and loading conditions than the arteries.[38,39] The discrepancies found in this work underscore the need for careful consideration of the assumptions of a model for a given application and subsequent validation of the model results.

(3) The development of a hierarchal modeling framework to incorporate fiber-level mechanisms of growth and remodeling, which was used to illustrate that strain-protected degradation and collagen deposition can lead to strain homeostasis. The mechanisms of growth and remodeling are not well understood and are not taken into account in current tissue-level, homeostatic models. Micro-mechanical models have great utility to understand such fiber-level processes, but are not often implemented into tissue-level frameworks. In this work a micro-mechanical model for collagen fibers developed in 1976 by Comninou and Yannas[45] was for the first time incorporated into a tissue-level anisotropic constitutive model, specifically the fully-integrated distributed fiber model described in contribution (2). This hierarchal model was used to describe the strain-dependent enzymatic degra-

dation of collagen at the fiber level, based on available experimental data in the literature. The model was capable of predicting tissue-level experiments based on model calibration to fibril-level experiments. A key contribution of this work was the illustration that the non-cellular mechanisms of strain-protected degradation and collagen deposition can give rise to strain homeostasis, supporting these processes as potential mechanisms of growth and remodeling.

7.3 Limitations

Several important limitations of this work should be acknowledged. First of all, because the aim of the work in Chapters 2-3 was to develop the inflation test and analysis method, a very limited number of samples (6) with a wide range of mechanical behavior were reported, precluding definitive conclusions about skin biomechanics. However, observed trends were consistent with what is reported in the literature. Additionally, the inflation analysis method assumes that the tissue is homogenous both in and through the plane. While this assumption is reasonable for skin tissue, it does ignore the changes in collagen density near the bottom of the dermis and might limit the utility of the method for other tissues. The test method was also used in Chapter 6 to show that skin and ocular tissues did not exhibit significant preconditioning effects when tested by inflation. This was hypothesized to occur because the fully fixed boundary condition of the inflation test prevents non-affine rotation of the

collagen fibers within the tissue during cyclic loading. However, this assumes that collagen fibers are sufficiently long to span the diameter of the tissue tested (7.5 cm). It is more likely that shorter collagen fibers overlap to create a network that spans the diameter of the tissue, but this is unproved. Therefor the mechanisms of the preconditioning response and the reasons for the minimal preconditioning response seen in this work remain unclear, and more tissue systems would need to be tested to determine if the results are generalizable for all planar tissues.

In this work, only elastic mechanical properties were considered. Skin tissues are known to be viscoelastic, and to avoid confounding the results, skin was loaded at very slow, consistent loading rates to measure the quasi-static response. The fully integrated distributed fiber model used in Chapters 3-4 also described elastic behavior only. Further, the modeling approach assumes an affine deformation of the fibers and ground matrix, i.e. the fibers and surrounding ground matrix deform together without interaction terms. The model also assumes that all fibers have the same initial crimp, material stiffness, both in the plane and through the thickness of the tissue, and that the density of the fibers is constant throughout the tissue. The model description of the fiber distribution as one fiber family distributed about a preferred orientation described by a von Mises function is an idealization, and the fiber structure was not confirmed with histology or imaging studies. However, the stiffest direction identified for skin tissue was in agreement with the known dominant fiber direction from the literature.

In Chapter 4, the same anisotropic hyperelastic model used to describe skin was applied to bovine cornea while describing individual fibers as planar sinusoidal elastica beams. However, unlike skin, the cornea is composed of alternating layers of collagen fibers referred to as lamellae. These lamellae can have characteristic crimp and are modeled as fibers in this work. However, lamellae are instead made up of collagen fibers and are a higher-order structure in the cornea. Describing the lamellae as fibers resulted in elastica parameters that did not agree with geometric parameters measured by imaging and histology. These parameters were also obtained from limited data points for equilibrated tissue, resulting in a non-unique parameter set that may be more compliant than *in vivo* tissue. Additionally, the assumption of uniform fiber crimp and length may have impacted the tissue-level degradation predictions. Collagenous tissues are more accurately described as a distribution of collagen crimps and lengths. In the case of a distribution of crimp, the longest and least-crimped fibers are expected to degrade more rapidly. This could partially account for the under-prediction of the experimental absolute creep rates. Non-affine deformation of the fibers could also contribute to this discrepancy. Fibers that deform non-affinely with the matrix may be subject to smaller stretches than the bulk tissue itself, and therefor be more quickly degraded.

The model for strain-protected enzymatic degradation, though based on an Eyring description for the change in the chemical activation energy, does not take into account the stochastic nature of the reaction. Degradation is also prescribed on the

fiber level, but model parameters were calibrated to single-fibril experiments. Ignoring this length scale difference may over-predict the effect of stretch protection, as fibrils packed into fibers may experience strain shielding. Again, viscoelastic effects were not considered when modeling degradation-induced creep experiments. These two limitations could contribute to the lower absolute creep rates predicted by the model for bovine cornea. In contrast, the higher absolute creep rates predicted for bovine pericardium may have arisen from differences in enzyme concentration and Ca^{2+} between these experiments and the fibril-level experiments used for model calibration. Finally, other important potential remodeling mechanisms were not considered. Collagen deposition was assumed to proceed by simply increasing the fiber radius, though other authors have modeled collage deposition by the formation of new collagen fibers in a pre-stretched state.[51,70] More significantly, cellular effects were ignored, such as the ability of the cells to apply force to the collagen fibers and modulate the collagen crimp angle. It is likely that the inclusion of these effects could result in a stress, rather than strain, homeostasis.

7.4 Future Directions

Future directions include both improving the hierarchical model developed in this work and applying the model to new applications. In the near term, a primary focus should be the incorporation of additional mechanisms into the growth and remodeling

problem. In particular, active cellular contraction is likely an important mechanism of growth and remodeling, and could be modeled as an added stress on an individual collagen fiber. Collagen crimp remodeling could also be modeled by modulating the crimp angle parameter, Θ_0. Both of these mechanisms could be dependent on the current stretch of the fiber. Further, in this work the deposition of collagen was modeled simply as a constant increase in existing collagen fiber diameter. It would be more accurate to model the deposition of collagen as modulating the collagen crimp, particularly as new fibers are deposited in a pre-stretched state, following Watton et al,[70] and to incorporate the strain-dependence of the deposition rate.[78] These mechanisms, paired with the degradation model and a more sophisticated collagen deposition model, may together result in a stress homeostasis for the tissue.

Another potential area of improvement for the hierarchal model would be to distinguish between the fiber and fibril length scale. It is likely that collagen fibers are not as dramatically protected from degradation as fibrils because as fibrils packed into fibers may be strain shielded. This could be taken into account by computing a fibril stretch based on the fiber stretch - either by phenomenological assumption i.e. fibril stretch is on average 75% of the fiber stretch, or by modeling the fibril packing to compute a translating factor. This would likely improve the accuracy of the degradation model, particularly over long time scales. Similarly, the mechanical model for the cornea would be improved by distinguishing between the fiber scale and the lamellae. This may result in geometric parameters that are in closer agreement

with those measured from imaging and histology.

The growth and remodeling model developed in this work is analytical and for a single material point, which limited test cases and analysis to simple uniaxial and biaxial loading of homogenous simulations. To simulate more complex geometries and loading cases, the model could be implemented into a Finite Element model. This would allow a more realistic simulation of the loading of the eye wall, and could allow for a non-homogenous fiber structure to be prescribed. Such a model could be used to predict the development of disease states such as glaucoma or myopia. Though the model was capable of predicting the normalized creep rates of constant force tissue degradation experiments, the absolute creep rates were under-predicted for bovine cornea and over-predicted for bovine pericardium. This discrepancy likely arises from processes not modeled in this work such as nonlinear viscoelasticity and diffusion effects. A heterogeneous finite element model could also be used to take into account diffusion effects, , while nonlinear viscoelasticity could be incorporated into the constitutive model. Both are expected to result in improved experimental prediction of degradation-induced creep tests.

The hierarchal modeling approach developed in this work could be applied to a variety of problems beyond human skin characterization and mechanistic studies of growth and remodeling considered here. An interesting combination and extension of both the human skin and remodeling work presented here would be to study progressive changes in the structure of skin, such as those associated with wound healing

and scar formation. Alternatively, the skin-stiffening disease Scleroderma, is a painful and debilitating condition of unknown causes associated with an increase in collagen in the skin, leading to dramatic stiffening that limits movement.[220] Finally, it has been illustrated in this study and others that skin may become more isotropic with age. Age-related changes in collagenous tissues are commonly ascribed to increased cross-linking between collagen fibers. The model developed in this work could be used to investigate if this increase in isotropy could also be due to growth and remodeling over time.

The model could also be applied to other tissue systems and disease states, and in particular other planar collagenous tissues that undergo pathological changes associated with remodeling, such as arteries or aneurisms. Further, the model could be extended to cardiac tissues with the incorporation of smooth muscle cells and active contraction. The model could also be used to investigate the contributions of different components of soft tissues, such as ground matrix - collagen interactions. For example, recent experimental evidence from our lab has illustrated that selectively removing proteoglycans from porcine sclera lengthens the toe region of the stress-strain curve.[221] It is hypothesized that disrupting the proteoglycan-collagen bonds leads to an effective increase in the crimp angle of the collagen fibers. The model could be used to test this hypothesis by modulating the crimp angle and comparing the result to experiments. Finally, the hierarchal degradation model could be applied to functional tissue engineering. Maintaining the mechanical integrity of engineered

tissues remains an ongoing challenge, particularly after implantation in the body. The enzymatic degradation model presented in this work could be used to simulate in vivo loading states to determine the loads needed to maintain the tissue integrity and prevent *in vivo* degradation, or to condition developing tissue *in vitro* for optimal mechanical strength.

Appendix A

Appendix: Experimental Details

A.1 Equipment Details

MTS driven syringe pump:

MTS Insight 5, 0.01 mm position accuracy, 1 kN load cell, 1.535 mV/V sensitivity.

Syringes:

Plunger of a 60 cc plastic syringe attached to MTS crosshead, syringe encased in aluminum and mounted on the base of the MTS machine.

Honeywell TJE pressure transducer:

P/N 068-075C-03TJG, 2 psig range, 0.1% full scale accuracy, data converted from analog to digital and written to a log file.

APPENDIX A. APPENDIX: EXPERIMENTAL DETAILS

Cameras:

Point Grey GRAS-20S4M/C, with 1/1.8" image sensors, positioned 0.38 m above the chamber 7.5 cm apart (12°angle between cameras), depth of field = 5.8 cm. Images collected at 0.5 Hz.

Lenses:

Edmund Optics, NT59-870, 16 mm focal length, f/8 aperture

Calibration Grid:

1" calibration grid (Correlated Solutions, #055893)

Software:

VicSnap 2009 (image capture), Vic3D 2009 (image correlation), both by Correlated Solutions

Powdered Graphite:

AGS Mr. Zip Graphite Powdered Libricant (MZ-5), applied to the tissue surface through a stainless steel mesh with 61 µm openings (TWP Inc. p/n 50X250S0016W48T).

A.2 Inflation Chamber Design

Note: Portions of this section have previously appeared in my Master's Thesis[87].

The stainless steel inflation chamber is an assembly of three main components: a top ring, main chamber, and bottom plate. Engineering drawings of all three components and the assembly are shown in Fig. A.1. The top ring was used to clamp the tissue and fixture onto the main chamber. The main chamber was connected to MTS driven syringe by 4 feet of 1/8" ID silicone tubing at the 0.35 cm diameter inlet port. The inlet port also connected to the pressure transducer and a relief valve via a custom connector and a union cross adaptor (Swagelok). This connector is fashioned from a compression tube fitting (McMaster-Carr), stainless steal sleeve (McMaster-Carr), and 1/8" ID tube-to-thread adaptor (Swagelok). A small lip on the inner diameter of the upper surface of the chamber was included to hold the fixture in place, and the 1.25 cm diameter support post was included for mounting the chamber. The bottom plate attaches to the bottom of the main chamber. Four light ports (McMaster-Carr Part# 46755K32 and #4464K212) were attached to the center of the plate, spaced 1.6 cm apart. Silicone oil encased in latex was clamped between the bottom plate and the main chamber to diffuse the fiber optic light. Twelve screws (McMaster-Carr part #96242A573) were used to secure the top ring and bottom plate to the chamber. Two O-rings (McMaster-Carr #5018T224) were used to seal the chamber to the diffuser and to the fixture.

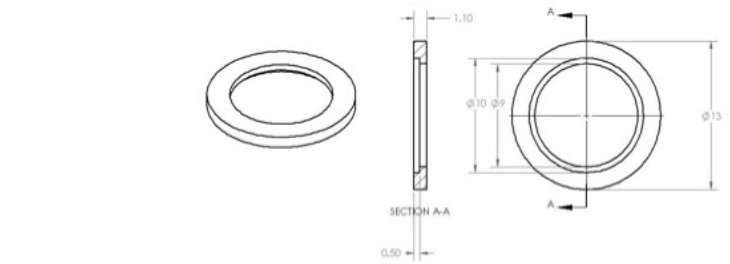

(a)

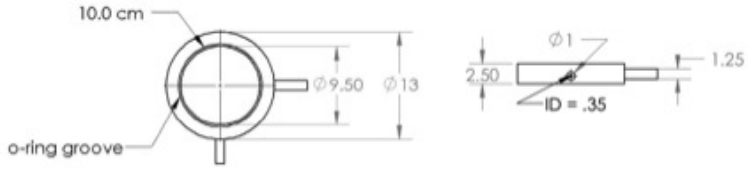

(b)

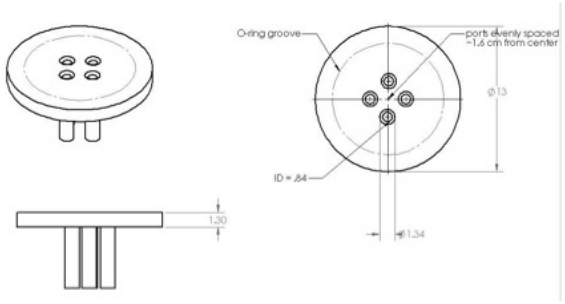

(c)

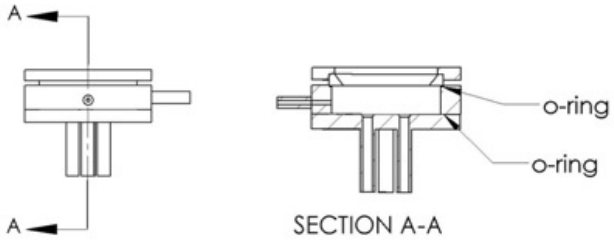

(d)

Figure A.1: Custom pressure chamber: (a) top ring, (b) main chamber, (c) bottom plate, (d) complete assembly.

A.3 PID Control of Pressure

Note: Portions of this section have previously appeared in my Master's Thesis[87].

The PID loop was manually tuned, prioritizing a stable response. The PID parameters for loading, unloading, and the 15 minute hold are summarized in Table A.1. Figure A.2 plots pressure-time behavior for these parameters for a representative skin sample. The PID loop directly controlled the crosshead displacement rather than pressure, so inertial effects could lead to overcompensation and instabilities in chamber pressure. This effect was compounded by the stiffening behavior of the specimens.

	Loading	Unloading	Hold
P	25000	200	1000
I	0	0.05	1000
D	0	0	0

Table A.1: Optimized PID parameters for loading, unloading, and hold.

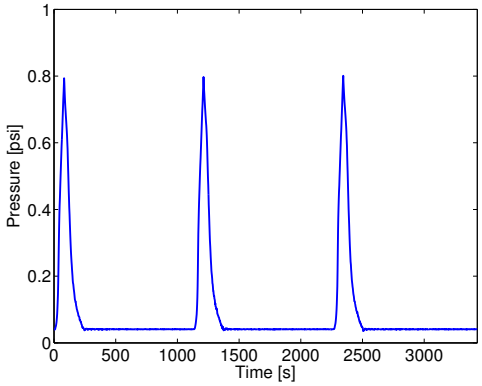

Figure A.2: Resulting pressure-time behavior for PID parameters detailed in Table A.1 (43/M/C).

A.4 Skin Testing Protocol

Test Set-up:

16mm focal length lenses

Large pressure chamber (attach light ports)

Large (60cc) syringe, MTS stop adjusted to large syringe

7.5cm ID fixture, spray painted white, x and y axis marked from template

1 calibration grid target

Sample Testing Parameters:

Test baseline = 0.04 psi

Max pressure = 0.8 psi

Pressure rate = 0.01 psi/s, 0.1 psi/s

Experimental Protocol:

1. Thaw sample in PBS overnight in fridge
2. Record Room Temp and Humidity
3. Trim off all fat. May have to re-soak at end and trim some more.
4. Measure thickness at edges (top/bottom/left/right) with calipers. Take 3 measurements at each location.
5. Glue specimen to fixture so that head direction is aligned with y-axis marked

on fixture. Turn over, trans-illuminate, and mark edges of fixture ID with pen. Score on this side and impregnate with glue. Let dry. Trim excess skin, and add line of glue at boundary. Let dry. (15-30 minutes or until glue changes from purple to clear).

6. Ensure chamber is level. Attach pressure transducer to chamber and support with stand. Ensure cameras are 15 above chamber. Ensure chamber is centered in both fields of view. Zero pressure transducer channel in TestWorks4.

7. Fill syringe with PBS with chamber valve open. Ensure no bubbles in line. Lower syringe until sealed (maintain meniscus). Close valve, fill chamber with PBS. Load sample and secure with 6 screws. Note baseline/bring to 0.04psi.

8. Manually increase pressure to determine when syringe will bottom out (i.e. make sure you can get to 0.8 psi).

9. Speckle sample and fixture with graphite and 60micrometer mesh.

10. Focus cameras (at wide open aperture, 3ms exposure time) on x-axis part of fixture. Return to 8/f aperture, 25ms.

11. Swing chamber/transducer out of the way. Turn off lights, put paper on bench, shine lights on paper. Use 1 Calibration Target to take about 20 images. Calibrate system, check C.I. and that error ¡ 0.03. Save as project file w/date.

12. Replace chamber in field of view. Take 3 images at baseline pressure. Run correlation and ensure good speckle, level, etc.

13. Place Humidity chamber over sample. Place saturated honeycomb and humidity/temp reader inside chamber. Target 40% humidity.

14. Hold sample at baseline for 15 minutes. (Run Initial15minhold method on Testworks).

15. Ensure Analog data is being read. Start VicSnap acquisition. Start selected TestWorks method.

16. Freeze sample (still on fixture). Wipe everything down with bleach.

Image Correlation Procedure:

1. Select main AOI as close to edges as reasonable (want circle for centering)
   (a) Use subset =50
   (b) Select 3 points and complete
   (c) Ensure all images find the point
2. Select 4 more AOIs rectangles around grid markers on fixture
3. Import calibration
4. Correlate 1-2 images, ensuring that postprocesing is none (not autoplane)

5. Correct stereo sytem (Callibrate Camera Orientatin)
6. Recorrelate 1-2 images
7. Select coordinant system (3-point). Save as 3pt-date
8. Save project, outside of folder containing images.
9. Delete 4 rectangular AOIs
10. Run complete correlation. Record maximum error & error at beginning.
11. Apply transform to all images

Data Extraction Procedure:

1. Extract node data at apex. Make note of node coordinates

   FILE NAME: Test#_grid_MM.DD.YY.csv

2. Extract grid data (every 5 pixels) for all images of loading curve

   NOTE: Save all data (including project file) to folder above images. Transfer a copy with a flash drive.

   FILE NAME: Test#_apex_MM.DD.YY.csv

3. Rename and copy test.csv file.

   FILE NAME: Test#_MM.DD.YY.csv

Stress/Strain Data Analysis:

1. Copy Image, Time, and Pressure from node data and test files into excel. Convert Pressure from psi to kPa. Input Radius (37.5 mm) and initial thickness.

2. Identify image with max pressure for all 3 loadings, and end of unloading for all 3.

3. Load image into Nov10EllipsoidFit.m (see Sec. C.1) and fit to general ellipse

4. Use eigenvectors to determine counter-clockwise rotation angle needed to align stiffest/fiber direction (b) with x-axis.

5. Run Nov10EllipsoidFit.m for all images on loading curve. Copy a, b, and c into excel file.

6. Input angle into Jun16FittedStrains.m (see Sec. C.2). Run for max pressure image. Check contours (esp. W over distorted, U and V) to make sure everything is aligned properly. (W oval should be vertical, U and V should not be rotated/skewed). Check that strains are calculated at (0,0,Z) $\rightarrow$ check that Xv(1)=Yh(1)=0, and that Xv(centerH)=Yh(centerV)=0. Adjust if necessary and update in Jun16FittedStrainsGrid.m as well.

7. Run Jun16FittedStrainsGrid.m (see Sec. C.3) for all images on loading /unloading curve for all 3 load/unload cycles (including angle as an input).

8. Copy resulting strains into excel file and compute associated stretches [stretch = sqrt(2*strain+1)]

9. Calculate deformed thickness [original thickness/(StretchF*StretchP)]

10. Calculate StressFiber (circ.) and StressPerp(long,).

11. Determine baseline (i.e. where stress and strain pick up). Zero all subsequent pressures accordininly and only plot stress/strain for those points.

Fitting Constitutive Model Parameters:

1. Select image corresponding to the end of the toe region

2. Input stretches, pressure, initial thickness, rotation angle, and initial guess for parameters into the file 'parameterFittingConsistent_Aug30.m' (see Sec. C.4).

3. Select constitutive relation to fit parameters for from file 'constitutiveRelation.m' by commenting out the other models

4. Run file 'parameterFittingConsistent_Aug30.m'.

Appendix B

Appendix: Jacobians for Remodeling Simulations

B.1 Solve for single degrading elastica

Nonlinear system, degradation ODE discretized with backward Euler scheme:

$$\begin{aligned} f_1 &= \overline{\lambda}_{app} - \frac{1}{L}\int_0^L \lambda_f \frac{\cos(\theta)}{\cos(\Theta_0)} dX_1 \\ f_2 &= D - D_{prev} + \Delta G_1 \exp\left[-\frac{\overline{\epsilon^2}}{2G_2}\right] \end{aligned} \tag{B.1}$$

Newton-Raphson Solver:

$$\begin{bmatrix} \alpha^{n+1} \\ D^{n+1} \end{bmatrix} = \begin{bmatrix} \alpha^n \\ D^n \end{bmatrix} - J^{-1} \begin{bmatrix} f_1 \\ f_2 \end{bmatrix} \tag{B.2}$$

APPENDIX B. APPENDIX: JACOBIANS FOR REMODELING SIMULATIONS

With the Jacobian:

$$J = \begin{bmatrix} \frac{df_1}{d\alpha} & \frac{df_1}{dD} \\ \\ \frac{df_2}{d\alpha} & \frac{df_2}{dD} \end{bmatrix}, \tag{B.3}$$

until convergence, $res \leq tol$:

$$res = |\sqrt{f_1^2 + f_2^2}| \tag{B.4}$$

Derivatives for Jacobian:

$$\begin{aligned} \frac{df_1}{d\alpha} &= -\frac{1}{L}\int_0^L \left[\frac{\partial \lambda_f}{\partial \alpha}\frac{\cos(\theta)}{\cos(\Theta_0)} - \lambda_f \frac{\sin(\theta)}{\cos(\Theta_0)}\frac{\partial \theta}{\partial \alpha}\right] dX_1 \\ \frac{df_1}{dD} &= -\frac{1}{L}\int_0^L \left[\frac{\partial \lambda_f}{\partial D}\frac{\cos(\theta)}{\cos(\Theta_0)} - \lambda_f \frac{\sin(\theta)}{\cos(\Theta_0)}\frac{\partial \theta}{\partial D}\right] dX_1 \\ \frac{df_2}{d\alpha} &= -\Delta G_1 \exp\left(-\frac{\overline{\epsilon^2}}{2G_2}\right)\frac{\overline{\epsilon}}{G_2}\frac{\partial \overline{\epsilon}}{\partial \alpha} \\ \frac{df_2}{dD} &= 1 - \Delta G_1 \exp\left(-\frac{\overline{\epsilon^2}}{2G_2}\right)\frac{\overline{\epsilon}}{G_2}\frac{\partial \overline{\epsilon}}{\partial D} \end{aligned} \tag{B.5}$$

where:

$$\frac{\partial \lambda_f}{\partial \alpha} = \cos(\theta) - \alpha \sin(\theta)\frac{\partial \theta}{\partial \alpha} \tag{B.6}$$

$$\begin{aligned} \frac{\partial \lambda_f}{\partial D} &= \frac{\partial}{\partial D}\left[1 + \alpha\cos(\theta)\right] \\ &= -\alpha \sin(\theta)\frac{\partial \theta}{\partial D} \end{aligned} \tag{B.7}$$

$$\frac{\partial \theta}{\partial \alpha} = \frac{-\beta(4+8\alpha)\Theta_0}{(4\alpha(1+\alpha)+\beta)^2} \tag{B.8}$$

$$\begin{aligned}\frac{\partial \theta}{\partial D} &= \frac{\partial}{\partial D}\left[\frac{\beta_0 D^2 \Theta_0}{4\alpha(1+\alpha)+\beta_0 D^2}\right] \\ &= \frac{2\beta_0 D\Theta_0}{4\alpha(1+\alpha)+\beta_0 D^2} - \frac{2\beta_0^2 D^3 \Theta_0}{(4\alpha(1+\alpha)+\beta_0 D^2)^2}\end{aligned} \tag{B.9}$$

$$\frac{\partial \overline{\epsilon}}{\partial \alpha} = \frac{1}{L}\int_0^L \frac{\partial \lambda_f}{\partial \alpha} dX_1 \tag{B.10}$$

$$\frac{\partial \overline{\epsilon}}{\partial D} = \frac{1}{L}\int_0^L \frac{\partial \lambda_f}{\partial D} dX_1 \tag{B.11}$$

B.2 Biaxial Stress for Degrading Tissue

Nonlinear system:

$$\begin{aligned} f_1 &= \mu\left(\lambda_{11}^2 - \frac{1}{\lambda_{11}^2\lambda_{22}^2}\right) + \int_{-\pi}^{\pi} \frac{\partial \Psi}{\partial \overline{\lambda}} \frac{1}{\overline{\lambda}} \lambda_{11}^2 \cos^2(\phi)\rho(\phi)d\phi - \sigma_{11,app} \\ f_2 &= \mu\left(\lambda_{22}^2 - \frac{1}{\lambda_{11}^2\lambda_{22}^2}\right) + \int_{-\pi}^{\pi} \frac{\partial \Psi}{\partial \overline{\lambda}} \frac{1}{\overline{\lambda}} \lambda_{22}^2 \sin^2(\phi)\rho(\phi)d\phi - \sigma_{22,app} \end{aligned} \tag{B.12}$$

Newton-Raphson Solver for stretch:

$$\begin{bmatrix} \lambda_{11}^{n+1} \\ \\ \lambda_{22}^{n+1} \end{bmatrix} = \begin{bmatrix} \lambda_{11}^{n} \\ \\ \lambda_{22}^{n} \end{bmatrix} - J^{-1} \begin{bmatrix} f_1 \\ \\ f_2 \end{bmatrix} \tag{B.13}$$

With the Jacobian:

$$J = \begin{bmatrix} \frac{df_1}{d\lambda_{11}} & \frac{df_1}{d\lambda_{22}} \\ \\ \frac{df_2}{d\lambda_{11}} & \frac{df_2}{d\lambda_{22}} \end{bmatrix}, \tag{B.14}$$

until convergence, $res \leq tol$:

$$res = |\sqrt{f_1^2 + f_2^2}| \tag{B.15}$$

Derivatives for Jacobian:

$$\begin{aligned}
\frac{df_1}{d\lambda_{11}} &= 2\mu\left(\lambda_{11} + \frac{1}{\lambda_{11}^3\lambda_{22}^2}\right) \\
&\quad + \int_{-\pi}^{\pi}\left[\left(\frac{\partial^2\Psi}{\partial\overline{\lambda}^2}\frac{\partial\overline{\lambda}}{\partial\lambda_{11}}\right)\left(\frac{\lambda_{11}^2}{\overline{\lambda}}\right) + \left(\frac{\partial\Psi}{\partial\overline{\lambda}}\right)\left(\frac{2\lambda_{11}}{\overline{\lambda}} - \frac{\lambda_{11}^2}{\overline{\lambda}^2}\frac{\partial\overline{\lambda}}{\partial\lambda_{11}}\right)\right]\cos^2(\phi)\rho(\phi)d\phi \\
\frac{df_1}{d\lambda_{22}} &= 2\mu\left(\frac{1}{\lambda_{11}^2\lambda_{22}^3}\right) \\
&\quad + \int_{-\pi}^{\pi}\left[\left(\frac{\partial^2\Psi}{\partial\overline{\lambda}^2}\frac{\partial\overline{\lambda}}{\partial\lambda_{22}}\right)\left(\frac{\lambda_{11}^2}{\overline{\lambda}}\right) + \left(\frac{\partial\Psi}{\partial\overline{\lambda}}\right)\left(-\frac{\lambda_{11}^2}{\overline{\lambda}^2}\frac{\partial\overline{\lambda}}{\partial\lambda_{22}}\right)\right]\cos^2(\phi)\rho(\phi)d\phi \\
\frac{df_2}{d\lambda_{11}} &= 2\mu\left(\frac{1}{\lambda_{11}^3\lambda_{22}^2}\right) \\
&\quad + \int_{-\pi}^{\pi}\left[\left(\frac{\partial^2\Psi}{\partial\overline{\lambda}^2}\frac{\partial\overline{\lambda}}{\partial\lambda_{11}}\right)\left(\frac{\lambda_{22}^2}{\overline{\lambda}}\right) + \left(\frac{\partial\Psi}{\partial\overline{\lambda}}\right)\left(-\frac{\lambda_{22}^2}{\overline{\lambda}^2}\frac{\partial\overline{\lambda}}{\partial\lambda_{11}}\right)\right]\sin^2(\phi)\rho(\phi)d\phi \\
\frac{df_2}{d\lambda_{22}} &= 2\mu\left(\lambda_{22} + \frac{1}{\lambda_{11}^2\lambda_{22}^3}\right) \\
&\quad + \int_{-\pi}^{\pi}\left[\left(\frac{\partial^2\Psi}{\partial\overline{\lambda}^2}\frac{\partial\overline{\lambda}}{\partial\lambda_{22}}\right)\left(\frac{\lambda_{22}^2}{\overline{\lambda}}\right) + \left(\frac{\partial\Psi}{\partial\overline{\lambda}}\right)\left(\frac{2\lambda_{22}}{\overline{\lambda}} - \frac{\lambda_{22}^2}{\overline{\lambda}^2}\frac{\partial\overline{\lambda}}{\partial\lambda_{22}}\right)\right]\sin^2(\phi)\rho(\phi)d\phi
\end{aligned} \tag{B.16}$$

where:

$$\Psi = \Psi_b + \Psi_a \tag{B.17}$$

$$\begin{aligned}\Psi_b &= \frac{D^2}{L}\int_0^L \frac{E\beta}{8}\left(\theta-\Theta_0\right)^2 dX_1 \\ &= \frac{D^2}{L}\int_0^L \frac{ED^2\beta_0}{8}\left(\theta-\Theta_0\right)^2 dX_1\end{aligned} \tag{B.18}$$

$$\Psi_a = \frac{D^2}{L}\int_0^L \frac{E}{2}(\lambda_f-1)^2 dX_1 \tag{B.19}$$

$$D = D_{prev} - \Delta G_1 \exp\left(-\frac{\overline{\epsilon^2}}{2G_2}\right) \tag{B.20}$$

B.2.1 Macro-stretch partial derivatives

$$\begin{aligned}\frac{\partial\overline{\lambda}}{\partial\lambda_{11}} &= \frac{\lambda_{11}\cos^2(\phi)}{\overline{\lambda}} \\ \frac{\partial\overline{\lambda}}{\partial\lambda_{22}} &= \frac{\lambda_{22}\sin^2(\phi)}{\overline{\lambda}}\end{aligned} \tag{B.21}$$

B.2.2 Strain energy partial derivatives

$$\frac{\partial\Psi}{\partial\overline{\lambda}} = \frac{\partial\Psi_b}{\partial\alpha}\frac{\partial\alpha}{\partial\overline{\lambda}} + \frac{\partial\Psi_a}{\partial\alpha}\frac{\partial\alpha}{\partial\overline{\lambda}} \tag{B.22}$$

$$\frac{\partial^2\Psi}{\partial\overline{\lambda}^2} = \left(\frac{\partial^2\Psi_b}{\partial\alpha\partial\overline{\lambda}}\frac{\partial\alpha}{\partial\overline{\lambda}} + \frac{\partial\Psi_b}{\partial\alpha}\frac{\partial^2\alpha}{\partial\overline{\lambda}^2}\right) + \left(\frac{\partial^2\Psi_a}{\partial\alpha\partial\overline{\lambda}}\frac{\partial\alpha}{\partial\overline{\lambda}} + \frac{\partial\Psi_a}{\partial\alpha}\frac{\partial^2\alpha}{\partial\overline{\lambda}^2}\right) \tag{B.23}$$

$$\frac{\partial\Psi_b}{\partial\alpha} = \frac{D^2}{L}\int_0^L \left[\frac{E\beta}{4}\left(\theta-\Theta_0\right)\frac{d\theta}{d\alpha}\right] dX_1 \tag{B.24}$$

$$\frac{\partial \Psi_a}{\partial \alpha} = \frac{D^2}{L} \int_0^L \left[E\left(\lambda_f - 1\right) \frac{d\lambda_f}{d\alpha} \right] dX_1 \tag{B.25}$$

$$\begin{aligned} \frac{\partial^2 \Psi_b}{\partial \alpha \partial \overline{\lambda}} &= \frac{\partial}{\partial \overline{\lambda}} \left[\frac{E\beta_0}{4L} \int_0^L D^4(\theta - \Theta_0) \frac{\partial \theta}{\partial \alpha} dX_1 \right] \\ &= \frac{E\beta_0}{4L} \int_0^L \left[4D^3 \frac{\partial D}{\partial \overline{\lambda}} (\theta - \Theta_0) \frac{\partial \theta}{\partial \alpha} + D^4 \left(\frac{\partial \theta}{\partial \overline{\lambda}} \right) \left(\frac{\partial \theta}{\partial \alpha} \right) + D^4 (\theta - \Theta_0) \frac{\partial^2 \theta}{\partial \alpha} \partial \overline{\lambda} \right] dX_1 \end{aligned} \tag{B.26}$$

$$\begin{aligned} \frac{\partial^2 \Psi_a}{\partial \alpha \partial \overline{\lambda}} &= \frac{\partial}{\partial \overline{\lambda}} \left[\frac{E}{L} \int_0^L D^2(\lambda_f - 1) \frac{\partial \lambda_f}{\partial \alpha} dX_1 \right] \\ &= \frac{E}{L} \int_0^L \left[2D \frac{\partial D}{\partial \overline{\lambda}} (\lambda_f - 1) \frac{\partial \lambda_f}{\partial \alpha} + D^2 \left(\frac{\partial \lambda_f}{\partial \overline{\lambda}} \frac{\partial \lambda_f}{\partial \alpha} \right) + D^2 (\lambda_f - 1) \frac{\partial^2 \lambda_f}{\partial \alpha \partial \overline{\lambda}} \right] dX_1 \end{aligned} \tag{B.27}$$

B.2.3 Elastica parameter partial derivatives

B.2.3.1 Partial derivatives of α

$$\frac{\partial \alpha}{\partial \overline{\lambda}} = \left[\frac{1}{L} \int_0^L \left(\frac{\partial \lambda_f}{\partial \alpha} \frac{\cos(\theta)}{\cos(\Theta_0)} - \frac{\lambda_f \sin(\theta)}{\cos(\Theta_0)} \frac{\partial \theta}{\partial \alpha} \right) dX_1 \right]^{-1} \tag{B.28}$$

$$\begin{aligned}\frac{\partial \alpha^2}{\partial \overline{\lambda}^2} &= \frac{\partial}{\partial \overline{\lambda}}\left[\left[\frac{1}{L}\int_0^L \left(\frac{\partial \lambda_f}{\partial \alpha}\frac{\cos(\theta)}{\cos(\Theta_0)} - \frac{\lambda_f \sin(\theta)}{\cos(\Theta_0)}\frac{\partial \theta}{\partial \alpha}\right) dX_1\right]^{-1}\right] \\ &= -\left[\frac{1}{L}\int_0^L \left(\frac{\partial \lambda_f}{\partial \alpha}\frac{\cos(\theta)}{\cos(\Theta_0)} - \frac{\lambda_f \sin(\theta)}{\cos(\Theta_0)}\frac{\partial \theta}{\partial \alpha}\right) dX_1\right]^{-2} * \\ &\left(\frac{1}{L}\int_0^L \left[\frac{\partial^2 \lambda_f}{\partial \alpha \partial \overline{\lambda}} - \lambda_f \frac{\partial \theta}{\partial \overline{\lambda}}\frac{\partial \theta}{\partial \alpha}\right)\frac{\cos(\theta)}{\cos(\Theta_0)} - \left(\frac{\partial \lambda_f}{\partial \alpha}\frac{\partial \theta}{\partial \overline{\lambda}} + \frac{\partial \lambda_f}{\partial \overline{\lambda}}\frac{\partial \theta}{\partial \alpha} + \lambda_f \frac{\partial^2 \theta}{\partial \alpha \partial \overline{\lambda}}\frac{\sin(\theta)}{\cos(\Theta_0)}\right] dX_1\right)\end{aligned} \tag{B.29}$$

B.2.3.2 Partial derivatives of λ_f

$$\frac{\partial \lambda_f}{\partial \overline{\lambda}} = \frac{\partial \lambda_f}{\partial \alpha}\frac{\partial \alpha}{\partial \overline{\lambda}} + \frac{\partial \lambda_f}{\partial D}\frac{\partial D}{\partial \overline{\lambda}} \tag{B.30}$$

$$\frac{\partial \lambda_f}{\partial \alpha} = \cos(\theta) - \alpha \sin(\theta)\frac{\partial \theta}{\partial \alpha} \tag{B.31}$$

$$\begin{aligned}\frac{\partial \lambda_f}{\partial D} &= \frac{\partial}{\partial D}\left[1 + \alpha \cos(\theta)\right] \\ &= -\alpha \sin(\theta)\frac{\partial \theta}{\partial D}\end{aligned} \tag{B.32}$$

$$\begin{aligned}\frac{\partial^2 \lambda_f}{\partial \alpha \partial \overline{\lambda}} &= \frac{\partial}{\partial \overline{\lambda}}\left[\cos(\theta) - \alpha \sin(\theta)\frac{\partial \theta}{\partial \alpha}\right] \\ &= -\sin(\theta)\frac{\partial \theta}{\partial \overline{\lambda}} - \alpha\left(\cos(\theta)\frac{\partial \theta}{\partial \overline{\lambda}} + \sin(\theta)\frac{\partial^2 \theta}{\partial \alpha \partial \overline{\lambda}}\right)\end{aligned} \tag{B.33}$$

B.2.3.3 Partial derivatives of θ

$$\frac{\partial \theta}{\partial \overline{\lambda}} = \frac{\partial \theta}{\partial \alpha}\frac{\partial \alpha}{\partial \overline{\lambda}} + \frac{\partial \theta}{\partial D}\frac{\partial D}{\partial \overline{\lambda}} \tag{B.34}$$

$$\frac{\partial \theta}{\partial \alpha} = \frac{-\beta(4+8\alpha)\Theta_0}{(4\alpha(1+\alpha)+\beta)^2} \tag{B.35}$$

$$\begin{aligned}\frac{\partial \theta}{\partial D} &= \frac{\partial}{\partial D}\left[\frac{\beta_0 D^2 \Theta_0}{4\alpha(1+\alpha)+\beta_0 D^2}\right] \\ &= \frac{2\beta_0 D\Theta_0}{4\alpha(1+\alpha)+\beta_0 D^2} - \frac{2\beta_0^2 D^3 \Theta_0}{(4\alpha(1+\alpha)+\beta_0 D^2)^2}\end{aligned} \tag{B.36}$$

$$\begin{aligned}\frac{\partial^2 \theta}{\partial \alpha \partial \overline{\lambda}} &= \frac{\partial}{\partial \overline{\lambda}}\left[\frac{-D^2\beta_0(4+8\alpha)\Theta_0}{(4\alpha(1+\alpha)+D^2\beta_0)^2}\right] \\ &= \frac{-2D\frac{\partial D}{\partial \overline{\lambda}}\beta_0(4+8\alpha)\Theta_0 - D^2\beta_0 8\frac{\partial \alpha}{\partial \overline{\lambda}}\Theta_0}{(4\alpha(1+\alpha)+D^2\beta_0)^2} + \\ &\quad \frac{2D^2\beta_0(4+8\alpha)\Theta_0\left[(4+8\alpha)\frac{\partial \alpha}{\partial \overline{\lambda}} + 2D\frac{\partial D}{\partial \overline{\lambda}}\beta_0\right]}{(4\alpha(1+\alpha)+D^2\beta_0)^3}\end{aligned} \tag{B.37}$$

B.2.3.4 Partial derivatives of D

$$\frac{\partial D}{\partial \overline{\lambda}} = -\Delta G_1 \exp\left(-\frac{\overline{\epsilon^2}}{2G_2}\right)\left(-\frac{\overline{\epsilon}}{G_2}\frac{\partial \overline{\epsilon}}{\partial \overline{\lambda}}\right) \tag{B.38}$$

$$\frac{\partial \overline{\epsilon}}{\partial \overline{\lambda}} = \frac{1}{L}\int_0^L \frac{\partial \lambda_f}{\partial \alpha} dX_1 \tag{B.39}$$

Appendix C

Appendix: Skin Analysis Files

Table of Contents:

(See Sec. A.4 for data analysis protocols.)

ellipsoid_fit.m (by Yury Petrov, available for download)

rsquare.m (by Felix Hebeler, available for download)

ellipse_fit.m (by Tal Hendel, available for download)

RotateZ.m

plotContour.m

horizontalLagrange.m

verticalLagrange.m

fittedExx.m

fittedEyy.m

Aug29_dateExtract.m

calculateCurvatureWphi.m

fitMuNested.m

fitFiberNestedRevolved2D.m

constitutiveRelation.m

C.1 Nov10EllipsoidFit.m

```
function [a,b,c, evecs, center] = Nov10EllipsoidFit(Data,Image, percent)
%Computes principal radii & orientations for an image  (Image = image
% number from data file) based on an ellipsoid fit for the the 3D
% displacement  using a specified percent of the image (i.e. 50%)
% from the center.

%Code to load image file:
%gridFileName = 'Test1_grid_1.31.11.csv';
%Data=dlmread(gridFileName,',',1,0);

%define columns
File_Number=Data(:,1);
X=Data(:,3);
Y=Data(:,4);
Z=Data(:,5);
U=Data(:,6);
V=Data(:,7);
W=Data(:,8);

% Pull out selected Picture (Image = Image number from Data file)
count=1;
for i=1:length(File_Number)
if isequal(File_Number(i),Image);
X0(count,1)=X(i);
Y0(count,1)=Y(i);
Z0(count,1)=Z(i);
Ui(count,1)=U(i);
Vi(count,1)=V(i);
Wi(count,1)=W(i);
count=count+1;
end
end

%Create deformed XYZ
x=X0+Ui;
y=Y0+Vi;
z=Z0+Wi;

%select middle of curve
percent=percent/100;
middlePercent=percent;
r=(x.^2+y.^2).^.5;
rLimit=middlePercent.*max(r);
count=1;
```

```
for i=1:length(x)
    if r(i) <= rLimit
        xMiddle(count,1)=x(i);
        yMiddle(count,1)=y(i);
        zMiddle(count,1)=z(i);
        count=count+1;
    end
end

xapex=xMiddle;
yapex=yMiddle;
zapex=zMiddle;

x=xapex;
y=yapex;
z=zapex;

%fit to ellipsoid
[center, radii, evecs, v]=ellipsoid_fit([x y z],0);
%0 = general elliptical fit
%1 = ellipsoid with axis at x,y,z
%3 = sphere
b=radii(1);
a=radii(2);
c=radii(3); %all in mm


end

%Code to automatically extract for all images:
%{
count=1;
for i=11:45
[a(count,1), b(count,1), c(count,1)]=Nov10EllipsoidFit(Data,i, 75);
count=count+1
end
%}
```

C.2 Jun16FittedStrains.m

```
% Jun16FittedStrains.m:
%
% Computes strains along fiber and perpendicular directions for a
% Data file, given Image number and rotation angle (in degrees,
% counterclockwise) so that the stiffnest direction (identified with
% Nov10EllipsoidFit.m) is aligned with x-direction. Computes strains
% using both the central difference method and fitted polynomials
% differentiated analytically.
% Prints plots of smoothed displacements, and strain measures. Also
% prints strain "error" (variability  within 5mm of apex) and
% strains for  both methods in both the fiber and perpendicular
% direction at the  apex. This file is intended to be used for
% inspection  before running Jun16FittedStrainsGrid.m for all
% images.
% NOTE: in code, X=fiber direction, Y=perpendicular direction.

% Code to load image file:
% gridFileName = 'Test1_grid_1.31.11.csv';
% Data=dlmread(gridFileName,',',1,0);

%INPUTS:
Image=20;  %Image number from data file for analysis
degrees=0; %Angle in degrees to rotate COUNTERCLOCKWISE
order=9; %Order of polynomial to fit displacments for strain calculation

%define columns
File_Number=Data(:,1);
X=Data(:,3);
Y=Data(:,4);
Z=Data(:,5);
Ui=Data(:,6);
Vi=Data(:,7);
Wi=Data(:,8);

% Pull out selected Picture
count=1;
for i=1:length(File_Number)
if isequal(File_Number(i),Image);
X0(count,1)=X(i);
Y0(count,1)=Y(i);
Z0(count,1)=Z(i);
U(count,1)=Ui(i);
V(count,1)=Vi(i);
W(count,1)=Wi(i);
```

```
count=count+1;
end
end

%Shift X0, Y0, Z0 so center is (0,0,0)
cx=(max(X0)+min(X0))/2;
cy=(max(Y0)+min(Y0))/2;
cz=min(Z0);
for i=1:length(X0)
X0c(i)=X0(i)-cx;
Y0c(i)=Y0(i)-cy;
Z0c(i)=Z0(i)-cz;
end

%Rotate XYZ and UVW data about z axis so that fibers are along x-axis
[ X0r,Y0r,Z0r ] = RotateZ( degrees,X0c,Y0c,Z0c );
[ Ur,Vr,Wr ] = RotateZ( degrees,U,V,W );
U=Ur;
V=Vr;
W=Wr;
X0=X0r;
Y0=Y0r;
Z0=Z0r;

% Calculate X,Y,Z at Max Pressure
Xm=X0+U;
Ym=Y0+V;
Zm=Z0+W;

%Define larger grid
x1=[min(X0):.25:max(X0)];
y1=[min(Y0):.25:max(Y0)];
[X1,Y1]=meshgrid(x1,y1);
NumberGridPoints=length(x1)^2;

%Smooth Data over Initial Geometry
Xgrid=griddata(X0,Y0,X0,X1,Y1,'cubic');
Ygrid=griddata(X0,Y0,Y0,X1,Y1,'cubic');
Zgrid=griddata(X0,Y0,Z0,X1,Y1,'cubic');
Ugrid=griddata(X0,Y0,U,X1,Y1,'cubic');
Vgrid=griddata(X0,Y0,V,X1,Y1,'cubic');
Wgrid=griddata(X0,Y0,W,X1,Y1,'cubic');

%Plot out-of-plane displacment over undeformed and deformed geometry
plotContour(Wgrid,X1,Y1)
title('W over undeformed geometry')

x1m=[min(Xm):.25:max(Xm)];
y1m=[min(Ym):.25:max(Ym)];
[X1m,Y1m]=meshgrid(x1m,y1m);
```

```
Wmgrid=griddata(Xm,Ym,W,X1m,Y1m,'cubic');

plotContour(Wmgrid,X1m,Y1m)
title('W over deformed geometry')

%Pull out Horizontal & Vertical line data for strain calculations
Size=size(Ygrid);

lineNumberH=round(Size(1,1)/2);

Xh=Xgrid(lineNumberH,:)';
Yh=Ygrid(lineNumberH,:)';
Zh=Zgrid(lineNumberH,:)';
Uh=Ugrid(lineNumberH,:)';
Vh=Vgrid(lineNumberH,:)';
Wh=Wgrid(lineNumberH,:)';

k=~isnan(Xh);
Xh=Xh(k);
Yh=Yh(k);
Zh=Zh(k);
Uh=Uh(k);
Vh=Vh(k);
Wh=Wh(k);

lineNumberV=round(Size(1,2)/2);

Xv=Xgrid(:,lineNumberV);
Yv=Ygrid(:,lineNumberV);
Zv=Zgrid(:,lineNumberV);
Uv=Ugrid(:,lineNumberV);
Vv=Vgrid(:,lineNumberV);
Wv=Wgrid(:,lineNumberV);

k=~isnan(Yv);
Xv=Xv(k);
Yv=Yv(k);
Zv=Zv(k);
Uv=Uv(k);
Vv=Vv(k);
Wv=Wv(k);

k=~isnan(Xh);
Xh=Xh(k);
Yh=Yh(k);
Zh=Zh(k);
Uh=Uh(k);
Vh=Vh(k);
Wh=Wh(k);
```

```
%Plot U,V,W displacement components along y=0 and x=0
figure
plot(Xh,Uh)
hold
plot(Xh,Vh,'r')
plot(Xh,Wh,'k')
legend('U','V','W')
title('Displacments at y=0')

figure
plot(Yv,Uv)
hold
plot(Yv,Vv,'r')
plot(Yv,Wv,'k')
legend('U','V','W')
title('Displacements at x=0')


%Calculate Exx and Eyy by central difference method
[Xcd,Exxcd,label]=horizontalLagrange(0,Xgrid,Ygrid,Zgrid,Ugrid,Vgrid,Wgrid);
[Ycd,Eyycd,lebel]=verticalLagrange(0,Xgrid,Ygrid,Zgrid,Ugrid,Vgrid,Wgrid);

%Calculate strains by fitting polynomials to U,V,W and ...
   differentiating analytically
[x,Exx]=fittedExx(order,Xh,Uh,Vh,Wh);
[y,Eyy]=fittedEyy(order,Yv,Uv,Vv,Wv);

%Plot comparision of both calculations for Exx and Eyy
orderLabel=num2str(order);
figure
plot(Xcd(2:length(Xcd)-1),Exxcd,'.r')
hold
plot(Ycd(2:length(Ycd)-1),Eyycd,'.')
plot(x,Exx)
plot(y,Eyy)
legend('Fiber Direction', 'Perpendicular direction')
title(['Strains in fiber and perpendicular direction, order ...
   ',orderLabel])

%Print analytical fit strains at apex
centerH=round(length(Exx)/2);
centerV=round(length(Eyy)/2);
%ExxApex=Exxcd(centerH)
%EyyApex=Eyycd(centerV)

%Calculate percent strain error for Central difference strains
range=5; % in mm
irange=range*4;

MaxExxCD=max(Exxcd(centerH-1-irange:centerH-1+irange));
```

```
MinExxCD=min(Exxcd(centerH-1-irange:centerH-1+irange));
MaxEyyCD=max(Eyycd(centerV-1-irange:centerV-1+irange));
MinEyyCD=min(Eyycd(centerV-1-irange:centerV-1+irange));

rangeExxCD=(MaxExxCD-MinExxCD)*100;
rangeEyyCD=(MaxEyyCD-MinEyyCD)*100;
errorExxCD=rangeExxCD/2
errorEyyCD=rangeEyyCD/2

%Calculate percent strain error for analytical fit strains
MaxExx=max(Exx(centerH-irange:centerH+irange));
MinExx=min(Exx(centerH-irange:centerH+irange));
MaxEyy=max(Eyy(centerV-irange:centerV+irange));
MinEyy=min(Eyy(centerV-irange:centerV+irange));

rangeExx=(MaxExx-MinExx)*100;
rangeEyy=(MaxEyy-MinEyy)*100;
errorExxFitted=rangeExx/2
errorEyyFitted=rangeEyy/2

%Print both strain calculations in fiber and perp. direction at apex
ExxCD_apex=Exxcd(centerH-1)*100
EyyCD_apex=Eyycd(centerV-1)*100
ExxFitted_apex=Exx(centerH)*100
EyyFitted_apex=Eyy(centerV)*100
```

C.3 Jun16FittedStrainsGrid.m

```
function [FiberStrain,PerpStrain] = ...
    Jun16FittedStrainsGrid(Data,Image,angle)
% Functional form of Jun16FittedStrains.m (see for further details)
% Returns strain in the fiber and perpedicular direction at the
% apex given an Image number and rotation angle, Strains are
% calculated by fitting a  polynomial to the displacements and
% differentiating analytically.

order=9; %order for polynomial fit

%define columns
File_Number=Data(:,1);
X=Data(:,3);
Y=Data(:,4);
Z=Data(:,5);
Ui=Data(:,6);
Vi=Data(:,7);
Wi=Data(:,8);

% Pull out selected Picture
count=1;
for i=1:length(File_Number)
if isequal(File_Number(i),Image);
X0(count,1)=X(i);
Y0(count,1)=Y(i);
Z0(count,1)=Z(i);
U(count,1)=Ui(i);
V(count,1)=Vi(i);
W(count,1)=Wi(i);
count=count+1;
end
end

%Shift X0, Y0, Z0 so center is (0,0,0)
cx=(max(X0)+min(X0))/2;
cy=(max(Y0)+min(Y0))/2;
cz=min(Z0);
for i=1:length(X0)
X0c(i)=X0(i)-cx;
Y0c(i)=Y0(i)-cy;
Z0c(i)=Z0(i)-cz;
end

%Rotate XYZ and UVW data about z axis so that fibers are along x-axis
```

```
degrees=angle; %Rotates COUNTERCLOCKWISE!!!
[ X0r,Y0r,Z0r ] = RotateZ( degrees,X0c,Y0c,Z0c );
[ Ur,Vr,Wr ] = RotateZ( degrees,U,V,W );
U=Ur;
V=Vr;
W=Wr;
X0=X0r;
Y0=Y0r;
Z0=Z0r;


% Calculate X,Y,Z at Max Pressure
Xm=X0+U;
Ym=Y0+V;
Zm=Z0+W;

%Define larger grid
x1=[min(X0):.25:max(X0)];
y1=[min(Y0):.25:max(Y0)];
[X1,Y1]=meshgrid(x1,y1);
NumberGridPoints=length(x1)^2;

%Smooth Data over Initial Geometry
Xgrid=griddata(X0,Y0,X0,X1,Y1,'cubic');
Ygrid=griddata(X0,Y0,Y0,X1,Y1,'cubic');
Zgrid=griddata(X0,Y0,Z0,X1,Y1,'cubic');
Ugrid=griddata(X0,Y0,U,X1,Y1,'cubic');
Vgrid=griddata(X0,Y0,V,X1,Y1,'cubic');
Wgrid=griddata(X0,Y0,W,X1,Y1,'cubic');

Wmgrid=griddata(Xm,Ym,W,X1,Y1,'cubic');

%Pull out Horizontal & Vertical line data
Size=size(Ygrid);

lineNumberH=round(Size(1,1)/2);

Xh=Xgrid(lineNumberH,:)';
Yh=Ygrid(lineNumberH,:)';
Zh=Zgrid(lineNumberH,:)';
Uh=Ugrid(lineNumberH,:)';
Vh=Vgrid(lineNumberH,:)';
Wh=Wgrid(lineNumberH,:)';

k=~isnan(Xh);
Xh=Xh(k);
Yh=Yh(k);
Zh=Zh(k);
Uh=Uh(k);
Vh=Vh(k);
```

```
Wh=Wh(k);


lineNumberV=round(Size(1,2)/2);

Xv=Xgrid(:,lineNumberV);
Yv=Ygrid(:,lineNumberV);
Zv=Zgrid(:,lineNumberV);
Uv=Ugrid(:,lineNumberV);
Vv=Vgrid(:,lineNumberV);
Wv=Wgrid(:,lineNumberV);

k=~isnan(Yv);
Xv=Xv(k);
Yv=Yv(k);
Zv=Zv(k);
Uv=Uv(k);
Vv=Vv(k);
Wv=Wv(k);

k=~isnan(Xh);
Xh=Xh(k);
Yh=Yh(k);
Zh=Zh(k);
Uh=Uh(k);
Vh=Vh(k);
Wh=Wh(k);

%Calculate Exx and Eyy by central difference
[Xcd,Exxcd,label]=horizontalLagrange(0,Xgrid,Ygrid,Zgrid,Ugrid,Vgrid,Wgrid);
[Ycd,Eyycd,lebel]=verticalLagrange(0,Xgrid,Ygrid,Zgrid,Ugrid,Vgrid,Wgrid);

%Fit polynomials to U,V,W and use to calculate Exx and Eyy
orderLabel=num2str(order);
[x,Exx]=fittedExx(order,Xh,Uh,Vh,Wh);
[y,Eyy]=fittedEyy(order,Yv,Uv,Vv,Wv);

%Pull out apex values to output
centerH=round(length(Exx)/2);
centerV=round(length(Eyy)/2);
ExxApex=Exx(centerH);
EyyApex=Eyy(centerV);
FiberStrain=ExxApex;
PerpStrain=EyyApex;

end

% Code to run over a series of images:
%{
count=1;
```

```
for i=11:45
[FiberStrain(count,1),PerpStrain(count,1)] = ...
   Jun16FittedStrainsGrid(Data,i,ANGLE);
count=count+1
end
%}
```

C.4 parameterFittingConsistent_Aug30.m

```
% parameterFittingConsistent_Aug30.m
%
% Fits constitutive model parameters (mu, kappa, k1, k2) given
% Stretches (fiber + perpendicular direction, computed by
% Jun16FittedStrainsGrid.m), Pressure, thickness, and initial
% guess. Matrix shear modulus is fit to toe region only, while fiber
% parameters are fit to entire data set.

%Load raw data files:
FileName='Test1_grid_1.31.11.csv';
Data=dlmread(FileName,',',1,0);

%INPUTS:
StretchDIC_F=[  1.000077919 1.000081177 1.001842164 1.005329437 ...
    1.010686471 1.017964124 1.027378777 1.039174633 1.053516928 ...
    1.070503835 1.089584957 1.10989573  1.130266346 1.148841371 ...
    1.161277387 1.168076535 1.172353611 1.173903104 1.174549644 ...
    1.175510943 1.175861413 1.175984139 1.176272325 1.176668494 ...
    1.177173227 1.17633339  1.177605755 1.177200277 1.178002901 ...
    1.178201152 1.17848202  1.178569841 1.178793714 1.178888273 ...
    1.179509361 1.179645979 1.17995341  1.180249617 1.179858291 ...
    1.180528291];   %DIC measured strech, fiber direction
StretchDIC_P=[  1.000015431 1.00009998  1.00188064  1.005630312 ...
    1.011161845 1.018683742 1.0285423   1.040646061 1.055477981 ...
    1.072822494 1.093179224 1.116214688 1.142704643 1.171982477 ...
    1.203485199 1.235077588 1.268005789 1.293038369 1.307644175 ...
    1.317582384 1.322611726 1.326049555 1.329419857 1.332560268 ...
    1.33402996  1.338404402 1.337848183 1.337683333 1.339617468 ...
    1.341860969 1.341897206 1.343312162 1.344158386 1.345665887 ...
    1.347148279 1.350604126 1.350099629 1.349794307 1.35065207  ...
    1.353087795];   %DIC measured strech, perp. direction
Pressure_tared=[    0   -0.003447379    0.01875374  0.011307402 ...
    0.031853779 0.044402237 0.070188629 0.09459607  0.130310913 ...
    0.170714191 0.215254323 0.27441134  0.339773639 0.432163387 ...
    0.546616358 0.728224265 1.033110432 1.479614914 1.937840484 ...
    2.265341455 2.497832671 2.670339498 2.843260011 2.990118342 ...
    3.123738738 3.277491825 3.418696455 3.563210567 3.708276261 ...
    3.846309302 3.986548665 4.132028044 4.268820029 4.407266755 ...
    4.557572464 4.683470732 4.836396449 4.977049497 5.112462531 ...
    5.239601855];   %Experimental Pressures

to=4.38;        %Tissue initial thickness
toe=14;         %Image corresponding to end of the toe region
firstImage=3;   %First image to use for data fitting
```

```
MaxImage=42;     %Last image to use for data fitting
rotAngle=0;      %Angle to rotate image so fiber direction = x-direction
percent=75;      %Select center % to use for ellipse fitting

mu0=4;                   % matrix shear modulus initial guess
param0=[.01, 10, 1];     % [kappa, k1, k2] initial guess


%Fit meridians to ellipse to determine curvature and stress resultants:
count=1;
for i=firstImage:MaxImage
[Xy,Zy, Yx ,Zx] = Aug29_dateExtract(Data,i, rotAngle, percent);
[ R1(count), R2(count) ] = calculateCurvatureWphi( Xy,Zy, Yx ,Zx );
count=count+1
end

K1=1./R1;   %compute curvature from radius of curvature (fiber)
K2=1./R2;   %compute curvature from radius of curvature (perp.)
Pressure=Pressure_tared;
t=to./(StretchDIC_F.*StretchDIC_P); %compute deformed thickness

%Compute Stress Resultants (fiber + perp. direction)
NfluggeF(1)=0;
NfluggeP(1)=0;
NfluggeF=0.5.*Pressure.*R2;
NfluggeP=Pressure.*R2.*(2.*R1-R2)./(2.*R1);

% Calculate Stretches through thickness for integration
StretchFm=StretchDIC_F-K1.*t.*0.5;  %Compute stretch at midplane (fiber)
StretchPm=StretchDIC_P-K2.*t.*0.5;  %Compute stretch at midplane (perp.)
StretchFin=StretchDIC_F-K1.*t;  %Compute stretch at inner surface ...
    (fiber)
StretchPin=StretchDIC_P-K2.*t;  %Compute stretch at inner surface ...
    (perp.)

% Fit Parameters to Stress Resultants:
mu=fitMuNested(StretchDIC_F, StretchDIC_P, Pressure, t, K1, K2, ...
    StretchFm,StretchPm,StretchFin,StretchPin, NfluggeF, NfluggeP, ...
    mu0, toe);
[param, ResultantF, ResultantP, Nx, Ny, costInitial, ...
    costFinal]=fitFiberNestedRevolved2D(StretchFm, StretchPm, R1, ...
    R2, Pressure, t, mu, param0, NfluggeF, NfluggeP);

%Print fitting results
mu
kappa=param(1)
k1=param(2)
k2=param(3)

%Plot model fit:
```

```
figure
plot(Pressure,NfluggeF,'.r')
hold
plot(Pressure,NfluggeP,'.k')
plot(Pressure,ResultantF,'r')
plot(Pressure,ResultantP,'k')
xlabel('Pressure')
ylabel('Resultant')
legend('Expt-F','Expt-P','Fit - F','Fit - P')

figure
h1=plot(StretchDIC_F,Nx,'k');
hold on
h2=plot(StretchDIC_P,Ny,'--k');
h3=plot(StretchDIC_F,ResultantF,'ok');
h4=plot(StretchDIC_P,ResultantP,'^k');
h5=xlabel('In-Plane Stretch at Surface');
h6=ylabel('In-Plane Stress Resultant [kPa]');
h8=legend('Expt-F','Expt-P','Fit - F','Fit - P');
h7=title('Model');
set(gca,'FontSize',18)
set(h3,'MarkerSize',8)
set(h4,'MarkerSize',8)
set(h1,'LineWidth',4)
set(h2,'LineWidth',4)
set(h5,'FontSize',18)
set(h6,'FontSize',18)
set(h7,'FontSize',18)
set(h8,'FontSize',18,'Location','NorthEast')
```

C.5 Called Functions

C.5.1 RotateZ.m

```
function [ Ur,Vr,Wr ] = RotateZ( degrees,U,V,W )
%Rotates a displacement field about the Z axis by specified angle, ...
   couterclockwise.

theta=degrees/180*pi;

Rz=[cos(theta), -sin(theta), 0;
    sin(theta), cos(theta), 0;
    0, 0, 1];


for i=1:length(W)
    temp1 = [U(i); V(i); W(i)];
    temp2 = Rz*temp1;
    Ur(i,1) = temp2(1);
    Vr(i,1) = temp2(2);
    Wr(i,1) = temp2(3);
end
end
```

C.5.2 plotContour.m

```
function [] = plotContour( Data,X,Y )
%Colored Surface Plot of grid data

figure
surface(X,Y,Data,'EdgeColor','none');
axis equal
colorbar

end
```

C.5.3 horizontalLagrange.m

```
function [ Xh,Exx,yLabel ] = ...
   horizontalLagrange(delta,Xgrid,Ygrid,Zgrid,Ugrid,Vgrid,Wgrid)
% Computes  Central Difference Large Deformation Green-Lagrange Strain
% Along a horizontal line at y=delta

    if delta==0
        gridSize=size(Ygrid);
        lineNumberH=round(gridSize(1,1)/2);
    else ...
       lineNumberH=round(gridSize(1,1)/2)-round(gridSize(1,1)/(delta*2));
    end


    Xh=Xgrid(lineNumberH,:)';
    Yh=Ygrid(lineNumberH,:)';
    Zh=Zgrid(lineNumberH,:)';
    Uh=Ugrid(lineNumberH,:)';
    Vh=Vgrid(lineNumberH,:)';
    Wh=Wgrid(lineNumberH,:)';

    %"TRIM" OUT NaN
    k=~isnan(Xh);
    Xh=Xh(k);
    Yh=Yh(k);
    Zh=Zh(k);
    Uh=Uh(k);
    Vh=Vh(k);
    Wh=Wh(k);

    yLabel=num2str(mean(Yh));

    %Calculate Exx by central difference
    for j=1:(length(Uh)-2)
        dUdX(j)=(Uh(j+2)-Uh(j))/(Xh(j+2)-Xh(j));
        dVdX(j)=(Vh(j+2)-Vh(j))/(Xh(j+2)-Xh(j));
        dWdX(j)=(Wh(j+2)-Wh(j))/(Xh(j+2)-Xh(j));

        Exx(1,j)=dUdX(j)+0.5*(dUdX(j)^2+dVdX(j)^2+dWdX(j)^2);

    end

end
```

C.5.4 verticalLagrange.m

```
function [ Yv,Eyy,xLabel] = verticalLagrange( ...
    delta,Xgrid,Ygrid,Zgrid,Ugrid,Vgrid,Wgrid )
% Computes  Central Difference Large Deformation Green-Lagrange Strain
% Along a vertical line at x=delta

    if delta==0
        lineNumberV=round(length(Xgrid)/2);
    else ...
       lineNumberV=round(length(Xgrid)/2)-round(length(Xgrid)/(delta*2));
    end


    Xv=Xgrid(:,lineNumberV);
    Yv=Ygrid(:,lineNumberV);
    Zv=Zgrid(:,lineNumberV);
    Uv=Ugrid(:,lineNumberV);
    Vv=Vgrid(:,lineNumberV);
    Wv=Wgrid(:,lineNumberV);

    %"TRIM" OUT NaN
    k=~isnan(Yv);
    Xv=Xv(k);
    Yv=Yv(k);
    Zv=Zv(k);
    Uv=Uv(k);
    Vv=Vv(k);
    Wv=Wv(k);

    xLabel=num2str(mean(Xv));

    %Calculate Eyy by central difference
    for j=1:(length(Vv)-2)
        dUdy(j)=(Uv(j+2)-Uv(j))/(Yv(j+2)-Yv(j));
        dVdy(j)=(Vv(j+2)-Vv(j))/(Yv(j+2)-Yv(j));
        dWdy(j)=(Wv(j+2)-Wv(j))/(Yv(j+2)-Yv(j));

        Eyy(1,j)=dVdy(j)+0.5*(dUdy(j)^2+dVdy(j)^2+dWdy(j)^2);

    end

end
```

C.5.5 fittedExx.m

```
function [ x,Exx ] = fittedExx( order,x,U,V,W )
% Computes Large Deformation Green-Lagrange Strain by fitting
% a polynomial to displacements and differentiating analytically
% along a horizontal line at y=delta

    pU=polyfit(x,U,order);
    plotpolyU=polyval(pU,x);
    RsquareU=rsquare(U,plotpolyU);

    pV=polyfit(x,V,order);
    plotpolyV=polyval(pV,x);
    RsquareV=rsquare(V,plotpolyV);

    pW=polyfit(x,W,order);
    plotpolyW=polyval(pW,x);
    RsquareW=rsquare(W,plotpolyW);

    for i=1:order
    dUdx(i)=pU(i)*(order+1-i);
    dVdx(i)=pV(i)*(order+1-i);
    dWdx(i)=pW(i)*(order+1-i);
    end

    plotdU=polyval(dUdx,x);
    plotdV=polyval(dVdx,x);
    plotdW=polyval(dWdx,x);

    for i=1:length(plotdU)
        Exx(i)=plotdU(i)+.5*(plotdU(i)^2+plotdV(i)^2+plotdW(i)^2);
    end

end
```

C.5.6 fittedEyy.m

```
function [ y,Eyy ] = fittedEyy( order,y,U,V,W )
% Computes Large Deformation Green-Lagrange Strain by fitting
% a polynomial to displacements and differentiating analytically
% along a vertical line at x=delta

    pU=polyfit(y,U,order);
    plotpolyU=polyval(pU,y);
    RsquareU=rsquare(U,plotpolyU);

    pV=polyfit(y,V,order);
    plotpolyV=polyval(pV,y);
    RsquareV=rsquare(V,plotpolyV);

    pW=polyfit(y,W,order);
    plotpolyW=polyval(pW,y);
    RsquareW=rsquare(W,plotpolyW);

    for i=1:order
    dUdy(i)=pU(i)*(order+1-i);
    dVdy(i)=pV(i)*(order+1-i);
    dWdy(i)=pW(i)*(order+1-i);
    end

    plotdU=polyval(dUdy,y);
    plotdV=polyval(dVdy,y);
    plotdW=polyval(dWdy,y);

    for i=1:length(plotdU)
        Eyy(i)=plotdV(i)+.5*(plotdU(i)^2+plotdV(i)^2+plotdW(i)^2);
    end

    orderLabel=num2str(order);

end
```

C.5.7 Aug29_dateExtract.m

```
function [Xy,Zy, Yx ,Zx] = Aug29_dateExtract(Data,Image, rotAngle, ...
    percent)
% Smooths displamcements and pulls out meridians for a specified image,
% rotation, and percent of image to use.

    %define columns
    File_Number=Data(:,1);
    X=Data(:,3);
    Y=Data(:,4);
    Z=Data(:,5);
    Ui=Data(:,6);
    Vi=Data(:,7);
    Wi=Data(:,8);

    % Pull out selected Picture (Max Pressure)
    count=1;
    for i=1:length(File_Number)
    if isequal(File_Number(i),Image);
    X0(count,1)=X(i);
    Y0(count,1)=Y(i);
    Z0(count,1)=Z(i);
    U(count,1)=Ui(i);
    V(count,1)=Vi(i);
    W(count,1)=Wi(i);
    count=count+1;
    end
    end

    %Rotate XYZ and UVW data about z axis so that fibers are along ...
       x-axis
    degrees=rotAngle; %Rotates COUNTERCLOCKWISE
    [ X0r,Y0r,Z0r ] = RotateZ( degrees,X0,Y0,Z0 );
    [ Ur,Vr,Wr ] = RotateZ( degrees,U,V,W );
    U=Ur;
    V=Vr;
    W=Wr;
    X0=X0r;
    Y0=Y0r;
    Z0=Z0r;

    %Shift (X0,Y0,Z0) so center is (0,0,0)
    cx=(max(X0)+min(X0))/2;
    cy=(max(Y0)+min(Y0))/2;
    xC=X0-cx;
    yC=Y0-cy;
```

```
X0c=X0-cx;
Y0c=Y0-cy;

x=xC;
y=yC;
X0=X0c;
Y0=Y0c;

%select middle of curve
percent=percent/100;
middlePercent=percent;
r=(x.^2+y.^2).^.5;
rLimit=middlePercent.*max(r);
count=1;

for i=1:length(x)
    if r(i) <= rLimit
        X0Middle(count,1)=X0(i);
        Y0Middle(count,1)=Y0(i);
        Z0Middle(count,1)=Z0(i);
        UMiddle(count,1)=U(i);
        VMiddle(count,1)=V(i);
        WMiddle(count,1)=W(i);
        count=count+1;
    end
end

Uapex=UMiddle;
Vapex=VMiddle;
Wapex=WMiddle;
X0apex=X0Middle;
Y0apex=Y0Middle;
Z0apex=Z0Middle;


%Smooth over grid
xg1=[min(X0apex):(max(X0apex)-min(X0apex))/100:max(X0apex)];
yg1=[min(Y0apex):(max(Y0apex)-min(Y0apex))/100:max(Y0apex)];
[X1,Y1]=meshgrid(xg1,yg1);
NumberGridPoints=length(xg1)^2;

Ugrid=griddata(X0apex,Y0apex,Uapex,X1,Y1,'cubic');
Vgrid=griddata(X0apex,Y0apex,Vapex,X1,Y1,'cubic');
Wgrid=griddata(X0apex,Y0apex,Wapex,X1,Y1,'cubic');

X0grid=griddata(X0apex,Y0apex,X0apex,X1,Y1,'cubic');
Y0grid=griddata(X0apex,Y0apex,Y0apex,X1,Y1,'cubic');
Z0grid=griddata(X0apex,Y0apex,Z0apex,X1,Y1,'cubic');

%pull out data to fit to ellipse, Y=0 (along fiber)
```

```
    SizeY=size(Y0grid);
    lineNumberY=round(SizeY(1,1)/2);

    Uy=Ugrid(lineNumberY,:)';
    Vy=Vgrid(lineNumberY,:)';
    Wy=Wgrid(lineNumberY,:)';
    X0y=X0grid(lineNumberY,:)';
    Y0y=Y0grid(lineNumberY,:)';
    Z0y=Z0grid(lineNumberY,:)';

    k=~isnan(X0y);
    Uy=Uy(k);
    Vy=Vy(k);
    Wy=Wy(k);
    X0y=X0y(k);
    Y0y=Y0y(k);
    Z0y=Z0y(k);

    %pull out data to fit to ellipse, X=0 (along perp)
    SizeX=size(X0grid);
    lineNumberX=round(SizeX(1,2)/2);

    Ux=Ugrid(:,lineNumberX);
    Vx=Vgrid(:,lineNumberX);
    Wx=Wgrid(:,lineNumberX);
    X0x=X0grid(:,lineNumberX);
    Y0x=Y0grid(:,lineNumberX);
    Z0x=Z0grid(:,lineNumberX);

    k2=~isnan(X0x);
    Ux=Ux(k);
    Vx=Vx(k2);
    Wx=Wx(k2);
    X0x=X0x(k2);
    Y0x=Y0x(k2);
    Z0x=Z0x(k2);

    %Report Deformed Coordinants
    Xy=X0y+Uy;
    Zy=Z0y+Wy;
    Yx=Y0x+Vx;
    Zx=Z0x+Wx;


end
```

C.5.8 calculateCurvatureWphi.m

```
function [ R1, R2 ] = calculateCurvatureWphi( Xy,Zy, Yx, Zx )
% Computes curvaturess by fitting meridians to an ellipse.

    % Fiber direction:
    FiberData(:,1)=Xy;
    FiberData(:,2)=Zy;
    [Major1, minor1, x1, z1, phi1_fit] = ellipse_fit( ...
       FiberData(:,1), FiberData(:,2));
    c1=minor1;
    a1=Major1;
    R1=(a1^2*c1^2)/(a1^2*sin(-phi1_fit)^2+c1^2*cos(-phi1_fit)^2)^(3/2);


    % Perpendicular directioN:
    PerpData(:,1)=Yx;
    PerpData(:,2)=Zx;
    [Major2, minor2, y2, z2, phi2_fit] = ellipse_fit( PerpData(:,1), ...
       PerpData(:,2));
    c2=minor2;
    b2=Major2;
    R2=(b2^2)/(b2^2*sin(-phi2_fit)^2+c2^2*cos(phi2_fit)^2)^(1/2);

end
```

C.5.9 fitMuNested.m

```
function [mu] = fitMuNested(StretchDIC_F, StretchDIC_P, Pressure, t, ...
   K1, K2, StretchFm,StretchPm,StretchFin,StretchPin,  NfluggeF, ...
   NfluggeP, mu0, toe)
   % Fits shear matrix (mu) to toe region of stress resultant - ...
      pressure data

    %Pull out toe region only:
    StretchOutF_toe=StretchDIC_F(1:toe);
    StretchOutP_toe=StretchDIC_P(1:toe);
    Pressure_toe=Pressure(1:toe);
    t_toe=t(1:toe);
    K1t=K1(1:toe);
    K2t=K2(1:toe);
    StretchFm_toe=StretchFm(1:toe);
    StretchPm_toe=StretchPm(1:toe);
    StretchFin_toe=StretchFin(1:toe);
    StretchPin_toe=StretchPin(1:toe);
    NfluggeF_toe=NfluggeF(1:toe);
    NfluggeP_toe=NfluggeP(1:toe);

    %Integrate through thickess (toe region only):
    resolution=1000;
    Y_tf=zeros(toe, resolution+1);
    Y_tp=zeros(toe, resolution+1);
    IntF=zeros(toe,1);
    IntP=zeros(toe,1);

    %Fiber Integration (toe region only):
    for i=1:length(StretchOutF_toe)
    zt=-t_toe(i)/2:t_toe(i)/resolution:t_toe(i)/2;
    Y_tf(i,:)=(StretchFm_toe(i)+K1t(i).*zt).^2-((StretchFm_toe(i)+K1t(i).*zt).*(Stre
    IntF(i,:)=trapz(zt,Y_tf(i,:));
    end

    %Perp Integration (toe region only):
    for i=1:length(StretchOutP_toe)
    zt=-t_toe(i)/2:t_toe(i)/resolution:t_toe(i)/2;
    Y_tp(i,:)=(StretchPm_toe(i)+K1t(i).*zt).^2-((StretchFm_toe(i)+K1t(i).*zt).*(Stre
    IntP(i,:)=trapz(zt,Y_tp(i,:));
    end

    %Fit matrix shear modulus (toe region only):
    [mu] = fminsearch(@muCostFunction,mu0);
        function cost = muCostFunction(mu)
```

```
            cost = sum(sqrt(( mu.*IntF' - ...
               NfluggeF_toe).^2)+(mu.*IntP' - NfluggeP_toe).^2);
        end
end
```

C.5.10 fitFiberNestedRevolved2D.m

```
function [param, ResultantF, ResultantP, Nx, Ny, cost, ...
   exitflag]=fitFiberNestedRevolved2D(StretchFmstiff, ...
   StretchPmstiff, R1, R2, Pstiff, tstiff, mu, param0, Nx, Ny)
   % Fits fiber family parameters (kappa, k1, k2) to stress ...
      resultant - pressure data

    %Select tolerances for fminsearch
    options=optimset('Display','Iter','TolFun',10^-10, 'TolX',10^-6);
    param=param0;

   % Minimize cost function to determine parameters
   [param, cost, exitflag]=fminsearch(@fiberCostFunction,param0);
   function cost = fiberCostFunction(param)
    %param=[0.25 5 100];

        K1=1./R1;
        K2=1./R2;

        kappa=param(1);
        k1=param(2);
        k2=param(3);

        %fiber Integration
        for i=1:length(StretchFmstiff)
        z=-tstiff(i)/2:tstiff(i)/1000:tstiff(i)/2;
        StretchFstiff(i,:)=StretchFmstiff(i)+K1(i).*z;
        StretchPstiff(i,:)=StretchPmstiff(i)+K2(i).*z;
        [ Yf(i,:), Yp(i,:) ] = constitutiveRelation( mu, kappa, k1, ...
           k2, StretchFstiff(i,:), StretchPstiff(i,:) );
        ResultantF(i,:)=trapz(z,Yf(i,:));
        ResultantP(i,:)=trapz(z,Yp(i,:));
        end

        ResultantFT=ResultantF';
        ResultantPT=ResultantP';

        cost = sum( sqrt((Nx - ResultantFT).^2 + (Ny - ...
           ResultantPT).^2 ));

      end

end
```

C.5.11 constitutiveRelation.m

```
function [ StressF, StressP ] = constitutiveRelation( mu, kappa,k1, ...
    k2, StretchF, StretchP )
   % Computes stress given material parameters and stretch, for one of
   % three constitutive models (use comments to select desired
   % constitutive relation)

    %Fully integrated fiber dispersion model

    dtheta = pi/100;
    theta = [dtheta:dtheta:pi];
    vonMises= exp(kappa*cos(2*theta))/(pi*besseli(0,kappa));
    jacobian = vonMises*dtheta;
    sum(jacobian);

    nsteps =length(StretchF);
    StressF = mu.*(StretchF.^2-(StretchF.*StretchP).^(-2));
    StressP = mu.*(StretchP.^2-(StretchF.*StretchP).^(-2));
    StressFP = 0.0*StressF;
    for k=1:nsteps
        IF = StretchF(k)^2;
        IP = StretchP(k)^2;
        I4 = IF*cos(theta).^2 + IP*sin(theta).^2;
        E = I4 -1;
        StressF(k) = StressF(k) + ...
            IF*sum(2.0*k1*E.*exp(k2*E.^2).*cos(theta).^2.*jacobian);
        StressP(k) = StressP(k) + ...
            IP*sum(2.0*k1*E.*exp(k2*E.^2).*sin(theta).^2.*jacobian);
        StressFP(k) = StressFP(k) + ...
            sqrt(IP*IF)*sum(2.0*k1*E.*exp(k2*E.^2).*sin(theta).*cos(theta).*jacobian)
    end


   %Gasser-Odgen-Holzapfel (2006) model with 3D fiber dispersion
    %{
        I4= StretchF.^2;
        I1=StretchF.^2 + StretchP.^2 + (StretchF.*StretchP).^-2;
        alpha=kappa.*I1 + (1-3.*kappa).*I4 - 1;

        StressF=(mu+2.*kappa.*k1.*alpha.*exp(k2.*alpha.^2)).*...
            (StretchF.^2-(StretchF.*StretchP).^-2)+...
            (2.*k1.*(1-3.*kappa).*alpha.*exp(k2.*alpha.^2)).*StretchF.^2;
        StressP=(mu+2.*kappa.*k1.*alpha.*exp(k2.*alpha.^2)).*...
            (StretchP.^2-(StretchF.*StretchP).^-2);
    %}
```

```
    %Gasser-Odgen-Holzapfel (2006) model with 2D fiber dispersion
    %{
        E=kappa.*StretchP.^2+(1-kappa).*StretchF.^2-1;
        StressF=mu.*(StretchF.^2-(StretchF.*StretchP).^(-2))+...
            2.*k1.*StretchF.^2.*E.*(1-kappa).*exp(k2.*E.^2);
        StressP=mu.*(StretchP.^2-(StretchF.*StretchP).^(-2))+...
            2.*k1.*StretchP.^2.*E.*kappa.*exp(k2.*E.^2);
    %}


end
```

Appendix D

Appendix: Remodeling Simulation Matlab Files

Table of Contents:

by Zariean et al[83] using parameters fit by FitFlynn_axialRodOnly.m and FitUniaxialData_ZareianEquillibrium.m.

constantStress_Biaxial_areaChange.m (Section D.4)

Simulates the degradation of a tissue for an applied biaxial stress state.

constantPressure_withDeposition.m (Section D.5)

Simulates a constant pressure, followed by a step increase or decrease, applied to a spherical tissue with both collagen degradation and deposition.

Called functions: (Section D.6)

herrorbar.m (by Jos van der Geest, available for download)

fitUniaxial_analytical

stress_noDeg.m

singleFiber.m

UniaxialCreep_noDeg_analytical.m

UniaxialCreep_degAndDamage_totalAreaLoss.m

stress_degAndDamage.m

singleFiber_degAndDamage_meanSE.m

ApplyStress_noDeg.m

ApplyStress_degAndDamage.m

ApplyStress_degAndDamage_withDeposition.m

stress_degAndDamage_withDeposition.m

APPENDIX D. APPENDIX: REMODELING SIMULATION MATLAB FILES

singleFiber_degAndDamage_withDeposition.m

dfGrowdT.m

D.1 FitFlynn_axialRodOnly.m

```
% FitFlynn_axialRodOnly.m
% Simulates first ~1000 seconds of single-fibril degradation experiments
% reported by Flynn et al. (2013) given mechanical and kinetic ...
   parameters.
% Damage can also be included by including damage parameters. Solves the
% nonlinear system with a Newton-Raphson iterative scheme. Prints a
% plot of radius vs. time for both experimental data and model ...
   simulation,
% as well as fiber stress vs. time plot.

clear all
clc
close all

%Flynn 2013 data - Zero Load
time_zero_exp = [   0   301 602 903];
diam_zero_exp = [   413.014 332.877 249.658 155.137];
ptime_zero = [0 300 600 900];
pstrain_zero = [0 -.1 0.5 1.8];

%Flynn 2013 data - Low load
time_low_exp = [    308 602 910];
diam_low_exp = [    245.548 235.274 215.753];
ptime_low = [300 600 2700];
pstrain_low = [0  0.3 0.3];

%Flynn 2013 data - Control
time_control_exp =[ 7   301 602 903];
diam_control_exp =[ 222.945 220.89  227.055 240.411];

%Define Constants
E0 = 0.7; %GPa
Force_array = [0,46,1054]; %nN
Probe_array = [2400.1, 1500.1, Force_array(3)]; %nN
maxProbe_array = [900 900 900]; %time of last mechanical probe
Gamma_array = [206.5, 133.25, 111.473]; %nm
color = ['r','k','b'];
delta = 0.1; %timestep for degradation (s)
tol = 10e-12; %tolerance for newton-raphson solver

%Kinetic Degradation Parmeters
G1 = 6.7e-4;
G2 = 1.0e-6;
```

```
%Damage Parameters
H = 100;  % Turn damage off (H too high for damage to proceed)
%H = 0.053; % Turn Damage on
C = .05;

%Initialize Figures
figure(1)
set(gca,'FontSize',18)
hold
xlabel('time [s]','FontSize',24)
plot(time_zero_exp,diam_zero_exp,'xr','MarkerSize',8)
plot(time_low_exp,diam_low_exp,'*k','MarkerSize',8)
plot(time_control_exp,diam_control_exp,'ob','MarkerSize',8)
axis([0 1000 150 450])

figure(2)
set(gca,'FontSize',18)
hold

%Loop over all 3 load levels
for k=1:3

    % Clear previous loop's variables
    clear Force_deg Force_load Force_unload Force_total Force
    clear D eta StretchF  Stretch totalStrain
    clear Stress
    clear r r0 r_compute time_maxprobe
    clear time

    % Select applied force and initial fiber radius
    Force_app = Force_array(k);
    R = Gamma_array(k);

    % Simulate mechanical probing --> compute force vs time
    Force_probe = Probe_array(k);
    maxProbe = maxProbe_array(k);
    loadRate = 100; %nN/s
    degInterval=300;

    Force_load = [Force_app:loadRate*delta:Force_probe];
    Force_unload = [Force_probe:-loadRate*delta:Force_app];
    degmax0 = degInterval - length(Force_load)*delta;
    degmax1 = degInterval - ...
        (length(Force_load)+length(Force_unload))*delta;
    Force_deg0 = Force_app .* ones(1,degmax0/delta);
    Force_deg1 = Force_app .* ones(1,degmax1/delta);
    Force_total_1 = [Force_deg0,Force_load, Force_unload];
    Force_total_2 = [Force_deg1,Force_load, Force_unload];
```

```
count=length(Force_total_1);

Force(1,1:length(Force_total_1)) = Force_total_1;

for probeT = [300:300:maxProbe-300]
    Force(1,[1+count:length(Force_total_2)+count]) = ...
       [Force_total_2];
    count=count+length(Force_total_2);
end

tmax = length(Force)*delta-delta;
time_plot = [0:delta:tmax];

%Initial conditions
i = 1;
temp(1)=0;
it =0;
count = 2;
D(1) = 1;
eta(1) = 0;
StretchF(1) = 1/(1-Force(1)/(E0*(1-eta(1))*pi*D(i)^2*R^2));
Stress(1) = (1-eta(1)).*E0*(StretchF(1)-1);
time(1)=0;

%Timestepping to solve nonlinear system
for t= delta:delta:tmax
    i=i+1;
    time(i)=t;

    %Initial Guess
    D(i)=D(i-1);
    eta(i) = eta(i-1);
    StretchF(i) = StretchF(i-1);

    f1 = D(i)- D(i-1)  + ...
       delta*G1*exp((-(1-eta(i))*(StretchF(i)-1)^2)/(2*G2)); ...
       %origional
    f2 = Force(i) - E0*(1-eta(i))*pi*D(i)^2*R^2*(1 - 1/StretchF(i));
    if (1-eta(i))*(StretchF(i)-1)/H <= 1
        f3 = eta(i)-eta(i-1);
    else
        f3 = eta(i) -eta(i-1) - ...
           delta*C*((1-eta(i))*(StretchF(i)-1)/H -1);
    end
    Residual = abs(sqrt(f1^2 +f2^2+f3^2));

    %Iterate
    while abs(Residual) > tol

        % Compute Jacobian
```

```
            df1dD = 1;
            df1dSe = ...
                delta*G1*exp(-(1-eta(i))*(StretchF(i)-1)^2/(2*G2))*...
                 (-(1-eta(i))*(StretchF(i)-1)/G2);
            df1de = ...
                delta*G1*exp(-(1-eta(i))*(StretchF(i)-1)^2/(2*G2))*...
                 ((StretchF(i)-1)^2)/(2*G2);

            df2dD = 2*E0*(1-eta(i))*pi*D(i)*R^2*(1-1/StretchF(i));
            df2dSe = -E0*(1-eta(i))*pi*D(i)^2*R^2*StretchF(i)^(-2);
            df2de = E0*pi*D(i)^2*R^2*(1-1/StretchF(i));

            if (1-eta(i))*(StretchF(i)-1)/H <= 1
                df3dD = 0;
                df3dSe = 0;
                df3de = 1;
            else
                df3dD = 0;
                df3dSe =  -delta*C*(1-eta(i))/H;
                df3de = 1+delta*C*(StretchF(i)-1)/H;
            end

            J = [df1dD  df2dD   df3dD;
                 df1dSe df2dSe  df3dSe;
                 df1de  df2de   df3de];

            % Update guess
            temp  = [D(i), StretchF(i), eta(i)] - [f1, f2, f3] /J;
            D(i) = temp(1);
            StretchF(i) = temp(2);
            eta(i) = temp(3);

            % Check if new guess is below tolerance
            f1 = D(i)- D(i-1)  + ...
                delta*G1*exp((-(1-eta(i))*(StretchF(i)-1)^2)/(2*G2)); ...
                %origional
            f2 = Force(i) - E0*(1-eta(i))*pi*D(i)^2*R^2*(1 - ...
                1/StretchF(i));
            if (1-eta(i))*(StretchF(i)-1)/H <= 1
                f3 = eta(i)-eta(i-1);
            else
                f3 = eta(i) -eta(i-1) - ...
                    delta*C*((1-eta(i))*(StretchF(i)-1)/H -1);
            end
            Residual = abs(sqrt(f1^2 +f2^2+f3^2));

        end

    end
```

```
    %Compute degraded and deformed radius, degradation rate, fiber ...
       strain
    gamma0 = D.*R;
    gamma = gamma0 ./ sqrt(StretchF);
    dr0dt = (max(gamma0)-min(gamma0))/(max(time)-min(time));
    strainF = (StretchF-1);

    % Compute "apparent" radius from change in fiber stiffness
    % (equivilent to model fiber radius for no damage)
    if k <3
        count=1;
        for l = 2:length(Force)-1
            if Force(l) > Force(l-1) && Force(l) > Force(l+1)
                r_compute(count) = ...
                   sqrt(Force(l)/(pi*E0*strainF(l)));  % in nm
                time_maxprobe(count) = time(l);
                count=count+1;
            end
        end
    else
        r_compute = sqrt(Force./(pi.*E0.*strainF));
        time_maxprobe =time;
    end

    %Plot fiber radius vs. time
    figure(1)
    if k <3
    plot([0,time_maxprobe],[Gamma_array(k)*2,r_compute.*2],..
        ['--o',color(k)],'LineWidth',2)
    else
    plot([0,time_maxprobe],[Gamma_array(k)*2,r_compute.*2],...
        ['--',color(k)],'LineWidth',2)
    end
    ylabel('Fibril diameter [nm]','FontSize',24)
    h1=legend('Expt - 0 nN','Expt - 46 nN','Expt - control','Model - ...
       0 nN','Model - 46 nN','Model - 1054 nN');
    set(h1,'Location','NorthEast')

    %Plot fiber stress vs. time
    figure(2)
    plot(E0.*(1-eta).*(StretchF-1),color(k))
    ylabel('Stress [GPa]')
    legend('zero','load','high')


end
```

D.2 FitUniaxialData_ZareianEquillibrium.m

```
% FitUniaxialData_ZareianEquillibrium.m
% Simulates uniaxial extension of a non-degrading tissue strips
% held under constant force. Compares the stress-strech behavior
% to that reported by Zareian et al. (2010) for bovine cornea
% strips, where each data point is measured after 15 minutes
% of creep (equillibrium). Plots stress-stretch results for
% both simulation and experiment.

clear all
close all
clc

%Input Parameters
E0 = .05; %Gpa
crimpAngle = 30; %Crimp angle in degrees.
AB = crimpAngle*2*pi/360; %Crimp angle in radians
Beta0 = 0.02;
b_disp = 0;
mu = 2.6e-5;

a = AB;
b = 1;
xStep = (2*pi/b)/100;
X1=[0:xStep:2*pi/b];
X2 =a.*sin(b.*X1);
Theta0 = a*b.*cos(b.*X1);
L = max(X1);

%Degredation params
G1 = 6.8e-4;
G2 = 2e-6;
H = 0.05;
C=0.01;

%Discretization in phi and tolerance for nonlinear solve
dphi = pi/50;
phi = [0:dphi:pi];
tol = 1e-12;
%delta = 10;
%tmax = 1000;

% Data extracted from Zareian et al. (2010)
stretchEqm = [1.0377, 1.0524, 1.0759];
```

```
stretchEqm_error = [0.0044, 0.0036, 0.0105];
Force_matrix = [0.1e-9, 0.25e-9, 0.5e-9]; %GN
A0 = (4.5/1000^2); % m^2
Stress11_matrix = Force_matrix.*stretchEqm./A0;
Stress22_target = 0;

% Specify max force and discretization
Force_max = max(Force_matrix);
forceStep = (Force_max)/10;
Force = [0:forceStep:Force_max];

% Initial Guess
alpha_ramp= zeros(1,length(phi));
Stretch11_array = [1:(max(stretchEqm)-1)/10:max(stretchEqm)];
Stretch22_array = ones(1,length(Force));

%Timestepping to solve for stretch given applied forces
tic
for i = 2:length(Stretch11_array)

    i
    [ Stretch22_array(i), Stress11_ramp(i),Stress22_ramp(i), ...
       alpha_ramp(i,:), it, residual ] = fitUniaxial_analytical( ...
       Stretch11_array(i), Stretch22_array(i-1), mu, b_disp, E0, ...
       Beta0, Theta0, X1, alpha_ramp(i-1,:), dphi, tol, ...
       Stress22_target );


end
toc

% Plot Stress-Streth relationship for simulation and experiment
figure
set(gca,'FontSize',24)
h1=herrorbar(stretchEqm, Stress11_matrix.*10^6, stretchEqm_error,'*r')
hold
h2=plot( Stretch11_array, Stress11_ramp.*10^6,'k')
set(h1,'MarkerSize',10)
set(h1,'LineWidth',1.25')
set(h2,'LineWidth',1.5)
xlabel('\lambda_{11}','Fontsize',24)
ylabel('\sigma_{11} [kPa]','Fontsize',24)
legend([h1(2),h2], 'Experiment','Model')
```

D.3 Zareian_Prediction.m

```
% Zarien_Prediction.m
% Simulates the first 360 s of the degradation of bovine cornea
% strips under uniaxial constant force reported by Zariean et al. ...
   (2010).
% Simulates all 3 load levels (load, medium, high). Capable of including
% damage if parameters are included. Plots stretch vs. time for
% both experimental data and simulation, and remaining fiber mass
% distribution at the end of degradation for each force level.

clear all
close all
clc

tic

%Elastica and Tissue Mechanical Parameters
E0 = 0.05;
crimpAngle = 30;
AB = crimpAngle*2*pi/360; %Crimp angle in radians
Beta0 = 0.02;
b_disp = 0;
mu = 2.6e-5;

%Degredation params
G1 = 6.7e-4;
G2 = 1e-6;
H = 1e6; % NO DAMAGE
%H = 0.053; %Enable to model damage
C = 0.05;

%Descritize
a = AB;
b = 1;
xStep = (2*pi/b)/100;
X1=[0:xStep:2*pi/b];
X2 =a.*sin(b.*X1);
Theta0 = a*b.*cos(b.*X1);
L = max(X1);
dphi = pi/100;
phi = [0:dphi:pi];
vonMises= exp(b_disp.*cos(2.*phi))./(2*pi*besseli(0,b_disp));
tol = 1e-12;
delta = 5;
```

```
tmax = 360;
n=3;

%Force levels and initial cross-sectional area
Force_matrix = [0.1e-9, 0.25e-9, 0.5e-9]; %GN
Stress22_target = 0;  %uniaxial tension BC
A0 = (4.5/1000^2); % m^2

% Data from Zariean 2010 degradation studies:
% (time in minutes vs percent strain, for Low, Medium,
% and High force levels, both lower and upper
% bounds of reported strain from multiple experiments).

Low_lower  =  [15.040   3.380
            18.064  4.507
            21.008  6.056
            23.952  7.254
            27.056  8.169
            30.000  9.014];

Low_upper = [15.040 4.296
            18.064  5.493
            21.008  6.901
            23.952  7.958
            27.056  8.873
            30.000  9.930];

Med_lower = [15.080 5.000
            17.968  5.274
            21.016  6.370
            24.064  7.192
            27.032  7.945
            30.000  8.836];

Med_upper = [14.920 5.753
            17.968  6.233
            21.016  7.123
            24.064  8.014
            27.032  8.836
            30.000  9.726];

High_lower = [15.000    6.745
            18.011  7.500
            21.021  8.585
            24.032  9.906
            27.042  10.991
            30.106  12.264];

High_upper = [15.000    9.009
            18.011  9.670
```

```
            21.074  10.708
            24.032  11.651
            27.042  13.066
            30.053  14.434];

% Compute stretch and error bars from experimental data
t_exp1 = (Low_upper(:,1) - Low_upper(1,1)).*60;
Low_mean = (Low_upper(:,2)+Low_lower(:,2))./2;
Low_error = Low_upper(:,2)-Low_mean;
stretch_exp1 = sqrt(2.*Low_mean./100+1);
stretch_exp1_upper = sqrt(2.*Low_upper(:,2)./100+1);
stretch_exp1_error = stretch_exp1_upper - stretch_exp1;

t_exp2 = (Med_upper(:,1) - Med_upper(1,1)).*60;
Med_mean = (Med_upper(:,2)+Med_lower(:,2))./2;
Med_error = Med_upper(:,2)-Med_mean;
stretch_exp2 = sqrt(2.*Med_mean./100+1);
stretch_exp2_upper = sqrt(2.*Med_upper(:,2)./100+1);
stretch_exp2_error = stretch_exp2_upper - stretch_exp2;

t_exp3 = (High_upper(:,1) - High_upper(1,1)).*60;
High_mean = (High_upper(:,2)+High_lower(:,2))./2;
High_error = High_upper(:,2)-High_mean;
stretch_exp3 = sqrt(2.*High_mean./100+1);
stretch_exp3_upper = sqrt(2.*High_upper(:,2)./100+1);
stretch_exp3_error = stretch_exp3_upper - stretch_exp3;

%Initialize Plots
figure(1)
set(gca,'FontSize',18)
errorbar(t_exp1(1:n),stretch_exp1(1:n),stretch_exp1_error(1:n),'--*b')
hold
errorbar(t_exp2(1:n),stretch_exp2(1:n),stretch_exp2_error(1:n),'--*k')
errorbar(t_exp3(1:n),stretch_exp3(1:n),stretch_exp3_error(1:n),'--*r')
xlabel('time [s]')
ylabel('\lambda_{11}')
legend('Expt - 0.1 N','Expt - 0.25 N','Expt - 0.5 N','Model - 0.1 ...
   N','Model - 0.25 N','Model - 0.50 N')

color = [ 'b','k','r'];
Force_array = [ '0.25 N';'0.25 N';'0.50 N'];

% Loop over all 3 force levels applied
for k = 1:3

    % Ramp up to applied constant force
    Force_max = Force_matrix(k);
    forceStep = (Force_max)/10;
    Force = [0:forceStep:Force_max];
```

```
%Initial Guess for Ramp-Up
alpha_ramp= zeros(1,length(phi));
Stretch11_array = ones(1,length(Force));
Stretch22_array = ones(1,length(Force));

for i = 2:length(Force)
    i
    [ Stretch11_array(i), Stretch22_array(i), ...
       Stress11_ramp(i),Stress22_ramp(i), alpha_ramp(i,:), ...
       avgStrainf0(i,:)] = UniaxialCreep_noDeg_analytical( ...
       Stretch11_array(i-1), Stretch22_array(i-1),  mu, b_disp, ...
       E0, alpha_ramp(i-1,:), Beta0, Theta0, X1, dphi, tol, ...
       Force(i), A0, Stress22_target );
end

%Initial guesses for degradation
Fg =   [1, 0, 0;
        0, 1, 0;
        0, 0, 1];

alpha(1,:) = alpha_ramp(i,:);
D(1,:) = ones(1,length(phi));
xi(1,:) = zeros(1,length(phi));

Stretch11(1) = Stretch11_array(i);
Stretch22(1) = Stretch22_array(i);
Stress11 = Stress11_ramp(i);
Stress11_deg(1) = Stress11;
Stress22_deg(1) = Stress22_target;

Stretch11_e(1) = Stretch11(1);
Stretch22_e(1) = Stretch22(1);

i=1;

% Timestep for tissue degradation nonlinear solve for stretches
for t = delta:delta:tmax
    t
    i=i+1;

    % Compute elastic stretch from initial guess:
    Stretch11_e(i-1) = Stretch11(i-1)/Fg(1,1);
    Stretch22_e(i-1) = Stretch22(i-1)/Fg(2,2);

    % Solve for elastic stretch given stress state:
    [ Stretch11_e(i), Stretch22_e(i), Stress11_deg(i) ...
       ,Stress22_deg(i), alpha(i,:), D(i,:), xi(i,:), ...
       avgStrainf(i,:), Fg ] = ...
       UniaxialCreep_degAndDamage_totalAreaLoss( ...
       Stretch11_e(i-1), Stretch22_e(i-1), alpha(i-1,:), ...
```

```
            D(i-1,:), xi(i-1,:), G1, G2, C, H, mu, b_disp, E0, ...
            Beta0, Theta0, X1, Stress22_target, Force_max, A0, ...
            delta, dphi, tol );

        %Compute total stretch from elastic stretch and growth tensor:
        Stretch11(i) = Stretch11_e(i)*Fg(1,1);
        Stretch22(i) = Stretch22_e(i)*Fg(2,2);
        Stretch33(i) = Fg(3,3)/(Stretch11_e(i)*Stretch22_e(i));

        strain(i) = 1/2*(Stretch11(i)^2-1);
        time(i) = t;
        macroStretch(i,:) = ...
            sqrt(Stretch11(i)^2.*cos(phi).^2+Stretch22(i)^2.*sin(phi).^2 ...
            );
        avgStressf(i,:) = E0.*(1-xi(i,:)).*avgStrainf(i,:);

    end

    %For Initially Isotropic:
    MassDist_initial = D(1,:).^2;
    MassDist_final = D(i,:).^2;

    %Plot Results
    figure(1)
    plot(time, Stretch11,color(k))
    Stretch11_creep(k,:)=Stretch11;

    %Polar plot of fiber mass distribution
    figure
    h0=polar([phi-pi,phi],[MassDist_initial,MassDist_initial],'--k');
    hold
    h1=polar([phi-pi,phi],[MassDist_final,MassDist_final],[color(k)]);
    set(h1,'LineWidth',2);
    set(h0,'LineWidth',2);
    set(gca,'FontSize',18)
    title(['Mass Fraction(\phi ) = D^2(\phi ), Force = ...
        ',Force_array(k,:)])
    legend('Initial','Degraded (6 min.)')

end


% Compute creep rates (assuming linear)
temp1 = polyfit(t_exp1(1:n),stretch_exp1(1:n),1);
temp2 = polyfit(t_exp2(1:n),stretch_exp2(1:n),1);
temp3 = polyfit(t_exp3(1:n),stretch_exp3(1:n),1);
rateExp1 = temp1(1)     %Print experimental creep rates
rateExp2 = temp2(1)
rateExp3 = temp3(1)
```

```
temp01 = polyfit(time,Stretch11_creep(1,:),1);
temp02 = polyfit(time,Stretch11_creep(2,:),1);
temp03 = polyfit(time,Stretch11_creep(3,:),1);
rateMod1 = temp01(1)    %Print simulation creep rates
rateMod2 = temp02(1)
rateMod3 = temp03(1)

%Print Relative creep rates
rateExp1/rateExp3 %Experimental
rateExp2/rateExp3
rateMod1/rateMod3 %Simulation
rateMod2/rateMod3

% Add figure legend
figure(1)
legend('Exp - 0.1N','Exp - 0.25N','Exp -0.5N','Model - 0.1N','Model ...
    - 0.25N','Model - 0.5N')
```

D.4 constantStress_Biaxial_areaChange.m

```
% constantStress_Biaxial_areaChange.m
%
% Simulates a degrading tissue subject to constant biaxial stress (or,
% uniaxial stress when Stress22 = 0). First ramps up to biaxial stress
% state without degradation, then simulates degradation while stress is
% held constant. Plots total mass loss vs time, stretch vs. time, and
% a polar plot of the fiber mass distribution for the final timestep.

clear all
close all
clc

% Elastica Mechanical Parameters
E0 = 0.05; % GPa
crimpAngle = 30;
AB = crimpAngle*2*pi/360; %Crimp angle in radians
Beta0 = 0.02;
b_disp = 0; % isotropics
mu = 2.6e-5; % GPa
A0 = (4.5/1000^2); % tissue initial cross-sectional area, [m^2]

% Degredation Parameters
G1 = 6.7e-4;
G2 = 1e-6;

% Damage Parameters
H = 1e6; % Turn damage off (H too high for damage to proceed)
%H = 0.053; % Turn damage on
C = 0.05;

% Loading Conditions
Stress11_target = 40e-6; % in GPa
Stress22_target = 30e-6;  % in GPa

%Numerical Parameters
a = AB;
b = 1;
xStep = (2*pi/b)/100;
X1=[0:xStep:2*pi/b];
X2 =a.*sin(b.*X1);
Theta0 = a*b.*cos(b.*X1);
L = max(X1);
dphi = pi/100;
```

```
phi = [0:dphi:pi];
vonMises= exp(b_disp.*cos(2.*phi))./(2*pi*besseli(0,b_disp));
tol = 1e-12;
delta = 10;
tmax = 4000;

% Discretize
stressStep11 = (Stress11_target)/10;
stressStep22 = (Stress22_target)/10;
Stress11_ramp = [0:stressStep11:Stress11_target];
Stress22_ramp = [0:stressStep22:Stress22_target];

%Initial Guess for Ramp-Up
alpha_ramp= zeros(1,length(phi));
Stretch11_ramp = ones(1,length(Stress11_ramp));
Stretch22_ramp = Stretch11_ramp;

% Ramp up to target stress state (initial guess for degradation)
for i = 2:length(Stress11_ramp)
    i
    [ Stretch11_ramp(i), Stretch22_ramp(i), ~,~, alpha_ramp(i,:), ~] ...
       = ApplyStress_noDeg( Stretch11_ramp(i-1), ...
       Stretch22_ramp(i-1),  mu, b_disp, E0, alpha_ramp(i-1,:), ...
       Beta0, Theta0, X1, dphi, tol, Stress11_ramp(i), ...
       Stress22_ramp(i) );

end

%Initial guesses for degradation
Fg = [1, 0, 0;
      0, 1, 0;
      0, 0, 1];

alpha(1,:) = alpha_ramp(i,:);
D(1,:) = ones(1,length(phi));
xi(1,:) = zeros(1,length(phi));

%Initialize Stretch and Stress Arrays
Stretch11(1) = Stretch11_ramp(i);
Stretch22(1) = Stretch22_ramp(i);
Stretch33(1) = 1/(Stretch11(1)*Stretch22(1));
Stretch11_e(1) = Stretch11(1);
Stretch22_e(1) = Stretch22(1);
Stretch33_e(1) = 1/(Stretch11_e(1)*Stretch22_e(1));
Stretch33_g(1) =1;
Stress11 = Stress11_target;
Stress22 = Stress22_target;

totalMassFrac(1) = 1;
```

```
% Degradation Simulation - discretized over time
i=1;
tic
for t = delta:delta:tmax
    t
    i=i+1;
    time(i) = t;

    % Compute elastic stretch from Fe and Fg(n-1):
    Stretch11_e(i-1) = Stretch11(i-1)/Fg(1,1);
    Stretch22_e(i-1) = Stretch22(i-1)/Fg(2,2);

    % Iteratively solve for elastic stretch given biaxial stress state,
    % Compute Fg for next timestep.
    [ Stretch11_e(i), Stretch22_e(i), ~ ,~, alpha(i,:), D(i,:), ...
       xi(i,:), avgStrainf(i,:), Fg ] = ApplyStress_degAndDamage( ...
       Stretch11_e(i-1), Stretch22_e(i-1), alpha(i-1,:), D(i-1,:), ...
       xi(i-1,:), G1, G2, C, H, mu, b_disp, E0, Beta0, Theta0, X1, ...
       Stress11_target, Stress22_target, delta, dphi, tol );

    %Compute total stretch (F = FeFg)
    Stretch11(i) = Stretch11_e(i)*Fg(1,1);
    Stretch22(i) = Stretch22_e(i)*Fg(2,2);
    Stretch33(i) = Fg(3,3)/(Stretch11_e(i)*Stretch22_e(i));
    Stretch33_e(i) = 1/(Stretch11_e(i)*Stretch22_e(i));

    D_min = min(D(i,:))
    xi_max = max(xi(i,:));
    totalMassFrac(i) = 1/pi * trapz(phi,D(i,:).^2);
    Stretch33_g(i) = Fg(3,3);

end
toc

MassDist_initial = D(1,:).^2;
MassDist_final = D(i,:).^2;

% Print plot of total mass fraction remaining vs time
figure
set(gca,'FontSize',18)
h3=plot(time, totalMassFrac,'--k')
set(h3,'LineWidth',2);
xlabel('time [s]')
ylabel('Total Mass Fraction Remaining')
axis([0 max(t) 0 1])

% Print plot of stretch vs time during degradation
figure
set(gca,'FontSize',18)
hold
```

```
set(gca,'FontSize',18)
h00=plot(time, Stretch11,'--k');
set(h00,'LineWidth',2);
xlabel('time [s]')
ylabel('Stretch11')

% Print polar plot of initial & final mass distribution function
figure
set(gca,'FontSize',24)
h1=polar([phi-pi,phi],[MassDist_initial,MassDist_initial],':c');
hold
h4=polar([phi-pi,phi],[MassDist_final,MassDist_final],'r');
set(h4,'LineWidth',4);
legend('0 s','4000 s')
```

D.5 constantPressure_withDeposition.m

```
% constantPressure_withDeposition.m
%
% Simulates a spherical tissue subject to a constant pressure,
% followed by a step increase or decrease in pressure, while both
% collagen degradation and deposition proceed. Plots tissue thickness,
% stress, and stretch with time before and after perturbation.

clear all
close all
clc

% Elastica Mechanical Parameters
E0 = 0.05; % GPa
crimpAngle = 30;
AB = crimpAngle*2*pi/360; %Crimp angle in radians
Beta0 = 0.02;
b_disp = 0;
mu = 2.6e-5; %GPa

% Spherical tissue geometric parameters
t0 = 1; % mm
R0=12.5; % mm

%Degredation and deposition parameters
G1 = 6.7e-4; % degradation parameter
G2 = 1e-6;   % degradation parameter
kd = 1e-4;   % deposition parameter


% Damage parameters
H = 1e6; % Turn damage off (H too high for damage to proceed)
%H = 0.053; % Turn damage on
C = 0.05;

% Loading state and time
P_init=2e-6; % initial pressure [GPa]
P_peturb = 1.75e-6; % peteurbed pressure [GPa]
t_peturb = 4000; % perturbation time [s]
tmax = 8000; % total simulation time [s]

%Numerical Parameters
a = AB;
b = 1;
```

```
xStep = (2*pi/b)/100;
X1=[0:xStep:2*pi/b];
X2 =a.*sin(b.*X1);
Theta0 = a*b.*cos(b.*X1);
L = max(X1);
dphi = pi/100;
phi = [0:dphi:pi];
vonMises= exp(b_disp.*cos(2.*phi))./(2*pi*besseli(0,b_disp));
tol = 1e-12;
delta = 10;

% Stress state for pressure applied to thin spherical shell
P0 = P_init;
Stress11_target = (P0*R0)/(2*t0);
Stress22_target = Stress11_target;
stressStep = (Stress11_target)/10;
Stress11_ramp = [0:stressStep:Stress11_target];
Stress22_ramp = [0:stressStep:Stress22_target];

%Initial Guess for Ramp-Up
alpha_ramp= zeros(1,length(phi));
Stretch11_ramp = ones(1,length(Stress11_ramp));
Stretch22_ramp = Stretch11_ramp;

% Ramp up to target stress state (initial guess for degradation)
for i = 2:length(Stress11_ramp)

    i;
    [ Stretch11_ramp(i), Stretch22_ramp(i), ~,~, alpha_ramp(i,:), ~] ...
       = ApplyStress_noDeg( Stretch11_ramp(i-1), ...
       Stretch22_ramp(i-1),  mu, b_disp, E0, alpha_ramp(i-1,:), ...
       Beta0, Theta0, X1, dphi, tol, Stress11_ramp(i), ...
       Stress22_ramp(i) );

end

%Initial guesses for degradation
Fg = [1, 0, 0;
      0, 1, 0;
      0, 0, 1];

alpha(1,:) = alpha_ramp(i,:);
D(1,:) = ones(1,length(phi));
xi(1,:) = zeros(1,length(phi));

%Initialize Stretch and Stress Arrays
Stretch11(1) = Stretch11_ramp(i);
Stretch22(1) = Stretch22_ramp(i);
Stretch33(1) = 1/(Stretch11(1)*Stretch22(1));
Stretch11_e(1) = Stretch11(1);
```

```
Stretch22_e(1) = Stretch22(1);
Stretch33_e(1) = 1/(Stretch11_e(1)*Stretch22_e(1));
Stretch33_g(1) =1;
Stress11 = Stress11_target;
Stress22 = Stress22_target;

totalMassFrac(1) = 1;

i=1;

for t = delta:delta:tmax
    t
    i=i+1;
    time(i) = t;

    % Compute elastic stretch from Fe and Fg(n-1):
    Stretch11_e(i-1) = Stretch11(i-1)/Fg(1,1);
    Stretch22_e(i-1) = Stretch22(i-1)/Fg(2,2);

    % Apply perturbation if t is past perturbation time
    if t > t_peturb
        P0 = P_peturb;
    end

    % Compute current thickness, radius and stresses based on previous
    % timestep values of Fe and Fg
    t = t0*Fg(3,3)/(Stretch11_e(i-1)*Stretch22_e(i-1));
    R = R0*Stretch11_e(i-1);
    Stress11_target = (P0*R)/(2*t);
    Stress22_target = Stress11_target;

    % Compute stretches given applied Stress state
    [ Stretch11_e(i), Stretch22_e(i), Stress11(i) ,Stress22(i), ...
       alpha(i,:), D(i,:), xi(i,:), avgStrainf(i,:), Fg ] = ...
       ApplyStress_degAndDamage_withDeposition( Stretch11_e(i-1), ...
       Stretch22_e(i-1), alpha(i-1,:), D(i-1,:), xi(i-1,:), G1, G2, ...
       C, H, mu, b_disp, E0, Beta0, Theta0, X1, Stress11_target, ...
       Stress22_target, delta, dphi, tol, kd );

    %Compute total stretch (F = FeFg)
    Stretch11(i) = Stretch11_e(i)*Fg(1,1);
    Stretch22(i) = Stretch22_e(i)*Fg(2,2);
    Stretch33(i) = Fg(3,3)/(Stretch11_e(i)*Stretch22_e(i));
    Stretch33_e(i) = 1/(Stretch11_e(i)*Stretch22_e(i));

    D_min = min(D(i,:))
    xi_max = max(xi(i,:));
    totalMassFrac(i) = 1/pi * trapz(phi,D(i,:).^2);
    Stretch33_g(i) = Fg(3,3);
```

```
end

% Plot thickness vs. time, before and after perturbation:
figure
set(gca,'FontSize',18)
hold
h00=plot(time, Stretch33_g.*t0,'--k');
set(h00,'LineWidth',2);
xlabel('time [s]')
ylabel('Thickness')

% Plot stretch vs. time, before and after perturbation:
figure
set(gca,'FontSize',18)
hold
h00=plot(time, Stretch11,'r');
set(h00,'LineWidth',2);
xlabel('time [s]')
ylabel('Stretch11')

% Plot stress vs. time, before and after perturbation:
figure
set(gca,'FontSize',18)
hold
h01=plot(time, Stress11.*10^6,'--b');
set(h01,'LineWidth',2);
xlabel('time [s]')
ylabel('Stress11 [KPa]')
```

D.6 Called functions

D.6.1 fitUniaxial_analytical.m

```
function [ Stretch22, Stress11,Stress22, alphaNew, it, residual ] = ...
    fitUniaxial_analytical( Stretch11, Stretch22_initial, mu, ...
    b_disp, E, Beta, Theta0, X1, alphaPrev, dphi, tol, ...
    Stress22_target )
% Computes Stretch22 for Stress22 (=0 for uniaxial tension),
% by a Newton-Raphson iterative scheme, when Stretch11 is known
% and given an initial guess for Stretch22 and the internal variable
% alpha(phi). [NO DEGRADATION]

    % Check if initial guess is within tolerance, and compute jacobian
    Stretch22 = Stretch22_initial;
    [ Stress11, Stress22, alphaNew, avgStrain, dStress22dStretch22, ~...
         ] = stress_noDeg( Stretch11, Stretch22, alphaPrev, mu, ...
       b_disp, E, Beta, Theta0, X1, dphi, tol );
    residual = Stress22-Stress22_target;

    % Iterate to solve for Stretch22
    it=0;
    if abs(residual) > tol

        while abs(residual) > tol

            it = it+1;

            %Update guess
            Stretch22_update = Stretch22 - residual/dStress22dStretch22;
            Stretch22 = Stretch22_update;

            %Check Residual
            [ Stress11, Stress22, alphaNew, avgStrain, ...
               dStress22dStretch22, ~  ] = stress_noDeg( Stretch11, ...
               Stretch22, alphaPrev, mu, b_disp, E, Beta, Theta0, ...
               X1, dphi, tol );
            residual = Stress22 - Stress22_target;

        end

    it;

end
```

D.6.2 stress_noDeg.m

```
function [ Stress11, Stress22, alpha, avgStrain, ...
   dStress22dStretch22, J ] = stress_noDeg( Stretch11, Stretch22, ...
   alphaPrev, mu, b_disp, E, Beta, Theta0, X1, dphi, tol )
% Computes the plane stress state (Stress11 and Stress22) given a
% biaxial stretch state for a tissue modeled as a distribution of
%  elasticas in an  isotropic ground matrix. Requires an initial guess
% for the internal  variable alpha(phi). [NO DEGRADATION]

    % Discretize in phi, compute fiber distribution function and
    % array of fiber micro-stretches:
    phi = [0:dphi:pi];
    vonMises= exp(b_disp.*cos(2.*phi))./(2*pi*besseli(0,b_disp));
    macroStretch = ...
        sqrt(Stretch11.^2.*cos(phi).^2+Stretch22.^2.*sin(phi).^2 );

    % Solve for fiber displacment and stress at each angle, phi
    for i = 1:length(phi)
        [ alpha(i), theta, stretchF, dSEbendDmacro(i), ...
           dSEaxialDmacro(i), avgStrain(i), dSEdMacro2(i)] = ...
           singleFiber( macroStretch(i), alphaPrev(i), E, Beta, ...
           Theta0, X1, tol );
    end

    % Sum all fiber contributions and add to matrix stress for total
    % tissue stress :
    Stress11 = mu*(Stretch11^2-(Stretch11*Stretch22)^(-2)) + ...
       2*trapz(phi, (dSEbendDmacro + ...
       dSEaxialDmacro).*(macroStretch).^(-1).*Stretch11^2.*cos(phi).^2...
        .*vonMises);
    Stress22 = mu*(Stretch22^2-(Stretch11*Stretch22)^(-2)) + ...
       2*trapz(phi, (dSEbendDmacro + ...
       dSEaxialDmacro).*(macroStretch).^(-1).*Stretch22^2.*sin(phi).^2...
        .*vonMises);

    %Compute Jacobian for Newton-Raphson
    dMacrodStretch11 = (Stretch11.*cos(phi).^2)./macroStretch;
    dMacrodStretch22 = (Stretch22.*sin(phi).^2)./macroStretch;

    dStress11dStretch11 = ...
       2*mu*(Stretch11+1/(Stretch11^3*Stretch22^2)) + 2.*trapz(phi, ...
       (dSEdMacro2.*dMacrodStretch11.*Stretch11^2./macroStretch + ...
       (dSEbendDmacro + ...
       dSEaxialDmacro).*(2.*Stretch11./macroStretch - ...
       (Stretch11^2./macroStretch.^(2)).*dMacrodStretch11)).*cos(phi).^2...
```

```
        .*vonMises);
    dStress11dStretch22 = 2*mu/(Stretch11^2*Stretch22^3) + ...
       2.*trapz(phi, ...
       (dSEdMacro2.*dMacrodStretch22.*Stretch11.^2./macroStretch + ...
       (dSEbendDmacro + ...
       dSEaxialDmacro).*(-Stretch11^2./macroStretch.^2).*dMacrodStretch22)...
        .*cos(phi).^2.*vonMises);
    dStress22dStretch11 = 2*mu/(Stretch11^3*Stretch11^2) + ...
       2*trapz(phi, ...
       (dSEdMacro2.*dMacrodStretch11.*Stretch22^2./macroStretch + ...
       (dSEbendDmacro + ...
       dSEaxialDmacro).*(-Stretch22^2./macroStretch.^2).*dMacrodStretch11)...
        .*sin(phi).^2.*vonMises);
    dStress22dStretch22 ...
       =2*mu*(Stretch22+1/(Stretch11^2*Stretch22^3)) + ...
       2.*trapz(phi, ...
       dSEdMacro2.*dMacrodStretch22.*(macroStretch).^(-1)...
        .*(Stretch22.^2.*sin(phi).^2).*vonMises + (dSEbendDmacro + ...
           dSEaxialDmacro).*(2.*Stretch22./macroStretch - ...
           Stretch22^2.*macroStretch.^(-2).*dMacrodStretch22).*sin(phi).^2...
        .*vonMises);

    J = [ dStress11dStretch11   dStress22dStretch11;
          dStress11dStretch22   dStress22dStretch22];


end
```

D.6.3 singleFiber.m

```
function [ alpha, theta, stretchF, dSEbendDmacro, dSEaxialDmacro, ...
    avgStrain, dSEdMacro2 ] = singleFiber( macroStretch_app, ...
    alphaPrev, E, Beta, Theta0, X1, tol )
% Computes deformed shape (theta), fiber stretch, and internal variable
% alpha for a single elastica given an applied macro-stretch and an
% initial guess for alpha using a Newton-Raphson scheme.
% [NO DEGRADATION]

    %Initial guess
    alpha=alphaPrev;
    L = max(X1);

    %Check initial guess residual
    theta = (Beta.*Theta0)./(4*alpha + 4*alpha^2 +Beta);
    stretchF = 1+alpha.*cos(theta);
    macroStretch = 1/L*trapz(X1,stretchF.*cos(theta)./cos(Theta0));
    avgStrain = mean(stretchF-1);

    f1 = macroStretch_app - macroStretch;
    Residual = f1;

    it=0;

    % Iterate to solve for alpha given macro-stretch
    while abs(Residual) > tol

        it=it+1;

        %Compute jacobian and update guess
        dthetadAlpha = (-Beta*(4+8*alpha).*Theta0)./(4*alpha ...
            +4*alpha^2+Beta)^2;
        dStretchFdAlpha = cos(theta) - alpha.*sin(theta).*dthetadAlpha;
        dMacrodAlpha = 1/max(X1) ...
            *trapz(X1,dStretchFdAlpha.*cos(theta)./cos(Theta0) - ...
            stretchF.*sin(theta)./cos(Theta0).*dthetadAlpha);

        df1dAlpha = -dMacrodAlpha;

        temp = alpha - f1/df1dAlpha;

        alpha = temp;

        %Check residual of updated guess
        theta = (Beta.*Theta0)./(4*alpha + 4*alpha^2 +Beta);
```

```
        stretchF = 1+alpha.*cos(theta);
        macroStretch = 1/L*trapz(X1,stretchF.*cos(theta)./cos(Theta0));
        avgStrain = mean(stretchF-1);

        f1 = macroStretch_app - macroStretch;
        Residual = f1;

    end

    it;

    % Compute fiber strain energy and derivatives needed to compute ...
       stress
    % for converged alpha:

    SEbend = 1/L*trapz(X1, E*Beta/8 *(theta-Theta0).^2);
    SEaxial = 1/L*trapz(X1, E/2.*(stretchF-1).^2);

    dthetadalpha = (-Beta*(4+8*alpha).*Theta0)./(4*alpha ...
       +4*alpha^2+Beta)^2;
    dstretchFdalpha = cos(theta) - alpha.*sin(theta).*dthetadalpha;
    dalphadMacro = ...
       (1/L*trapz(X1,dstretchFdalpha.*cos(theta)./cos(Theta0) - ...
       (stretchF.*sin(theta)./cos(Theta0)).*dthetadalpha))^(-1);

    dSEbendDalpha = 1/L*trapz(X1, E*Beta/4 ...
       *(theta-Theta0).*dthetadalpha);
    dSEaxialDalpha = 1/L*trapz(X1,E*(stretchF-1).*dstretchFdalpha);

    dSEbendDmacro = dSEbendDalpha * dalphadMacro;
    dSEaxialDmacro = dSEaxialDalpha * dalphadMacro;

    % Compute derivatives for tissue-level jacobian:

    D=1;
    dDdMacro = 0;
    Beta0 = Beta;

    dthetadD = 2.*Beta0.*D.*Theta0/(4*alpha*(1+alpha)+Beta0.*D^2) - ...
       2*Beta0^2.*D^3.*Theta0/(4*alpha*(1+alpha)+Beta0.*D^2)^2;
    dthetadMacro = dthetadalpha.*dalphadMacro + dthetadD.*dDdMacro;

    dstretchFdD = -alpha.*sin(theta).*dthetadD;
    dstretchFdMacro = dstretchFdalpha .* dalphadMacro + ...
       dstretchFdD.*dDdMacro;

    dthetadalphadMacro = (-2*D.*dDdMacro.*Beta0.*(4+8*alpha).*Theta0 ...
       - ...
       D^2.*Beta0.*8*dalphadMacro.*Theta0)/(4*alpha*(1+alpha)+Beta0.*D^2)^2 ...
       + ...
```

```
        (2*D^2*Beta0*(4+8*alpha).*Theta0.*((4+8*alpha).*dalphadMacro ...
        +2*D*dDdMacro.*Beta0)) / (4*alpha*(1+alpha)+Beta0.*D^2)^3;
    dstretchFdalphadMacro = -sin(theta).*dthetadMacro - ...
        alpha.*(cos(theta).*dthetadMacro + ...
        sin(theta).*dthetadalphadMacro);

    dalphadMacro2 = ...
        -(1/L*trapz(X1,dstretchFdalpha.*cos(theta)./cos(Theta0) - ...
        stretchF.*sin(theta)./cos(Theta0).*dthetadalpha))^(-2) ...
        *1/L*trapz(X1, (dstretchFdalphadMacro - ...
        stretchF.*dthetadMacro.*dthetadalpha).*cos(theta)./cos(Theta0) ...
        - (dstretchFdalpha.*dthetadMacro+ ...
        dstretchFdMacro.*dthetadalpha + stretchF.*dthetadalphadMacro ...
        ).*sin(theta)./cos(Theta0));

    dSEbenddalphadMacro = E*Beta0/(4*L) * ...
        trapz(X1,4*D^3.*dDdMacro.*(theta-Theta0).*dthetadalpha + ...
        D^4.*dthetadMacro.*dthetadalpha + ...
        D^4.*(theta-Theta0).*dthetadalphadMacro);
    dSEaxialdalphadMacro = ...
        E/L*trapz(X1,2*D.*dDdMacro.*(stretchF-1).*dstretchFdalpha + ...
        D^2.*dstretchFdMacro.*dstretchFdalpha ...
        +D^2.*(stretchF-1).*dstretchFdalphadMacro);

    dSEbenddMacro2 = dSEbenddalphadMacro * dalphadMacro + ...
        dSEbendDalpha*dalphadMacro2;
    dSEaxialdMacro2 = dSEaxialdalphadMacro * dalphadMacro + ...
        dSEaxialDalpha * dalphadMacro2;

    dSEdMacro2 = dSEbenddMacro2 +dSEaxialdMacro2;


end
```

D.6.4 UniaxialCreep_noDeg_analytical.m

```
function [ Stretch11, Stretch22, Stress11,Stress22, alphaNew, ...
    avgStrain ] = UniaxialCreep_noDeg_analytical( Stretch11_initial, ...
    Stretch22_initial,  mu, b_disp, E0, alphaprev, Beta0, Theta0, ...
    X1, dphi, tol, Force, A0, Stress22_target )
% Solves for Stretch11 and Stretch22 for a given uniaxial force,
% reference cross-sectional area, and Sigma22 (=0 for uniaxial tension).
% Requires an initial guess for Stretch11, Stretch22, and the
% internal variable alpha(phi). [NO DEGRADATION]

    %Initial guess:
    Stretch11 = Stretch11_initial;
    Stretch22 = Stretch22_initial;

    %Check residual for initial guess and compute jacobian:
    [ Stress11, Stress22, alphaNew, avgStrain, ~, J ] = ...
       stress_noDeg( Stretch11, Stretch22, alphaprev, mu, b_disp, ...
       E0, Beta0, Theta0, X1, dphi, tol );

    f1 = Stress11 - Force*Stretch11/A0;
    f2 = Stress22 - Stress22_target;

    residual = abs(sqrt(f1^2 + f2^2));


    it=0;

    % Iterate to solve for Stretch11, Stretch22:
    if abs(residual) > tol

        while abs(residual) > tol

            it = it+1;

            % Adjust jacobian for Cauchy Stress
            J = J - [Force/A0 0;
                     0        0];

            % Update initial guess:
            temp = [Stretch11, Stretch22] - [f1, f2]/J;
            Stretch11 = temp(1);
            Stretch22 = temp(2);

            % Check residual of updated initial guess:
```

```
            [ Stress11, Stress22, alphaNew, avgStrain, ~, J ] = ...
                stress_noDeg( Stretch11, Stretch22, alphaprev, mu, ...
                b_disp, E0, Beta0, Theta0, X1, dphi, tol );

            f1 = Stress11 - Force*Stretch11/A0;
            f2 = Stress22 - Stress22_target;

            residual = abs(sqrt(f1^2 + f2^2));

        end

end
```

D.6.5 UniaxialCreep_degAndDamage_totalAreaLoss.m

```
function [ Stretch11, Stretch22, Stress11,Stress22, alphaNew, DNew, ...
    xiNew, avgStrain, Fg ] = ...
    UniaxialCreep_degAndDamage_totalAreaLoss( Stretch11_initial, ...
    Stretch22_initial, alphaprev, Dprev, xiprev, G1, G2, C, H, mu, ...
    b_disp, E0, Beta0, Theta0, X1, Stress22_target, Force, A0, ...
    delta, dphi, tol )
% Solves for Stretch11, Stretch22, and fiber degradation D(phi)
% while degradation proceeds over time for a given uniaxial force,
% reference cross-sectional area,  and Sigma22 (=0 for uniaxial
% tension). Requires an initial guess for Stretch11, Stretch22,
% the internal variable alpha(phi), and the fiber degradation D(phi).

    % Initial Guess
    Stretch11 = Stretch11_initial;
    Stretch22 = Stretch22_initial;

    % Check residual for initial guess and compute jacobian:
    [Stress11, Stress22, alpha, D, xi, avgStrain, ~,J, Fg] = ...
       stress_degAndDamage( Stretch11, Stretch22, alphaprev, Dprev, ...
       xiprev, G1, G2, C, H, mu, b_disp, E0, Beta0, Theta0, X1, ...
       dphi, delta, tol );

    f1 = Stress11 - Force*Stretch11/(A0*Fg(2,2)*Fg(3,3));
    f2 = Stress22 - Stress22_target;

    residual = abs(sqrt(f1^2 + f2^2));

    it=0;

    %Proceed if intial guess does not satify tolerance
    if abs(residual) > tol

        % Iterate to solve for Stretch11, Stretch22, and D(phi):
        while abs(residual) > tol

            it = it+1;

            % Adjust jacobian for Cauchy Stress
            J = J - [Force/(A0*Fg(2,2)*Fg(3,3))    0;
                     0         0];

            % Update initial guess:
            temp = [Stretch11, Stretch22] - [f1, f2]/J;
            Stretch11 = temp(1);
```

```
            Stretch22 = temp(2);

            % Check residual of updated initial guess:
            [Stress11, Stress22, alpha, D, xi, avgStrain, ~, J, Fg] ...
                = stress_degAndDamage( Stretch11, Stretch22, ...
                alphaprev, Dprev, xiprev, G1, G2, C, H, mu, b_disp, ...
                E0, Beta0, Theta0, X1, dphi, delta, tol );

            f1 = Stress11 - Force*Stretch11/(A0*Fg(2,2)*Fg(3,3));
            f2 = Stress22 - Stress22_target;

            residual = abs(sqrt(f1^2 + f2^2));

            % DEFINE OUTPUT VARIABLES %
            alphaNew = alpha;
            DNew = D;
            xiNew = xi;

        end

    else
        % Output variables if initial guess satisfies residual
        alphaNew = alpha;
        DNew = D;
        xiNew = xi;


    end
end
```

D.6.6 stress_degAndDamage.m

```
function [ Stress11, Stress22, alpha, D, xi, avgStrain, ...
   dStress22dStretch22, J, Fg ] = stress_degAndDamage( Stretch11, ...
   Stretch22, alphaPrev, Dprev, xiprev, G1, G2, C, H, mu, b_disp, ...
   E0, Beta0, Theta0, X1, dphi, delta, tol )
% Computes the plane stress state (Stress11 and Stress22) and fiber
% degradation, D(phi),at a given time for a biaxial stretch state.
% Requires an initial guess for the internal  variable alpha(phi)
% and the fiber degradation parameter, D(phi).

    % Discretize in phi, compute fiber distribution function and ...
       array of fiber
    % micro-stretches:
    phi = [0:dphi:pi];
    vonMises= exp(b_disp.*cos(2.*phi))./(2*pi*besseli(0,b_disp));
    macroStretch = ...
       sqrt(Stretch11^2.*cos(phi).^2+Stretch22.^2.*sin(phi).^2 );

    % Solve for fiber stress and degradation at each angle, phi:
    for i = 1:length(phi)
        [ alpha(i), D(i), xi(i), theta, stretchF, dSEbendDmacro(i), ...
           dSEaxialDmacro(i), it, avgStrain(i), dSEdMacro2(i) ] = ...
           singleFiber_degAndDamage_meanSE( macroStretch(i), ...
           alphaPrev(i),Dprev(i), xiprev(i), G1, G2, C, H, E0, ...
           Beta0, Theta0, X1, delta, tol );
    end

    %Compute Growth tensor for next timestep
    Fg = [1, 0,  0;
          0, 1,  0;
          0, 0,  2*trapz(phi,D.*vonMises)];

    % Sum all fiber contributions and add to matrix stress for total ...
       tissue stress
    Stress11 = (mu*(Stretch11^2-(Stretch11*Stretch22)^(-2)) + ...
       2*trapz(phi, (dSEbendDmacro + ...
       dSEaxialDmacro).*(macroStretch).^(-1).*Stretch11^2.*cos(phi).^2...
        .*vonMises));
    Stress22 = (mu*(Stretch22^2-(Stretch11*Stretch22)^(-2)) + ...
       2*trapz(phi, (dSEbendDmacro + ...
       dSEaxialDmacro).*(macroStretch).^(-1).*Stretch22^2.*sin(phi).^2...
        .*vonMises));

    %Compute Jacobian for Newton-Raphson
    dMacrodStretch11 = (Stretch11.*cos(phi).^2)./macroStretch;
```

```
    dMacrodStretch22 = (Stretch22.*sin(phi).^2)./macroStretch;

    dStress11dStretch11 = ...
       2*mu*(Stretch11+1/(Stretch11^3*Stretch22^2)) + 2.*trapz(phi, ...
       (dSEdMacro2.*dMacrodStretch11.*Stretch11^2./macroStretch + ...
       (dSEbendDmacro + ...
       dSEaxialDmacro).*(2.*Stretch11./macroStretch - ...
       (Stretch11^2./macroStretch.^(2)).*dMacrodStretch11)).*cos(phi).^2...
        .*vonMises);
    dStress22dStretch22 = ...
       2*mu*(Stretch22+1/(Stretch11^2*Stretch22^3)) + 2.*trapz(phi, ...
       dSEdMacro2.*dMacrodStretch22.*(macroStretch).^(-1).*(Stretch22.^2...
        .*sin(phi).^2).*vonMises + (dSEbendDmacro + ...
           dSEaxialDmacro).*(2.*Stretch22./macroStretch - ...
           Stretch22^2.*macroStretch.^(-2).*dMacrodStretch22).*sin(phi).^2...
        .*vonMises);

    dStress11dStretch22 = 2*mu/(Stretch11^2*Stretch22^3) + ...
       2*trapz(phi, ...
       (dSEdMacro2.*dMacrodStretch22.*Stretch11^2./macroStretch + ...
       (dSEbendDmacro + ...
       dSEaxialDmacro).*(-Stretch11^2./macroStretch.^2).*dMacrodStretch22)...
        .*cos(phi).^2.*vonMises);
    dStress22dStretch11 = 2*mu/(Stretch11^3*Stretch11^2) + ...
       2*trapz(phi, ...
       (dSEdMacro2.*dMacrodStretch11.*Stretch22^2./macroStretch + ...
       (dSEbendDmacro + ...
       dSEaxialDmacro).*(-Stretch22^2./macroStretch.^2).*dMacrodStretch11)...
        .*sin(phi).^2.*vonMises);

    J = [ dStress11dStretch11   dStress22dStretch11;
          dStress11dStretch22   dStress22dStretch22];

end
```

D.6.7 singleFiber_degAndDamage_meanSE.m

```
function [ alpha, D, xi, theta, stretchF, dSEbendDmacro, ...
    dSEaxialDmacro, it, avgStrain_out, dSEdMacro2 ] = ...
    singleFiber_degAndDamage_meanSE( macroStretch_app, ...
    alphaPrev,Dprev, xiprev, G1, G2, C, H, E0, Beta0, Theta0, X1, ...
    delta, tol )
% Computes deformed shape (theta), fiber stretch, fiber degradation, D,
% and internal variable, alpha for a single elastica given an applied
% macro-stretch, timestep, and an intial guess for alpha and D,
% using a Newton-Raphson scheme.

    L = max(X1);

    %Initial Guess (previous step)
    alpha=alphaPrev;
    D = Dprev;
    xi = xiprev;

    %Check initial guess residual
    theta = (Beta0*D^2.*Theta0)./(4*alpha + 4*alpha^2 + Beta0*D^2);
    stretchF = 1+alpha.*cos(theta);
    avgStrain = mean(stretchF-1);
    avgStrain_out =  avgStrain; %Compression allowed

    if avgStrain <= 0   % Compressive strain does not inhibit rate law!
        avgStrain =0;
    end
    if mean(stretchF-1) <= 0
        mean_e2 = 0;
    else
        mean_e2=mean((stretchF-1).^2);
    end

    f1 = macroStretch_app - ...
       1/L*trapz(X1,stretchF.*cos(theta)./cos(Theta0));
    f2 = D-Dprev + delta*G1*exp(-(1-xi)*mean_e2/(2*G2));%origional
    if (1-xi)*avgStrain/H > 1
        f3 = xi - xiprev -delta*C*((1-xi)*avgStrain/H -1);
    else
        f3 = xi - xiprev;
    end

    Residual = abs(sqrt(f1^2+f2^2 +f3^2));

    % Iterate to solve for D and alpha given macro-stretch
```

```
it=0;
while Residual > tol

    %Compute jacobian:
    dthetadalpha = ...
        -(Beta0*D^2.*Theta0.*(4+8*alpha))./(4*alpha+4*alpha^2 + ...
        Beta0*D^2)^2;
    dthetadD = (2*Beta0*D.*Theta0)/(4*alpha ...
        +4*alpha^2+Beta0*D^2) - ...
        (2*Beta0^2*D^3.*Theta0)/(4*alpha+4*alpha^2+Beta0*D^2)^2;

    dstretchFdalpha = cos(theta) - alpha.*sin(theta) .*dthetadalpha;
    dstretchFdD = -alpha.*sin(theta).*dthetadD;

    davgStraindalpha = 1/L*trapz(X1, dstretchFdalpha);
    davgStraindD = 1/L*trapz(X1, dstretchFdD);

    df1dalpha = -1/L*trapz(X1, ...
        dstretchFdalpha.*cos(theta)./cos(Theta0) - ...
        (stretchF.*sin(theta)./cos(Theta0)).*dthetadalpha);
    df1dD = -1/L*trapz(X1, dstretchFdD.*cos(theta)./cos(Theta0) ...
        - (stretchF.*sin(theta)./cos(Theta0)).*dthetadD);
    df1dxi = 0;

    df2dalpha = delta*G1*exp(-((1-xi)*avgStrain^2)/(2*G2)) * ...
        (-((1-xi)*avgStrain/G2) * davgStraindalpha);
    df2dD = 1+delta*G1*exp(-((1-xi)*avgStrain^2)/(2*G2)) * ...
        (-((1-xi)*avgStrain/G2) * davgStraindD);
    df2dxi = 0;

    if (1-xi)*avgStrain/H > 1
        df3dalpha = -(delta*C*(1-xi)/H) *davgStraindalpha;
        df3dD = -(delta*C*(1-xi)/H) *davgStraindD;
        df3dxi = 1 + delta*C*avgStrain/H;
    else
        df3dalpha = 0;
        df3dD = 0;
        df3dxi = 1;
    end

    J = [df1dalpha          df2dalpha       df3dalpha;
         df1dD              df2dD           df3dD;
         df1dxi             df2dxi          df3dxi];

    % Update guess:
    temp  = [alpha, D, xi] - [f1, f2, f3] /J;
    alpha = temp(1);
    D = temp(2);
    xi = temp(3);
```

```
    %Check residual of updated guess
    theta = (Beta0*D^2.*Theta0)./(4*alpha + 4*alpha^2 + Beta0*D^2);
    stretchF = 1+alpha.*cos(theta);
    avgStrain = mean(stretchF-1);
    avgStrain_out =  avgStrain; % Compression allowed
    mean_e2=mean((stretchF-1).^2);

        if avgStrain <= 0   % Compressive strain does not ...
           inhibit rate law
            avgStrain =0;
        end
        if mean(stretchF-1) <= 0
            mean_e2 = 0;
        else
            mean_e2=mean((stretchF-1).^2);
        end

    f1 = macroStretch_app - ...
       1/L*trapz(X1,stretchF.*cos(theta)./cos(Theta0));
    f2 = D-Dprev + delta*G1*exp(-(1-xi)*mean_e2/(2*G2));%origional

    if (1-xi)*avgStrain/H > 1
        f3 = xi - xiprev -delta*C*((1-xi)*avgStrain/H -1);
    else
        f3 = xi - xiprev;
    end

    Dprev;
    D;
    Residual = abs(sqrt(f1^2+f2^2+f3^2)) ;


    % Remove fiber completely after D falls below 0.018
    % (convergence issue)
    if D < 0.018
        D=0;
        Residual =0;
    end


end

it;

% No negative fiber radii
if D <= 0
    D = 0 ;
end
```

```
% Compute fiber strain energy and derivatives needed to compute ...
    stress
% for converged D and alpha:

Beta = Beta0*D^2;
E = E0*(1-xi);

SEbend = 1/L*trapz(X1, E*Beta/8 *(theta-Theta0).^2);
SEaxial = 1/L*trapz(X1, E/2.*(stretchF-1).^2);

dthetadalpha = (-Beta*(4+8*alpha).*Theta0)./(4*alpha ...
    +4*alpha^2+Beta)^2;
dstretchFdalpha = cos(theta) - alpha.*sin(theta).*dthetadalpha;
dalphadMacro = ...
    (1/L*trapz(X1,dstretchFdalpha.*cos(theta)./cos(Theta0) - ...
    (stretchF.*sin(theta)./cos(Theta0)).*dthetadalpha))^(-1);

dSEbendDalpha = D^2/L*trapz(X1, E*Beta/4 ...
    *(theta-Theta0).*dthetadalpha);
dSEaxialDalpha = D^2/L*trapz(X1,E*(stretchF-1).*dstretchFdalpha);


dSEbendDmacro = dSEbendDalpha * dalphadMacro;
dSEaxialDmacro = dSEaxialDalpha * dalphadMacro;

% Compute derivatives for tissue-level jacobian:
davgStraindMacro = 1/L*trapz(X1,dstretchFdalpha.*dalphadMacro);
dDdMacro = -delta*G1*exp(-avgStrain^2 / (2*G2)) *(-avgStrain/G2) ...
    * davgStraindMacro;

if (1-xi)*avgStrain/H > 1
    dxidMacro = ((delta*C/H)*(1+delta*C*avgStrain/H)^(-1) - ...
        (xiprev + delta*C*(avgStrain/H ...
        -1))*(delta*C/H)*(1+delta*C*avgStrain/H)^(-2))* ...
        davgStraindMacro;
else
    dxidMacro = 0;
end

dthetadD = 2.*Beta0.*D.*Theta0/(4*alpha*(1+alpha)+Beta0.*D^2) - ...
    2*Beta0^2.*D^3.*Theta0/(4*alpha*(1+alpha)+Beta0.*D^2)^2;
dthetadMacro = dthetadalpha.*dalphadMacro + dthetadD.*dDdMacro;

dstretchFdD = -alpha.*sin(theta).*dthetadD;
dstretchFdMacro = dstretchFdalpha .* dalphadMacro + ...
    dstretchFdD.*dDdMacro;

dthetadalphadMacro = (-2*D.*dDdMacro.*Beta0.*(4+8*alpha).*Theta0 ...
    - ...
    D^2.*Beta0.*8*dalphadMacro.*Theta0)/(4*alpha*(1+alpha)+Beta0.*D^2)^2 ...
```

```
        + ...
        (2*D^2*Beta0*(4+8*alpha).*Theta0.*((4+8*alpha).*dalphadMacro ...
        +2*D*dDdMacro.*Beta0)) / (4*alpha*(1+alpha)+Beta0.*D^2)^3;
    dstretchFdalphadMacro = -sin(theta).*dthetadMacro - ...
        alpha.*(cos(theta).*dthetadMacro + ...
        sin(theta).*dthetadalphadMacro);

    dalphadMacro2 = ...
        -(1/L*trapz(X1,dstretchFdalpha.*cos(theta)./cos(Theta0) - ...
        stretchF.*sin(theta)./cos(Theta0).*dthetadalpha))^(-2) ...
        *1/L*trapz(X1, (dstretchFdalphadMacro - ...
        stretchF.*dthetadMacro.*dthetadalpha).*cos(theta)./cos(Theta0) ...
        - (dstretchFdalpha.*dthetadMacro+ ...
        dstretchFdMacro.*dthetadalpha + stretchF.*dthetadalphadMacro ...
        ).*sin(theta)./cos(Theta0));

    dSEbenddalphadMacro = ...
        (-E0*Beta0/(4*L)*trapz(X1,D^4.*(theta-Theta0).*dthetadalpha))*dxidMacro ...
        + E0*(1-xi)*Beta0/(4*L) * ...
        trapz(X1,4*D^3.*dDdMacro.*(theta-Theta0).*dthetadalpha + ...
        D^4.*dthetadMacro.*dthetadalpha + ...
        D^4.*(theta-Theta0).*dthetadalphadMacro);
    dSEaxialdalphadMacro = (-E0/L *trapz(X1, ...
        D^2.*(stretchF-1).*dstretchFdalpha))*dxidMacro + ...
        E0*(1-xi)/L*trapz(X1,2*D.*dDdMacro.*(stretchF-1).*dstretchFdalpha ...
        + D^2.*dstretchFdMacro.*dstretchFdalpha ...
        +D^2.*(stretchF-1).*dstretchFdalphadMacro);

    dSEbenddMacro2 = dSEbenddalphadMacro * dalphadMacro + ...
        dSEbendDalpha*dalphadMacro2;
    dSEaxialdMacro2 = dSEaxialdalphadMacro * dalphadMacro + ...
        dSEaxialDalpha * dalphadMacro2;

    dSEdMacro2 = dSEbenddMacro2 +dSEaxialdMacro2;

end
```

D.6.8 ApplyStress_noDeg.m

```
function [ Stretch11, Stretch22, Stress11,Stress22, alphaNew, ...
    avgStrain ] = ApplyStress_noDeg( Stretch11_initial, ...
    Stretch22_initial,  mu, b_disp, E0, alphaprev, Beta0, Theta0, ...
    X1, dphi, tol, Stress11_target, Stress22_target )
% Solves for Stretch11 and Stretch22 for a biaxial stress state (or
% uniaxial stress state when Stress22 =0). Requires an initial guess
% for Stretch11, Stretch22, and the internal variable alpha(phi).
% [NO DEGRADATION].

    %Initial guess:
    Stretch11 = Stretch11_initial;
    Stretch22 = Stretch22_initial;

    %Check residual for initial guess and compute jacobian:
    [ Stress11, Stress22, alphaNew, avgStrain, ~, J ] = ...
        stress_noDeg( Stretch11, Stretch22, alphaprev, mu, b_disp, ...
        E0, Beta0, Theta0, X1, dphi, tol );

    f1 = Stress11 - Stress11_target;
    f2 = Stress22 - Stress22_target;
    residual = abs(sqrt(f1^2 + f2^2));

    % Iterate to solve for Stretch11, Stretch22:
    it=0;
    if abs(residual) > tol

        while abs(residual) > tol
            it = it+1;

            % Update initial guess:
            temp = [Stretch11, Stretch22] - [f1, f2]/J;
            Stretch11 = temp(1);
            Stretch22 = temp(2);

            % Check residual of updated initial guess:
            [ Stress11, Stress22, alphaNew, avgStrain, ~, J ] = ...
                stress_noDeg( Stretch11, Stretch22, alphaprev, mu, ...
                b_disp, E0, Beta0, Theta0, X1, dphi, tol );

            f1 = Stress11 - Stress11_target;
            f2 = Stress22 - Stress22_target;
            residual = abs(sqrt(f1^2 + f2^2));
        end
    end
end
```

D.6.9 ApplyStress_degAndDamage.m

```
function [ Stretch11, Stretch22, Stress11,Stress22, alphaNew, DNew, ...
    xiNew, avgStrain, Fg ] = ApplyStress_degAndDamage( ...
    Stretch11_initial, Stretch22_initial, alphaprev, Dprev, xiprev, ...
    G1, G2, C, H, mu, b_disp, E0, Beta0, Theta0, X1, ...
    Stress11_target, Stress22_target, delta, dphi, tol )
% Solves for Stretch11, Stretch22, and fiber degradation D(phi)
% while degradation proceeds over time for a prescribed biaxial
% stress state (=0 for uniaxial  tension). Requires an initial
% guess for Stretch11, Stretch22,  the internal variable
% alpha(phi), and the fiber degradation D(phi).

    % Initial Guess
    Stretch11 = Stretch11_initial;
    Stretch22 = Stretch22_initial;

    % Check residual for initial guess and compute jacobian:
    [Stress11, Stress22, alpha, D, xi, avgStrain, ~,J, Fg] = ...
        stress_degAndDamage( Stretch11, Stretch22, alphaprev, Dprev, ...
        xiprev, G1, G2, C, H, mu, b_disp, E0, Beta0, Theta0, X1, ...
        dphi, delta, tol );

    f1 = Stress11 - Stress11_target;
    f2 = Stress22 - Stress22_target;
    residual = abs(sqrt(f1^2 + f2^2));

    it=0;

    %Proceed if intial guess does not satify tolerance
    if abs(residual) > tol

        % Iterate to solve for Stretch11, Stretch22, and D(phi):
        while abs(residual) > tol

            it = it+1;

            % Update initial guess:
            temp = [Stretch11, Stretch22] - [f1, f2]/J;
            Stretch11 = temp(1);
            Stretch22 = temp(2);

            % Check residual of updated initial guess:
            [Stress11, Stress22, alpha, D, xi, avgStrain, ~, J, Fg] ...
                = stress_degAndDamage( Stretch11, Stretch22, ...
                alphaprev, Dprev, xiprev, G1, G2, C, H, mu, b_disp, ...
```

```
                E0, Beta0, Theta0, X1, dphi, delta, tol );

            f1 = Stress11 - Stress11_target;
            f2 = Stress22 - Stress22_target;

            residual = abs(sqrt(f1^2 + f2^2));

            % Define output variables
            alphaNew = alpha;
            DNew = D;
            xiNew = xi;

        end

    else

        % Output variables if initial guess satisfies residual
        alphaNew = alpha;
        DNew = D;
        xiNew = xi;

    end
end
```

D.6.10 ApplyStress_degAndDamage_withDeposition.m

```
function [ Stretch11, Stretch22, Stress11,Stress22, alphaNew, DNew, ...
    xiNew, avgStrain, Fg ] = ...
    ApplyStress_degAndDamage_withDeposition( Stretch11_initial, ...
    Stretch22_initial, alphaprev, Dprev, xiprev, G1, G2, C, H, mu, ...
    b_disp, E0, Beta0, Theta0, X1, Stress11_target, Stress22_target, ...
    delta, dphi, tol, growthParam )
% Solves for Stretch11, Stretch22, and fiber degradation D(phi)
% while degradation AND DEPOSITION proceed over time for a
% prescribed biaxial stress state (=0 for uniaxial  tension).
% Requires an initial guess for Stretch11, Stretch22,  the
% internal variable alpha(phi), and the fiber degradation D(phi).

    % Initial Guess
    Stretch11 = Stretch11_initial;
    Stretch22 = Stretch22_initial;

    % Check residual for initial guess and compute jacobian:
    [Stress11, Stress22, alpha, D, xi, avgStrain, ~,J, Fg] = ...
       stress_degAndDamage_withDeposition( Stretch11, Stretch22, ...
       alphaprev, Dprev, xiprev, G1, G2, C, H, mu, b_disp, E0, ...
       Beta0, Theta0, X1, dphi, delta, tol, growthParam );

    f1 = Stress11 - Stress11_target;
    f2 = Stress22 - Stress22_target;
    residual = abs(sqrt(f1^2 + f2^2));

    it=0;

    %Proceed if initial guess does not satify tolerance
    if abs(residual) > tol

        % Iterate to solve for Stretch11, Stretch22, and D(phi):
        while abs(residual) > tol

            it = it+1;

            % Update initial guess:
            temp = [Stretch11, Stretch22] - [f1, f2]/J;
            Stretch11 = temp(1);
            Stretch22 = temp(2);

            % Check residual of updated initial guess:
            [Stress11, Stress22, alpha, D, xi, avgStrain, ~, J, Fg] ...
               = stress_degAndDamage_withDeposition( Stretch11, ...
```

```
                Stretch22, alphaprev, Dprev, xiprev, G1, G2, C, H, ...
                mu, b_disp, E0, Beta0, Theta0, X1, dphi, delta, tol, ...
                growthParam );

            f1 = Stress11 - Stress11_target;
            f2 = Stress22 - Stress22_target;
            residual = abs(sqrt(f1^2 + f2^2));

            % Define output variables
            alphaNew = alpha;
            DNew = D;
            xiNew = xi;

        end

    else

        % Output variables if initial guess satisfies residual
        alphaNew = alpha;
        DNew = D;
        xiNew = xi;


    end
end
```

D.6.11 stress_degAndDamage_withDeposition.m

```
function [ Stress11, Stress22, alpha, D, xi, avgStrain, ...
    dStress22dStretch22, J, Fg ] = ...
    stress_degAndDamage_withDeposition( Stretch11, Stretch22, ...
    alphaPrev, Dprev, xiprev, G1, G2, C, H, mu, b_disp, E0, Beta0, ...
    Theta0, X1, dphi, delta, tol, growthParam )
% Computes the plane stress state (Stress11 and Stress22) and fiber
% radius, D(phi), at a given time for a biaxial stretch state while
% both degradation and DEPOSITION proceed over time.
% Requires an initial guess for the internal  variable alpha(phi)
% and the fiber radius parameter, D(phi).

    % Discretize in phi, compute fiber distribution function and ...
       array of fiber
    % micro-stretches:
    phi = [0:dphi:pi];
    vonMises= exp(b_disp.*cos(2.*phi))./(2*pi*besseli(0,b_disp));
    macroStretch = ...
       sqrt(Stretch11^2.*cos(phi).^2+Stretch22.^2.*sin(phi).^2 );

    % Solve for fiber stress and degradation at each angle, phi:
    for i = 1:length(phi)
        phi_print = phi(i)  ;
        macroStretch_print = macroStretch(i);
        [ alpha(i), D(i), xi(i), theta, stretchF, dSEbendDmacro(i), ...
           dSEaxialDmacro(i), it, avgStrain(i), dSEdMacro2(i) ] = ...
           singleFiber_degAndDamage_withDeposition( ...
           macroStretch(i), alphaPrev(i),Dprev(i), xiprev(i), G1, ...
           G2, C, H, E0, Beta0, Theta0, X1, delta, tol, growthParam );
    end

    %Compute Growth tensor for next timestep
    Fg = [1, 0,  0;
          0, 1,  0;
          0, 0,  2*trapz(phi,D.*vonMises)];

    % Sum all fiber contributions and add to matrix stress for total ...
       tissue stress
    Stress11 = (mu*(Stretch11^2-(Stretch11*Stretch22)^(-2)) + ...
       2*trapz(phi, (dSEbendDmacro + ...
       dSEaxialDmacro).*(macroStretch).^(-1).*Stretch11^2.*cos(phi).^2...
        .*vonMises));
    Stress22 = (mu*(Stretch22^2-(Stretch11*Stretch22)^(-2)) + ...
       2*trapz(phi, (dSEbendDmacro + ...
       dSEaxialDmacro).*(macroStretch).^(-1).*Stretch22^2.*sin(phi).^2...
```

```
        .*vonMises));

    %Compute Jacobian for Newton-Raphson
    dMacrodStretch11 = (Stretch11.*cos(phi).^2)./macroStretch;
    dMacrodStretch22 = (Stretch22.*sin(phi).^2)./macroStretch;

    dStress11dStretch11 = ...
        2*mu*(Stretch11+1/(Stretch11^3*Stretch22^2)) + 2.*trapz(phi, ...
        (dSEdMacro2.*dMacrodStretch11.*Stretch11^2./macroStretch + ...
        (dSEbendDmacro + ...
        dSEaxialDmacro).*(2.*Stretch11./macroStretch - ...
        (Stretch11^2./macroStretch.^(2)).*dMacrodStretch11)).*cos(phi).^2...
         .*vonMises);
    dStress22dStretch22 = ...
        2*mu*(Stretch22+1/(Stretch11^2*Stretch22^3)) + 2.*trapz(phi, ...
        dSEdMacro2.*dMacrodStretch22.*(macroStretch).^(-1)...
         .*(Stretch22.^2.*sin(phi).^2).*vonMises + (dSEbendDmacro + ...
            dSEaxialDmacro).*(2.*Stretch22./macroStretch - ...
            Stretch22^2.*macroStretch.^(-2).*dMacrodStretch22).*sin(phi).^2...
         .*vonMises);

    dStress11dStretch22 = 2*mu/(Stretch11^2*Stretch22^3) + ...
        2*trapz(phi, ...
        (dSEdMacro2.*dMacrodStretch22.*Stretch11^2./macroStretch + ...
        (dSEbendDmacro + ...
        dSEaxialDmacro).*(-Stretch11^2./macroStretch.^2).*dMacrodStretch22)...
         .*cos(phi).^2.*vonMises);
    dStress22dStretch11 = 2*mu/(Stretch11^3*Stretch11^2) + ...
        2*trapz(phi, ...
        (dSEdMacro2.*dMacrodStretch11.*Stretch22^2./macroStretch + ...
        (dSEbendDmacro + ...
        dSEaxialDmacro).*(-Stretch22^2./macroStretch.^2).*dMacrodStretch11)...
         .*sin(phi).^2.*vonMises);

    J = [ dStress11dStretch11   dStress22dStretch11;
          dStress11dStretch22   dStress22dStretch22];

end
```

D.6.12 singleFiber_degAndDamage_withDeposition.m

```
function [ alpha, D, xi, theta, stretchF, dSEbendDmacro, ...
    dSEaxialDmacro, it, avgStrain_out, dSEdMacro2 ] = ...
    singleFiber_degAndDamage_withDeposition( macroStretch_app, ...
    alphaPrev,Dprev, xiprev, G1, G2, C, H, E0, Beta0, Theta0, X1, ...
    delta, tol, growthParam )
% Computes deformed shape (theta), fiber stretch, fiber radius, D,
% and internal variable, alpha for a single elastica while both
% degradation and DEPOSITION proceed with time, given an applied
% macro-stretch, timestep, and an intial guess for alpha and D,
% using a Newton-Raphson scheme

    L = max(X1);

    %Initial Guess (previous step)
    alpha=alphaPrev;
    D = Dprev;
    xi = xiprev;

    %Check initial guess residual
    theta = (Beta0*D^2.*Theta0)./(4*alpha + 4*alpha^2 + Beta0*D^2);
    stretchF = 1+alpha.*cos(theta);
    avgStrain = mean(stretchF-1);
    avgStrain_out =  avgStrain; %Compression allowed
        if avgStrain <= 0
            avgStrain =0;
        end
        if mean(stretchF-1) <= 0
            mean_e2 = 0;
        else
            mean_e2=mean((stretchF-1).^2);
        end

    % Compute residual for current guess
    f1 = macroStretch_app - ...
       1/L*trapz(X1,stretchF.*cos(theta)./cos(Theta0));

    [ fGrow, dGrowdlambda ] = dfGrowdT( growthParam, avgStrain, ...
       mean_e2 );
        % compute deposition contribution
    fDeg = G1*exp(-(1-xi)*mean_e2/(2*G2));
    f2 = D-Dprev + delta*(fDeg -fGrow);

    if (1-xi)*avgStrain/H > 1
        f3 = xi - xiprev -delta*C*((1-xi)*avgStrain/H -1);
```

```
else
    f3 = xi - xiprev;
end

Residual = abs(sqrt(f1^2+f2^2 +f3^2));

% Iterate to solve for D and alpha given macro-stretch
it=0;
while Residual > tol
    it=it+1;

    %Compute jacobian:
    dthetadalpha = ...
       -(Beta0*D^2.*Theta0.*(4+8*alpha))./(4*alpha+4*alpha^2 + ...
       Beta0*D^2)^2;
    dthetadD = (2*Beta0*D.*Theta0)/(4*alpha ...
       +4*alpha^2+Beta0*D^2) - ...
       (2*Beta0^2*D^3.*Theta0)/(4*alpha+4*alpha^2+Beta0*D^2)^2;

    dstretchFdalpha = cos(theta) - alpha.*sin(theta) .*dthetadalpha;
    dstretchFdD = -alpha.*sin(theta).*dthetadD;

    davgStraindalpha = 1/L*trapz(X1, dstretchFdalpha);
    davgStraindD = 1/L*trapz(X1, dstretchFdD);

    df1dalpha = -1/L*trapz(X1, ...
       dstretchFdalpha.*cos(theta)./cos(Theta0) - ...
       (stretchF.*sin(theta)./cos(Theta0)).*dthetadalpha);
    df1dD = -1/L*trapz(X1, dstretchFdD.*cos(theta)./cos(Theta0) ...
       - (stretchF.*sin(theta)./cos(Theta0)).*dthetadD);
    df1dxi = 0;

    dDegdlambda = G1*exp(-((1-xi)*avgStrain^2)/(2*G2)) * ...
       -((1-xi)*avgStrain/G2);
    df2dalpha = delta*(dDegdlambda -dGrowdlambda)  * ...
       davgStraindalpha;
    df2dD = 1+delta*G1*exp(-((1-xi)*avgStrain^2)/(2*G2)) * ...
       (-((1-xi)*avgStrain/G2) * davgStraindD);
    df2dxi = 0;

    if (1-xi)*avgStrain/H > 1
        df3dalpha = -(delta*C*(1-xi)/H) *davgStraindalpha;
        df3dD = -(delta*C*(1-xi)/H) *davgStraindD;
        df3dxi = 1 + delta*C*avgStrain/H;
    else
        df3dalpha = 0;
        df3dD = 0;
        df3dxi = 1;
    end
```

```
J = [df1dalpha          df2dalpha       df3dalpha;
     df1dD              df2dD           df3dD;
     df1dxi             df2dxi          df3dxi];

% Update guess:
temp  = [alpha, D, xi] - [f1, f2, f3] /J;
alpha = temp(1);
D = temp(2);
xi = temp(3);

%Check residual of updated guess
theta = (Beta0*D^2.*Theta0)./(4*alpha + 4*alpha^2 + Beta0*D^2);
stretchF = 1+alpha.*cos(theta);
avgStrain = mean(stretchF-1);
avgStrain_out =  avgStrain; % Compression allowed
mean_e2=mean((stretchF-1).^2);

    if avgStrain <= 0 % Compressive strain does not inhibit ...
       rate law
        avgStrain =0;
    end
    if mean(stretchF-1) <= 0
        mean_e2 = 0;
    else
        mean_e2=mean((stretchF-1).^2);
    end

f1 = macroStretch_app - ...
   1/L*trapz(X1,stretchF.*cos(theta)./cos(Theta0));

[ fGrow, dGrowdlambda ] = dfGrowdT( growthParam, avgStrain, ...
   mean_e2 );
fDeg = G1*exp(-(1-xi)*mean_e2/(2*G2)); %origional
f2 = D-Dprev + delta*(fDeg -fGrow);

if (1-xi)*avgStrain/H > 1
    f3 = xi - xiprev -delta*C*((1-xi)*avgStrain/H -1);
else
    f3 = xi - xiprev;
end

Residual = abs(sqrt(f1^2+f2^2+f3^2)) ;

% Remove fiber completely after D falls below 0.018
% (convergence issue)
if D < 0.018
    D=0;
    Residual =0;
end
```

```
end

% No negative fiber radii
if D <= 0
    D = 0 ;
end


% Compute fiber strain energy and derivatives needed to compute ...
   stress
% for converged D and alpha:

Beta = Beta0*D^2;
E = E0*(1-xi);

SEbend = 1/L*trapz(X1, E*Beta/8 *(theta-Theta0).^2);
SEaxial = 1/L*trapz(X1, E/2.*(stretchF-1).^2);

dthetadalpha = (-Beta*(4+8*alpha).*Theta0)./(4*alpha ...
   +4*alpha^2+Beta)^2;
dstretchFdalpha = cos(theta) - alpha.*sin(theta).*dthetadalpha;
dalphadMacro = ...
   (1/L*trapz(X1,dstretchFdalpha.*cos(theta)./cos(Theta0) - ...
   (stretchF.*sin(theta)./cos(Theta0)).*dthetadalpha))^(-1);

dSEbendDalpha = D^2/L*trapz(X1, E*Beta/4 ...
   *(theta-Theta0).*dthetadalpha);
dSEaxialDalpha = D^2/L*trapz(X1,E*(stretchF-1).*dstretchFdalpha);


dSEbendDmacro = dSEbendDalpha * dalphadMacro;
dSEaxialDmacro = dSEaxialDalpha * dalphadMacro;

% Compute derivatives for tissue-level jacobian:
davgStraindMacro = 1/L*trapz(X1,dstretchFdalpha.*dalphadMacro);
dDdMacro = -delta*G1*exp(-avgStrain^2 / (2*G2)) *(-avgStrain/G2) ...
   * davgStraindMacro;

if (1-xi)*avgStrain/H > 1
    dxidMacro = ((delta*C/H)*(1+delta*C*avgStrain/H)^(-1) - ...
        (xiprev + delta*C*(avgStrain/H ...
        -1))*(delta*C/H)*(1+delta*C*avgStrain/H)^(-2))* ...
        davgStraindMacro;
else
    dxidMacro = 0;
end

dthetadD = 2.*Beta0.*D.*Theta0/(4*alpha*(1+alpha)+Beta0.*D^2) - ...
   2*Beta0^2.*D^3.*Theta0/(4*alpha*(1+alpha)+Beta0.*D^2)^2;
```

```
    dthetadMacro = dthetadalpha.*dalphadMacro + dthetadD.*dDdMacro;

    dstretchFdD = -alpha.*sin(theta).*dthetadD;
    dstretchFdMacro = dstretchFdalpha .* dalphadMacro + ...
        dstretchFdD.*dDdMacro;

    dthetadalphadMacro = (-2*D.*dDdMacro.*Beta0.*(4+8*alpha).*Theta0 ...
        - ...
        D^2.*Beta0.*8*dalphadMacro.*Theta0)/(4*alpha*(1+alpha)+Beta0.*D^2)^2 ...
        + ...
        (2*D^2*Beta0*(4+8*alpha).*Theta0.*((4+8*alpha).*dalphadMacro ...
        +2*D*dDdMacro.*Beta0)) / (4*alpha*(1+alpha)+Beta0.*D^2)^3;
    dstretchFdalphadMacro = -sin(theta).*dthetadMacro - ...
        alpha.*(cos(theta).*dthetadMacro + ...
        sin(theta).*dthetadalphadMacro);

    dalphadMacro2 = ...
        -(1/L*trapz(X1,dstretchFdalpha.*cos(theta)./cos(Theta0) - ...
        stretchF.*sin(theta)./cos(Theta0).*dthetadalpha))^(-2) ...
        *1/L*trapz(X1, (dstretchFdalphadMacro - ...
        stretchF.*dthetadMacro.*dthetadalpha).*cos(theta)./cos(Theta0) ...
        - (dstretchFdalpha.*dthetadMacro+ ...
        dstretchFdMacro.*dthetadalpha + stretchF.*dthetadalphadMacro ...
        ).*sin(theta)./cos(Theta0));

    dSEbenddalphadMacro = ...
        (-E0*Beta0/(4*L)*trapz(X1,D^4.*(theta-Theta0).*dthetadalpha))*dxidMacro ...
        + E0*(1-xi)*Beta0/(4*L) * ...
        trapz(X1,4*D^3.*dDdMacro.*(theta-Theta0).*dthetadalpha + ...
        D^4.*dthetadMacro.*dthetadalpha + ...
        D^4.*(theta-Theta0).*dthetadalphadMacro);
    dSEaxialdalphadMacro = (-E0/L *trapz(X1, ...
        D^2.*(stretchF-1).*dstretchFdalpha))*dxidMacro + ...
        E0*(1-xi)/L*trapz(X1,2*D.*dDdMacro.*(stretchF-1).*dstretchFdalpha ...
        + D^2.*dstretchFdMacro.*dstretchFdalpha ...
        +D^2.*(stretchF-1).*dstretchFdalphadMacro);

    dSEbenddMacro2 = dSEbenddalphadMacro * dalphadMacro + ...
        dSEbendDalpha*dalphadMacro2;
    dSEaxialdMacro2 = dSEaxialdalphadMacro * dalphadMacro + ...
        dSEaxialDalpha * dalphadMacro2;

    dSEdMacro2 = dSEbenddMacro2 +dSEaxialdMacro2;

end
```

D.6.13 dfGrowdT.m

```
function [ fGrow, dGrowdlambda ] = dfGrowdT( growthParam, avgStrain, ...
    mean_e2 )
% Computes the collagen deposition rate as well as the dependence of the
% rate on the applied macro-stretch for Newton-Raphson solver. Multiple
% deposition laws are available; comment all but desired deposition law.

% Deposition parameters
kg1 = growthParam(1);
%kg1=0; % enable for no deposition

% OPTION 1: Constant Deposition Law
fGrow = kg1;
dGrowdlambda = 0;


% OPTION 2: Linear Deposition Law
%{
fGrow = kg1.*avgStrain;
dGrowdlambda = kg1;
%}

% OPTION 3: 3 Parameter Growth Curve
%{
Ka = growthParam(1);
Kb = growthParam(2);
Kc = growthParam(3);

%Sample values:
%Ka=1e-4; %Upper growth limit
%Kb=15;   %Horizontal lag time
%Kc=1000; %growth rate

fGrow = Ka.*exp(-Kb*exp(-Kc.*avgStrain));

dGrowdlambda = Ka.*Kb*Kc*exp(-Kb*exp(-Kc.*mean_e2));
%}

end
```

Bibliography

[1] R. B. Martin, D. B. Burr, and N. A. Sharkey, *Skeletal tissue mechanics*. Springer, 1998.

[2] L. A. Taber, "Biomechanics of growth, remodeling, and morphogenesis," *Applied mechanics reviews*, vol. 48, no. 8, pp. 487–545, 1995.

[3] J. W. Ruberti and N. J. Hallab, "Strain-controlled enzymatic cleavage of collagen in loaded matrix," *Biochemical and biophysical research communications*, vol. 336, no. 2, pp. 483–489, 2005.

[4] A. P. Bhole, B. P. Flynn, M. Liles, N. Saeidi, C. A. Dimarzio, and J. W. Ruberti, "Mechanical strain enhances survivability of collagen micronetworks in the presence of collagenase: implications for load-bearing matrix growth and stability," *Philosophical Transactions of the Royal Society A: Mathematical, Physical and Engineering Sciences*, vol. 367, no. 1902, pp. 3339–3362, 2009.

[5] J. A. Buckwalter, C. Saltzman, and T. Brown, "The impact of osteoarthritis:

implications for research," *Clinical orthopaedics and related research*, vol. 427, pp. S6–S15, 2004.

[6] C. Cook and P. Foster, "Epidemiology of glaucoma: what's new?" *Canadian Journal of Ophthalmology/Journal Canadien d'Ophtalmologie*, vol. 47, no. 3, pp. 223–226, 2012.

[7] D. Ambrosi, G. Ateshian, E. Arruda, S. Cowin, J. Dumais, A. Goriely, G. A. Holzapfel, J. Humphrey, R. Kemkemer, E. Kuhl *et al.*, "Perspectives on biological growth and remodeling," *Journal of the Mechanics and Physics of Solids*, vol. 59, no. 4, pp. 863–883, 2011.

[8] M. J. Buehler, "Nature designs tough collagen: explaining the nanostructure of collagen fibrils," *Proceedings of the National Academy of Sciences*, vol. 103, no. 33, pp. 12 285–12 290, 2006.

[9] C. R. Ethier and C. A. Simmons, *Introductory biomechanics: from cells to organisms*. Cambridge University Press, 2007.

[10] I. Brown, "Scanning electron microscopy of human dermal fibrous tissue." *Journal of anatomy*, vol. 113, no. Pt 2, p. 159, 1972.

[11] R. D. Young, "The ultrastructural organization of proteoglycans and collagen in human and rabbit scleral matrix," *Journal of cell science*, vol. 74, no. 1, pp. 95–104, 1985.

[12] B. Gallagher and D. Maurice, "Striations of light scattering in the corneal stroma," *Journal of ultrastructure research*, vol. 61, no. 1, pp. 100–114, 1977.

[13] E. H. COURTISS, J. Longacre, G. Destefano, L. BRIZIO, and K. HOLMSTRAND, "The placement of elective skin incisions," *Plastic and reconstructive surgery*, vol. 31, no. 1, pp. 31–44, 1963.

[14] J. K. Pijanka, B. Coudrillier, K. Ziegler, T. Sorensen, K. M. Meek, T. D. Nguyen, H. A. Quigley, and C. Boote, "Quantitative mapping of collagen fiber orientation in non-glaucoma and glaucoma posterior human sclerae," *Investigative ophthalmology & visual science*, vol. 53, no. 9, pp. 5258–5270, 2012.

[15] H. Aghamohammadzadeh, R. H. Newton, and K. M. Meek, "X-ray scattering used to map the preferred collagen orientation in the human cornea and limbus," *Structure*, vol. 12, no. 2, pp. 249–256, 2004.

[16] K. Langer, "Zur anatomie und physiologie der haut," *Uber die Spaltbarkeit der Cutis. Sitzuungsber Math Cl Kaiserlich Acad Wiss*, vol. 44, pp. 19–49, 1861.

[17] A. Delalleau, G. Josse, J.-M. Lagarde, H. Zahouani, and J.-M. Bergheau, "A nonlinear elastic behavior to identify the mechanical parameters of human skin in vivo," *Skin Research and Technology*, vol. 14, no. 2, pp. 152–164, 2008.

[18] M. S. Sacks, "Biaxial mechanical evaluation of planar biological materials," *Journal of Elasticity*, vol. 61, no. 1-3, pp. 199–246, 2000.

[19] Y. Li, J. A. Nemes, and A. A. Derdouri, "Membrane inflation of polymeric materials: Experiments and finite element simulations," *Polymer Engineering and Science*, vol. 41, no. 8, pp. 1399–1412, 2001.

[20] Y. Lanir and Y. C. Fung, "Two dimensional mechanical properties of rabbit skin. ii. experimental results," *Journal of Biomechanics*, vol. 7, no. 2, pp. 171–182, 1974.

[21] K. Billiar and M. Sacks, "A method to quantify the fiber kinematics of planar tissues under biaxial stretch," *Journal of biomechanics*, vol. 30, no. 7, pp. 753–756, 1997.

[22] K. L. Billiar and M. S. Sacks, "Biaxial mechanical properties of the native and glutaraldehyde-treated aortic valve cusp: Part ii - a structural constitutive model," *Journal of Biomechanical Engineering*, vol. 122, no. 4, pp. 327–336, 2000.

[23] P. Zioupes, J. C. Barbenel, and J. Fisher, "Mechanical and optical anisotropy of bovine pericardium," *Medical and Biological Engineering and Computing*, vol. 30, no. 1, pp. 76–82, 1992.

[24] E. S. Drexler, T. P. Quinn, A. J. Slifka, C. N. McCowan, J. E. Bischoff, J. E. Wright, D. D. Ivy, and R. Shandas, "Comparison of mechanical behavior among the extrapulmonary arteries from rats," *Journal of Biomechanics*, vol. 40, no. 4, pp. 812–819, 2007.

[25] B. L. Boyce, J. M. Grazier, R. E. Jones, and T. D. Nguyen, "Full-field deformation of bovine cornea under constrained inflation conditions," *Biomaterials*, vol. 29, no. 28, pp. 3896–3904, 2008.

[26] K. M. Myers, B. Coudrillier, B. L. Boyce, and T. D. Nguyen, "The inflation response of the posterior bovine sclera," *Acta Biomaterialia*, vol. 6, no. 11, pp. 4327–4335, 2010.

[27] T. T. Tower, M. R. Neidert, and R. T. Tranquillo, "Fiber alignment imaging during mechanical testing of soft tissues," *Annals of Biomedical Engineering*, vol. 30, no. 10, pp. 1221–1233, 2002.

[28] T. C. Gasser, R. W. Ogden, and G. A. Holzapfel, "Hyperelastic modelling of arterial layers with distributed collagen fibre orientations," *Journal of the Royal Society Interface*, vol. 3, no. 6, pp. 15–35, 2006.

[29] R. Grytz and G. Meschke, "Constitutive modeling of crimped collagen fibrils in soft tissues," *Journal of the mechanical behavior of biomedical materials*, vol. 2, no. 5, pp. 522–533, 2009.

[30] A. J. M. Spencer *et al.*, *Continuum theory of the mechanics of fibre-reinforced composites*. Springer, 1984, vol. 282.

[31] Y. C. B. Fung, "Biorheology of soft tissues," *Biorheology*, vol. 10, no. 2, pp. 139–155, 1973.

[32] P. Tong and Y. C. Fung, "The stress strain relationship for the skin," *Journal of Biomechanics*, vol. 9, no. 10, pp. 649–657, 1976.

[33] Y. C. Fung, *Mechanical Properties of Living Tissues.* Springer, 1993.

[34] Y. Fung, K. Fronek, and P. Patitucci, "Pseudoelasticity of arteries and of its mathematical expression," *Americal Journal of Physiology - Heart and Circulatory Physiology*, vol. 237, no. 5, pp. H620–H631, 1979.

[35] C. Chuong and Y. Fung, "Three-dimensional stress distribution in arteries," *Journal of biomechanical engineering*, vol. 105, no. 3, pp. 268–274, 1983.

[36] Y. Lanir and Y. C. Fung, "Two dimensional mechanical properties of rabbit skin. i. experimental system," *Journal of Biomechanics*, vol. 7, no. 1, pp. 29–34, 1974.

[37] Y. Lanir, "A structural theory for the homogeneous biaxial stress-strain relationships in flat collagenous tissues," *Journal of biomechanics*, vol. 12, no. 6, pp. 423–436, 1979.

[38] A. N. Annaidh, K. Bruyre, M. Destrade, M. D. Gilchrist, C. Maurini, M. Ottnio, and G. Saccomandi, "Automated estimation of collagen fibre dispersion in the dermis and its contribution to the anisotropic behaviour of skin," *Annals of Biomedical Engineering*, vol. 40, no. 8, pp. 1666–1678, 2012.

[39] A. Pandolfi and G. A. Holzapfel, "Three-dimensional modeling and computational analysis of the human cornea considering distributed collagen fibril orientations," *Journal of Biomechanical Engineering*, vol. 130, no. 6, 2008.

[40] D. H. Cortes, S. P. Lake, J. A. Kadlowec, L. J. Soslowsky, and D. M. Elliott, "Characterizing the mechanical contribution of fiber angular distribution in connective tissue: Comparison of two modeling approaches," *Biomechanics and Modeling in Mechanobiology*, vol. 9, no. 5, pp. 651–658, 2010.

[41] A. Pandolfi and M. Vasta, "Fiber distributed hyperelastic modeling of biological tissues," *Mechanics of Materials*, vol. 44, pp. 151–162, 2012.

[42] A. D. Freed and T. C. Doehring, "Elastic model for crimped collagen fibrils," *Journal of biomechanical engineering*, vol. 127, no. 4, pp. 587–593, 2005.

[43] J. Palmer, C. Castro, M. Arslan, and M. Boyce, "Constitutive models for the force-extension behavior of biological filaments," in *IUTAM Symposium on Cellular, Molecular and Tissue Mechanics*. Springer, 2010, pp. 141–159.

[44] K. Garikipati, S. Göktepe, and C. Miehe, "Elastica-based strain energy functions for soft biological tissue," *Journal of the Mechanics and Physics of Solids*, vol. 56, no. 4, pp. 1693–1713, 2008.

[45] M. Comninou and I. V. Yannas, "Dependence of stress-strain nonlinearity of

connective tissues on the geometry of collagen fibres," *Journal of Biomechanics*, vol. 9, no. 7, pp. 427–433, 1976.

[46] C. Buckley, D. Lloyd, and M. Konopasek, "On the deformation of slender filaments with planar crimp: theory, numerical solution and applications to tendon collagen and textile materials," *Proceedings of the Royal Society of London. A. Mathematical and Physical Sciences*, vol. 372, no. 1748, pp. 33–64, 1980.

[47] R. Grytz, I. A. Sigal, J. W. Ruberti, G. Meschke, and J. Crawford Downs, "Lamina cribrosa thickening in early glaucoma predicted by a microstructure motivated growth and remodeling approach," *Mechanics of Materials*, vol. 44, pp. 99–109, 2012.

[48] R. Grytz and G. Meschke, "A computational remodeling approach to predict the physiological architecture of the collagen fibril network in corneo-scleral shells," *Biomechanics and modeling in mechanobiology*, vol. 9, no. 2, pp. 225–235, 2010.

[49] W. Grossman, "Cardiac hypertrophy: useful adaptation or pathologic process?" *The American journal of medicine*, vol. 69, no. 4, pp. 576–584, 1980.

[50] H. Ju, S. Zhao, D. S. Jassal, and I. M. Dixon, "Effect of at1 receptor blockade on cardiac collagen remodeling after myocardial infarction," *Cardiovascular research*, vol. 35, no. 2, pp. 223–232, 1997.

[51] J. Humphrey and K. Rajagopal, "A constrained mixture model for growth

and remodeling of soft tissues," *Mathematical models and methods in applied sciences*, vol. 12, no. 03, pp. 407–430, 2002.

[52] L. J. Sandell and T. Aigner, "Articular cartilage and changes in arthritis. an introduction: cell biology of osteoarthritis," *Arthritis Res*, vol. 3, no. 2, pp. 107–113, 2001.

[53] J. Urban, S. Roberts *et al.*, "Degeneration of the intervertebral disc," *Arthritis Research and Therapy*, vol. 5, no. 3, pp. 120–138, 2003.

[54] B. Coudrillier, J. Tian, S. Alexander, K. M. Myers, H. A. Quigley, and T. D. Nguyen, "Biomechanics of the human posterior sclera: age-and glaucoma-related changes measured using inflation testing," *Investigative ophthalmology & visual science*, vol. 53, no. 4, pp. 1714–1728, 2012.

[55] R. Skalak, "Growth as a finite displacement field," in *Proceedings of the IUTAM Symposium on Finite Elasticity*. Springer, 1982, pp. 347–355.

[56] R. Skalak, G. Dasgupta, M. Moss, E. Otten, P. Dullemeijer, and H. Vilmann, "Analytical description of growth," *Journal of Theoretical Biology*, vol. 94, no. 3, pp. 555–577, 1982.

[57] E. K. Rodriguez, A. Hoger, and A. D. McCulloch, "Stress-dependent finite growth in soft elastic tissues," *Journal of biomechanics*, vol. 27, no. 4, pp. 455–467, 1994.

[58] M. Rausch, A. Dam, S. Göktepe, O. Abilez, and E. Kuhl, "Computational modeling of growth: systemic and pulmonary hypertension in the heart," *Biomechanics and modeling in mechanobiology*, vol. 10, no. 6, pp. 799–811, 2011.

[59] S. Göktepe, O. J. Abilez, K. K. Parker, and E. Kuhl, "A multiscale model for eccentric and concentric cardiac growth through sarcomerogenesis," *Journal of theoretical biology*, vol. 265, no. 3, pp. 433–442, 2010.

[60] S. Baek, K. Rajagopal, and J. Humphrey, "A theoretical model of enlarging intracranial fusiform aneurysms," *Journal of biomechanical engineering*, vol. 128, no. 1, pp. 142–149, 2006.

[61] J. Humphrey and G. A. Holzapfel, "Mechanics, mechanobiology, and modeling of human abdominal aorta and aneurysms," *Journal of biomechanics*, vol. 45, no. 5, pp. 805–814, 2012.

[62] L. A. Taber and J. D. Humphrey, "Stress-modulated growth, residual stress, and vascular heterogeneity," *Journal of biomechanical engineering*, vol. 123, no. 6, pp. 528–535, 2001.

[63] L. A. Taber and R. Perucchio, "Modeling heart development," *Journal of elasticity and the physical science of solids*, vol. 61, no. 1-3, pp. 165–197, 2000.

[64] A. Ramasubramanian and L. A. Taber, "Computational modeling of mor-

phogenesis regulated by mechanical feedback," *Biomechanics and modeling in mechanobiology*, vol. 7, no. 2, pp. 77–91, 2008.

[65] R. C. Kerckhoffs, J. H. Omens, and A. D. McCulloch, "A single strain-based growth law predicts concentric and eccentric cardiac growth during pressure and volume overload," *Mechanics research communications*, vol. 42, pp. 40–50, 2012.

[66] R. C. Kerckhoffs, "Computational modeling of cardiac growth in the post-natal rat with a strain-based growth law," *Journal of biomechanics*, vol. 45, no. 5, pp. 865–871, 2012.

[67] N. J. Driessen, M. A. Cox, C. V. Bouten, and F. P. Baaijens, "Remodelling of the angular collagen fiber distribution in cardiovascular tissues," *Biomechanics and modeling in mechanobiology*, vol. 7, no. 2, pp. 93–103, 2008.

[68] I. Hariton, T. Gasser, G. Holzapfel *et al.*, "Stress-driven collagen fiber remodeling in arterial walls," *Biomechanics and modeling in mechanobiology*, vol. 6, no. 3, pp. 163–175, 2007.

[69] E. Kuhl, K. Garikipati, E. M. Arruda, and K. Grosh, "Remodeling of biological tissue: mechanically induced reorientation of a transversely isotropic chain network," *Journal of the Mechanics and Physics of Solids*, vol. 53, no. 7, pp. 1552–1573, 2005.

[70] P. N. Watton, Y. Ventikos, and G. A. Holzapfel, "Modelling the growth and stabilization of cerebral aneurysms," *Mathematical Medicine and Biology*, vol. 26, no. 2, pp. 133–164, 2009.

[71] N. Driessen, W. Wilson, C. Bouten, and F. Baaijens, "A computational model for collagen fibre remodelling in the arterial wall," *Journal of theoretical biology*, vol. 226, no. 1, pp. 53–64, 2004.

[72] N. J. Driessen, R. A. Boerboom, J. M. Huyghe, C. V. Bouten, and F. P. Baaijens, "Computational analyses of mechanically induced collagen fiber remodeling in the aortic heart valve," *Journal of biomechanical engineering*, vol. 125, no. 4, pp. 549–557, 2003.

[73] E. Kuhl and G. A. Holzapfel, "A continuum model for remodeling in living structures," *Journal of Materials Science*, vol. 42, no. 21, pp. 8811–8823, 2007.

[74] R. Gleason and J. Humphrey, "A mixture model of arterial growth and remodeling in hypertension: altered muscle tone and tissue turnover," *Journal of vascular research*, vol. 41, no. 4, pp. 352–363, 2004.

[75] A. Valentin and J. Humphrey, "Evaluation of fundamental hypotheses underlying constrained mixture models of arterial growth and remodelling," *Philosophical Transactions of the Royal Society A: Mathematical, Physical and Engineering Sciences*, vol. 367, no. 1902, pp. 3585–3606, 2009.

[76] A. Valentín, J. Humphrey, and G. A. Holzapfel, "A finite element-based constrained mixture implementation for arterial growth, remodeling, and adaptation: Theory and numerical verification," *International journal for numerical methods in biomedical engineering*, vol. 29, no. 8, pp. 822–849, 2013.

[77] J. Foolen, C. C. Van Donkelaar, S. Soekhradj-Soechit, and K. Ito, "European society of biomechanics sm perren award 2010: an adaptation mechanism for fibrous tissue to sustained shortening," *Journal of biomechanics*, vol. 43, no. 16, pp. 3168–3176, 2010.

[78] R. A. Boerboom, M. P. Rubbens, N. J. Driessen, C. V. Bouten, and F. P. Baaijens, "Effect of strain magnitude on the tissue properties of engineered cardiovascular constructs," *Annals of biomedical engineering*, vol. 36, no. 2, pp. 244–253, 2008.

[79] R. J. Camp, M. Liles, J. Beale, N. Saeidi, B. P. Flynn, E. Moore, S. K. Murthy, and J. W. Ruberti, "Molecular mechanochemistry: low force switch slows enzymatic cleavage of human type i collagen monomer," *Journal of the American Chemical Society*, vol. 133, no. 11, pp. 4073–4078, 2011.

[80] B. P. Flynn, G. E. Tilburey, and J. W. Ruberti, "Highly sensitive single-fibril erosion assay demonstrates mechanochemical switch in native collagen fibrils," *Biomechanics and modeling in mechanobiology*, vol. 12, no. 2, pp. 291–300, 2013.

[81] C. Huang and I. Yannas, "Mechanochemical studies of enzymatic degradation of insoluble collagen fibers," *Journal of biomedical materials research*, vol. 11, no. 1, pp. 137–154, 1977.

[82] K. E.-K. Wyatt, J. W. Bourne, and P. A. Torzilli, "Deformation-dependent enzyme mechanokinetic cleavage of type i collagen," *Journal of biomechanical engineering*, vol. 131, no. 5, p. 051004, 2009.

[83] R. Zareian, K. P. Church, N. Saeidi, B. P. Flynn, J. W. Beale, and J. W. Ruberti, "Probing collagen/enzyme mechanochemistry in native tissue with dynamic, enzyme-induced creep," *Langmuir*, vol. 26, no. 12, pp. 9917–9926, 2010.

[84] F. Baaijens, C. Bouten, and N. Driessen, "Modeling collagen remodeling," *Journal of biomechanics*, vol. 43, no. 1, pp. 166–175, 2010.

[85] M. Hadi, E. Sander, J. Ruberti, and V. Barocas, "Simulated remodeling of loaded collagen networks via strain-dependent enzymatic degradation and constant-rate fiber growth," *Mechanics of Materials*, vol. 44, pp. 72–82, 2012.

[86] B. Coudrillier, C. Boote, H. A. Quigley, and T. D. Nguyen, "Scleral anisotropy and its effects on the mechanical response of the optic nerve head," *Biomechanics and modeling in mechanobiology*, vol. 12, no. 5, pp. 941–963, 2013.

[87] T. M. Koys, "An inflation test method for the evaluation of the anisotropic

properties of human skin tissues," Master's thesis, The Johns Hopkins University, Baltimore, MD, June 2011.

[88] T. K. Tonge, L. S. Atlan, L. M. Voo, and T. D. Nguyen, "Full-field bulge test for planar anisotropic tissues: Part i–experimental methods applied to human skin tissue," *Acta biomaterialia*, vol. 9, no. 4, pp. 5913–5925, 2013.

[89] T. K. Tonge, L. M. Voo, and T. D. Nguyen, "Full-field bulge test for planar anisotropic tissues: Part ii–a thin shell method for determining material parameters and comparison of two distributed fiber modeling approaches," *Acta biomaterialia*, vol. 9, no. 4, pp. 5926–5942, 2013.

[90] T. K. Tonge, B. J. Murienne, B. Coudrillier, S. Alexander, W. Rothkopf, and T. D. Nguyen, "Minimal preconditioning effects observed for inflation tests of planar tissues," *Journal of biomechanical engineering*, vol. 135, no. 11, p. 114502, 2013.

[91] C. W. J. Oomens, D. H. van Campen, and H. J. Grootenboer, "A mixture approach to the mechanics of skin," *Journal of Biomechanics*, vol. 20, no. 9, pp. 877–885, 1987.

[92] I. A. Brown, "A scanning electron microscope study of the effects of uniaxial tension on human skin," *British Journal of Dermatology*, vol. 89, no. 4, pp. 383–393, 1973.

[93] M. Satin, *Strategies in Regenerative Medicine*. Springer Science + Business Media, 2009.

[94] A. N. Annaidh, K. Bruyre, M. Destrade, M. D. Gilchrist, and M. Ottnio, "Characterizing the anisotropic mechanical properties of excised human skin," *Journal of the Mechanical Behavior of Biomedical Materials*, vol. 5, pp. 139–148, 2012.

[95] S. M. Belkoff, E. C. Naylor, R. Walshaw, E. Lanigan, C. Lee, and R. C. Haut, "Effects of subcutaneous expansion on the mechanical properties of porcine skin," *Journal of Surgical Research*, vol. 58, no. 2, pp. 117–123, 1995.

[96] Y. . Zeng, C. . Xu, J. Yang, G. . Sun, and X. . Xu, "Biomechanical comparison between conventional and rapid expansion of skin," *British journal of plastic surgery*, vol. 56, no. 7, pp. 660–666, 2003.

[97] Y. . Zeng, Y. . Liu, C. . Xu, X. . Xu, H. Xu, and G. . Sun, "Biomechanical properties of skin in vitro for different expansion methods," *Clinical Biomechanics*, vol. 19, no. 8, pp. 853–857, 2004.

[98] E. J. F. Timmenga, T. T. Andreassen, H. J. Houthoff, and P. J. Klopper, "The effect of mechanical stress on healing skin wounds: An experimental study in rabbits using tissue expansion," *British journal of plastic surgery*, vol. 44, no. 7, pp. 514–519, 1991.

[99] G. Pierard and C. Lapiere, "Microanatomy of the dermis in relation to relaxed

skin tension lines and langer's lines," *American Journal of Dermatopathology*, vol. 9, no. 3, pp. 219–224, 1987.

[100] H. Oxlund, J. Manschot, and A. Viidik, "The role of elastin in the mechanical properties of skin," *Journal of Biomechanics*, vol. 21, no. 3, pp. 213–218, 1988.

[101] S. L. Evans, "On the implementation of a wrinkling, hyperelastic membrane model for skin and other materials," *Computer methods in biomechanics and biomedical engineering*, vol. 12, no. 3, pp. 319–332, 2009.

[102] M. G. Dunn, F. H. Silver, and D. A. Swann, "Mechanical analysis of hypertrophic scar tissue: Structural basis for apparent increased rigidity," *Journal of Investigative Dermatology*, vol. 84, no. 1, pp. 9–13, 1985.

[103] O. A. Shergold, N. A. Fleck, and D. Radford, "The uniaxial stress versus strain response of pig skin and silicone rubber at low and high strain rates," *International Journal of Impact Engineering*, vol. 32, no. 9, pp. 1384–1402, 2006.

[104] Z. Huang, D. Zhou, and Q. . Ren, "Nonlinear anisotropic composite biomechanical modeling of human skin," *Journal of Shanghai Jiaotong University (Science)*, vol. 15, no. 3, pp. 363–367, 2010.

[105] H. Eshel and Y. Lanir, "Effects of strain level and proteoglycan depletion on preconditioning and viscoelastic responses of rat dorsal skin," *Annals of Biomedical Engineering*, vol. 29, no. 2, pp. 164–172, 2001.

[106] G. W. Dombi, R. C. Haut, and W. G. Sullivan, "Correlation of high-speed tensile strength with collagen content in control and lathyritic rat skin," *Journal of Surgical Research*, vol. 54, no. 1, pp. 21–28, 1993.

[107] D. C. Schneider, T. M. Davidson, and A. M. Nahum, "In vitro biaxial stress-strain response of human skin," *Archives of Otolaryngology*, vol. 110, no. 5, pp. 329–333, 1984.

[108] R. Reihsner, B. Balogh, and E. J. Menzel, "Two-dimensional elastic properties of human skin in terms of an incremental model at the in vivo configuration," *Medical Engineering and Physics*, vol. 17, no. 4, pp. 304–313, 1995.

[109] R. Reihsner and E. J. Menzel, "On the orthogonal anisotropy of human skin as a function of anatomical region," *Connective tissue research*, vol. 34, no. 2, pp. 145–160, 1996.

[110] Y. A. Kvistedal and P. M. F. Nielsen, "Estimating material parameters of human skin in vivo," *Biomechanics and Modeling in Mechanobiology*, vol. 8, no. 1, pp. 1–8, 2009.

[111] A. Delalleau, G. Josse, J. . Lagarde, H. Zahouani, and J. . Bergheau, "Characterization of the mechanical properties of skin by inverse analysis combined with the indentation test," *Journal of Biomechanics*, vol. 39, no. 9, pp. 1603–1610, 2006.

[112] F. M. Hendriks, D. Brokken, C. W. J. Oomens, D. L. Bader, and F. P. T. Baaijens, "The relative contributions of different skin layers to the mechanical behavior of human skin in vivo using suction experiments," *Medical Engineering and Physics*, vol. 28, no. 3, pp. 259–266, 2006.

[113] J. C. Dick, "The tension and resistance to stretch of human skin and other membranes with results from a series of normal and oedematous cases," *Journal of Physiology*, vol. 112, no. 1-2, pp. 102–113, 1951.

[114] J. W. Ahlfors and K. L. Billiar, "Biomechanical and biochemical characteristics of a human fibroblast-produced and remodeled matrix," *Biomaterials*, vol. 28, no. 13, pp. 2183–2191, 2007.

[115] T. Tsakalakos and A. Jankowski, "Mechanical properties of composition-modulated metallic foils," *Annual Review of Materials Science*, vol. 16, no. 1, pp. 293–313, 1986.

[116] J. J. Vlassak and W. D. Nix, "A new bulge test technique for the determination of young's modulus and poisson's ratio of thin films," *Journal of Materials Research*, vol. 7, no. 12, pp. 3242–3249, 1992.

[117] R. J. Jaccodine and W. A. Schlegel, "Measurement of strains at si-sio2 interface," *Journal of Applied Physics*, vol. 37, no. 6, pp. 2429–2434, 1966.

[118] L. R. Schmidt and J. F. Carley, "Biaxial stretching of heat-softened plastic

sheets using an inflation technique," *International Journal of Engineering Science*, vol. 13, no. 6, pp. 563–578, 1975.

[119] R. Rivlin and D. Saunders, "Large elastic deformations of isotropic materials. vii. experiments on the deformation of rubber," *Philosophical transactions of the royal society*, vol. 243, no. 865, pp. 251–288, 1951.

[120] A. Hamdi, M. Nat Abdelaziz, N. At Hocine, P. Heuillet, and N. Benseddiq, "A fracture criterion of rubber-like materials under plane stress conditions," *Polymer Testing*, vol. 25, no. 8, pp. 994–1005, 2006.

[121] N. Reuge, F. M. Schmidt, Y. Le Maoult, M. Rachik, and F. Abb, "Elastomer biaxial characterization using bubble inflation technique. i: Experimental investigations," *Polymer Engineering and Science*, vol. 41, no. 3, pp. 522–531, 2001.

[122] K.-T. Wan and S.-C. Lim, "The bending to stretching transition of a pressurized blister test," *International journal of fracture*, vol. 92, no. 4, pp. 43–47, 1998.

[123] W. Song, F. Mirza, and J. Vlachopoulos, "Finite element analysis of inflation of an axisymmetric sheet of finite thickness," *Journal of Rheology*, vol. 35, no. 1, pp. 93–111, 1991.

[124] J. Hildebrandt, H. Fukaya, and C. J. Martin, "Stress-strain relations of tissue

sheets undergoing uniform two-dimensional stretch." *Journal of applied physiology*, vol. 27, no. 5, pp. 758–762, 1969.

[125] R. N. Baird and W. M. Abbott, "Elasticity and compliance of canine femoral and jugular vein segments," *American Journal of Physiology - Heart and Circulatory Physiology*, vol. 233, no. 1, pp. H15–H21, 1977.

[126] S. P. Marra, F. E. Kennedy, J. N. Kinkaid, and M. F. Fillinger, "Elastic and rupture properties of porcine aortic tissue measured using inflation testing," *Cardiovascular Engineering*, vol. 6, no. 4, pp. 123–131, 2006.

[127] J. E. Bischoff, E. S. Drexler, A. J. Slifka, and C. N. McCowan, "Quantifying nonlinear anisotropic elastic material properties of biological tissue by use of membrane inflation," *Computer methods in biomechanics and biomedical engineering*, vol. 12, no. 3, pp. 353–369, 2009.

[128] G. Machado, D. Favier, and G. Chagnon, "Membrane curvatures and stress-strain full fields of axisymmetric bulge tests from 3d-dic measurements. theory and validation on virtual and experimental results," *Experimental Mechanics*, pp. 1–16, 2011.

[129] R. Marangoni, A. A. Glaser, J. Must, G. S. Brody, T. G. Beckwith, G. R. Walker, and W. L. White, "Effect of storage and handling techniques on skin tissue properties," *Annals of the New York Academy of Sciences*, vol. 136, pp. 441–453, 1966.

[130] J. M. Lee and S. E. Langdon, "Thickness measurement of soft tissue biomaterials: A comparison of five methods," *Journal of Biomechanics*, vol. 29, no. 6, pp. 829–832, 1996.

[131] P. Provenzano, R. Lakes, T. Keenan, and R. Vanderby Jr., "Nonlinear ligament viscoelasticity," *Annals of Biomedical Engineering*, vol. 29, no. 10, pp. 908–914, 2001.

[132] S. Timoshenko and S. Woinowsky-Krieger, *Theory of Plates and Shells*. Mcgraw-Hill, 1959.

[133] R. J. Roark, *Formulas for Stress and Strain, 4th ed.* New York: McGraw-Hill, 1965.

[134] M. Flugge, *Stresses in Shells*. Springer-Verlag, 1960.

[135] J. Lu, X. Zhou, and M. L. Raghavan, "Inverse method of stress analysis for cerebral aneurysms," *Biomechanics and Modeling in Mechanobiology*, vol. 7, no. 6, pp. 477–486, 2008.

[136] B. Ma, J. Lu, R. E. Harbaugh, and M. L. Raghavan, "Nonlinear anisotropic stress analysis of anatomically realistic cerebral aneurysms," *Journal of Biomechanical Engineering*, vol. 129, no. 1, pp. 88–96, 2007.

[137] X. Zhou, M. L. Raghavan, R. E. Harbaugh, and J. Lu, "Patient-specific wall

stress analysis in cerebral aneurysms using inverse shell model," *Annals of Biomedical Engineering*, vol. 38, no. 2, pp. 478–489, 2010.

[138] X. Zhao, M. L. Raghavan, and J. Lu, "Identifying heterogeneous anisotropic properties in cerebral aneurysms: A pointwise approach," *Biomechanics and Modeling in Mechanobiology*, vol. 10, no. 2, pp. 177–189, 2011.

[139] M. A. Hajdu, D. D. Heistad, J. E. Siems, and G. L. Baumbach, "Effects of aging on mechanics and composition of cerebral arterioles in rats," *Circulation research*, vol. 66, no. 6, pp. 1747–1754, 1990.

[140] H. K. Graham, R. Akhtar, C. Kridiotis, B. Derby, T. Kundu, A. W. Trafford, and M. J. Sherratt, "Localised micro-mechanical stiffening in the ageing aorta," *Mechanisms of ageing and development*, vol. 132, no. 10, pp. 459–467, 2011.

[141] T. Sugihara, T. Ohura, K. Homma, and H. H. Igawa, "The extensibility in human skin: Variation according to age and site," *British journal of plastic surgery*, vol. 44, no. 6, pp. 418–422, 1991.

[142] A. J. Bailey, "Molecular mechanisms of ageing in connective tissues," *Mechanisms of ageing and development*, vol. 122, no. 7, pp. 735–755, 2001.

[143] I. Sack, B. Beierbach, J. Wuerfel, D. Klatt, U. Hamhaber, S. Papazoglou, P. Martus, and J. Braun, "The impact of aging and gender on brain viscoelasticity," *NeuroImage*, vol. 46, no. 3, pp. 652–657, 2009.

[144] C. C. Cothren, E. E. Moore, W. L. Biffl, D. J. Ciesla, C. E. Ray Jr., J. L. Johnson, J. B. Moore, J. M. Burch, D. B. Hoyt, T. H. Cogbill, C. H. Shatney, and M. T. Dayton, "Anticoagulation is the gold standard therapy for blunt carotid injuries to reduce stroke rate," *Archives of Surgery*, vol. 139, no. 5, pp. 540–546, 2004.

[145] H. Hama, T. Yamamuro, and T. Takeda, "Experimental studies on connective tissue of the capsular ligament. influences of aging and sex hormones," *Acta Orthopaedica Scandinavica*, vol. 47, no. 5, pp. 473–479, 1976.

[146] L. Pedersen, B. Hansen, and G. B. E. Jemec, "Mechanical properties of the skin: A comparison between two suction cup methods," *Skin Research and Technology*, vol. 9, no. 2, pp. 111–115, 2003.

[147] M. Small and W. D. Nix, "Analysis of the accuracy of the bulge test in determining the mechanical properties of thin films," *Journal of Materials Research*, vol. 7, no. 6, pp. 1553–1563, 1992.

[148] T. Nguyen, R. Jones, and B. Boyce, "A nonlinear anisotropic viscoelastic model for the tensile behavior of the corneal stroma," *Journal of biomechanical engineering*, vol. 130, no. 4, p. 041020, 2008.

[149] M. S. Sacks, "Incorporation of experimentally-derived fiber orientation into a structural constitutive model for planar collagenous tissues," *Journal of Biomechanical Engineering*, vol. 125, no. 2, pp. 280–287, 2003.

[150] M. J. A. Girard, J. C. Downs, C. F. Burgoyne, and J. . F. Suh, "Peripapillary and posterior scleral mechanics - part i: Development of an anisotropic hyperelastic constitutive model," *Journal of Biomechanical Engineering*, vol. 131, no. 5, 2009.

[151] U. Komaragiri, M. R. Begley, and J. G. Simmonds, "The mechanical response of freestanding circular elastic films under point and pressure loads," *Journal of Applied Mechanics, Transactions ASME*, vol. 72, no. 2, pp. 203–212, 2005.

[152] A. Libai and J. G. Simmonds, *The Non-Linear Theory of Elastic Shells, 2nd Ed.* Cambridge University Press, 1998.

[153] R. M. Pedrigi, G. David, J. Dziezyc, and J. D. Humphrey, "Regional mechanical properties and stress analysis of the human anterior lens capsule," *Vision research*, vol. 47, no. 13, pp. 1781–1789, 2007.

[154] S. K. Kyriacou, A. D. Shah, and J. D. Humphrey, "Inverse finite element characterization of nonlinear hyperelastic membranes," *Journal of Applied Mechanics, Transactions ASME*, vol. 64, no. 2, pp. 257–262, 1997.

[155] J. Ning, S. Xu, Y. Wang, S. M. Lessner, M. A. Sutton, K. Anderson, and J. E. Bischoff, "Deformation measurements and material property estimation of mouse carotid artery using a microstructure-based constitutive model." *Journal of Biomechanical Engineering*, vol. 132, no. 12, pp. 121 010:1–13, 2010.

[156] B. Schieck, W. Pietraszkiewicz, and H. Stumpf, "Theory and numerical analysis of shells undergoing large elastic strains," *International Journal of Solids and Structures*, vol. 29, no. 6, pp. 689–709, 1992.

[157] T. D. Nguyen and B. L. Boyce, "An inverse finite element method for determining the anisotropic properties of the cornea," *Biomechanics and Modeling in Mechanobiology*, vol. 10, no. 3, pp. 323–337, 2011.

[158] J. W. Y. Jor, M. P. Nash, P. M. F. Nielsen, and P. J. Hunter, "Estimating material parameters of a structurally based constitutive relation for skin mechanics," *Biomechanics and Modeling in Mechanobiology*, vol. 10, no. 5, pp. 767–778, 2011.

[159] J. E. Bischoff, E. M. Arruda, and K. Grosh, "A rheological network model for the continuum anisotropic and viscoelastic behavior of soft tissue," *Biomechanics and Modeling in Mechanobiology*, vol. 3, no. 1, pp. 56–65, 2004.

[160] C. Flynn and B. McCormack, "Finite element modelling of forearm skin wrinkling," *Skin research and technology*, vol. 14, no. 3, pp. 261–269, 2008.

[161] ——, "A simplified model of scar contraction," *Journal of biomechanics*, vol. 41, no. 7, pp. 1582–1589, 2008.

[162] S. M. Belkoff and R. C. Haut, "A structural model used to evaluate the changing

microstructure of maturing rat skin," *Journal of Biomechanics*, vol. 24, no. 8, pp. 711–720, 1991.

[163] G. Limbert, "A mesostructurally-based anisotropic continuum model for biological soft tissuesdecoupled invariant formulation," *Journal of the Mechanical Behavior of Biomedical Materials*, vol. 4, no. 8, pp. 1637–1657, 2011.

[164] Y. Lanir, "Constitutive equations for fibrous connective tissues," *Journal of biomechanics*, vol. 16, no. 1, pp. 1–12, 1983.

[165] R. Raghupathy and V. H. Barocas, "A closed-form structural model of planar fibrous tissue mechanics," *Journal of Biomechanics*, vol. 42, no. 10, pp. 1424–1428, 2009.

[166] S. Federico and W. Herzog, "Towards an analytical model of soft biological tissues," *Journal of Biomechanics*, vol. 41, no. 16, pp. 3309–3313, 2008.

[167] G. A. Holzapfel, T. C. Gasser, and R. W. Ogden, "A new constitutive framework for arterial wall mechanics and a comparative study of material models," *Journal of Elasticity*, vol. 61, no. 1-3, pp. 1–48, 2000.

[168] W. F. Harris, "Curvature of ellipsoids and other surfaces," *Ophthalmic and Physiological Optics*, vol. 26, no. 5, pp. 497–501, 2006.

[169] P. G. Agache, C. Monneur, J. L. Leveque, and J. De Rigal, "Mechanical prop-

erties and young's modulus of human skin in vivo," *Archives of Dermatological Research*, vol. 269, no. 3, pp. 221–232, 1980.

[170] M. Yamauchi, D. T. Woodley, and G. L. Mechanic, "Aging and cross-linking of skin collagen," *Biochemical and biophysical research communications*, vol. 152, no. 2, pp. 898–903, 1988.

[171] J. E. Jalil, C. W. Doering, J. S. Janicki, R. Pick, S. G. Shroff, and K. T. Weber, "Fibrillar collagen and myocardial stiffness in the intact hypertrophied rat left ventricle." *Circulation research*, vol. 64, no. 6, pp. 1041–1050, 1989.

[172] H. A. Quigley, M. E. Dorman-Pease, and A. E. Brown, "Quantitative study of collagen and elastin of the optic nerve head and sclera in human and experimental monkey glaucoma," *Current eye research*, vol. 10, no. 9, pp. 877–888, 1991.

[173] G. Himpel, E. Kuhl, A. Menzel, and P. Steinmann, "Computational modelling of isotropic multiplicative growth," *Comp Mod Eng Sci*, vol. 8, pp. 119–134, 2005.

[174] P. Sáez, E. Peña, M. A. Martínez, and E. Kuhl, "Computational modeling of hypertensive growth in the human carotid artery," *Computational Mechanics*, pp. 1–14, 2013.

[175] L. A. Taber, "Towards a unified theory for morphomechanics," *Philosophical*

Transactions of the Royal Society A: Mathematical, Physical and Engineering Sciences, vol. 367, no. 1902, pp. 3555–3583, 2009.

[176] J. Humphrey and K. Rajagopal, "A constrained mixture model for arterial adaptations to a sustained step change in blood flow," *Biomechanics and modeling in mechanobiology*, vol. 2, no. 2, pp. 109–126, 2003.

[177] W. Kroon, T. Delhaas, T. Arts, and P. Bovendeerd, "Computational modeling of volumetric soft tissue growth: application to the cardiac left ventricle," *Biomechanics and modeling in mechanobiology*, vol. 8, no. 4, pp. 301–309, 2009.

[178] B. P. Flynn, A. P. Bhole, N. Saeidi, M. Liles, C. A. DiMarzio, and J. W. Ruberti, "Mechanical strain stabilizes reconstituted collagen fibrils against enzymatic degradation by mammalian collagenase matrix metalloproteinase 8 (mmp-8)," *PLoS One*, vol. 5, no. 8, p. e12337, 2010.

[179] Y. Nabeshima, E. Grood, A. Sakurai, and J. Herman, "Uniaxial tension inhibits tendon collagen degradation by collagenase in vitro," *Journal of orthopaedic research*, vol. 14, no. 1, pp. 123–130, 1996.

[180] S.-W. Chang, B. P. Flynn, J. W. Ruberti, and M. J. Buehler, "Molecular mechanism of force induced stabilization of collagen against enzymatic breakdown," *Biomaterials*, vol. 33, no. 15, pp. 3852–3859, 2012.

[181] H. Demirkoparan, T. J. Pence, and A. Wineman, "Chemomechanics and home-

ostasis in active strain stabilized hyperelastic fibrous microstructures," *International Journal of Non-Linear Mechanics*, vol. 56, pp. 86–93, 2013.

[182] V. H. Barocas, K. D. Dorfman, and Y. Segal, "A model of strain-dependent glomerular basement membrane maintenance and its potential ramifications in health and disease," *Journal of biomechanical engineering*, vol. 134, no. 8, p. 081006, 2012.

[183] J. C. Ellsmere, R. A. Khanna, and J. Michael Lee, "Mechanical loading of bovine pericardium accelerates enzymatic degradation," *Biomaterials*, vol. 20, no. 12, pp. 1143–1150, 1999.

[184] K. D. Cunningham, F. Musani, D. A. Hart, N. G. Shrive, and C. B. Frank, "Collagenase degradation decreases collagen fibril diameters-an in vitro study of the rabbit medial collateral ligament," *Connective tissue research*, vol. 40, no. 1, pp. 67–74, 1999.

[185] M. Kroon and G. A. Holzapfel, "A model for saccular cerebral aneurysm growth by collagen fibre remodelling," *Journal of theoretical biology*, vol. 247, no. 4, pp. 775–787, 2007.

[186] A. R. Tzafriri, M. Bercovier, and H. Parnas, "Reaction diffusion model of the enzymatic erosion of insoluble fibrillar matrices," *Biophysical journal*, vol. 83, no. 2, pp. 776–793, 2002.

[187] V. Lubarda and A. Hoger, "On the mechanics of solids with a growing mass," *International journal of solids and structures*, vol. 39, no. 18, pp. 4627–4664, 2002.

[188] A. S. Adhikari, J. Chai, and A. R. Dunn, "Mechanical load induces a 100-fold increase in the rate of collagen proteolysis by mmp-1," *Journal of the American Chemical Society*, vol. 133, no. 6, pp. 1686–1689, 2011.

[189] A. S. Adhikari, E. Glassey, and A. R. Dunn, "Conformational dynamics accompanying the proteolytic degradation of trimeric collagen i by collagenases," *Journal of the American Chemical Society*, vol. 134, no. 32, pp. 13 259–13 265, 2012.

[190] E. C. Bass, E. V. Wistrom, C. J. Diederich, W. H. Nau, R. Pellegrino, J. Ruberti, and J. C. Lotz, "Heat-induced changes in porcine annulus fibrosus biomechanics," *Journal of biomechanics*, vol. 37, no. 2, pp. 233–240, 2004.

[191] J. Simo and J. Ju, "Strain-and stress-based continuum damage modelsi. formulation," *International journal of solids and structures*, vol. 23, no. 7, pp. 821–840, 1987.

[192] M. J. Munoz, J. A. Bea, J. F. Rodrguez, I. Ochoa, J. Grasa, A. Perez del Palomar, P. Zaragoza, R. Osta, and M. Doblare, "An experimental study of the mouse skin behaviour: Damage and inelastic aspects," *Journal of Biomechanics*, vol. 41, no. 1, pp. 93–99, 2008.

[193] M. . Lee, Y. C. Fung, R. Shabetai, and M. M. LeWinter, "Biaxial mechanical properties of human pericardium and canine comparisons," *American Journal of Physiology - Heart and Circulatory Physiology*, vol. 253, no. 1, 1987, cited By (since 1996): 10. [Online]. Available: www.scopus.com

[194] S. Cheng, E. C. Clarke, and L. E. Bilston, "The effects of preconditioning strain on measured tissue properties," *Journal of Biomechanics*, vol. 42, no. 9, pp. 1360–1362, 2009.

[195] A. Samani, J. Bishop, C. Luginbuhl, and D. B. Plewes, "Measuring the elastic modulus of ex vivo small tissue samples," *Physics in Medicine and Biology*, vol. 48, no. 14, pp. 2183–2198, 2003.

[196] J. P. Marquez, W. Legant, V. Lam, A. Cayemberg, E. Elson, and T. Wakatsuki, "High-throughput measurements of hydrogel tissue construct mechanics," *Tissue Engineering - Part C: Methods*, vol. 15, no. 2, pp. 181–190, 2009.

[197] A. Nava, E. Mazza, O. Haefner, and M. Bajka, "Experimental observation and modelling of preconditioning in soft biological tissues," in *Medical Simulation*. Springer, 2004, pp. 1–8.

[198] J. A. Stammen, S. Williams, D. N. Ku, and R. E. Guldberg, "Mechanical properties of a novel pva hydrogel in shear and unconfined compression," *Biomaterials*, vol. 22, no. 8, pp. 799–806, 2001.

[199] Z. Liu and K. Yeung, "On preconditioning and stress relaxation behavior of fresh swine skin in different fibre direction," in *ICBPE 2006 - Proceedings of the 2006 International Conference on Biomedical and Pharmaceutical Engineering*, 2006, pp. 221–226.

[200] B. L. Boyce, R. E. Jones, T. D. Nguyen, and J. M. Grazier, "Stress-controlled viscoelastic tensile response of bovine cornea," *Journal of Biomechanics*, vol. 40, no. 11, pp. 2367–2376, 2007.

[201] M. Girard, J. . F. Suh, R. T. Hart, C. F. Burgoyne, and J. C. Downs, "Effects of storage time on the mechanical properties of rabbit peripapillary sclera after enucleation," *Current eye research*, vol. 32, no. 5, pp. 465–470, 2007.

[202] D. Lari, D. Schultz, A. Wang, O. Lee, and J. Stewart, "Scleral mechanics: Comparing whole globe inflation and uniaxial testing," *Experimental Eye Research*, 2011.

[203] L. Schatzmann, P. Brunner, and H. Stäubli, "Effect of cyclic preconditioning on the tensile properties of human quadriceps tendons and patellar ligaments," *Knee Surgery, Sports Traumatology, Arthroscopy*, vol. 6, no. 1, pp. S56–S61, 1998.

[204] E. O. Carew, A. Garg, J. E. Barber, and I. Vesely, "Stress relaxation preconditioning of porcine aortic valves," *Annals of Biomedical Engineering*, vol. 32, no. 4, pp. 563–572, 2004.

[205] E. O. Carew, J. E. Barber, and I. Vesely, "Role of preconditioning and recovery time in repeated testing of aortic valve tissues: validation through quasilinear viscoelastic theory," *Annals of Biomedical Engineering*, vol. 28, no. 9, pp. 1093–1100, 2000.

[206] O. Lokshin and Y. Lanir, "Viscoelasticity and preconditioning of rat skin under uniaxial stretch: Microstructural constitutive characterization," *Journal of Biomechanical Engineering*, vol. 131, no. 3, 2009.

[207] B. K. Graf, R. Vanderby Jr., M. J. Ulm, R. P. Rogalski, and R. J. Thielke, "Effect of preconditioning on the viscoelastic response of primate patellar tendon," *Arthroscopy*, vol. 10, no. 1, pp. 90–96, 1994.

[208] A. Viidik, "Functional properties of collagenous tissues," *International review of connective tissue research*, vol. Vol. 6, pp. 127–215, 1973.

[209] K. P. Quinn and B. A. Winkelstein, "Preconditioning is correlated with altered collagen fiber alignment in ligament," *Journal of Biomechanical Engineering*, vol. 133, no. 6, 2011.

[210] H. Gregersen, J. L. Emery, and A. D. Mcculloch, "History-dependent mechanical behavior of guinea-pig small intestine," *Annals of Biomedical Engineering*, vol. 26, no. 5, pp. 850–858, 1998.

[211] J. L. Emery, J. H. Omens, and A. D. McCulloch, "Strain softening in rat left

ventricular myocardium," *Journal of Biomechanical Engineering*, vol. 119, no. 1, pp. 6–12, 1997.

[212] C. A. Meyer, E. Bertrand, O. Boiron, and V. Deplano, "Stereoscopically observed deformations of a compliant abdominal aortic aneurysm model," *Journal of biomechanical engineering*, vol. 133, no. 11, 2011.

[213] J. Soons, P. Lava, D. Debruyne, and J. Dirckx, "Full-field optical deformation measurement in biomechanics: Digital speckle pattern interferometry and 3d digital image correlation applied to bird beaks," *Journal of the Mechanical Behavior of Biomedical Materials*, vol. 14, pp. 186–191, 2012.

[214] Z. Hu, H. Xie, J. Lu, H. Wang, and J. Zhu, "Error evaluation technique for three-dimensional digital image correlation," *Applied optics*, vol. 50, no. 33, pp. 6239–6247, 2011.

[215] X.-D. Ke, H. Schreier, M. Sutton, and Y. Wang, "Error assessment in stereo-based deformation measurements," *Experimental mechanics*, vol. 51, no. 4, pp. 423–441, 2011.

[216] M. Fazzini, S. Mistou, O. Dalverny, and L. Robert, "Study of image characteristics on digital image correlation error assessment," *Optics and Lasers in Engineering*, vol. 48, no. 3, pp. 335–339, 2010.

[217] M. Sutton, X. Ke, S. Lessner, M. Goldbach, M. Yost, F. Zhao, and H. Schreier,

"Strain field measurements on mouse carotid arteries using microscopic three-dimensional digital image correlation," *Journal of Biomedical Materials Research Part A*, vol. 84, no. 1, pp. 178–190, 2008.

[218] H. Schreier, D. Garcia, and M. Sutton, "Advances in light microscope stereo vision," *Experimental mechanics*, vol. 44, no. 3, pp. 278–288, 2004.

[219] E. Ruvolo Jr, G. Stamatas, and N. Kollias, "Skin viscoelasticity displays site- and age-dependent angular anisotropy," *Skin pharmacology and physiology*, vol. 20, no. 6, pp. 313–321, 2007.

[220] R. T. Domsic, T. Rodriguez-Reyna, M. Lucas, N. Fertig, and T. A. Medsger, "Skin thickness progression rate: a predictor of mortality and early internal organ involvement in diffuse scleroderma," *Annals of the rheumatic diseases*, vol. 70, no. 1, pp. 104–109, 2011.

[221] B. Murienne, J. Jefferys, H. Quigley, and T. Nguyen, "The effects of glycosaminoglycans on the mechanical behavior of the posterior porcine sclera," *Acta Biomaterialia*, submitted 7/2014.

Vita

Theresa Koys Tonge was born in Milwaukee, Wisconsin in 1985. She received a B.S. in Chemical Engineering from the University of Illinois at Urbana Champaign in 2007 and was employed as an R&D Engineer at Cardinal Health in Waukegan, IL and Yorba Linda, CA. She joined Prof. Nguyen's lab at Johns Hopkins University in 2009, obtained an M.S.E. in Biomedical Engineering in 2011 and subsequently enrolled in the PhD program in the Department of Mechanical Engineering. Her research in soft tissue biomechanics has been published in *Acta Biomaterialia* and *Journal of Biomechanical Engineering*. She was awarded First Place at the Master's Level Student Paper Competition in Solid Mechanics at the 2011 ASME Summer Bioengineering Conference, and was a Finalist in the International Student Paper Competition at the 2012 SEM Conference. Starting in October 2014 she will begin employment as a Research Scientist at W. L. Gore and Associates in Elkton, MD.